

Measurement of absolute Drell-Yan cross-sections using a 190-GeV π beam at the COMPASS-II experiment

Marco Meyer-Conde

► To cite this version:

Marco Meyer-Conde. Measurement of absolute Drell-Yan cross-sections using a 190-GeV π beam at the COMPASS-II experiment. Nuclear Experiment [nucl-ex]. Université Paris-Saclay, 2019. English. NNT : 2019SACLS472 . tel-02459225

HAL Id: tel-02459225

<https://tel.archives-ouvertes.fr/tel-02459225>

Submitted on 29 Jan 2020

HAL is a multi-disciplinary open access archive for the deposit and dissemination of scientific research documents, whether they are published or not. The documents may come from teaching and research institutions in France or abroad, or from public or private research centers.

L'archive ouverte pluridisciplinaire **HAL**, est destinée au dépôt et à la diffusion de documents scientifiques de niveau recherche, publiés ou non, émanant des établissements d'enseignement et de recherche français ou étrangers, des laboratoires publics ou privés.

Measurement of Absolute Drell-Yan Cross-Sections using a 190-GeV π^- beam at the COMPASS-II Experiment

Thèse de Doctorat de l'Université Paris-Saclay
préparée à l'Université Paris-Sud

École doctorale n°576 Particules, Hadrons, Énergie, Noyau,
Instrumentation, Imagerie, Cosmos et Simulation (PHENICS)
Spécialité de Doctorat: Physique Hadronique

Thèse présentée et soutenue publiquement le 21 Novembre 2019
à l'Orme des Merisiers, Gif-sur-Yvette, France
par **Marco Meyer-Conde**

Composition du Jury :

Frédéric Fleuret

Directeur de Recherche (CNRS), École Polytechnique (LLR) **Président du Jury**

Catarina Quintans

Docteur, LIP (Portugal) **Rapporteur**

François Arleo

Docteur, École Polytechnique (LLR) **Rapporteur**

Michel Guidal

Directeur de Recherche (CNRS) **Examineur**

Craig D. Roberts

Professeur, Nanjing University (China) **Examineur**

Stéphane Platchkov

Docteur, CEA Saclay (DRF/IRFU/DPhN) **Directeur de Thèse**

Jen-Chieh Peng

Professeur, University of Illinois Urbana-Champaign (USA) **Co-Directeur de Thèse**

Vincent Andrieux

Docteur, University of Illinois Urbana-Champaign (USA) **Co-Encadrant de Thèse
(Invité)**

Aux femmes de ma vie, envers qui je serai éternellement reconnaissant.
À ma Maman, pour ton amour inconditionnel et m'avoir appris à terminer ce que je commence.
À ma Chère Emiko, pour ton soutien quotidien et indéfectible.

Acknowledgment

Beyond its scientific aspects, a Ph.D. thesis is not only a summary of work experience but also a true and deep life experience. It includes peaks and troughs of sadness, hope, and joy, but in the end, I am convinced that we always get what we deserve. These last years were certainly the most life-changing years I experienced. It definitely required passion, devotion, time, and a lot of coffee. I do not consider myself as a lucky person for standing here today and writing these last words. I learned over the last years that sometimes life is hard and you hardly get anything for free. Therefore we should always be proud of us as we are all stepping forward in many ways.

"Success is to be measured not so much by the position that one has reached in life as by the obstacles which he has overcome." — Booker T. Washington

First and foremost, I would like to express my gratitude toward the members of my Ph.D. committee and especially Dr. Frédéric Fleuret who presided it with rigor and integrity. I was honored to defend my Ph.D. thesis in attendance of Pr. Craig D. Roberts, Dr. Michel Guidal and would like to thank them for their time and the interest they showed in my research work. I also deeply thank Dr. François Arleo and Dr. Catarina Quintans for their attentive reading and their detailed reports. Finally, I am also grateful to my supervisors, Pr. Jen-Chieh Peng, Dr. Stephane Platchkov, and Dr. Vincent Andrieux for their support, help, and guidance during these last four years and the final rush before the thesis defense.

I would like to thank you Stephane for making me discover America and this afternoon visiting Chicago together. Such research work would not have been possible without the help of Pr. Matthias Grosse-Perdekamp and Pr. Jen-Chieh Peng who offered me continuous support and trusted me during all these years. During this journey as a Ph.D. student, I had the chance to travel and live in several places. Upon my arrival in Geneva, where I stayed for two years, I had the chance to meet great people working in the COMPASS collaboration. Starting with our spokesperson, Oleg Denisov, but also Johannes Bernhard and Caroline Kathrin Riedl who were the first people I met there. I would like to thank especially Nicolas du Fresne von Hohenesche for the climbing training; Annika Vauth for the hiking sessions we had; Dominik Steffen for the organization of these extreme expeditions; Christophe Menezes Pires for all the hardware knowledges you shared with me; Christian Dreisbach for this early morning we spent together during data taking to make my lame duck (Straws) working. Thank you, Benjamin Moritz Veit, for all the help you provided me while you already had a lot of work to do. Finally, thank you very much for the COMPASS youths at CERN that I may have forgotten. I also want to warmly thank Milena Du Manoir for being so kind to me and for helping me answer the tough questions.

Once I arrived in Paris, I revisited the lab that I left after my Master of Sciences. At this time, my fellows were also second years and I have special thoughts for Jason Hirtz and Aurelie Bonhomme, with whom I shared the first moments. Of course, I would like first to thank the IRFU institute – under the head of Anne-Isabelle Etievre – and the DPhN department where I have been working for a year. I gratefully acknowledge Franck Sabatié, and Hervé Moutarde for their true management skills, being receptive, and who provided appropriate responses regarding some complex situations. Thank you also to Isabelle Richard and Danielle Coret who were of the greatest and nicest company during my breaks and helped me to change my mind. Isabelle, may my orchid be reborn thanks to your green thumb. I cannot forget to thank all the members of the COMPASS group in Saclay: Damien Neyret, Fabienne Kunne, and Yann Bedfer, who together showed me the right way and helped me gain rigor. Thank you Nicole D'Hose I will surely keep you posted, as you always cared so well about me and other young students. Of course, I wish all the best to the last COMPASS successors, Charles-Joseph Naïm and

Brian Ventura. Moreover, among the Saclay youths, I also want to thank Christopher Filosa for being – whatever happens – always so positive; again Brian for the technical and pythonic discussions we had; little Zoé Favier who is certainly the most promising physicist I know, although she just doesn't know it yet; Po-Ju Lin for the depth and the clarity of our discussions; Nicolas Pierre, as we indeed kept track of each other during several years since high-school, I owe you a lot since the University, and I am glad for the time we shared either at CERN, in the car back to Strasbourg, or Paris. I also had the chance to share my office with Antoine Vidon. In this perspective, I would like to truly thank you for making my life in Paris so pleasant. May all our secrets remain ours. Also, without you, I wouldn't have the chance to meet Emiko which was undoubtedly the best moment of my life in 2018.

Along this path, the greatest opportunity I had, was to go to America, experience a new life in the city of Champaign and to finally meet the *Alma Matter*. At this time, I think the words, *Learning, and Labor*, appeared to have never been truer. Despite I was living in the USA, I spent most of my time chatting with my young European love, who already knows how much I care about her. Knowing this, the most famous quote from Bussy-Rabutin revealed to be true. Hopefully, during these hard times, I had the chance to also meet amazing people overseas. Starting with my roommates, Marco De La Rosa and Larone Brim. I had a great time with you guys. Thank you again Larone, such a good mood every day made me smile and changed my daily life. You will always be welcome to France and I hope to see you again. I would like to thank also Shivangi Prasad and Jason Dove to whom I wish the best for their thesis defense. I also thank a lot Ching Him Hugo Leung for the numerous physics discussions and I wish you the best for the remaining time. Finally, I would like also to thank Riccardo Longo for your help, our numerous discussions in Champaign, and hope I gave you in return. I am also truly grateful to also get support from overseas from Bakur Parsamyan who provided wise advice in the analysis but also share from his past experiences. Your advice was definitely the right one.

In addition to this, I have special thoughts towards Pr. Wen-Chen Chang and its team I worked with, namely Takahiro Sawada, Márcia Quaresma, Yu-Shiang Lian, and Chia-Yu Hsieh. I had the chance to travel twice to Taiwan, and surprisingly celebrate twice these famous typhoon holidays. In the early days, I enjoyed working with you Takahiro during these shifts at CERN, and I hope to get new opportunities for working with you soon. Thank you Yu-Shiang for bringing me to the night market, sharing some Japanese dishes in Taipei 101, and of course, thank you for all the help you provided. I wish to give back as much as I can in that regard. Also, thank you, Márcia, for always staying so positive and comprehensive. I learn a lot from you.

My deepest gratitude goes towards you, Vincent, for your patience and guidance. I stopped counting the time during days and nights we were discussing together, whatever the timezone I was. You provided me precious and wise advice even in these times when it gets especially hard and made me understand that a Ph.D. is never finished.

I have a special thought for the Rodicq-Ragazzi-Massebieau family, Marco, Françoise, Alice and Jeremy who have been in my life for many years and kept being supportive to me in any circumstances. Sometimes life goes up and down and I would like also to thank you, Jeanne, for these moments we shared. Despite the pain, you helped me to grow up, so I wish you to flourish in what you like to do.

Finally, I cannot forget my little Meyer-Roth-Schnur-Murray-Friant family for all the kindness and the love you gave me during these years. You always push me, support me, and without all of this I would not succeed. Of course, I can't name everyone, but perhaps Nour, Félix, Rémi, Jean-François, César, Florian, Pierre, and Aurélie who first came to my mind. I saved the best for last, so God bless Rodolphe, Valentin, Douglas, and Raphaël for always taking care of Emiko and me.

Table of Contents

Acknowledgment

Introduction	1
I Internal Structure of Hadrons	5
1 Modern Theory of the Strong Interaction	6
1.1 The Parton Model	6
1.2 Introduction to Quantum Chromodynamics (QCD)	7
1.3 Color Confinement and Asymptotic Freedom	8
1.4 The QCD improved Parton Model	9
2 The Deep Inelastic Scattering	11
3 The Drell-Yan Annihilation Process	14
3.1 Introduction to the Drell-Yan Process	14
3.2 General Expression of the Cross-Section	17
3.3 Lorentz Invariant Cross-Sections	18
3.4 Experimental Overview	19
4 Theoretical Overview: State-of-the-Art	21
4.1 Drell-Yan Angular Distributions and Lam-Tung Relation	21
4.2 Cold Nuclear Matter	23
4.3 A-dependence of Muon Pair Production	25
4.4 Soft-Gluon Resummation	26
4.5 Parton Distribution Functions of the π^-	27
4.5.1 Experimental Overview	27
4.5.2 Global Analysis of the Pion PDFs	30
4.5.3 Available Pion PDF Extractions	31
II The COMPASS-II Experiment	33
5 Hadron Beam Production	35
6 Target Setup and Beam Absorber	38
7 Trigger and Veto Systems	40
7.1 Single Muon Subsystems	40
7.2 Dimuon Trigger Logic	42
7.3 VETO Logic	43
7.4 Random Triggers	44
8 Tracking detectors	44
8.1 Very Small Area Trackers	44
8.2 Small Area Trackers	46
8.3 Large Area Trackers	47
9 Muon Identification	49

10 Data Acquisition System	50
10.1 Data Flow	50
10.2 DAQ Scalers	51
 III Straw Tube Detector	 53
11 Operating Principle	54
11.1 Proportional chambers	54
11.2 Straw Tube Technology	56
11.2.1 Detector Structure	56
11.2.2 Gas Mixture	58
11.2.3 Front-End Electronics	58
12 Calibration and Characterization in 2015	58
12.1 Calibration Methods	58
12.1.1 Alignment and Residual Distributions	59
12.1.2 Relation $R(T)$	60
12.1.3 T_0 Calibration	60
12.1.4 Detector Time Gate	60
12.1.5 X-ray Correction	61
12.2 Results: Performance Studies	62
13 Results: Hardware upgrades in 2016-2017	62
13.1 Gas System Upgrade	62
13.2 Air Contamination Measurement	64
13.3 Gas Filter Refurbishing	64
 IV First Level Data Production	 65
14 COMPASS Software Chain	66
14.1 Data Decoding and Calibration Database	66
14.2 Data Reconstruction	67
14.3 Monte-Carlo Simulation	68
15 Petascale Computing Resources	69
15.1 A New COMPASS Production Workflow	69
15.2 The Blue Waters Facility	71
15.3 A New Perspective: Frontera Supercomputer	71
16 New Production Framework: ESCALADE	72
16.1 Analysis Purpose	72
16.2 Software Architecture	73
16.3 Functional Checks	74
17 Results: Official COMPASS Drell-Yan Productions	74
18 Results: Official Monte-Carlo Simulations	76
 V Luminosity Measurement in 2015	 77
19 Introduction to Fixed Target Luminosity	78
19.1 Instantaneous Pion-Nucleon Luminosity, L	78
19.2 The Integrated Luminosity, \mathcal{L}	79

20 Transverse Nucleon Density	79
20.1 Nuclear Target Densities	80
20.2 Polarized-Target Nucleon Densities	80
20.2.1 Packing Factor, P_F	80
20.2.2 Component Fractions	82
20.2.3 Target Fiducial Volume	83
20.2.4 Isotopic Composition of the 2015 PT targets	84
20.2.5 Temperature Dependence	85
20.2.6 Summary Table	86
21 Beam Flux	87
21.1 Ionization Chamber Flux	87
21.2 Absolute Flux Estimation	88
21.2.1 Beam Track Reconstruction	89
21.2.2 Beam Meantime	90
21.2.3 Time in Spill Range	92
21.3 Beam Attenuation	93
21.3.1 Mean Free Path of a Pion	93
21.3.2 Cross Cell Selection	94
21.3.3 Flux Attenuation as a function of Z_{vtx}	94
21.4 Data Inhibition	97
21.4.1 DAQ Lifetime	98
21.4.2 VETO Lifetime	99
22 Stability Studies	102
22.1 Apparatus Stability	102
22.1.1 Spill by Spill Analysis	102
22.1.2 Run by Run Analysis	102
22.2 Beam Flux Stability	104
22.2.1 Bad Spill List	104
22.2.2 Period by Period Analysis	106
22.3 Uncorrelated Background Events	108
22.3.1 Contextualization	108
22.3.2 Beam Structure Study	109
23 Results: Systematic Uncertainties, Summary, Figure of Merit	111
 VI Measurement of Drell-Yan Cross-Sections	 113
24 Presentation of the 2015 Data Set	114
24.1 Data Taking Conditions	114
24.2 Event Selection	115
24.3 Additional Studies	119
24.3.1 Period Compatibility	119
24.3.2 Dimuon Data Yield	119
24.3.3 Combinatorial Background Estimation	121
24.3.4 Target Tomography and Beam Positioning	122
24.4 Drell-Yan Kinematic Distributions	124

25 Acceptance Correction	126
25.1 Introduction	126
25.2 Event Generation	127
25.3 Spectrometer Acceptance	130
25.3.1 Geometrical Acceptance	130
25.3.2 Event Migration and Detector Inefficiencies	131
25.3.3 Trigger System Efficiency	134
25.3.4 Overcorrection of the Beam Telescope Acceptance	137
25.4 Multi-Dimensional Acceptance	138
25.5 Model-Dependent Uncertainties	141
26 Introduction to the Absolute Drell-Yan Cross-Sections	145
26.1 The Drell-Yan Cross-Section Per Nucleon	145
26.2 Perturbative QCD Predictions at NNLO	145
26.2.1 Parton Level Monte Carlo, DYNNLO	145
26.2.2 Drell-Yan Predictions at COMPASS energy ($\sqrt{s} = 18.90$ GeV)	146
26.3 Discussion on the Single Differential Cross-Sections $d\sigma/dx_F$	149
26.4 Summary of the Final Uncertainties	150
27 Results: Extraction of the Drell-Yan 2015 Cross-Sections	151
27.1 Study of the Double Differential Drell-Yan Cross-Sections	151
27.1.1 Comparison with E615 data and DYNNLO simulation	151
27.1.2 Cross-Section $d^2\sigma/d\sqrt{\tau}dx_F$ in the COMPASS Kinematic Range	155
27.1.3 Summary Table	156
27.2 A-Dependence in Pion-Nucleus Interactions	158
27.2.1 Evaluation of the α parameter	158
27.2.2 Summary Table	160
27.3 Drell-Yan Cross-Sections at High- q_T	161
27.3.1 Transverse Momentum Distributions	161
27.3.2 The <i>Kaplan Form</i> : <i>Ad-Hoc</i> Fitting Function	161
27.3.3 Studies as a function of x_F , $M_{\mu\mu}$, \sqrt{s}	162
27.3.4 Invariant Cross-Sections at High- q_T , $Ed^3\sigma/d\vec{q}^3$	164
27.3.5 Summary Table	166
27.4 Invariant Double Drell-Yan Cross-Sections $M^2d^2\sigma/dx_1dx_2$	168
27.4.1 Motivations	168
27.4.2 Summary Table	169
Conclusions and Future Prospects	171
Appendix	173
Résumé en Français	191
Bibliography	197

Introduction

A bit of history

It has been 100 years from now, in 1919, that Ernest Rutherford made the proof of the existence of the proton using nitrogen nuclei targeted with alpha particles. Initially denoted as a *hydrogen atom*, the accurate definition of the proton appeared in 1920. A decade later in 1932, James Chadwick discovered the neutron and both protons and neutrons were considered at that time as *elementary particles*.

Owning of the discovery of a large variety of other particles, such as muons in 1937 by Carl D. Anderson, or the π meson in 1947 by Cecil F. Powell, the classification of these particles have appeared to be a challenging task. The great physics quest, also known as a quest for symmetries, began to organize this particle zoo. As a successful example, particles such as the proton and the neutron were eventually classified among other particles (Fig. 1a), following the Eightfold Way model [1] proposed by Murray Gell-Mann and Yuval Ne'eman in 1961. In 1964, this hadron classification model successfully led to the prediction of the baryon Ω^- (Fig. 1b) according to symmetry conservation. As an illustration, Fig. 1 shows the baryon octet and decuplet of the Eightfold Way model.

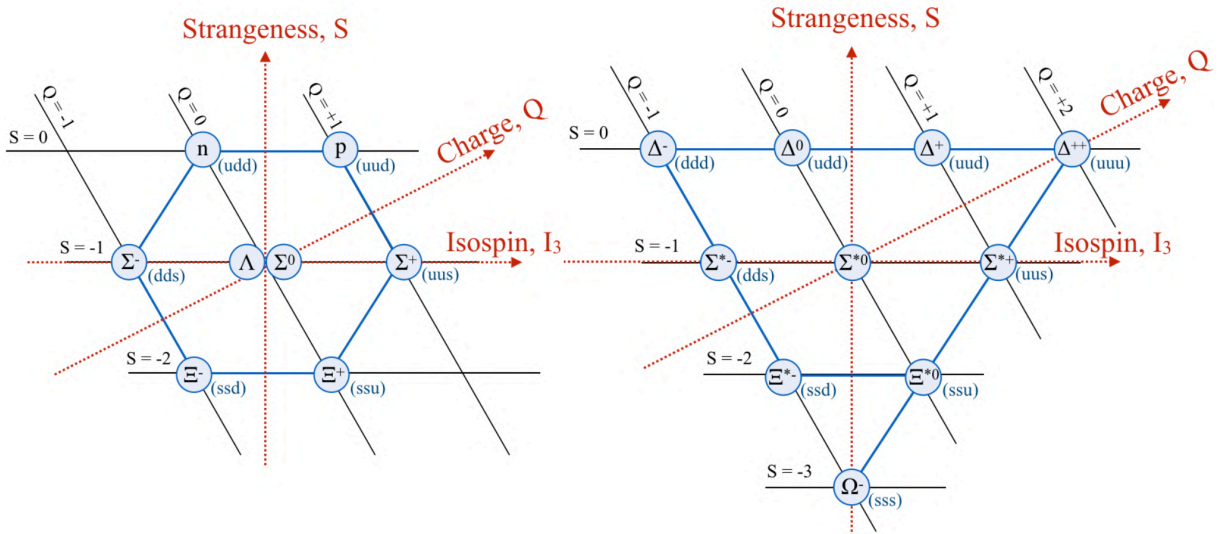


Figure 1: (a) Left: Baryon Octet $J^P = \frac{1}{2}^+$; (b) Right: Baryon Decuplet $J^P = \frac{3}{2}^+$

Later in 1964, Murray Gell-Mann and Georges Zweig postulated the existence of elementary subatomic particles in two independent papers [2] [3], known nowadays as quarks. These quarks are consequently assumed to arrange themselves into hadron particles. The first evidence of an internal structure in nucleons was revealed in late 1960 at SLAC¹ [4] using deep inelastic electron-nucleon scattering at high energy. In the early years, this model was composed of three quarks: the quark *up* and *down*, which compose neutrons and protons, and the *strange* quark (e.g., kaon).

¹Stanford Synchrotron Radiation Lightsource (Menlo Park, CA, USA)

The existence of charmed quarks was theorized first by Bjorken and Glashow in 1964 [6] and supported by Glashow, Iliopoulos, Maiani in 1970, as a *cure* of the hadron weak interactions in the description of the GIM mechanism [7].

Consequently, in 1974, the validity of the quark model was again strongly reinforced, when the discovery of the J/Ψ particle was confirmed at SLAC by Burton Richter et al. [8] and at BNL² by Samuel Ting *et al.* [5]. This breakthrough discovery, as part of the *November Revolution*, confirmed the existence of the charm quark.

Following this epoch of great discoveries aiming to establish a Standard Model of particle physics, some natural questions arose, such as the origin of quantum numbers and their relation with the intrinsic numbers of subatomic particles. Consequently later in 1987, the EMC³ collaboration measured a contribution of the quark spin to the total spin of the nucleon [9]. A possible decomposition of the nucleon spin into quark, gluon, and orbital contributions is proposed in Eq. 1 (spin sum rule), and illustrates the beginning of the proton spin puzzle.

$$\frac{1}{2} = \frac{1}{2} \Delta\Sigma(Q^2) + \Delta G(Q^2) + L_q(Q^2) + L_g(Q^2) \quad (1)$$

where $\Delta\Sigma$, is the quark spin contribution to the nucleon spin

ΔG , refers to the gluon spin contribution to the nucleon spin

$L_{q/g}$, is the orbital momentum of the quark, gluons respectively

and Q^2 , is the energy scale related to the photon virtuality

This example led to further investigations of the proton spin decomposition by several other experiments at CERN⁴, DESY⁵, SLAC, JLAB⁶, and RHIC⁷. It has recently been established that quarks carry only $30\% \pm 4\%$ of the nucleon spin at $Q^2 = 3 \text{ GeV}^2/c^2$. Additionally, ΔG was found as very close to zero [10] and the orbital momentum remains under study.

In 2005, the measurement of the non-zero Sivers function *via* Deep Inelastic Scattering (DIS) by HERMES [11] and COMPASS [12] raised the interest of the study of the Drell-Yan process by crossing

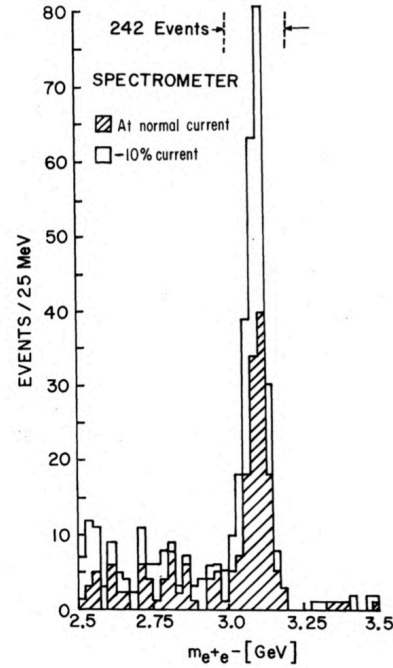


Figure 2: Mass spectrum showing the existence of the J/Ψ and taken from [5]

²Brookhaven National Laboratory (Upton, NY, USA)

³European Muon Collaboration

⁴European Organization for Nuclear Research (Meyrin, Switzerland)

⁵Deutsches Elektronen-Synchrotron (Hamburg, Germany)

⁶Thomas Jefferson National Accelerator Facility (Newport News, VA, USA)

⁷Relativistic Heavy Ion Collider at BNL (Upton, NY, USA)

symmetry with DIS. Indeed, the Drell-Yan process ($q\bar{q} \rightarrow \ell^- \ell^+$ at lowest order) is also an excellent tool to study the properties of the Quantum Chromodynamics (QCD) physics. Therefore, the measurement of the polarized single-spin asymmetries through Drell-Yan became a fundamental verification of TMD⁸ factorization in QCD [13].

Finally, Drell-Yan data offers valuable information about the partonic composition of the beam, but also information about cold nuclear matter effects in the target. Therefore, the evaluation of the Drell-Yan cross-section using COMPASS data might significantly contribute to a better knowledge of these topics.

Outline of this Ph.D. work

This Ph.D. work is decomposed into six chapters. The first chapter introduces the theoretical framework of the QCD theory and focuses on the Drell-Yan process. The interest in cross-section extraction will be then emphasized by summarizing the state-of-the-art of some Drell-Yan advanced analysis.

The second and third chapters refer to the hardware aspects of the COMPASS-II experiment. As the COMPASS-II spectrometer is a versatile apparatus, the second chapter highlights only the setup related to the Drell-Yan data taking. The third chapter provides further hardware information about the Straw detector, ST03, supported by the University of Illinois since 2014. Part of this Ph.D. work consisted of maintaining the ST03 detector from 2016 to 2018 in collaboration with the Joined Czech group from Prague.

The fourth chapter is mainly software related and includes an overview of the COMPASS reconstruction software, the MC simulation of the COMPASS apparatus, and the working principle of a new data production framework called ESCALADE to organize the large production of COMPASS data. During this work, a new petascale computing center was used for intensive computing jobs, such as track reconstructions of the COMPASS data or MC simulations.

Finally, the fifth and sixth chapters give the detailed methodology related to the extraction of the beam luminosity, the computation of the acceptance correction, and the Drell-Yan cross-section. The obtained results are eventually compared with the predictions of Drell-Yan cross-section and already published results.

Disclaimer

This manuscript is written in the light of the COMPASS analysis status of the Drell-Yan working group dated November 2019. The results presented in this Ph.D. thesis are a personal interpretation of the COMPASS 2015 data.

⁸Transverse Momentum Dependent

Chapter I

Internal Structure of Hadrons

1	Modern Theory of the Strong Interaction	6
1.1	The Parton Model	6
1.2	Introduction to Quantum Chromodynamics (QCD)	7
1.3	Color Confinement and Asymptotic Freedom	8
1.4	The QCD improved Parton Model	9
2	The Deep Inelastic Scattering	11
3	The Drell-Yan Annihilation Process	14
3.1	Introduction to the Drell-Yan Process	14
3.2	General Expression of the Cross-Section	17
3.3	Lorentz Invariant Cross-Sections	18
3.4	Experimental Overview	19
4	Theoretical Overview: State-of-the-Art	21
4.1	Drell-Yan Angular Distributions and Lam-Tung Relation	21
4.2	Cold Nuclear Matter	23
4.3	A-dependence of Muon Pair Production	25
4.4	Soft-Gluon Resummation	26
4.5	Parton Distribution Functions of the π^-	27
4.5.1	Experimental Overview	27
4.5.2	Global Analysis of the Pion PDFs	30
4.5.3	Available Pion PDF Extractions	31

This chapter describes some theoretical aspects related to the theory of Quantum Chromodynamics and focuses on the study of the Drell-Yan process involving a π^- beam. A state-of-the-art is also presented together with phenomenological aspects, where the COMPASS data might contribute.

1 | Modern Theory of the Strong Interaction

In analogy to the Van der Waals force, which binds atoms together to form molecules, the strong interaction binds quarks into nucleons. The strong force, known as one of the four fundamental forces in nature, has been described in the framework of Quantum Chromodynamics (QCD), in which quarks interact via gluons by exchanging color charges. At this time, QCD is widely accepted in the physics community as a pillar of the Standard Model (SM).

1.1 The Parton Model

In the early years, hadrons were assumed to be elementary particles. As an example, this assumption was reasonable in the low-energy limit described by the Rutherford scattering. However, the evidence of an internal structure was first raised from a series of electron-nucleon scattering experiments at SLAC starting in 1967 [14].

Indeed, at higher energy scale ($Q \gg \Lambda_{QCD}$) hadrons breaks up and reveals their composite nature made of quarks, antiquarks, and gluons initially called partons by Richard Feynman. The parton model, proposed by Feynman in 1969, describes the internal structure of nucleons as the composition of partons. In the case of two colliding hadrons A and B , the corresponding cross-section follows the expression :

$$d\sigma_{AB} \simeq \sum_{a,b} \int_0^1 dx_1 f_{a/A}(x_1) \times \int_0^1 dx_2 f_{b/B}(x_2) \times d\hat{\sigma}_{ab} \quad (1.1)$$

The labels a and b refer to partons in the nucleon A and B respectively. The density distribution $f_{a/A}(x_1)$, also known as Parton Distribution Function (PDF), is the probability of finding a parton a, b carrying a momentum fraction $x_{1,2}$ in the corresponding nucleon. Eq. 1.1 highlights the independent nature of the hard and the soft production mechanisms assumed by the factorization theorem [15, 16]. This theorem also ensures the *universality* of the measured PDF, regardless of the physics process involved. On the one hand, the hard-process, responsible for the short-range interactions, is described by the partonic cross-section $d\hat{\sigma}_{ab}$. On the other hand, the PDFs carry the soft information related to the initial-state. Figure 1.1 shows an illustrative example of the interaction between $u - \bar{u}$ quarks in a $\pi^- p$ interaction.

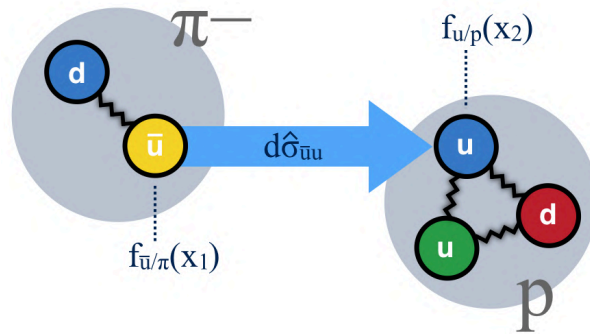


Figure 1.1: Illustration of the interaction between $u - \bar{u}$ quarks in a $\pi^- p$ collision, where u carries a fraction x_1 of the initial beam four-momentum and \bar{u} carries a fraction x_2 of the targeted proton four-momentum.

1.2 Introduction to Quantum Chromodynamics (QCD)

Near to the well-defined theory of Quantum Electrodynamics (QED), the Quantum Chromodynamics (QCD) is also known as a gauge theory. In its framework, the QED theory is described using the U(1) local gauge, while the more complex QCD theory is specified using a non-abelian SU(3) symmetry group. This QCD gauge theory involves eight massless gluons corresponding to the eight generators of the SU(3) symmetry. The Lagrangian of the free quark motion is expressed as follows:

$$\mathcal{L}_{\text{free}} = \sum_{q=1}^6 \bar{\psi}_i^{(q)} (i\not{D} - m_q) \psi_j^{(q)} \quad (1.2)$$

In Eq. 1.2, q refers to the six quark flavors ($N_f = 6$) subjected to the strong interaction. $\psi^{(q)}$ corresponds to the Dirac spinor of the quark q and m_q the mass of the quarks. i and j are color indices in the range $\{1..N_c\}$ with the number of color charges, $N_c = 3$. QCD requires that the Lagrangian must be invariant under the local SU(3) gauge transformation $U(x)$:

$$\psi(x) \longrightarrow \psi'(x) = U(x)\psi(x) = \exp \left[ig_s \vec{\alpha}(x) \cdot \hat{\mathbf{T}} \right] \psi(x)$$

where $\hat{\mathbf{T}} = \{T^a\} = \left\{ \frac{1}{2} \lambda^a \right\}$ are the eight generators of SU(3) related to

Gell-Mann matrices, λ_i , with a the color index $\in \{1..8\}$

$\vec{\alpha}(x) = \{\alpha^a(x)\}$ are eight functions of the space-time coordinates x (rotation angles).

$g_s = \sqrt{4\pi\alpha_s}$ refers to the QCD coupling variable

$U(x)$ is a unitary 3×3 matrix acting on the color state $\psi(x)$

Under this local gauge transformation, Eq. 1.2 becomes: $i\gamma^\mu (\partial_\mu + ig_s (\partial_\mu \vec{\alpha}(x)) \cdot \hat{\mathbf{T}} - m_q) \psi^{(q)} = 0$. In this equation, the terms $\partial_\mu \alpha^a(x)$ are identified as eight gauge fields G_μ^a . Moreover, the conservation of the local SU(3) symmetry requires the introduction of the covariant derivative term $\partial_\mu \rightarrow D_\mu = \partial_\mu + ig_s G_\mu^a T^a$ to ensure gauge invariance.

The dynamics of the gluon field is described by a Lagrangian kinematic term in Eq. 1.3. Moreover, the non-commutative nature of the SU(3) group led to the introduction of an additional term in the field-strength tensor: $G_{\mu\nu}^i = \partial_\mu G_\nu^i - \partial_\nu G_\mu^i - g_s f_{ijk} G_\mu^j G_\nu^k$

$$\mathcal{L}_{\text{kin}} = -\frac{1}{4} G_{\mu\nu}^a G_a^{\mu\nu} \quad (1.3)$$

Finally, the gauge-invariant QCD Lagrangian is given by the Eq. 1.4. The first line of this Lagrangian equation can be intuitively decomposed into four types of Feynman diagrams, as shown in Fig. 1.2.

$$\begin{aligned} \mathcal{L}_{\text{QCD}} &= \sum_{q=1}^{N_f} \bar{\psi}^{(q)} (i\not{D} - m_q) \psi^{(q)} - \frac{1}{4} G_{\mu\nu}^a G_a^{\mu\nu} \\ &= \underbrace{q\bar{q}}_{(a)} + \underbrace{G^2}_{(b)} + \underbrace{g_s q\bar{q}G + g_s G^3 + g_s^2 G^4}_{(c)+(d)} \end{aligned} \quad (1.4)$$

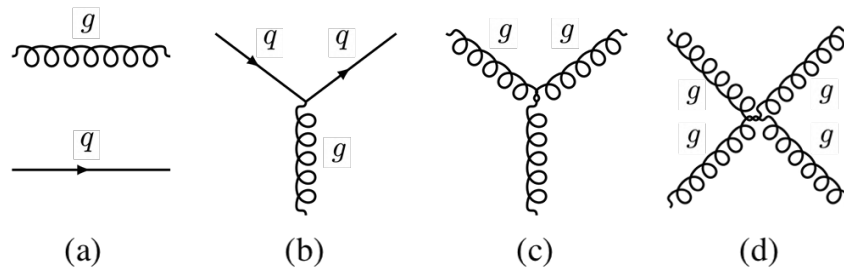


Figure 1.2: (a) Quark-gluon propagators; (b) Quark-Gluon coupling; (c,d) Self-interacting gauge bosons

The first case (a) corresponds to the propagators of quarks and gluons. The second term (b) describes the interaction between quarks and gluons. Finally, the last terms (c,d) are specific to the SU(3) local gauge-invariant theory and describes the self-interaction of the gluons as triple and quartic vertices.

1.3 Color Confinement and Asymptotic Freedom

In the QCD theory, the fundamental parameters are the quark masses m_q and the g_s quantity. The g_s parameter can also be expressed as the coupling strength $\alpha_s(Q^2) = g_s^2(Q^2)/4\pi$, where Q refers to the hard scale of a process. The origin of α_s evolution, as a function of Q^2 , comes from the scale dependence of the gauge theory in QCD. Eq. 1.5 arises from the renormalization theory:

$$\alpha_s(Q^2) = \frac{\alpha_s(\mu^2)}{1 + B \alpha_s(\mu^2) \ln \left(\frac{Q^2}{\mu^2} \right)}, \text{ with } B = \frac{(11N_c - 2N_f)}{12\pi} \quad (1.5)$$

In the regime of non-perturbative QCD, quarks are confined into a color-neutral hadron. This effect is known as the *confinement* phenomenon. Oppositely, in the perturbative QCD (pQCD) at large Q^2 , quarks behave like quasi-free particles. This second phenomenon described by Politzer [17], Gross, and Wilczek [18], is known as *asymptotic freedom*. A fundamental parameter Λ_{QCD} , in the order of few hundred MeV, defines the separation between the perturbative and non-perturbative regime.

As QCD is a gauge field theory, the effective strength of the interaction $\alpha_s(\mu^2)$ at the vertex point is determined by a renormalization factor μ . In the QED theory, this factor is chosen to avoid divergence of loop diagrams at large scale. Indeed, the electromagnetic coupling α_{QED} becomes stronger when Q^2 increases: it often refers to the *charge screening* of QED in the literature. At low energy scale, the coupling constant matches the measured fine structure constant: $\alpha(\mu^2 \simeq 0) = \frac{1}{4\pi\epsilon_0} \frac{e_0^2}{\hbar c}$.

By analogy to QED, the renormalization factor μ of the QCD theory is chosen to avoid divergences of the theory owing for example gluon self-interactions. In the perturbative regime ($\mu^2 \gg \Lambda_{QCD}^2$), a solution for Eq. 1.5 is obtained in the 1-loop approximation from the renormalization group equations (RGE):

$$\alpha_s(Q^2 \simeq \mu^2) = \frac{1}{B \ln \left(\frac{Q^2}{\Lambda_{QCD}^2} \right)}, \text{ with } \Lambda_{QCD} \simeq \text{few } 100 \text{ MeV} \quad (1.6)$$

For a given physics process, the strength of the coupling is expressed as a function of the hard scale Q , such that $Q^2 \simeq \mu^2$. Short-distance interactions, at a high momentum ($Q \gg \Lambda_{QCD}$), are well described by the perturbative QCD. Fig. 1.3 shows some experimental measurements of $\alpha_s(Q^2)$ in the

perturbative regime through different channels. On the opposite, the soft part, related to long-distance interactions, has a non-perturbative origin, cannot be described analytically, and consequently requires a phenomenological approach.

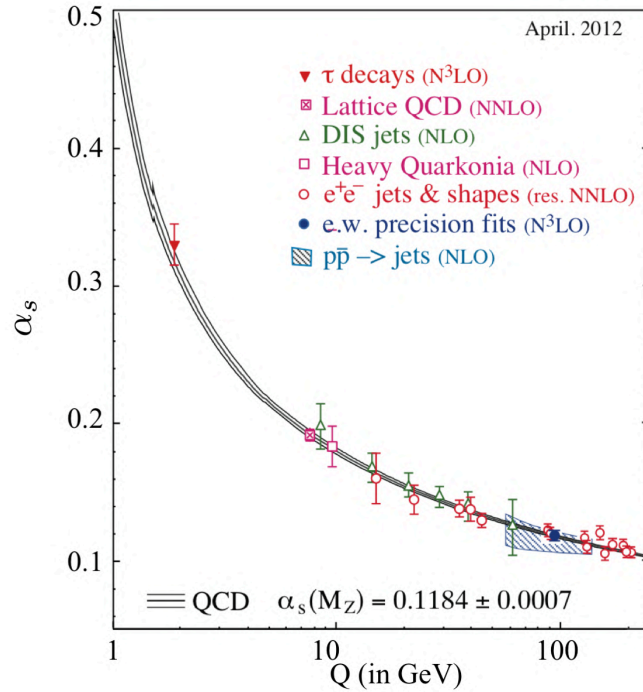


Figure 1.3: Evolution of the strong coupling constant α_s as a function of Q [19]

1.4 The QCD improved Parton Model

In the limit of an experimental measurement, the asymptotic freedom ($Q^2 \rightarrow +\infty$) will no longer be assumed and leads to the introduction of a finite energy Q_0 , such that $Q^2 \rightarrow Q_0^2$. It results in a QCD gluon field in the description of the parton model. Therefore, in addition to the initial renormalization factor μ , a second arbitrary scaling parameter μ_F is introduced to renormalize the collinear gluon contribution. In the following, μ_F is chosen as $\mu_F \simeq \mu$. Fig. 1.4 illustrates the screening of the gluon radiation in the initial-state when a virtual photon interacts below the threshold $Q^2 = Q_0^2$.

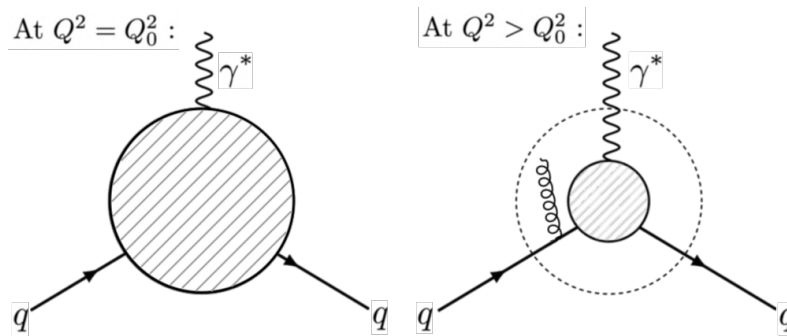


Figure 1.4: Illustration of the gluon radiation, this effect is of the order of $O(\alpha_s \ln(Q^2))$

Consequently, the following three processes involving gluons, allowed by the QCD Lagrangian, arise : gluon radiation ($q \rightarrow qg$), gluon splitting ($g \rightarrow gg$), and quark-antiquark pair production ($g \rightarrow q\bar{q}$). The

introduction of these corrective terms leads to a logarithmic dependence in Q^2 of the physical observables. The scale dependence of the PDFs¹ and FFs² is described by the DGLAP³ equations [20].

$$\begin{aligned} \frac{dq_i(x, Q^2)}{d\ln(Q^2)} &= \frac{\alpha_s(Q^2)}{2\pi} \int_x^1 \left(q_i(z, Q^2) P_{qq} \left(\frac{x}{z} \right) + g(z, Q^2) P_{qg} \left(\frac{x}{z} \right) \right) \frac{dz}{z} \\ \frac{dg(x, Q^2)}{d\ln(Q^2)} &= \frac{\alpha_s(Q^2)}{2\pi} \int_x^1 \left(\sum_i q_i(z, Q^2) P_{gq} \left(\frac{x}{z} \right) + g(z, Q^2) P_{gg} \left(\frac{x}{z} \right) \right) \frac{dz}{z} \end{aligned} \quad (1.7)$$

At the lowest order, these equations are driven by the four splitting functions : $P_{qq}, P_{qg}, P_{gq}, P_{gg}$. These functions, $P_{ji}(x/z)$, can be interpreted as a density probability of turning a parton i of momentum fraction z into a parton j carrying a momentum fraction x of the initial momentum.

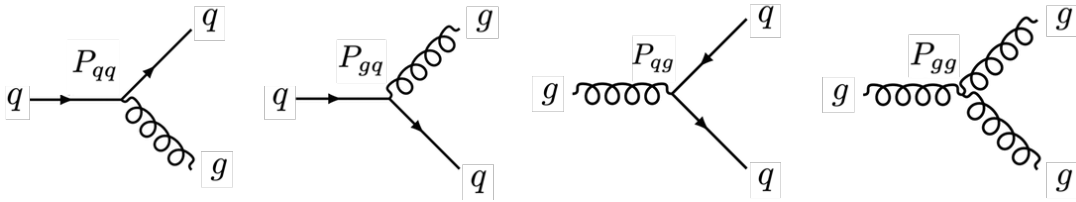


Figure 1.5: Feynman diagrams for lowest order splitting functions $P_{qq}, P_{qg}, P_{gq}, P_{gg}$.

Finally, Fig. 1.6 illustrates the Q^2 evolution introduced by the DGLAP equations for quark and gluon PDFs. This figure shows PDFs at two different energy scales. This results have been obtained from the quark and gluon PDFs extracted by the CT14 collaboration at NNLO⁴.

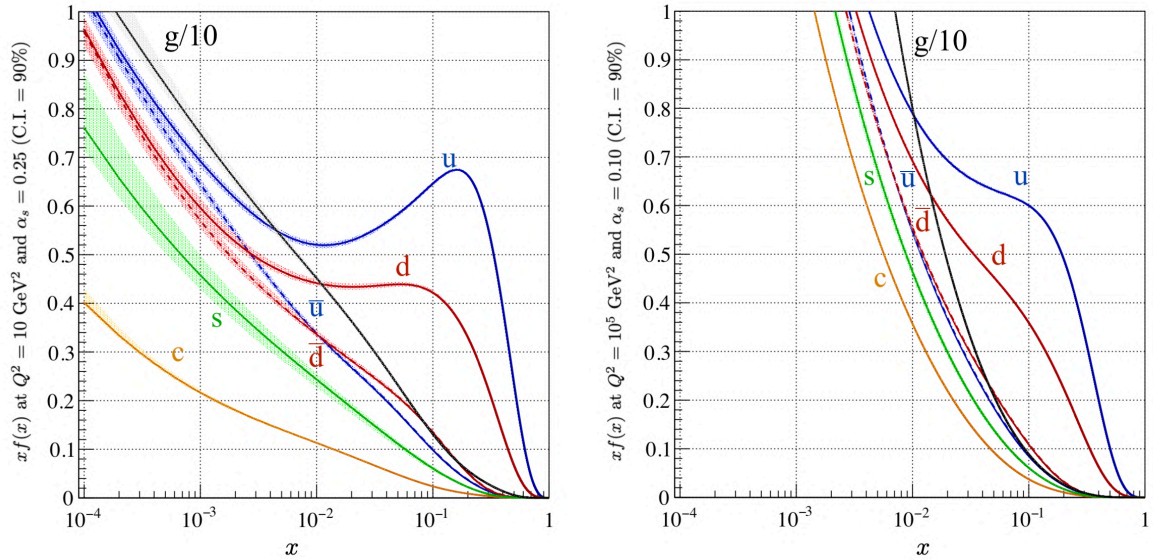


Figure 1.6: Comparison of the distribution $xf(x)$ from CT14nnlo (C.I = 90%) at $Q^2 = 10 \text{ GeV}^2$ (left) and $Q^2 = 10^5 \text{ GeV}^2$ (right).

¹Parton Distribution Functions

²Fragmentation Functions

³Dokshitzer-Gribov-Lipatov-Altarelli-Parisi

⁴Next-To-Next Leading Order

2 | The Deep Inelastic Scattering

Deep Inelastic Scattering (DIS) has played a fundamental role in determining the composite nature of the proton and the existence of quarks. Using a probe, such as e^- , that interacts in a well understood electromagnetic interaction, makes it a privileged channel for such studies. In DIS, only the outgoing lepton is measured. The hard scale Q is defined as the negative four-momentum squared of the virtual photon. At a large Q^2 scale, the DIS is an extension of the Rutherford scattering, where the lepton knocks a quark out of the nucleon. It is interesting to note that DIS is a highly inelastic process as far as the target nucleon is concerned. In the quark-parton model, DIS can be considered as an *elastic scattering* between the electron and the quark.

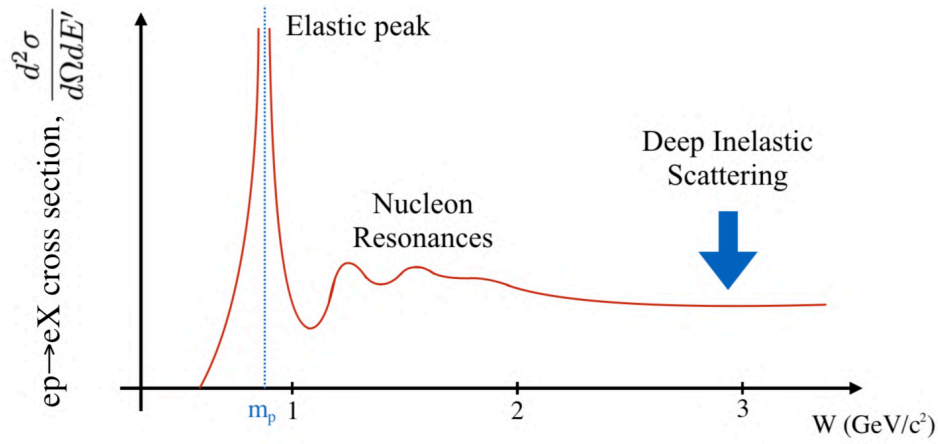


Figure 2.1: Typical behavior of the electron–proton differential cross section as a function of the invariant hadron mass W in the final-state. It illustrates the transition between elastic scattering, quasi-elastic (or nucleon resonances) and deep inelastic scattering [21]

At the Born level, DIS is a process described by the exchange of a virtual photon γ^* (or a weak boson Z^0 for collider energies) between an incoming lepton beam scattering off a nucleon target, as illustrated in Fig. 2.2.

$$\ell(k) + N(P) \longrightarrow \ell(k') + X$$

The momentum of the incoming and outgoing leptons are measured. The hadronic final-state X consists of many particles. This process is called *inclusive* when the hadronic final-state is not measured. The *semi-inclusive* DIS refers to the case where at least one hadron is measured in the final-state.

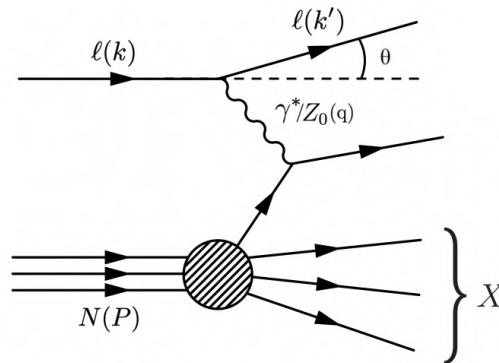


Figure 2.2: Feynman diagram of the inclusive deep inelastic process

Kinematic of DIS. Two independent variables, often chosen as (x, Q^2) , are sufficient to describe the inclusive DIS process. However, other kinematical combinations would also be possible. The kinematics of the DIS process is obtained from the four-momentum of the lepton k , and k' , in the initial and final-state. In the context of a fixed-target experiment, the target four-momentum vector is $P = (M, \vec{0})$. The Bjorken- x scaling variable is interpreted as the nucleon momentum fraction carried by the quark, and the hard scale of the reaction Q^2 is given by the negative four-momentum squared of the exchanged virtual photon. The center-of-mass energy of the photon-nucleon system is denoted $W = (P + q)^2$, and the DIS kinematic region is defined in the limit of $W \gg M^2$ and $Q^2 > 1$.

$$\begin{cases} Q^2 &= -q^2 = -(k - k')^2 \\ x &= \frac{Q^2}{2P \cdot q} \end{cases} \quad (2.1)$$

Other variables, such as the beam momentum fraction carried by the virtual photon denoted y or the photon energy ν in the target rest frame, are widely used in the literature and defined as follows.

$$y = \frac{P \cdot q}{P \cdot k} \quad \nu = \frac{P \cdot q}{M} \quad (2.2)$$

Quark Parton Model. The QPM¹ is defined in the *infinite momentum frame*. In that frame, the nucleon has a very large momentum such that the transverse component of partons is neglected. The expression of the unpolarized differential cross-section for DIS, Eq. 2.3 is derived from the contraction of the leptonic tensor $L^{\mu\nu}$ and hadronic tensor $W_{\mu\nu}$. In the QPM, the hadronic tensor is expressed as the incoherent sum of the interactions with each parton.

$$\frac{d^2\sigma}{dx dQ^2} = \frac{4\pi\alpha^2}{Q^4} \left[(1-y) \frac{F_2(x, Q^2)}{x} + y^2 F_1(x, Q^2) \right] \quad (2.3)$$

In the late 60s, two features related to the two spin-independent structure functions F_1 and F_2 were found at SLAC. The first one is known as Bjorken-scaling, where $F_1(x, Q^2)$ and $F_2(x, Q^2)$ were found to be almost Q^2 independent, indicative of the point-like nature of quarks. The two spin-independent structure functions, $F_1(x)$ and $F_2(x)$, interpreted as the number density of quarks and the quark momentum distribution functions respectively, are given in the QPM as:

$$\begin{cases} F_1(x) &= \frac{1}{2} \sum_q e_q^2 [q(x) + \bar{q}(x)] \\ F_2(x) &= x \sum_q e_q^2 [q(x) + \bar{q}(x)] \end{cases} \quad (2.4)$$

where $q(x)$ refers to the PDF of the interacting quark
 e_q corresponds to the quark charge

The second feature observed is the relation between $F_1(x)$ and $F_2(x)$, also known as the Callan-Gross relation [22]. This relation reflects the spin- $\frac{1}{2}$ nature of the quarks.

$$F_2(x) = 2xF_1(x) \quad (2.5)$$

¹Quark Parton Model

Scaling Violation. The world data of the proton structure function F_2^p is shown in Fig. 2.3. Over this broad coverage in x , this plot reveals the scaling violation of the Q^2 variable and the necessity to account for additional QCD corrections in the parton model. This correction is interpreted as the gluon contribution to the DIS cross-section.

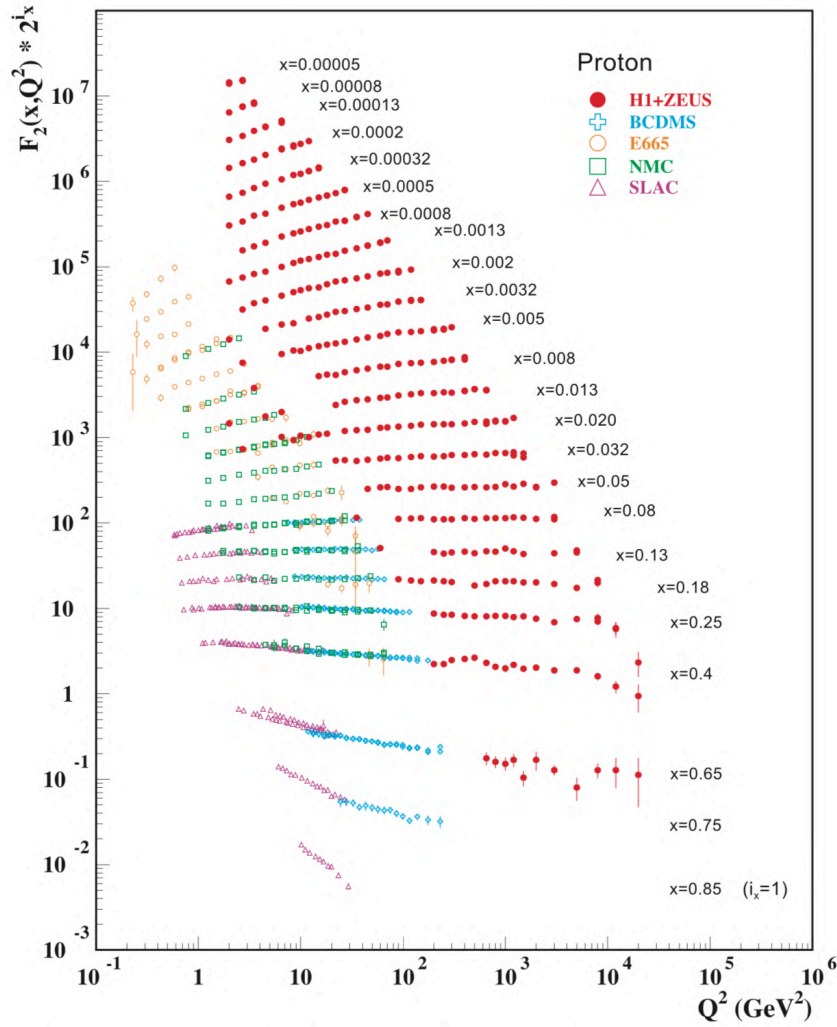


Figure 2.3: The world data of the proton structure function F_2^p as a function of Q^2 for different bins of x [23]

3 | The Drell-Yan Annihilation Process

3.1 Introduction to the Drell-Yan Process

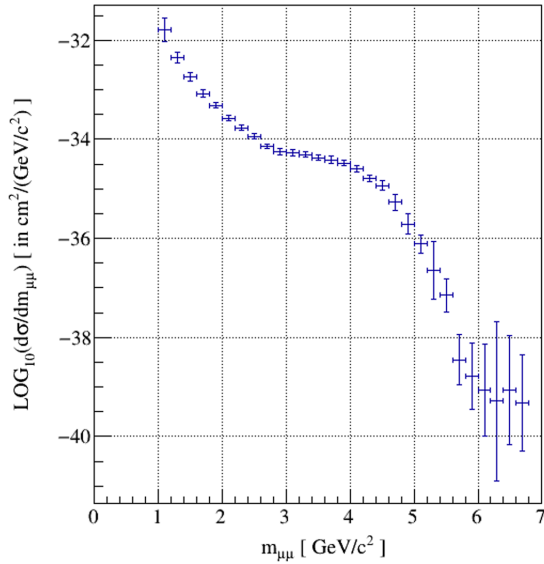


Figure 3.1: Differential cross-section as a function of the dimuon mass $m_{\mu\mu}$ in high-energy hadron collisions at $E_{\text{proton}} = 28.5$ GeV [24]

The first experiment measuring hadro-production of lepton pairs took place at AGS¹ in Brookhaven in 1968 and was reported few years later in November 1970. Christenson, Hicks, Lederman, Limon, Pope and Zavatini [24] measured the reaction products of the following collision at 28.5 GeV beam energy :

$$p + U \rightarrow \mu^- + \mu^+ + X$$

The remnant term X was not measured and the detection of penetrating muons is often preferred for experimental reasons compared to electrons. In Fig. 3.1, the dilepton cross-section, in the range $1 < M_{\mu\mu}/(\text{GeV}/c^2) < 6.7$, was later described as the combination of charmonium resonances (J/ψ and ψ') production around 3 GeV and 4 GeV and a continuous spectrum.

In August 1970, Sidney Drell and Tung-Mow Yan published a paper [25], which identified the mechanism responsible for this continuum and proposed the production model, which now bears their name. The Drell-Yan mechanism, describing the high mass lepton pair production in inelastic collisions, is illustrated as shown in Fig. 3.2.

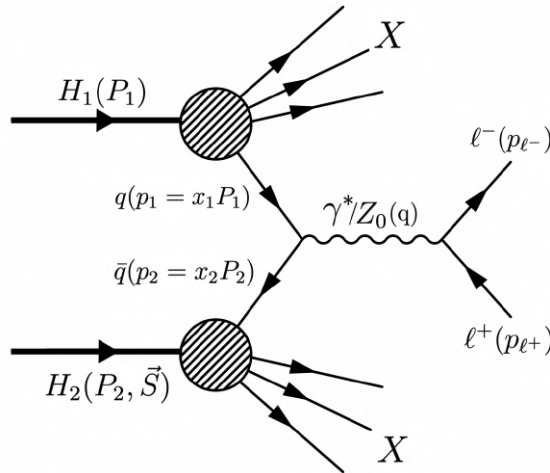


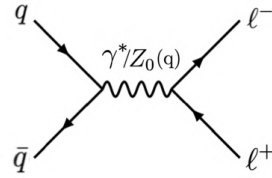
Figure 3.2: Feynman diagram of the Drell-Yan process, producing a lepton pair $\ell\bar{\ell}$ from the annihilation of a quark-antiquark pair $q\bar{q}$. The X terms are the remnant hadrons resulting from the inelastic interaction between the hadrons H_1 and H_2 .

¹Alternating Gradient Synchrotron

A general expression of the Drell-Yan process involves a quark-antiquark pair $q\bar{q}$ originating from two colliding hadrons H_1 and H_2 . These latter interact as follows:

$$H_1(P_1) + H_2(P_2, \vec{S}) \longrightarrow q(p_1) + \bar{q}(p_2) + X \longrightarrow \ell^-(p_{\ell^-}) + \ell^+(p_{\ell^+}) + X$$

At leading order, the quark-antiquark pair $q\bar{q}$ annihilates into a virtual photon $\gamma^*(q)$ or the weak boson Z^0 (Fig. 3.3). The mediating boson turns into a lepton pair $\ell\bar{\ell}$ measured by an experimental apparatus. The outgoing remnant hadrons X are not measured. P_1 and P_2 are the beam, and the target energy-momentum vectors, with S defined as the spin vector in the target rest frame (Fig. 3.4). The center-of-mass energy \sqrt{s} is related to the two hadronic vectors, as shown in Eq. 3.1. The four-momentum vector of the mediating particle is denoted $q = p_{\ell^-} + p_{\ell^+}$, where p_{ℓ^\pm} refer to the leptonic four-momentum vectors. Moreover, the hard scale Q is given by the measured mass M of the dilepton.



$$\begin{cases} Q^2 &= q^2 = M^2 \\ s &= (P_1 + P_2)^2 \end{cases} \quad (3.1)$$

Figure 3.3: Feynman diagram at leading order of the Drell-Yan reaction $q\bar{q} \rightarrow \ell^- \ell^+$

Quark four-momenta, p_1 and p_2 , are related to hadron four-momentum via the Bjorken scaling variable for each hadron, denoted x_1 and x_2 , as shown in Eq. 3.2. Other dimensionless variables, namely x_F and τ are deduced from x_1 and x_2 , as $x_F = x_1 - x_2$ and $\tau = M^2/s$.

$$\begin{cases} p_1 &= x_1 P_1 \\ p_2 &= x_2 P_2 \end{cases} \quad \text{with } x_{1,2} \text{ defined as } x_{1,2} = \frac{Q^2}{2P_{1,2} \cdot q} \quad (3.2)$$

Target Rest Frame. This reference frame, Fig. 3.4, is defined by the unit vector \hat{z} aligned with respect to the beam momentum. The \hat{x} unit vector is along the transverse component q_T of the virtual photon. Finally, the last unit vector is deduced as $\hat{y} = \hat{z} \times \hat{x}$. In this reference frame the main vectors are defined as follows:

$$\begin{cases} P_1 &= (E_1, 0, 0, P_{1z}) \\ P_2 &= (M_p, 0, 0, 0) \\ q &= (E_\gamma, q_T, 0, q_L) \\ S &= (0, S_T \cos \phi_S, S_T \sin \phi_S, S_L) \end{cases} \quad (3.3)$$

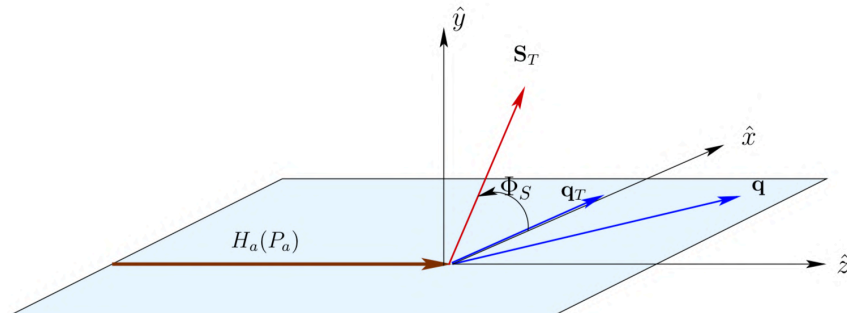


Figure 3.4: Definition of the azimuthal angle Φ_S of transverse target spin \mathbf{S}_T in the target rest frame [26]

Collins-Soper (CS). This frame is defined in the rest frame of the dilepton as shown in Fig. 3.5. The \hat{z} is aligned with respect to the bisector of \vec{P}_a and $-\vec{P}_b$ hadron momenta. The \hat{y} axis is perpendicular to the hadron plane formed by \vec{P}_a and \vec{P}_b , while \hat{x} axis lies on the hadron plane. In this frame, the leptonic four-momenta are :

$$\begin{cases} p_{\ell^-} = \frac{q}{2}(1, \sin \theta_{CS} \cos \varphi_{CS}, \sin \theta_{CS} \sin \varphi_{CS}, \cos \theta_{CS}) \\ p_{\ell^+} = \frac{q}{2}(1, -\sin \theta_{CS} \cos \varphi_{CS}, -\sin \theta_{CS} \sin \varphi_{CS}, -\cos \theta_{CS}) \end{cases} \quad (3.4)$$

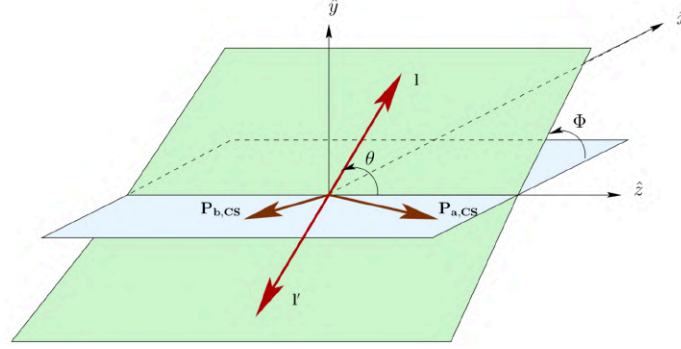


Figure 3.5: Definition of polar and azimuthal angles θ_{CS} and ϕ_{CS} of the lepton ℓ^- momentum in the Collins-Soper frame [26]

Degree of freedom of the Drell-Yan Process. The Drell-Yan process is often described by the two parameters (x_F, M) , but the kinematic of this process can also be expressed in terms of other variables, such as (x_1, x_2) . From an experimental point of view, the measurement requires eight parameters, namely the two four-momentum vectors of the measured leptons. These degrees of freedom can be reduced to six free parameters using the mass constraints for the two leptons. Moreover, different systems of equations can be used to describe the Drell-Yan process. However, a convenient system of six parameters might involve the following variables: $(M, x_F, q_T, \phi_{LAB}, \cos \theta_{CS}, \varphi_{CS})$. Additionally, for unpolarized Drell-Yan, the azimuthal symmetry reduces the degree of freedom to five variables (no ϕ_{LAB} dependence).

Correction diagrams. Additional diagrams are accounted at next-to-leading order and involve gluon interactions. These diagrams contribute to energy loss effects and the production of a large transverse momentum q_T . Fig. 3.6(a) shows the vertex correction diagram. Moreover, Fig. 3.6(b,c) involve the emission of a gluon, and together with Fig. 3.6(a) represent the annihilation diagrams. The *Compton* diagrams involving a gluon in the initial-state are shown Fig. 3.6(d,e) .

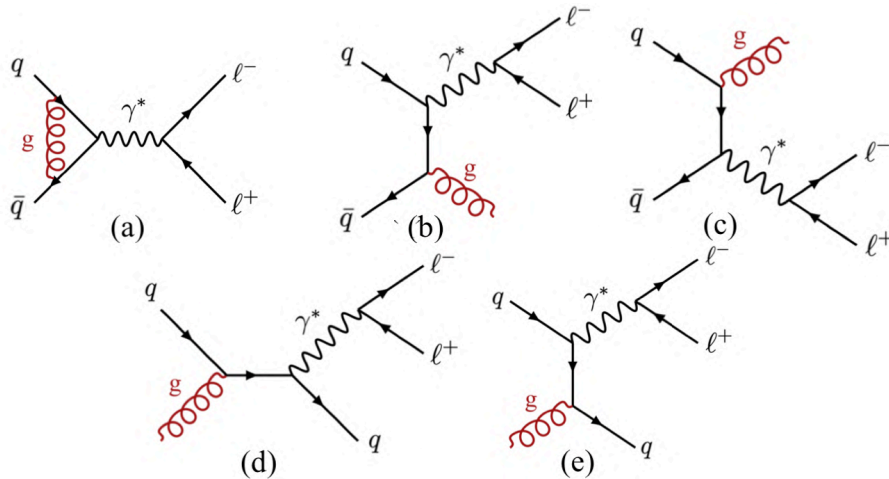


Figure 3.6: Correction diagrams at next-to-leading order of the Drell-Yan reaction $q\bar{q} \rightarrow \ell^- \ell^+$

3.2 General Expression of the Cross-Section

The factorization theorem allows decomposing the hadronic cross-section into the hard process and the soft part. Consequently, these terms are expressed independently in the following.

Hard cross-section. The underlying process behind the hadro-production of lepton pairs is described by the $q\bar{q}$ annihilation via the exchange of a virtual photon γ^* , as shown in Fig. 3.7.

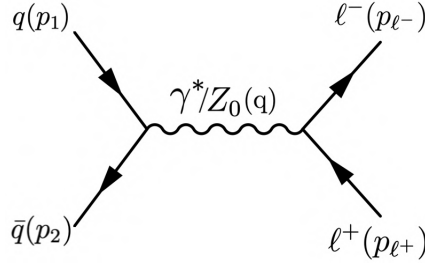


Figure 3.7: Feynman diagram at leading order of the partonic Drell-Yan reaction $q\bar{q} \rightarrow \ell^-\ell^+$

The Feynman rules of this diagram gives the following transition matrix element :

$$-i\mathcal{M} = [\bar{u}_q(p_2)(ie_q e \gamma^\mu)v_q(p_1)] \frac{g_{\mu\nu}}{q^2} [\bar{u}_\ell(p_{\ell+})(ie\gamma^\nu)v_\ell(p_{\ell-})] \quad (3.5)$$

The expression of the annihilation cross-section, $e^+e^- \rightarrow \ell^+\ell^-$, in QED is similar to the expression of the Drell-Yan cross-section in the QCD description. In the interaction between $q\bar{q} \rightarrow \ell^+\ell^-$, an additional term N_c is introduced as a result of the color conservation of the QCD theory. In the annihilation process, only the non-zero matrix elements related to $r\bar{r}$, $g\bar{g}$, $b\bar{b}$ color factors are possible. Consequently, the unpolarized cross-section is obtained by averaging over spin and color states as follows:

$$\langle |\mathcal{M}|^2 \rangle = \frac{1}{9} \sum_{color} \left(\frac{1}{4} \sum_{spin} | -i\mathcal{M} |^2 \right) = \frac{e^4 e_q^2}{N_c} (1 + \cos^2 \theta) \quad (3.6)$$

As a simple example, the expression of the differential cross-section $q\bar{q} \rightarrow \ell\bar{\ell}$ is given as follows.

$$\frac{d\sigma}{d\Omega} = \frac{1}{64\pi^2 \hat{s}} \langle |\mathcal{M}|^2 \rangle \quad (3.7)$$

where $\hat{s} = (p_1 + p_2)^2 \simeq x_1 x_2 s$ refers to the center-of-mass energy of the $q\bar{q}$ system.

Consequently, the known expression of the total cross-section $\hat{\sigma}(q\bar{q} \rightarrow \ell\bar{\ell})$ at the Born level is retrieved as shown in Eq. 3.8 by integrating over the full solid angle (4π steradians), and by neglecting the proton mass ($p_1^2 = p_2^2 \simeq 0$).

$$\hat{\sigma}(q\bar{q} \rightarrow \ell\bar{\ell}) = \frac{e_q^2}{N_c} \frac{4\pi\alpha^2}{3\hat{s}} \quad (3.8)$$

where $\alpha = e^2/4\pi$ is the fine structure constant

e_q is the quark charge

N_c is the number of colors

Soft non-perturbative contribution. In addition to the hard cross-section, a non-perturbative contribution, related to the definition of parton distribution functions of hadrons in Fig. 3.7, arises in the expression of the double differential cross-section as a function of dx_1 and dx_2 . The quark q_1 , originating from a beam particle, interacts with the antiquark \bar{q}_2 of a target nucleon. By symmetry, the two quark PDF combinations, $q_1(x_1)\bar{q}_2(x_2)$ and $\bar{q}_1(x_1)q_2(x_2)$, are possible and lead to the following differential form.

$$d^2\sigma = [q_1(x_1)\bar{q}_2(x_2) + \bar{q}_1(x_1)q_2(x_2)]\hat{\sigma}(q\bar{q} \rightarrow \ell\bar{\ell})dx_1dx_2 \quad (3.9)$$

As suggested by Eq. 1.1, the Drell-Yan differential cross-section can be expressed in terms of the two scaling variables (x_1, x_2) and the structure function $F(x_1, x_2)$ related to the quark PDFs, by summing over all quark flavors.

$$\frac{d^2\sigma}{dx_1dx_2} = \left(\frac{4\pi\alpha^2}{9M^2}\right) \sum_q e_q^2 [q_1(x_1)\bar{q}_2(x_2) + \bar{q}_1(x_1)q_2(x_2)] = \frac{1}{M^2}F(x_1, x_2) \quad (3.10)$$

3.3 Lorentz Invariant Cross-Sections

The invariance of the cross-section under Lorentz transformation is an advantage to facilitate comparisons with other measurements. As an example, Eq. 3.10 may be written in terms of the Lorentz invariant function $F(x_1, x_2)$:

$$M^2 \frac{d^2\sigma}{dx_1dx_2} = F(x_1, x_2) \quad (3.11)$$

Moreover, this invariant cross-section, Eq. 3.11, can also be expressed in terms of $(M_{\mu\mu}, x_F)$ using the change of variable theorem. This theorem allows to write down the following integral relation, using $G : (x_1, x_2) \mapsto (M^2 = sx_1x_2, x_F = x_1 - x_2)$

$$\begin{aligned} \iint \sigma(M, x_F) dx_F dM &= \iint \sigma(G(x_1, x_2)) \left| \det J_G(x_1, x_2) \right| dx_1 dx_2 \\ \Rightarrow M^3 \frac{d^2\sigma}{dM dx_F} &= \frac{2x_1x_2}{(x_1 + x_2)} \times F(x_1, x_2) \end{aligned} \quad (3.12)$$

The latter invariant cross-sections (Eq. 3.12 and Eq. 3.11) are both used under an integrated transverse momentum of the dimuon q_T . However, the invariant triple differential cross-section (Eq. 3.13) is expressed as a function of x_F , but carries also the information of the transverse momentum q_T . Along the same line of variable change (F being analog to the G application) and by assuming azimuthal symmetry, the triple differential cross-section can be expressed, as follows:

$$\begin{aligned} \int \sigma(\vec{q}) dq^3 &= \iiint \sigma(F(q_L, q_T, \phi_{LAB})) \left| \det J_F(q_L, q_T, \phi_{LAB}) \right| dq_L dq_T d\phi_{LAB} \\ \Rightarrow E \frac{d^3\sigma}{dq^3} &= \frac{4E}{\sqrt{s}} \times \frac{d^3\sigma}{dx_F dq_T^2 d\phi_{LAB}} \xrightarrow[\text{sym.}]{\phi_{LAB}} E \frac{d^3\sigma}{dq^3} = \frac{2E}{\pi\sqrt{s}} \times \frac{d^2\sigma}{dx_F dq_T^2} \end{aligned} \quad (3.13)$$

3.4 Experimental Overview

Following the first report about dimuon production at AGS, various experiments measured the dilepton production over the years using either proton-proton, proton-nucleus, or pion-nucleus collisions (Tab. 3.1). This non-exhaustive list highlights the worldwide interest to study and understand the dimuon spectrum. This interest culminated in 1983 when the UA1 and UA2 experiments at CERN discovered the W, Z bosons using the Drell-Yan process in $\bar{p} - p$ collision.

Table 3.1: Summary table of some muon pair production experiments [27]

Reactions	Experiments	Targets	\sqrt{s} [GeV]	$\delta_{\text{sys.}}$ (%)	References
$pp \longrightarrow e^+e^- + X$	R108	H ₂	62.4	12%	Angelis <i>et al.</i> (1979) [28]
	R808	H ₂	53; 64	50%	Kourkouvelis <i>et al.</i> (1979) [29]
$pp \longrightarrow \mu^+\mu^- + X$	R209	H ₂	44; 62	15%	Antreasyan <i>et al.</i> (1981) [30]
$pA \longrightarrow \mu^+\mu^- + X$	E288	Pt	19.4; 23.7; 27.4	$\gtrsim 25\%$	Ito <i>et al.</i> (1981) [31]
	E325	Cu	19.4; 23.7; 27.4	N/A	Antreasyan <i>et al.</i> (1979) [32]
	E444	C,Cu,W	20.5	15%	Anderson <i>et al.</i> (1979) [33]
	E439	W	27.4	11%	Smith <i>et al.</i> (1981) [34]
	NA3	Pt	27.4	12%	Badier <i>et al.</i> (1985) [35]
	E772	H ₂	38.7	N/A	Alde <i>et al.</i> (1990) [36]
	E605	Cu	38.7	$\simeq 18\%$	Moreno <i>et al.</i> (1991) [37]
$\bar{p}A \longrightarrow e^+e^- + X$	UA1	–	–	–	–
	UA2	H ₂	630	20%	Alitti <i>et al.</i> (1992) [38]
$\bar{p}A \longrightarrow \mu^+\mu^- + X$	E537	W	15.3	5%-13%	Anassontzis <i>et al.</i> (1988) [39]
$\pi^\pm A \longrightarrow \mu^+\mu^- + X$	E326	W	20.5	15%	Greenlee <i>et al.</i> (1985) [40]
	E444	C,Cu,W	20.5	15%	Anderson <i>et al.</i> (1979) [33]
	WA11	Be	16.8; 18.1	20%	Barate <i>et al.</i> (1979) [41]
	WA39	W	8.6	–	Corden <i>et al.</i> (1980) [42]
	NA3	Pt	16.8; 18.4; 22.9	12%-23%	Badier <i>et al.</i> (1983) [43]
	NA10	W	19.1; 23.2	$\simeq 10\%$	Betev <i>et al.</i> (1985) [44]
	E537	W	15.3	5%-13%	Anassontzis <i>et al.</i> (1988) [39]
	E615	W	21.7	16%	Conway <i>et al.</i> (1989) [45]

The NA10 and E615 experiments are of particular interest in comparison to the COMPASS Drell-Yan measurement on tungsten in 2015. Indeed, these experiments measured muon pairs originating from the interaction between an incoming π^- and a tungsten target at similar center-of-mass energies, $\sqrt{s} = 19.07$ GeV for NA10 [44] and $\sqrt{s} = 21.74$ GeV for E615 [45], compared to the COMPASS center-of-mass energy at $\sqrt{s} = 19.89$ GeV. The integrated cross-section and the corresponding K-factors are summarized in Tab. 3.2.

Table 3.2: K-factor obtained for some $\pi^- A \rightarrow \mu^+ \mu^- X$ reactions [27]

Experiment	Reaction	\sqrt{s} [GeV]	Integrated σ_0 [nb]	Prediction NLO	K-factor
NA10 (1985)	$\pi^- W \rightarrow \mu^+ \mu^-$	19.07	0.0803	0.0625	1.286 ± 0.005
E615 (1989)	$\pi^- W \rightarrow \mu^+ \mu^-$	21.74	0.1916	0.1801	1.064 ± 0.011

The K-factor is conventionally defined as the ratio between the observed experimental cross-section and a theoretical prediction (either LO, NLO, or NNLO). This factor was historically used to illustrate the effect of higher-order corrections. In Tab. 3.2, the K-factor is computed using a theoretical prediction at NLO. The NLO calculation is parametrized using SMRS \otimes MRS PDF sets [27] for the pion and the nucleon PDF, respectively.

Finally, results of the proton-induced Drell-Yan productions from NA3 [46] (triangles) at 400 GeV/c, E605 [37] (squares) at 800 GeV/c, and E772 [47] (circles) at 800 GeV/c is shown in Fig. 3.8. The parton model scaling properties is illustrated in this figure as in bins of x_F . The absolute lines are computed at NLO accuracy for p + d collisions at 800 GeV/c using the CTEQ4M structure functions [48].

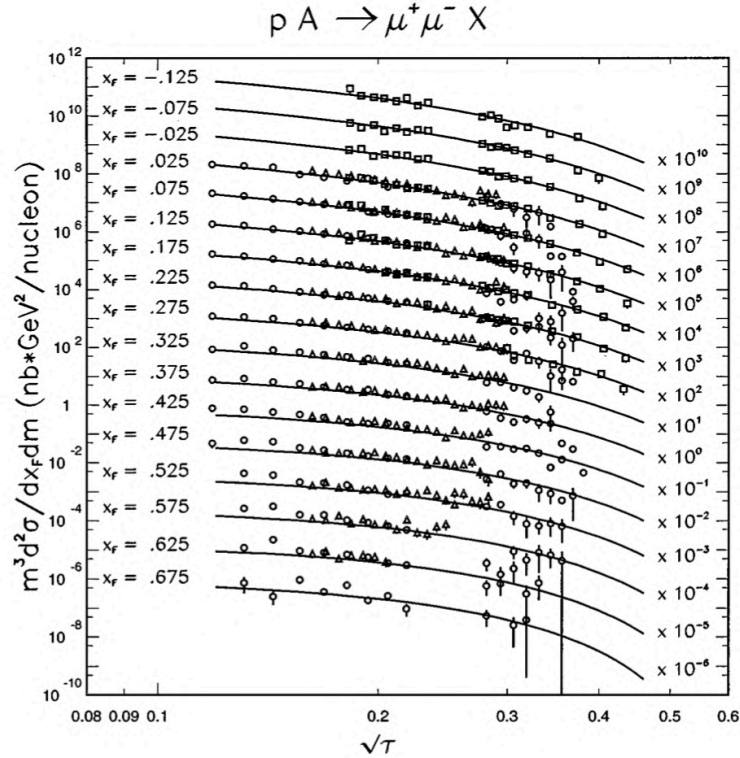


Figure 3.8: Proton-induced Drell-Yan production from various fixed target experiments. This picture is taken from [49]

4 | Theoretical Overview: State-of-the-Art

An overview of some recent theoretical studies related to the Drell-Yan process is shown in this section. It aims to introduce some existing interpretations resulting from the analysis of past experiments and to highlight the motivations of extracting Drell-Yan cross-sections from the COMPASS data.

4.1 Drell-Yan Angular Distributions and Lam-Tung Relation

In the CS¹ frame, Fig. 4.1, the angular differential cross-section of the lepton ℓ^- for unpolarized Drell-Yan is expressed as a function of the three (λ, μ, ν) coefficients :

$$\frac{1}{\sigma_0} \frac{d\sigma}{d\Omega} = \frac{3}{4\pi} \frac{1}{\lambda + 3} \left(1 + \lambda \cos^2 \theta + \mu \sin 2\theta \cos \Phi + \frac{\nu}{2} \sin^2 \theta \cos 2\Phi \right)$$

where (θ, ϕ) denote the polar and azimuthal angle of the lepton ℓ^- in the CS frame.

(λ, μ, ν) are the three unpolarized Drell-Yan angular coefficients

σ_0 is the angular integrated Drell-Yan cross-section.

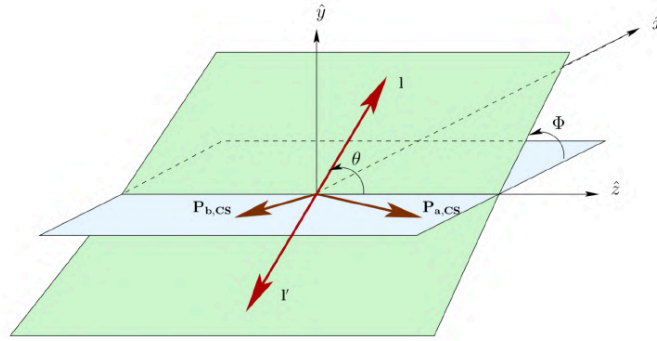


Figure 4.1: Definition of the Collins-Soper frame [26]

At the Born level, considering the collinear hypothesis, the partonic interaction $q\bar{q} \rightarrow \ell\bar{\ell}$ does not account for soft gluon exchanges or any QCD related processes. Consequently, the contribution of the primordial k_T is neglected. In this naive model, the well known $q\bar{q}$ annihilation cross-section Eq. 4.1 is retrieved, as the three asymmetry coefficients (λ, μ, ν) are expected to be equal to $(1, 0, 0)$.

$$\frac{1}{\sigma_0} \frac{d\sigma}{d\Omega} = \frac{3}{16\pi} (1 + \cos^2 \theta) \quad (4.1)$$

The introduction of the gluon emissions results in a transverse momentum of the dilepton and leads to a modification of the unpolarized angular coefficients : $(\lambda, \mu, \nu) \neq (1, 0, 0)$. These coefficients are expected to largely satisfy the Lam-Tung relation [50], Eq. 4.2 :

$$\lambda + 2\nu = 1 \quad (4.2)$$

This relation is analogous to the Callan-Gross relation and originates from the spin- $\frac{1}{2}$ nature of quarks. This relation was not expected to be sensitive to QCD corrections, unlike the Callan-Gross relation. The first measurements of Drell-Yan angular distributions were performed by the NA10 collaboration [51] (1986) and the E615 collaboration [45] (1989) using a π^+ beam over W target at 194 GeV/c

¹Collins-Soper

and 252 GeV/c respectively. More recently, the E866 collaboration [52, 53] (2007) measured the distributions with a proton beam on a deuterium target at 800 GeV/c. This result is shown in Fig. 4.2. A sizable dependence was observed as a function of q_T , and the violation of the Lam-Tung relation by E615 could not be explained by perturbative QCD corrections. Consequently, few years later, Boer suggested in 1998 [54] a possible contribution from a non-perturbative QCD effect might arise in the convolution of two unpolarized TMD PDFs : $\nu \propto h_1^{q\perp}(p) \otimes h_1^{q\perp}(\pi^-)$.

In 2011 and 2015, respectively CDF and CMS experiments published new results in their respective papers [56, 57]. The CDF collaboration seems to be in good agreement with the Lam-Tung relation, while CMS observed a clear violation. These new measurements raised the interest of various theoretical groups to determine whether this violation can be attributed to perturbative or non-perturbative QCD effect. As an example, the interpretation of the angular distributions of Z-boson production [55] brought new perspectives in the explanation of the Lam-Tung violation. Fig. 4.3 shows a comparison of CMS and CDF data with pure qG and $q\bar{q}$ productions as a function of q_T . This figure highlight the dependence of the λ and ν parameters as a function of a mixture of 72.5% $q\bar{q}$ and 27.5% qG respectively. Although a lot of efforts were involved in the understanding of the Lam-Tung violation, this relation remains under discussion and the COMPASS data might also provide valuable new insight.

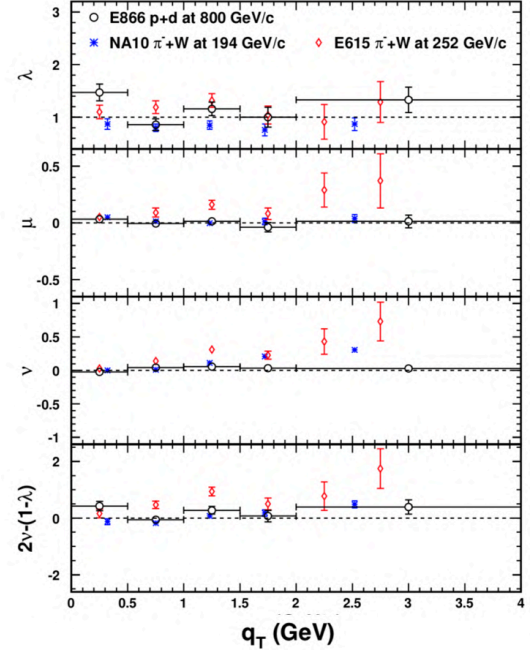


Figure 4.2: Measurement of the λ, μ, ν coefficients in CS frame as a function of q_T and evaluation of the Lam-Tung relation carried out by the E866, NA10 and E615 collaborations [55].

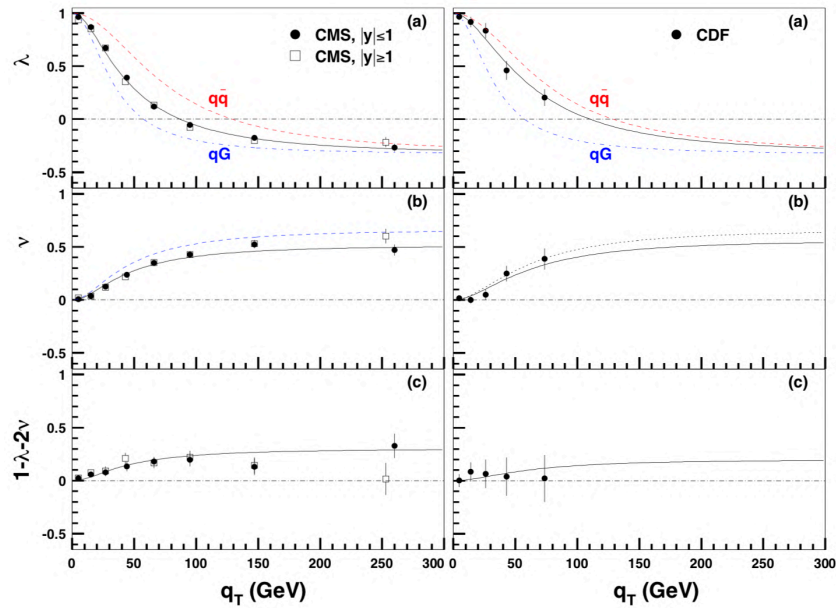


Figure 4.3: Comparison of CMS and CDF data with predictions for pure qG and $q\bar{q}$ productions [56, 57]

4.2 Cold Nuclear Matter

The modification of the measured cross-section per nucleon on a heavy nucleus compared to a light nucleus was observed for the first time by the EMC² collaboration in 1983 [58]. This effect, known as the EMC effect, has been extensively studied over the last 30 years. However, there is still no model at this time, which fully explains the initial observation. Nuclear dependences can be summarized into the three following items:

- **EMC Effect**, which is described by a modification of quark and gluon distributions (PDF) in bounded nucleons by a nuclear environment (1983). This effect is a function of the Bjorken- x of the target, as illustrated in Fig. 4.5.
- **Energy Loss Effect**, which describes the energy loss of quarks in the hadron beam while going across the nuclear target, as illustrated by Fig. 4.4a. This effect can be studied using either the Bjorken- x of the beam or x_F . As an example, this figure shows a decrease of the nuclear corrective factor at large x_F due to the energy loss of the quarks in the initial-state, as predicted by the BDMPS formalism [59].
- **Cronin Effect**, which describes the nuclear enhancement of high- p_T hadrons due to multiple interactions in nuclear matter, as illustrated Fig. 4.4b in terms of p_T .

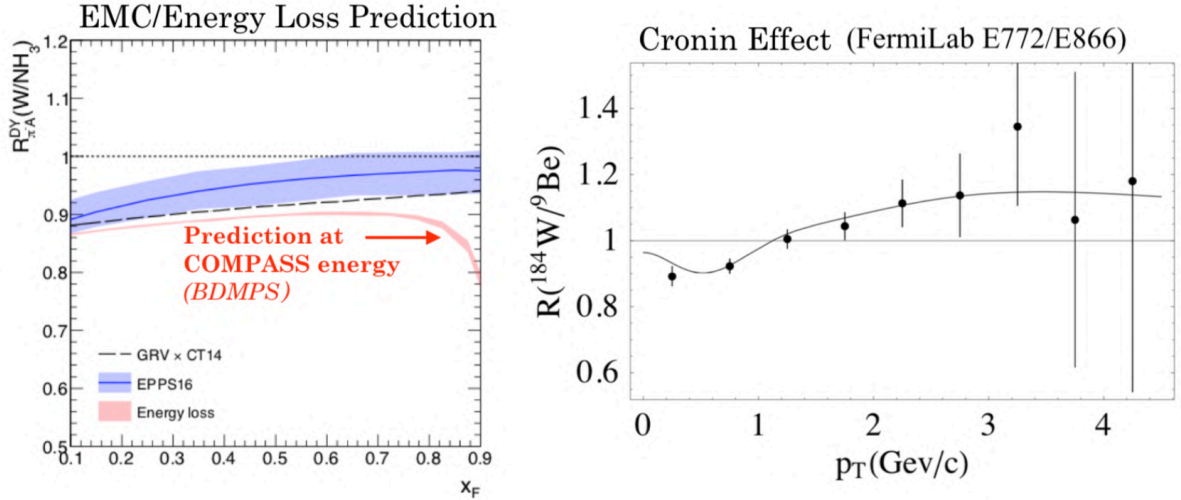


Figure 4.4: (a) Left: Prediction of the energy loss of the quarks in the initial-state [60] at COMPASS energy, using the BDMPS formalism; (b) Right: Illustration of the Cronin effect as a function of the p_T distribution visible in the ratio plot between heavy and light targets [61].

In Fig. 4.5, the combined data of the cross-section ratio from HERMES, SLAC-E139, and JLAB-E03103, highlight in a wide x range the nuclear dependence of the cross-section. It illustrates the Bjorken- x dependence of the ratio of cross-section, which is related to the structure-function in the measurement of the scattered electron via deep-inelastic scattering.

²European Muon Collaboration

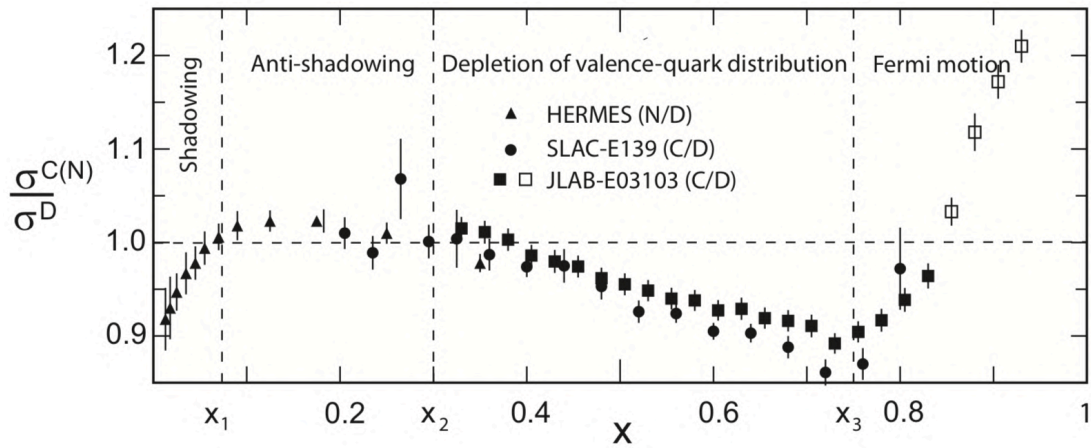


Figure 4.5: The ratio $\sigma_{C(N)}/\sigma_D$ as a function of x from HERMES [62], SLAC-E139 [63], and JLAB-E03103 [64]. (Adapted from [65])

The ratio $\sigma_{C(N)}/\sigma_D$ in Fig. 4.5 can be subdivided into four regions as the following:

- The *shadowing* region ($0 < x < x_1 = 0.06$); This region shows a cross-section ratio smaller than 1. The *nuclear shadowing* and *anti-shadowing* have a similar origin. These effects are produced by the coherence of quark-quark multiple scattering nuclear processes [66]. In addition, a destructive quantum-mechanical interference of the amplitude is responsible for the nuclear suppression at $x < 0.06$ [67].
- The *anti-shadowing* region ($x_1 < x < x_2 = 0.30$); In this region, the cross-section ratio is above 1.
- The *valence-quark depletion* region ($x_2 < x < x_3 = 0.8$); This region shows a nuclear suppression up to 10% as a function of x , also known as EMC effect. In this region, valence-quark distributions contribute more as x increases. At the highest x , the sea-quark is negligible.
- The *Fermi motion* region ($x_3 < x < 1$); This region shows a rapid increase of the ratio as x approaches 1. This behavior is explained by the Fermi motion of the bound nucleons in the nucleus.

4.3 A-dependence of Muon Pair Production

In the Drell-Yan process, the incoherent nature of the quark-antiquark annihilation leads to an expected linear dependence of the cross-section as a function of the atomic mass A . Consequently, the nuclear dependence of the cross-section per nuclei was historically [31, 43] parametrized using a power law as a function of the atomic mass A and an α parameter, such that :

$$\sigma(\pi A) = \sigma_A(\pi N) \times A^\alpha, \text{ where } N \text{ refers to the nucleon [31]} \quad (4.3)$$

Along this line, α is expected to be $2/3$ for the hadronic cross-section, and close to 1 for Drell-Yan cross-section. The latter values are empirical estimations and the dependence as a function of the kinematics is not well known. This α parameter can be obtained from the measurement between cross-sections, σ_{A_1} and σ_{A_2} , of two nuclei A_1 and A_2 respectively ($A_1 < A_2$) (Eq. 4.4) :

$$\alpha(A_2/A_1) = \ln\left(\frac{\sigma_{A_2}}{\sigma_{A_1}}\right) / \ln\left(\frac{A_2}{A_1}\right) \quad (4.4)$$

Various experiments have measured the α parameter presented in Eq. 4.4. As an example, an evaluation of the α parameter by Ito et al [31] at Fermilab in the 80's was performed using a proton beam at 400 GeV/c on both Pt and Be targets between $5 < M/(\text{GeV}/c^2) < 11$. The value of α as a function of the dimuon mass $M_{\mu\mu}$ and the p_T distribution is shown in Fig. 4.6. Another evaluation of the α value was performed using the NA10 data, π^- over W (and D_2) in the range $4.10 < M/(\text{GeV}/c^2) < 11.79$. Finally, the NA3 collaboration also published a ratio between H_2 and Pt targets [43]. Some known values of α are summarized as follows :

$$\left\{ \begin{array}{l} \alpha_{\text{Ito}} = 1.007 \pm 0.018 \text{ (stat.)} \pm 0.028 \text{ (sys.)} \\ \alpha_{\text{NA10}} = 0.998 \pm 0.006 \text{ (stat.)} \pm 0.013 \text{ (sys.) [68]} \\ \alpha_{\text{NA3}} = 1.03 \pm 0.03 \text{ } (\pi^\pm \text{ on Pt [43]}/\text{H}_2) \\ \alpha_{\text{CFS}} = 1.02 \pm 0.2 \text{ (p on Pt/Cu/Be [69])} \\ \alpha_{\text{CIP}} = 1.12 \pm 0.05 \text{ } (\pi^- \text{ on Pt/Cu/Be [70]}) \end{array} \right. \quad (4.5)$$

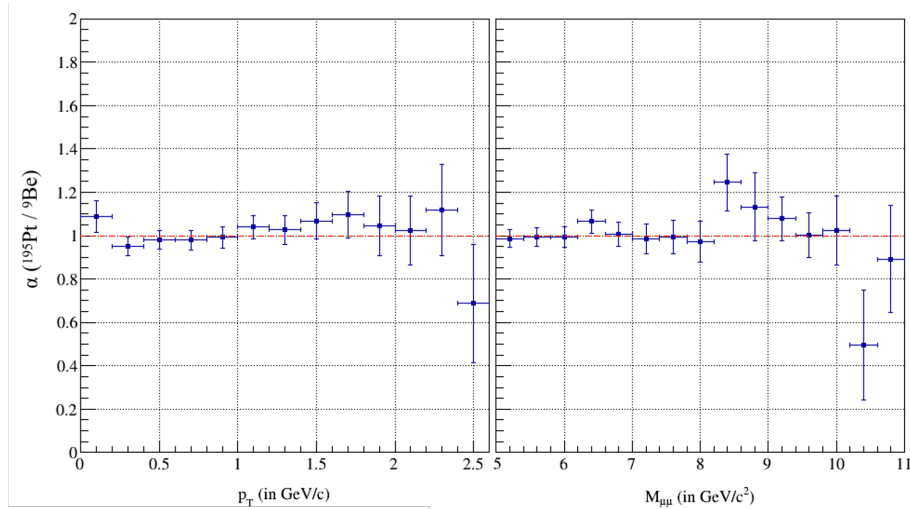


Figure 4.6: Values of α obtained from ratios of cross-sections $\sigma_{\text{Pt}}/\sigma_{\text{Be}}$ using a proton beam at 400 GeV/c from Ito *et al.* [31]. There is an additional 0.028 systematic uncertainty to include in the estimation of α at all masses and momentum.

4.4 Soft-Gluon Resummation

The detailed modeling and the interpretation of soft-gluon resummation are beyond the scope of this thesis but still require some introduction. As an example, refined interpretations of the Drell-Yan cross-sections were already intensively discussed in [71].

In the context of QCD theory, the *soft-gluon* radiation refers to the emission of gluon at very low energy. Below the energy threshold giving access to the final-state, the gluon emission originating either from quarks or gluons themselves is known as soft-gluon radiation. Soft-gluon radiations are induced by multiple scattering interactions in a nuclear medium and are modeled as a series of gluon interactions carrying small fraction ξ_k of energy, as illustrated in Fig. 4.7. The impact of soft-gluon resummation in the description of the Drell-Yan process is significant due to the presence of quarks in the initial-state.

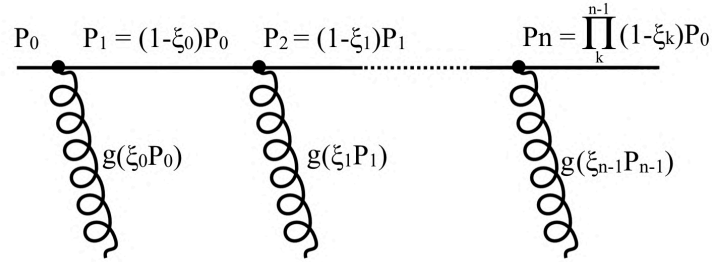


Figure 4.7: Illustration of the next-to-leading order soft gluon radiations

At the opposite of UV divergences (asymptotic freedom), a series of low energy interactions give rise to IR singularities. These IR divergences are a direct consequence of the massless nature of gluons. In other terms, some QCD correction diagrams of the soft-gluon radiations present divergent loop diagrams, which have to cancel because measured quantities are always finite. Consequently, a regularization is applied to the expression of the cross-section, which is known as next-to-leading-logarithm (NLL). This correction mainly plays a role in the fall-off at large x_F , as shown in Fig. 4.8. This figure shows the effect of the NLL resummation, using the E615 data for two bins of $\sqrt{\tau}$.

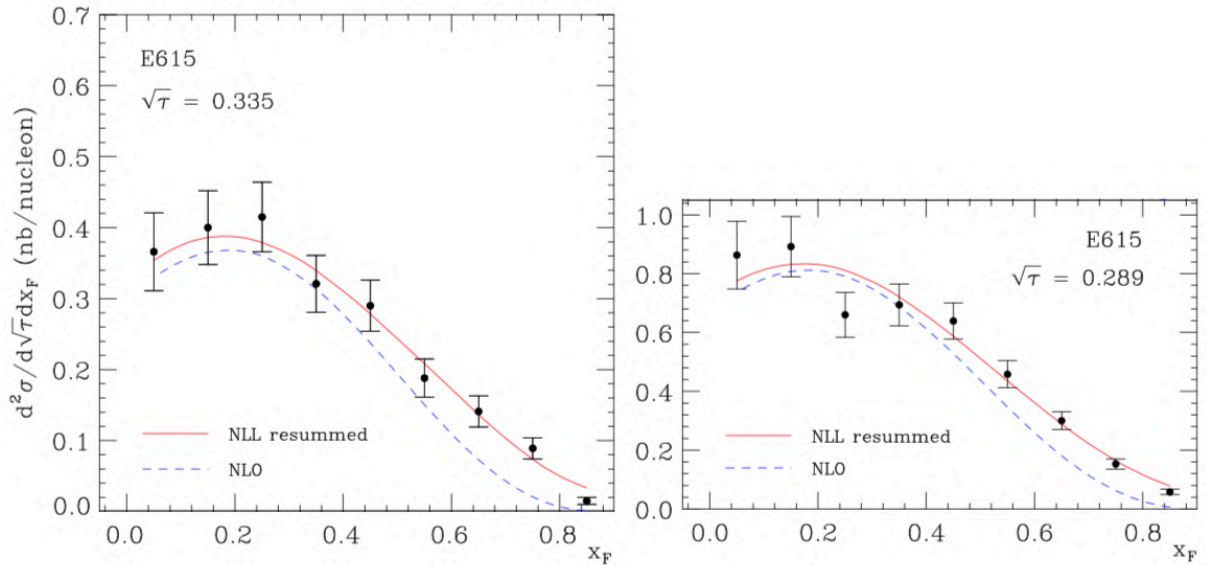


Figure 4.8: Comparison of NLO and NLL-resummed Drell-Yan cross section based on E615 data [72].

4.5 Parton Distribution Functions of the π^-

At the opposite of the nucleon structure, studied for more than 40 years, the access to the internal structure of mesons is a challenging task from a technical point of view. Indeed, there is no such simple target made out of pion target at rest in nature. Therefore, it requires some processes other than DIS to access the meson structure.

4.5.1 Experimental Overview

In the case of pion PDF, it is reasonable to assume charge symmetry as well as isospin symmetry (Eq. 4.6). As an example, such symmetries significantly reduce the complexity to the determination of a single valence-quark PDF, v_π , for both π^- and π^+ induced Drell-Yan data can be used.

$$v_\pi \equiv \bar{u}_v^{\pi^-} \equiv d_v^{\pi^-} \equiv u_v^{\pi^+} \equiv \bar{d}_v^{\pi^+} \quad (4.6)$$

The extraction of pion PDFs can be summarized into three parts: the determination of the valence-quark PDF v_π , the sea-quark PDF s_π , and the gluon PDF g_π .

Valence quark PDF in the pion. One way to study the valence quark is using the Drell-Yan process on fixed-targets. The Drell-Yan process is well understood theoretically, which makes it a good probe to understand the meson structure and flavor dependences. Second, the use of such process on a fixed-target allows for probing a wide range of the beam Bjorken- x . As an example using COMPASS 2015 data, the phase space probed as a function of x_1 (pion beam), and x_2 (nuclear targets) is shown in Fig. 4.9.

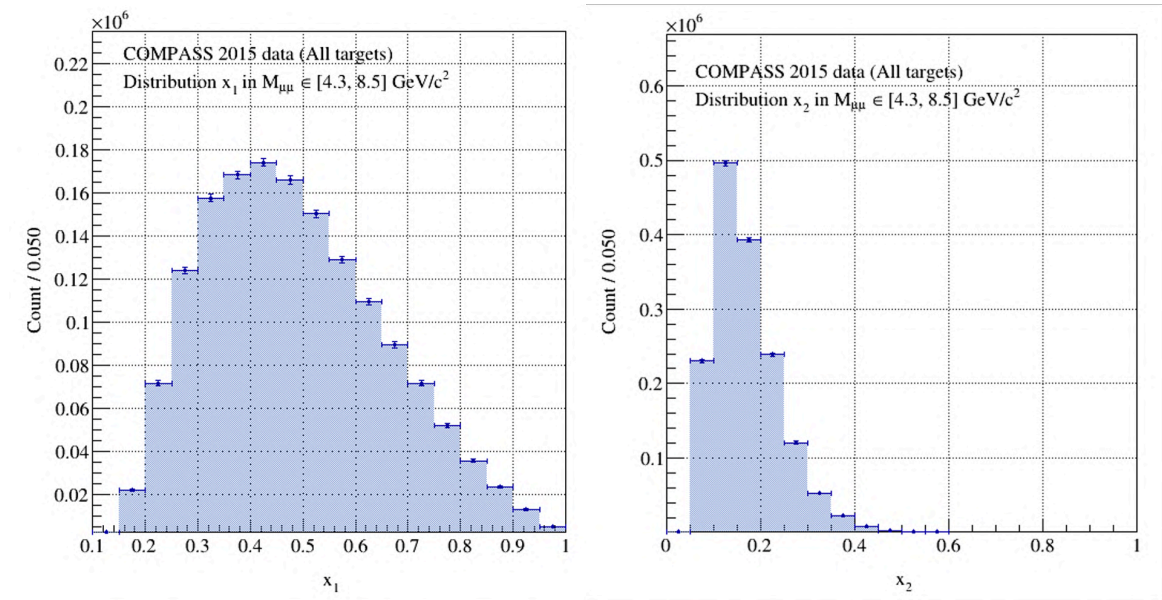


Figure 4.9: Kinematic range probed in terms of x_1 and x_2 using COMPASS 2015 data (All targets included)

The Drell-Yan cross-section at LO can be expressed in terms of the convolution between parton PDF in the beam together with the parton PDF in the target as follows :

$$\frac{d\sigma^2}{dx_1 dx_2} \propto \sum_{q=u,d,\dots} e_q^2 [q_B(x_1, Q^2) \bar{q}_T(x_2, Q^2) + \bar{q}_B(x_1, Q^2) q_T(x_2, Q^2)] \quad (4.7)$$

where $q_B(x_1, Q^2)$ is the PDF of a parton q from a beam particle B
 $\bar{q}_T(x_2, Q^2)$ is the PDF of a parton \bar{q} from a target nucleon T
 $\bar{q}_B(x_1, Q^2)$ is the PDF of a parton \bar{q} from a beam particle B
 $q_T(x_2, Q^2)$ is the PDF of a parton q from a target nucleon T

As an example, the hadron beam of 190 GeV/c used at COMPASS is mainly composed of π^- particles (described later in Ch. II, Tab. 5.1). Valence and sea quarks in the meson combine with quarks in the target in Eq. 4.7. The valence-valence, valence-sea and sea-sea convolutions are highlighted in Tab. 4.1. Due to the dominance of valence quarks in the explored kinematic, the contribution of the valence-valence term dominates the Drell-Yan cross-section. Therefore, an advanced analysis of the 2015-2018 COMPASS data $\pi^- A$ might allow better constraint to the valence quark distributions of the pion.

Table 4.1: Decomposition of the partonic convolutions involved in the Drell-Yan interaction $\pi^- p$

Valence-Valence	Valence-Sea	Sea-Sea
$\bar{u}_\pi u_p$	$d_\pi \bar{d}_p, \bar{d}_\pi d_p, ..$	$u_\pi \bar{u}_p, ..$

A summary of the available data to measure the valence PDF of the pion is shown in Tab. 4.2. However, experimental data of the pion via the Drell-Yan process are very limited and were all collected between 1979 and 1989.

Table 4.2: A summary of the Drell-Yan data, together with the value of the coefficients describing the v_π parametrization coefficients at LO

Experiment	Reaction	\sqrt{s} (GeV)	Coefficient α	Coefficient β
WA11 (1979)	$\pi^- Be \longrightarrow \mu^+ \mu^-$	18.11	–	–
E331/E444 (1979)	$\pi^- W \longrightarrow \mu^+ \mu^-$	20.54	0.5	1.23
WA39 (1980)	$\pi^- W \longrightarrow \mu^+ \mu^-$	8.66	–	–
NA3 (1983)	$\pi^- Pt \longrightarrow \mu^+ \mu^-$	21.74	0.45	1.17
NA10 (1985)	$\pi^- W \longrightarrow \mu^+ \mu^-$	19.07	0.39	0.98
E326 (1985)	$\pi^- W \longrightarrow \mu^+ \mu^-$	20.54	–	–
E615 (1989)	$\pi^- W \longrightarrow \mu^+ \mu^-$	21.74	0.60	1.26

In the early years, the analysis at LO of Drell-Yan data gave a first estimate of valence quark PDFs as a function of two coefficients (α, β) as given Eq. 4.8. These coefficients are also summarized in Tab. 4.2.

$$xv_\pi = Ax^\alpha(1-x)^\beta, \text{ with the constraint } \int_0^1 v_\pi(x)dx = 1 \quad (4.8)$$

Later in 2005, a new interpretation of the E615 data at NLO was released including a more recent PDF set for the nucleon, nuclear effects in the tungsten and non-perturbative calculations, such as DSE³ models [73]. Despite these major improvements, the interpretation at NLO accuracy was still not enough to describe E615 data and the fall-off in x in the cross-section, as previously discussed in Sec. 4.4 (Fig. 4.8).

³Dyson-Schwinger Equation

It will take few years to observe the impact of the NLL corrections in 2010 [72]. Applied to the original E615 cross-section, this additional correction leads to a pion PDF fall-off at large x , that is now compatible with the DSE prediction (Fig. 4.10). By including the NLL accuracy, the valence quark PDF in the pion was consequently parametrized using Eq. 4.9, where $\beta = 2.34$ at $Q = 4$ GeV.

$$xv_\pi(x) = Ax\alpha(1-x)^\beta(1+\gamma x^\delta) \quad (4.9)$$

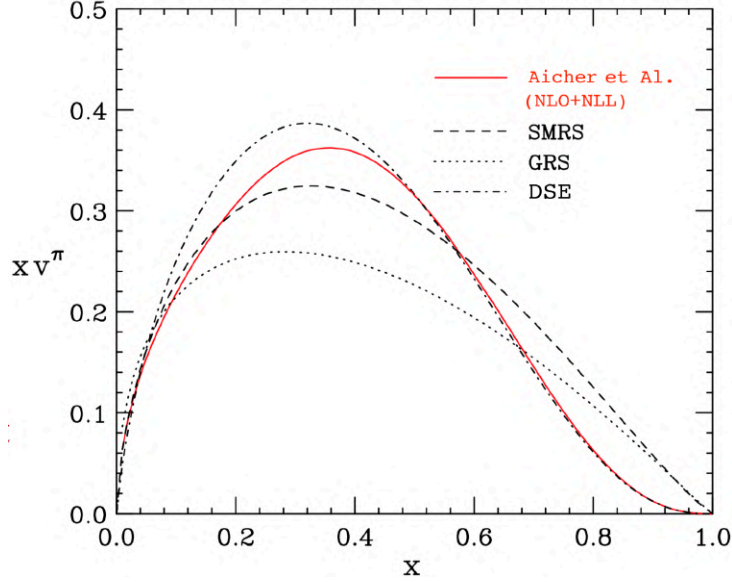


Figure 4.10: Effect of the NLO and NLL corrections at $Q = 4$ GeV in comparison to the pion valence v_π PDF extracted from the E615 data [72].

Sea quark PDF in the pion. In addition to the valence quark PDFs, the question of the pion sea was also raised. The first valence-sea separation was performed using the NA3 data [43] in a limited region at high- x_F ($0.2 < x < 1$). The collected data by NA3 collaboration are summarized in the Tab. 4.3. The perspective of measuring Drell-Yan pairs at COMPASS++/AMBER using both π^- and π^+ is considered and is further detailed in the recently published proposal [74].

Table 4.3: Summary of the NA3 measurements on a Pt target. The separation of the valence-sea is possible thanks to the π^-/π^+ at 200 GeV/c.

Beam Momentum	Beam Particle	No. Events	Luminosity (cm ⁻²)
NA3 - 150 GeV/c	π^-	15,768	$(5.0 \pm 0.7) \times 10^{38}$
NA3 - 200 GeV/c	π^-	4,961	$(11.4 \pm 1.3) \times 10^{37}$
	π^+	1767	$(8.8 \pm 1.0) \times 10^{37}$
NA3 - 280 GeV/c	π^-	11,559	$(2.8 \pm 0.3) \times 10^{38}$

Additionally, complementary results at lower x are obtained from HERA deep inelastic scattering. This extraction consists of using DIS scattering on a virtual pion originating from target nucleons and relies on the pion cloud model [75]. This model relies on a superposition of states in the proton, which can be seen as a fluctuation between a bare proton state and additional states, including pions. However, uncertainties on the pion cloud density remain significant, but further results might be expected from JLab and EIC measurements.

Gluonic PDF contribution in the pion. This contribution can be extracted from three different methods: prompt photon production at high- p_T [76] ($qg \rightarrow \gamma q$), leading π^+ and π^- comparison in high- p_T di-jets [77], and from J/Ψ production. In this case, the gluon contribution from pion was attempted to be described by experiments using a single parameter β with the following parametrization :

$$xg_\pi(x) = A(1-x)^\beta \quad (4.10)$$

The fit of this parameter for various data sets is summarized in Tab. 4.4. Nonetheless, the fitted parameter β shows quite different results, which vary from 1.20 to 2.38. Moreover, the β coefficient is provided without estimation of the uncertainty due to the hypothesis of the models.

Table 4.4: Summary of some experiments measuring the gluon PDF contribution to the π and the various extracted β coefficients

Experiment	Reaction	\sqrt{s} (GeV)	Coefficient β
WA70	$\pi^- H \rightarrow \mu^+ \mu^-$	22.91	1.94
NA3 (1983)	$\pi^- Pt \rightarrow \mu^+ \mu^-$	18.11	2.38
E537 (1993)	$\pi^- Be \rightarrow \mu^+ \mu^-$	15.31	1.20
	$\pi^- W \rightarrow \mu^+ \mu^-$	15.31	1.98
E609 (1995)	$\pi^- p \rightarrow \text{dijets}$	27.42	2.75

Finally, the gluon contribution would be better constrained by using the J/Ψ data if the production mechanism was better understood and not, so model dependent. Indeed, the large cross-section of this charmonium resonance would largely improve the global understanding of the gluonic contribution compared to the low cross-section of the Drell-Yan continuum.

4.5.2 Global Analysis of the Pion PDFs

A global analysis of the pion PDFs, based on a theoretical model, consists of extracting a parametrization simultaneously on multiple data sets. Such methods require enough flexibility to fit data. However, it presents various advantages. First, the fit can be constrained in the combined phase space probed by the data. Moreover, if multiple data sets are in overlap, the model is accommodated to fit both datasets.

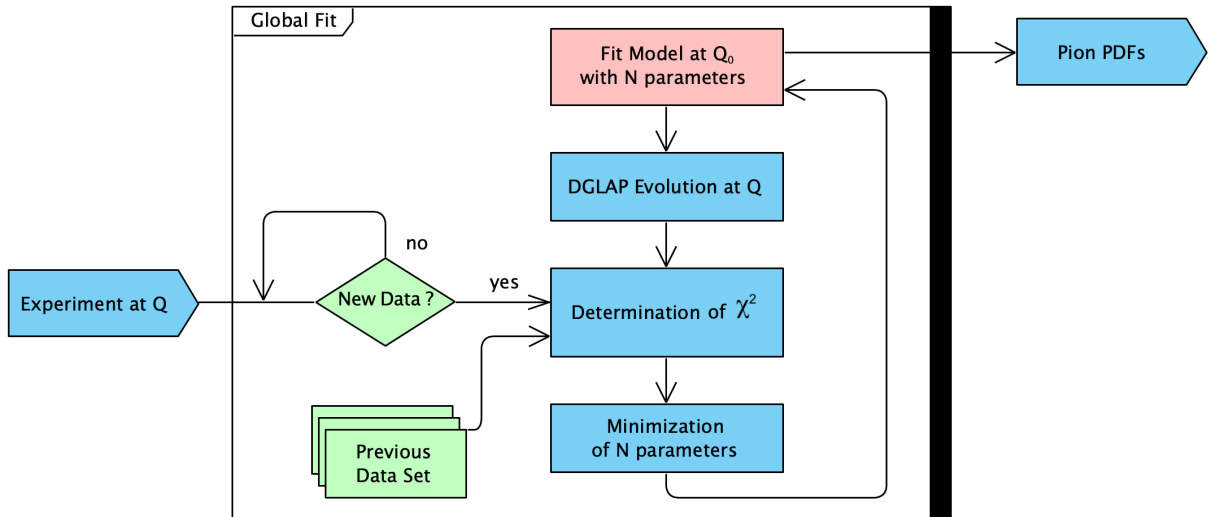


Figure 4.11: Workflow of a global fit analysis.

A diagram of the global fit analysis is presented in Fig. 4.11. This workflow illustrates how a fitting model is constrained at a given hard-scale Q . A χ^2 value is determined based on the experimental data, and a theoretical model evolved at the proper scale of Q . Various data sets are accumulated, and the χ^2 is simultaneously minimized based on all available data. Finally, the parametrization of the best-fit is returned and provide the central value of the PDFs.

Additionally, the convergence of the fit can be simplified by taking into account conservation of quantum numbers, momentum, or symmetries. As an example, the conservation of the number of valence quarks can be used (Eq. 4.11), as well as the momentum sum rule of the π^- (Eq. 4.12).

$$\int_0^1 dx [\bar{u}(x) - u(x)] = 1 \quad \int_0^1 dx [d(x) - \bar{d}(x)] = 1 \quad (4.11)$$

$$\int_0^1 dx [q(x) - \bar{q}(x)] = 0 \quad (\text{for other flavors})$$

$$\sum_{q_i} \int_0^1 dx [x q_i(x)] = 1, \text{ where } i = u, \bar{u}, d, \bar{d}, g, \dots \quad (4.12)$$

4.5.3 Available Pion PDF Extractions

Despite the lack of new pion scattering data, there are several motivations to improve pion PDF extraction using global analysis. In the past decades, various techniques were also developed to account for nucleon PDF uncertainties, but also very recently for the pion using MC extraction techniques [78]. Additionally, the implementation of the NLO accuracy and the NLL resummation provides a better description of the current data.

Recent improvements related to the interpretation of nuclear effects allow reducing uncertainties in the extraction of the pion PDFs due to its convolution with nucleons in the target. At this moment, the extraction of nuclear PDFs still presents significant uncertainties compared to the constraint of the proton PDF, but better constraints are expected in the future from new data. Finally, the same argumentation also applies to J/Ψ production cross-section data. Indeed, the underlying non-perturbative production mechanisms remain to be understood, but it has the advantage of a much higher cross-section compared to Drell-Yan. Consequently, one can expect to use the available data once the production is better understood to constrain the gluonic distribution better.

Finally, a historical summary of the global fit analysis of the pion PDFs from the literature is briefly presented :

- **Owens [79] in 1984** : This parametrization is extracted at LO and based on both Drell-Yan and J/Ψ data from E537, NA3, and WA39. These data only gives a constraint of the valence-quark PDF in the range $0.2 < x < 1$.
- **Aurenche *et al.* [80] in 1989** : In addition to its valence-quark extraction, the ABKFW model at LO used data from prompt-photon production ($qg \rightarrow \gamma q$) and was consequently able to extract the gluonic contribution.
- **Glück *et al.* [81] in 1991**, The GRV parametrization at NLO initially provided an extraction of the pion PDFs using valence NA3, NA10, E615 data. The extraction of the sea and the gluon

distribution was constrained based on the valence extraction at some low resolution scale Q , but also using Q^2 evolved prompt-photon production.

- **Sutton *et al.* [82] in 1991:** The SMRS model at NLO relies on the Drell-Yan data from NA3, NA10, and E615. The sea quark PDF varies from 5% to 20% and the gluon PDF constraint is provided using WA70 data.
- **Glück *et al.* [83] in 1999:** A few years later, the parametrization (*renamed GRS*) was revisited using a quark constituent model, which provides new constraints on the gluon and sea quark PDFs.
- **JAM18 Collaboration [78] in 2018:** More recently in 2018, very recent extractions of the pion PDF were performed using the first MC global analysis [78]. This ab initio technique for the extraction of the pion PDFs provides new constraints on valence, sea, and gluon PDFs, including an estimation of the PDF uncertainties.

Global fits using GRV, GRS, SMRS and JAM are compared in Fig. 4.12. This comparison shows a considerable variation of the valence-quark between model. Such modifications are also symptomatic of the model dependence of the extraction and should stress the need for collecting more data to constrain these models better. The results of the NA3 fit is also included and the error bars are uncertainties in the fit extraction. Finally, promising results from lattice QCD analysis are in full swing and would help to constrain the regions which suffer from a lack of experimental data [84]. Consequently, contributions, such as the gluon PDF or the low x region at $x < 0.2$, might also be better determined.

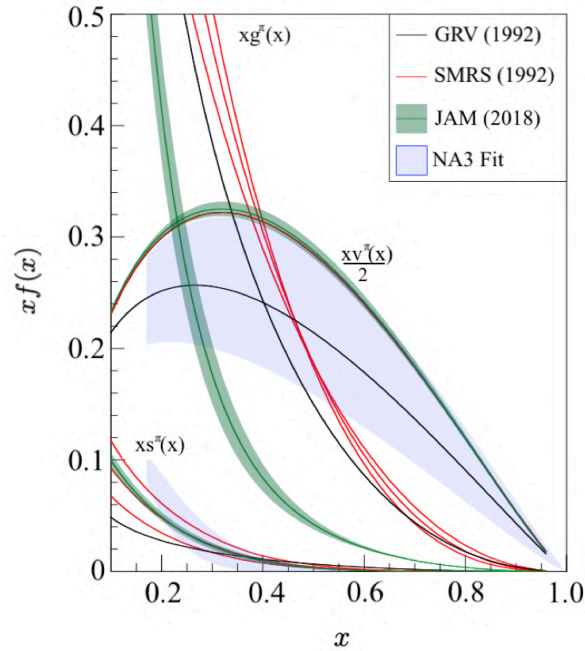


Figure 4.12: Comparison between gluons, valence-quark, and sea-quarks between GRV, GRS, SMRS, and JAM models at $Q^2 = 20 \text{ GeV}^2$ [74]. The three sea curves labelled SMRS correspond to three different hypotheses for the sea quark content. The valence contribution only refers to a single quark contribution out of two for pion (*e.g.* \bar{u} or d contribution for π^-)

Chapter II

The COMPASS-II Experiment

5	Hadron Beam Production	35
6	Target Setup and Beam Absorber	38
7	Trigger and Veto Systems	40
7.1	Single Muon Subsystems	40
7.2	Dimuon Trigger Logic	42
7.3	VETO Logic	43
7.4	Random Triggers	44
8	Tracking detectors	44
8.1	Very Small Area Trackers	44
8.2	Small Area Trackers	46
8.3	Large Area Trackers	47
9	Muon Identification	49
10	Data Acquisition System	50
10.1	Data Flow	50
10.2	DAQ Scalers	51

This chapter briefly describes the COMPASS⁴ apparatus and its 2015 features as used during the Drell-Yan 2015 data taking.

⁴Common Muon and Proton Apparatus for Structure and Spectroscopy

COMPASS is a High Energy Physics experiment at CERN in the North Area at the end of the M2 beamline of the Super Proton-Synchrotron. It is a fixed-target experiment, also known as NA58 experiment, and designed to probe the internal structure of the nucleon in many ways.

In 1996 the COMPASS-I proposal [85] was submitted to CERN. This proposal resulted from two distinct proposals conditionally approved in February 1997. At that time, one of the main goals was to study the spin structure of the nucleon using a muon beam. A second goal was to study the hadron spectroscopy using hadron beams. Consequently, COMPASS collaborators devoted their efforts in achieving a highly flexible and multipurpose setup. The first data were collected in 2001, and the first physics data taking started in 2002.

A second physics program was submitted and approved in 2010 [26] by the CERN Research Board. The data taking started in 2012. This second phase, known as COMPASS-II, extends the measurements to the three following physics cases :

- Experimental studies of chiral perturbation theory (Primakoff reactions)
- Pion-induced Drell-Yan muon pair production (Polarized Drell-Yan)
- Hard Exclusive photon and Meson Production (Deeply Virtual Compton Scattering)

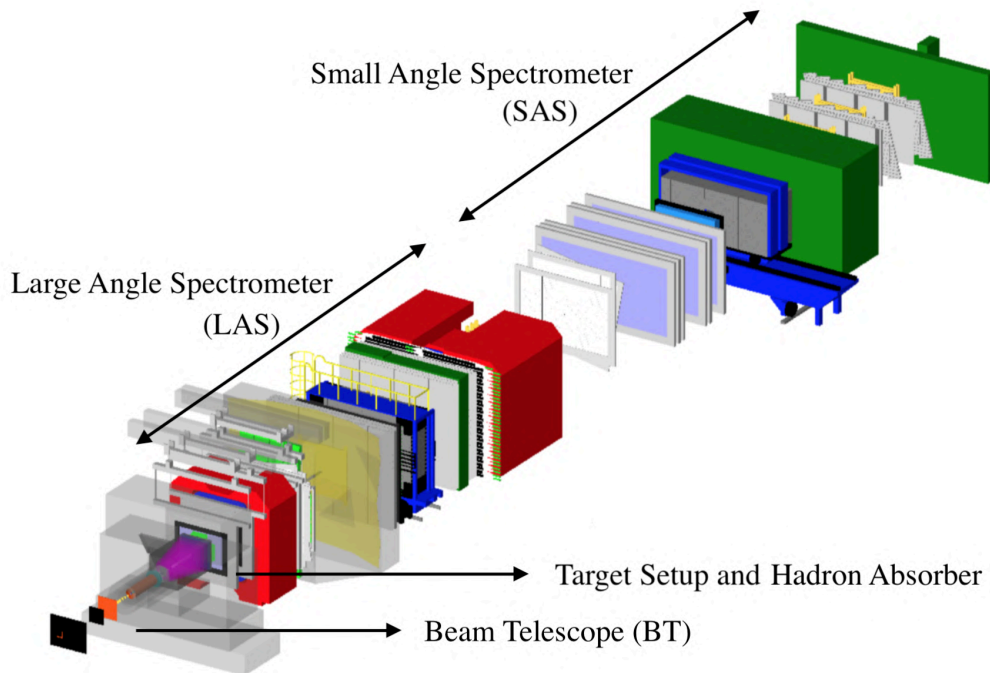


Figure 4.13: 2015 COMPASS setup used for the Drell-Yan measurement

Drell-Yan data were collected at COMPASS in 2014, 2015, and 2018. The COMPASS apparatus is described in many details in the following papers [26, 86, 87]. This chapter focuses on the 2015 COMPASS setup and introduces only key elements related to the Drell-Yan data taking.

The 2015 COMPASS setup is designed as illustrated in Fig. 4.13. The Beam Telescope (BT), located upstream of the target setup, is meant to track beam particles. The detection setup downstream of the targets is a two-staged spectrometer approximately 60 m long comprising two spectrometer magnets, SM1

and SM2. The SM1 magnet uses an integrated field of 1.0 Tm. It is located in the first stage, namely Large Angle Spectrometer (LAS) area, to study small momentum particles emitted at large angles. The SM2 magnet provides an integrated field of 4.4 Tm and bends high momentum charged particles in the second stage, namely Small Angle Spectrometer (SAS).

5 | Hadron Beam Production

The high energy beam used in the COMPASS experiment is created in the M2 beamline. This beam can either be a muon or a hadron beam. The primary proton beam sent from SPS¹ is converted into a secondary hadron beam at the entrance of the M2 beamline using the T6 ⁹Be production target (Fig. 5.1). Various beam intensities are achieved using different target thicknesses (either 40, 100, 200, or 500 mm). The beam optics is composed of an array of dipoles, quadrupoles, and toroidal magnets, namely SCRAP-ERS² and MIBs³, used to select the beam polarity, central momentum and to filter out beam impurities. A halo made of muons remains and originates from the natural π^\pm and K^\pm decays.

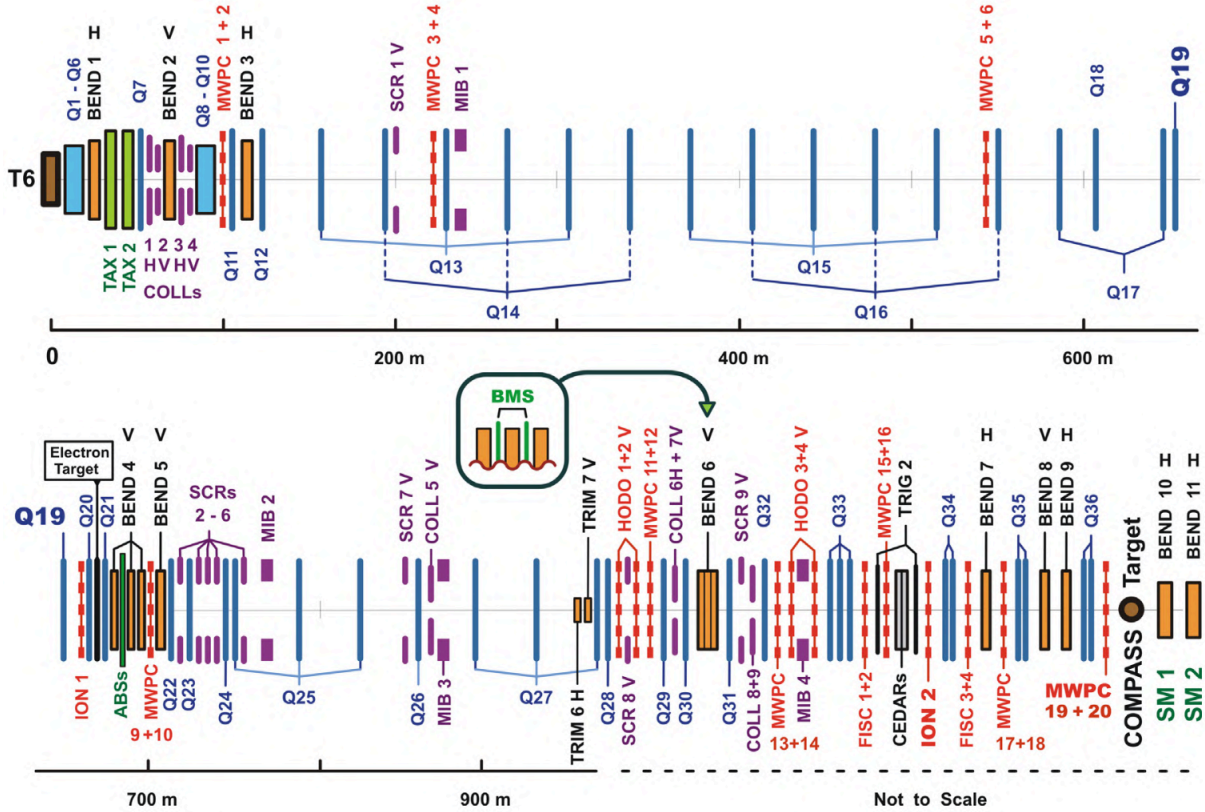


Figure 5.1: The CERN M2 beam line

A negative hadron beam with a momentum of 190 GeV/c was used in 2015. The intensity goes up to 10^8 hadrons per second, as measured by the ion chamber [88] at the entrance of the COMPASS hall. Moreover, this hadron beam is mainly composed of π^- . Some contaminations are expected from K^- and \bar{p} as given in Table 5.1.

¹Super Proton Synchrotron

²Collimator Technology

³Magnetized Iron Blocks

Table 5.1: The relative composition of the hadron beam at COMPASS for some typical momenta, as calculated from measured values [89]. Relative uncertainties amount to 1% for pions and protons, and 2 – 3% for kaons and antiprotons. The e^+/e^- contribution is still present at 100 GeV/c. Higher momentum particles rapidly decrease due to synchrotron radiation.

Momentum (GeV/c)	Positive beam			Negative beam		
	π^+	K^+	p	π^-	K^-	\bar{p}
100	61.8%	1.50%	36.7%	95.8%	1.80%	19.1%
160	36.0%	1.70%	62.3%	96.6%	2.30%	31.9%
190	24.0%	1.40%	74.6%	96.8%	2.40%	0.80%
200	20.5%	1.20%	78.3%	96.9%	2.40%	0.70%

The beam is delivered by pulses on a regular basis. A typical beam SPS pulse, also known as a spill, lasts for 5 seconds. The DAQ⁴ records data from the Begin-Of-Spill (BOS) signal to End-Of-Spill (EOS) signal. Physics data are only collected from 0.8 s to 5.6 s due to the SPS Veto as shown in Fig. 5.2.

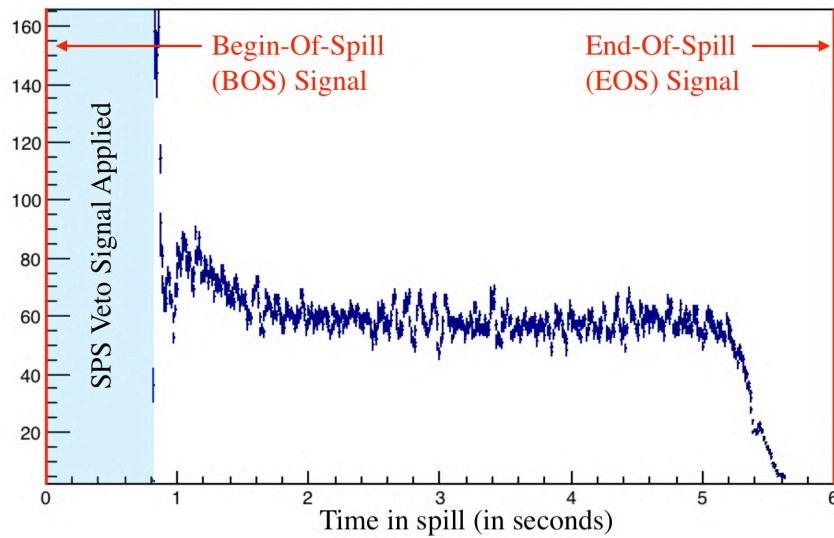


Figure 5.2: Typical example of time in spill profile, as collected during 2015 data taking (run 264738). The plot shows collected data from 0.8s to 5.6s. The SPS veto signal is applied at the beginning of the spill because of beam instability.

The 2015 beam momentum is estimated to be $190.9 \text{ GeV/c} \pm 3.231 \text{ GeV/c}$ (Fig. 5.3). This measurement was done in 2014 with a special run at low intensity using the Beam Momentum Station (BMS). The BMS (Fig. 5.4) surrounds the B6 magnet and is composed of four scintillator hodoscopes (BM01-BM04) and two scintillating fibers (BM05-BM06). Those stations measure each individual particle. In 2015, it could not operate at the nominal high intensity due to front-end electronics limitations. However, high intensity runs in 2014-2015 are expected to have a similar spread in momentum.

⁴Data Acquisition System

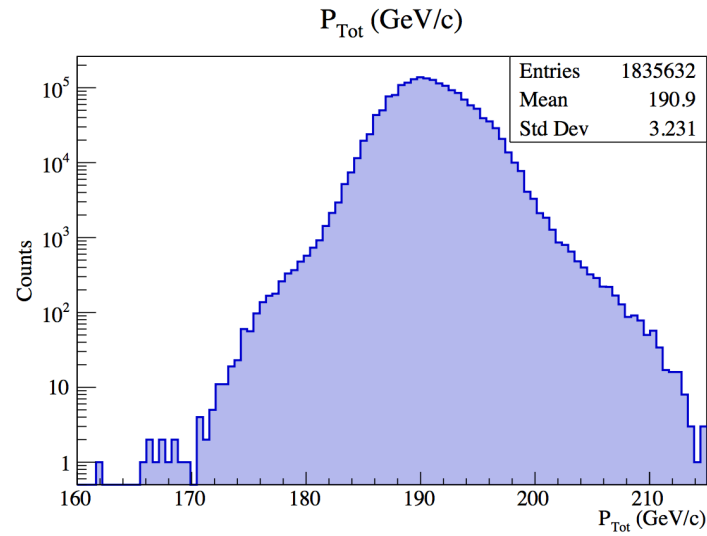


Figure 5.3: Measure of the momentum spread of the π^- beam used for Drell-Yan data taking

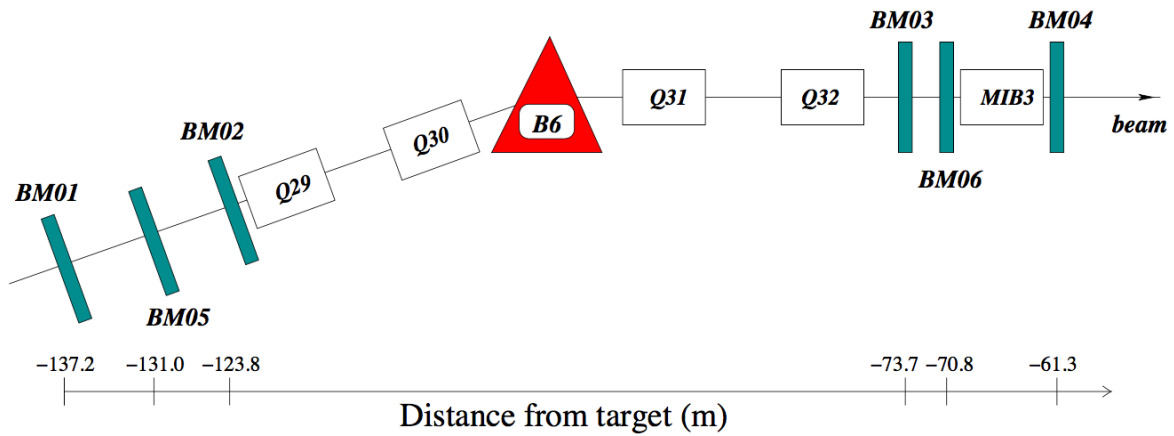


Figure 5.4: Layout of the BMS at the end of the M2 beam line, before entering the COMPASS Hall

6 | Target Setup and Beam Absorber

The COMPASS 2015 setup is composed of three different targets: A Polarized Target (PT) made of two cells of solid-state ammoniac in a liquid helium bath, an aluminum target, and a tungsten plug with the first few centimeters considered as a target. A sketch of the target setup, including the hadron absorber, is shown in Fig. 6.1.

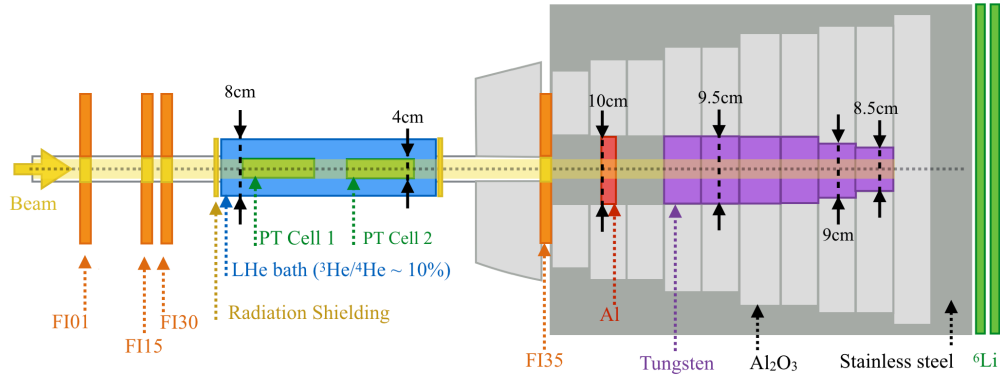


Figure 6.1: 2015 Target setup with the three targets, and the nearby scintillating fiber detectors, namely FI01, FI15, FI03, FI35, which are introduced later in Sec. 8.1

The target cells are placed in the dilution refrigerator, also known as PT cryostat. (Fig. 6.3) Two separated cylindrical cells, made of PCTFE¹ (Fig. 6.2), contain the NH₃ polarizable solid-state materials at low temperature. This polymer is a special material to avoid a perturbation of the polarization with excellent resistance to the experimental conditions at low temperature and pressure.

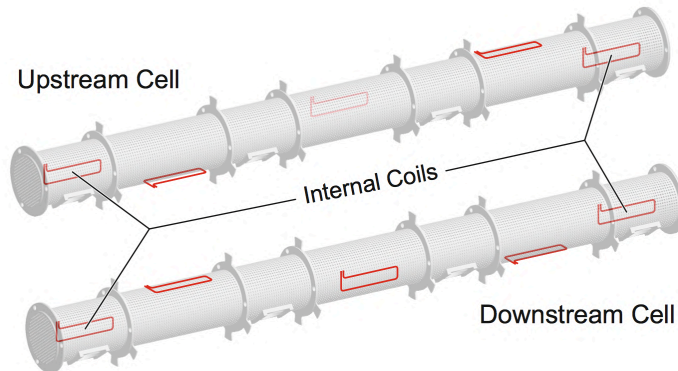


Figure 6.2: Diagram of the two PCTFE target holders, including the NMR coils used to measure the target polarization.

This PT system is essential for measurements of longitudinal or transverse spin asymmetries and is by far the most challenging and sensitive component of the Drell-Yan setup. The polarization is built using the Dynamic Nuclear Polarization (DNP) technique [90]. It consists of transferring the polarization of electrons to nucleons. Electrons are much easier to polarize than nucleons due to their higher magnetic moment. The solid target material is maintained at 60 mK during the polarization process in a LHe bath (³He/⁴He = 10%/90%) at the saturated vapor conditions. The longitudinal polarization is defined

¹ PolyChloroTriFluoroEthylene

as parallel to the beam propagation axis to go in the frozen-spin configuration. During longitudinal polarization, a superconducting solenoid magnet with a uniform field of 2.5 T is applied. Finally, the transverse polarization of the spin states is achieved by rotation of the magnetic field of 90° , which is ensured by a combination of the solenoid magnet with a dipole magnet of 0.63 T field. A typical value of the transverse spin polarization is about 70%, where only protons contribute to the polarization.

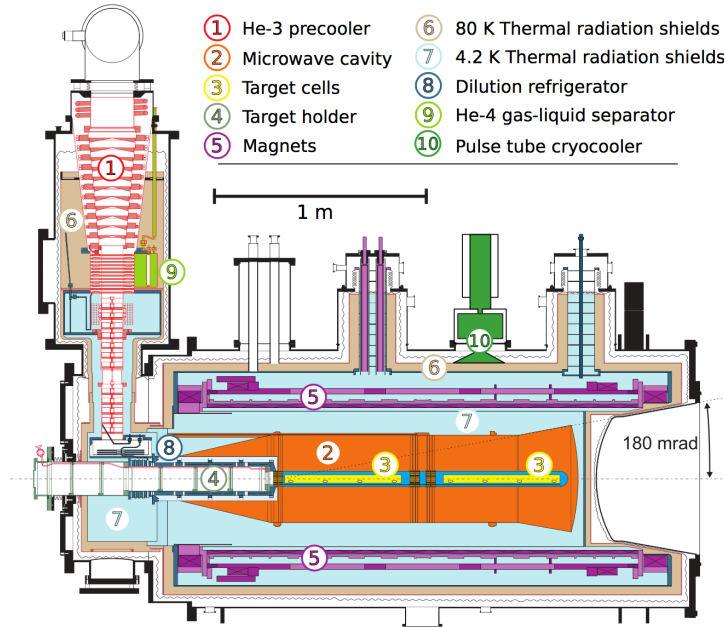


Figure 6.3: Representation of the COMPASS 2015 $^3\text{He}/^4\text{He}$ dilution refrigerator

The two polarized targets are 55 cm long, with a diameter of 4 cm and a gap of 20 cm in between cells. The dipole magnet of the PT target bends the beam about 1.63 mrad in the horizontal plane (academic exercise, Fig. 6.4). In practice, the incoming beam angle is obtained using a MC² simulation to better account for the non-uniform magnetic field. Consequently, the beam impinging on the target is steered to compensate for this deviation effect. The beam enters the PT target region with the corresponding opposite angle and enters the absorber collinear to the initial beam reference axis.

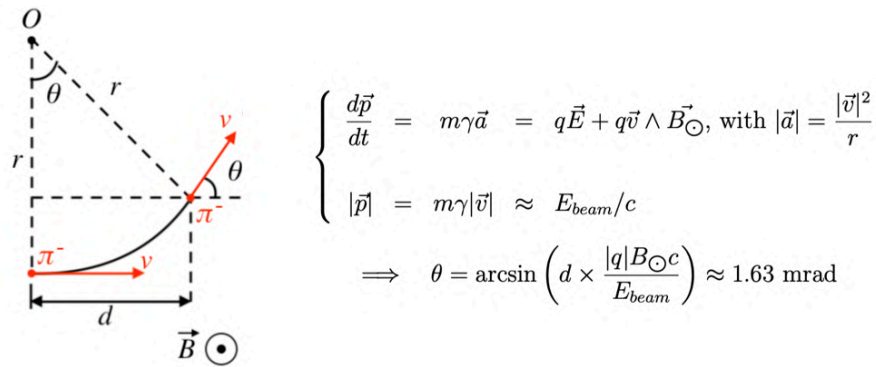


Figure 6.4: Propagation of a beam particle assuming an averaged uniform magnetic field, $\langle B_\odot \rangle \simeq 0.52$ T. The deviation angle is obtained by considering a relativistic π^- particle at $E_{beam} = 190$ GeV subjected to the Lorentz force (centripetal force). The distance $d \simeq 200$ cm corresponds to the length of the magnet as shown in Fig. 6.3

²Monte-Carlo Simulation

Finally, the hadron absorber is made of alumina tiles (Al_2O_3) inside a stainless steel frame. The end-cap nose of the hadron absorber is composed of aluminum, making a total thickness of 36 cm. The aluminum target is a cylindrical block of 7 cm length with a diameter of 10 cm and is used as an intermediate atomic mass for nuclear dependence studies. The tungsten plug is composed of three cylindrical blocks of 80 cm, 20 cm, 20 cm lengths and 9.5 cm, 9 cm, and 8.5 cm diameters, respectively. Only the first 10 cm of tungsten are usually used as a target due to the large beam absorption.

7 | Trigger and Veto Systems

The trigger system used for the detection of Drell-Yan dimuon events is composed of dimuon triggers. Dimuon triggers, described later in Sec. 7.2, are fired based on the single muon trigger signals, as described in the following.

7.1 Single Muon Subsystems

The single muon triggers are composed of three hodoscope subsystems, namely LAST, OT, and MT. Those triggers recognize single muon tracks. The hodoscopes are made out of horizontal slabs and consequently not sensitive to the magnet bending in the limit of the hodoscope acceptances. The overall picture of the relevant triggers and veto hodoscopes in the Drell-Yan 2015 data taking is shown in Fig. 7.1.

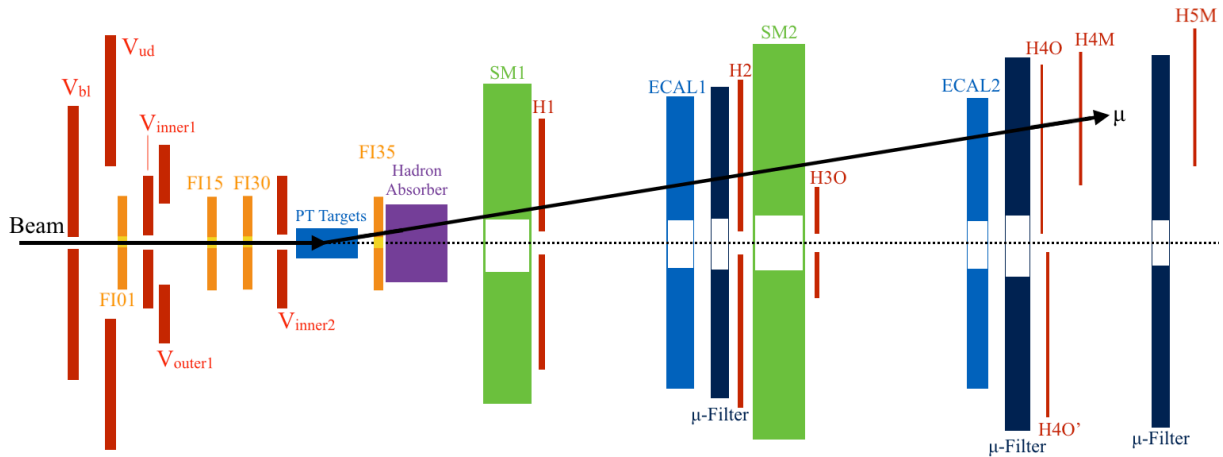


Figure 7.1: Top view sketch of the relevant hodoscopes used in the Drell-Yan 2015 data taking. The VETO hodoscope V_{ud} is not used, but remains in the 2015 setup

The list of the single muon Drell-Yan triggers is detailed in the following:

- **LAS trigger.** The LAS trigger consists of two hodoscope planes, H1 and H2. In 2015, each plane was composed of 32 slabs. They are located between SM1 and SM2 in the large-angle spectrometer area. H1 station consists of a single part hodoscope (HG01Y1). H2 is a two parts hodoscope (HG02Y1, HG02Y2) to avoid very long strips.
- **Outer trigger.** The OT logic is composed of two detection planes, H3O and H4O. The first hodoscope, HO03Y1, is composed of 18 slabs and located at the end of the LAS region. The second, H4O, is in the SAS¹ region and divided into two parts (HO04Y1, HO04Y2) made of 16 slabs each.

¹Small Angle Spectrometer

- **Middle trigger.** Finally, the middle trigger is made of two stations, namely HM04Y1 and HM05Y1. These hodoscopes are composed of 32 slabs each and located in the SAS region.

The trigger signal is built based on the coincidence between the corresponding hodoscopes. This principle is known as target pointing technique (Fig. 7.2). This signal is held for 25 ns, when no coincidence from veto signal, by using a flip-flop gate to avoid double counting. This technique uses a so-called coincidence matrix as already illustrated in Fig. 7.2. However, a matrix is defined for each single muon trigger as shown in Fig. 7.3 and optimized based on a Monte-Carlo simulation in a high Q^2 region to reject coincidences with background particles.

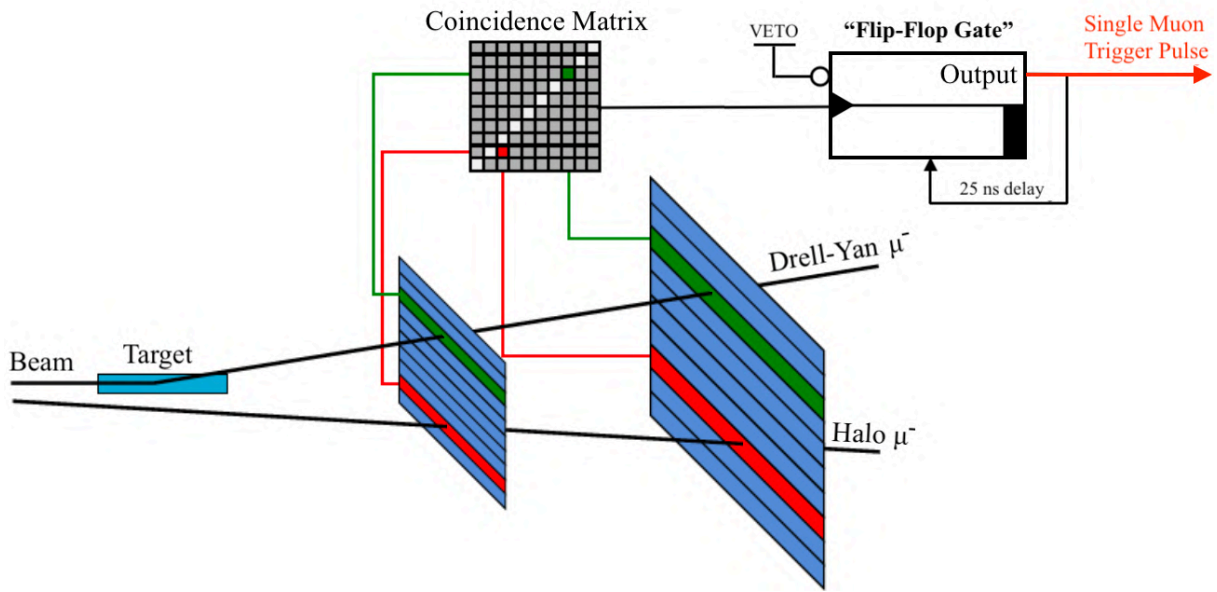


Figure 7.2: Sketch of the target pointing technique for μ^- (symetric with respect to μ^+). The trigger matrix pixel accepted are drawn in white. After coincidence matrix a flip-flop gate is used to generate only one trigger pulse. The signal in red is the trigger pulse sent to frontend electronics and the DAQ system

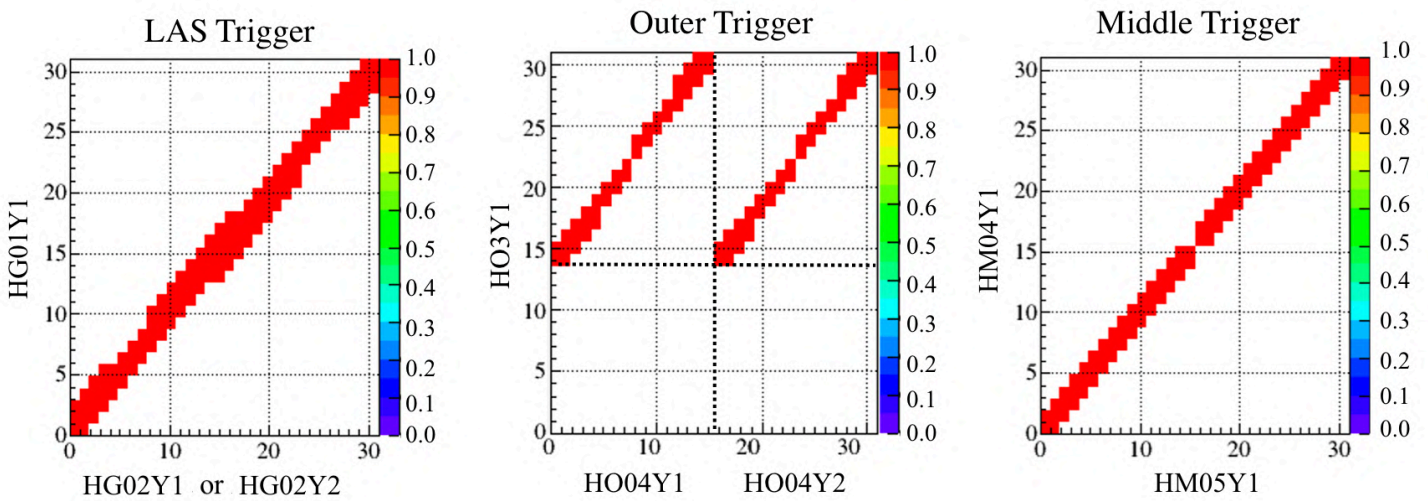


Figure 7.3: From left to right: Picture of the coincidence matrix for LAST (One for HG02Y1 and one for HG02Y2), OT (composed of a combined matrix for HOO4Y1 and HO04Y2 of 16 slabs each), and MT

7.2 Dimuon Trigger Logic

In 2015, three dimuon triggers were used, namely $\text{LAST} \otimes \text{LAST}$, $\text{OT} \otimes \text{LAST}$, $\text{MT} \otimes \text{LAST}$. Some parts of dimuon triggers are in overlap. Consequently, a trigger is called *inclusive*, when at least one of the dimuon trigger is fired in the event. A trigger is named *exclusive*, when the event is only triggered by one dimuon trigger.

Those dimuon triggers used for physics analysis cover a large range in $\sqrt{\tau}$ and x_F as shown in Fig. 7.4. These regions correspond to the coverage of the combined dimuon triggers. The region from $8.5 \text{ GeV}/c^2$ to $14 \text{ GeV}/c^2$ are latter removed from the analysis, because of Upsilon $\Upsilon(1S)$ contamination in the region from $8.5 \text{ GeV}/c^2$ to $11.5 \text{ GeV}/c^2$ and of the low acceptance coverage at larger mass. Moreover, an angular cut is applied to remove muons originating from the π^- (or K^-) beam decay. In 2015, the inclusive $\text{LAST} \otimes \text{LAST}$ dimuon trigger contribute approximatively to 62% of the total statistics, the inclusive $\text{OT} \otimes \text{LAST}$ trigger to 46% and the inclusive $\text{MT} \otimes \text{LAST}$ to 4%.

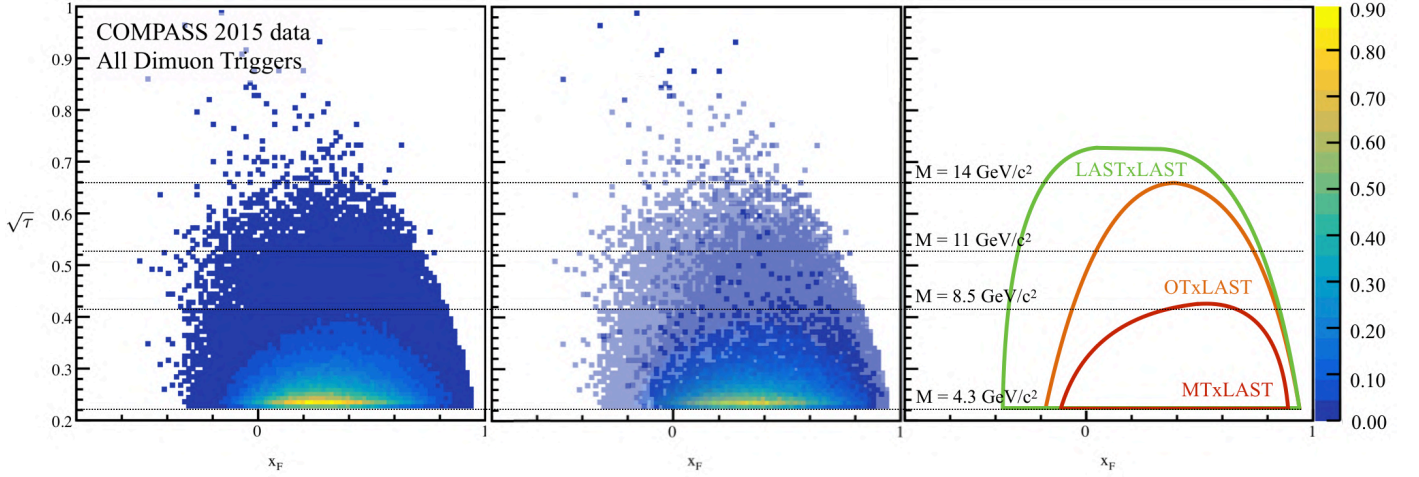


Figure 7.4: Left: The trigger coverage is expressed in terms of the scaling variables $\sqrt{\tau} = M/\sqrt{s}$ and $x_F = x_1 - x_2$ with a mass cut and beam decay muon removed; Middle: Decomposition of the dimuon trigger coverage using a gradient of opacity; Right: Contour of each dimuon trigger

Dimuon signals are obtained by a coincidence between single muon triggers. The overall picture of the dimuon trigger logic is introduced in Fig. 7.5. Middle and Outer triggers use coincidence modules. However, the LAS trigger involves an advanced programmable card, namely GANDALF² card. The dimuon signals are built following the rules hereinafter:

- **$\text{LAST} \otimes \text{LAST}$ (or LLAST).** This trigger requires at least two coincidences in the LAS region within 5 ns.
- **$\text{OT} \otimes \text{LAST}$ (or OLAST).** It requires at least one hit in each OT and LAST within 22 ns (value obtained after subtraction of the 3 ns minimum coincidence length of the CAEN N405 unit). The time window for combining signals is larger because LAS and Outer triggers are located in the LAS and SAS regions, respectively, and uses different electronics compared to LLAST .
- **$\text{MT} \otimes \text{LAST}$ (or MLAST).** The third dimuon trigger requires at least one coincidence in MT and LAST, respectively, and within 22 ns.

²Generic Advanced Numerical Device for Analog and Logic Functions

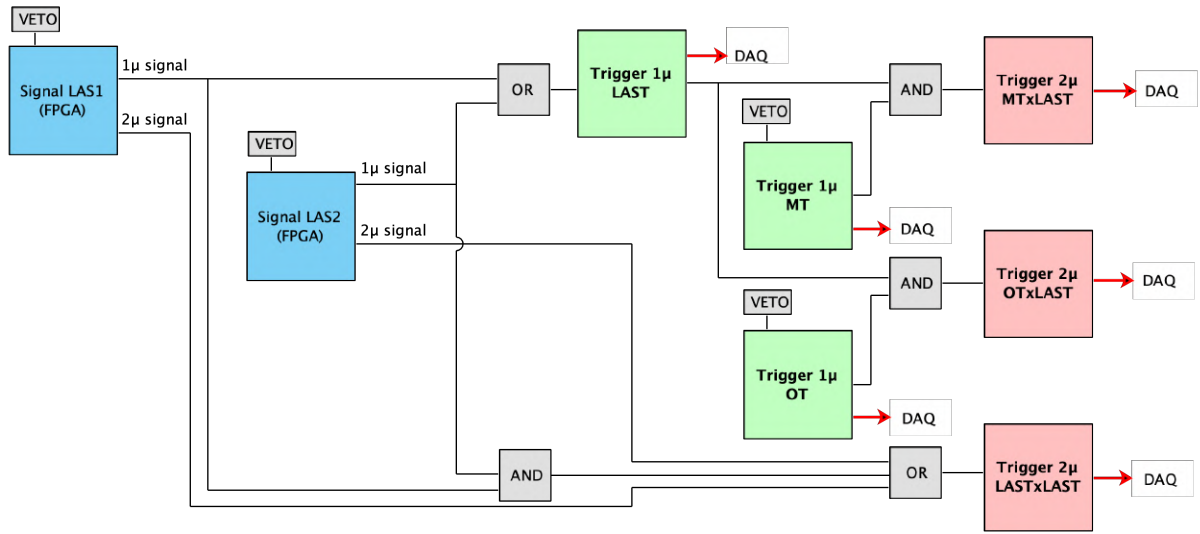


Figure 7.5: Diagram of the dimuon trigger logic (adapted from [91]). The special treatment for LAS trigger is detailed. The green boxes correspond to the single trigger signal used to obtain the dimuon trigger signal in the red boxes. In this picture, the FPGA LAS1 uses the combination of HG01Y1 and HGO2Y1, while FPGA LAS2 uses HG01Y1 and HG02Y2

7.3 VETO Logic

The VETO signal is used to avoid recording ambiguous events. As an example, these ambiguous events might originate from the coincidence between a halo beam track in the VETO hodoscope and a possible dimuon pair recognized by the trigger system. In this case, the VETO signal inhibits the physics trigger and does not record the event. The total VETO signal composed of four veto sub-signals and named V_{tot} . Fig. 7.6 illustrates some possible examples of vetoed signals.

$$V_{\text{tot}} = V_{\text{outer1}} \parallel V_{\text{inner1}} \parallel V_{\text{inner2}} \parallel V_{\text{beam line}}$$

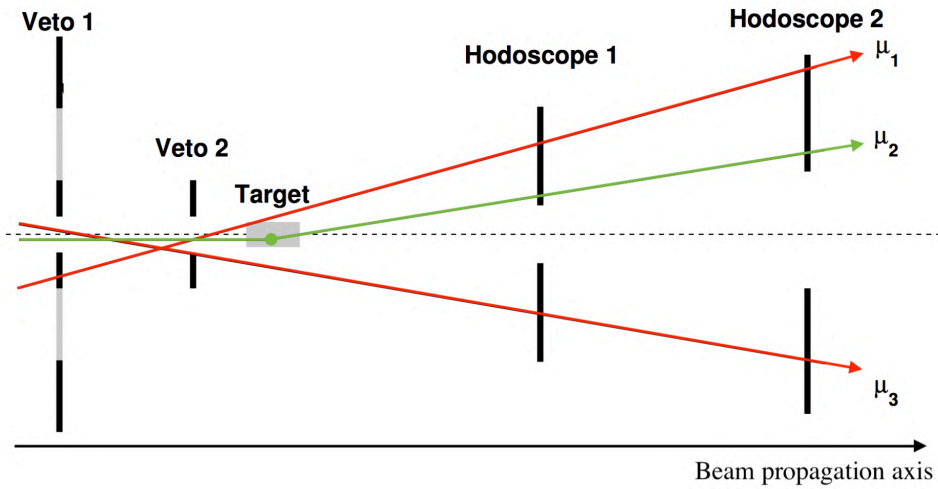


Figure 7.6: μ_1 and μ_3 are rejected by the VETO hodoscopes. μ_2 is accepted as it is pointing to trigger hodoscopes without firing VETO hodoscopes.

7.4 Random Triggers

The Random Trigger (RT) subsystem is fired by the coincidence of two photons with two photo-multiplier tubes. These photons originate from the ^{22}Na source via β^+ decay. (Fig. 7.7). Particles that fire a dimuon trigger are initiated by a beam track. Consequently, it is more likely to observe a beam particle when a physics trigger is fired. Therefore, this trigger is essential to estimate an unbiased beam flux.

The VETO logic is not applied to the RT events by the construction of the trigger logic to ensure a truly random trigger. RT³ events are recorded on a spill basis by the DAQ between the Begin-Of-Spill (BOS) signal and the End-Of-Spill (EOS) signal. Moreover, the total number of RT events should be comparable to the dimuon trigger rate to ensure proper sampling of the beam flux.

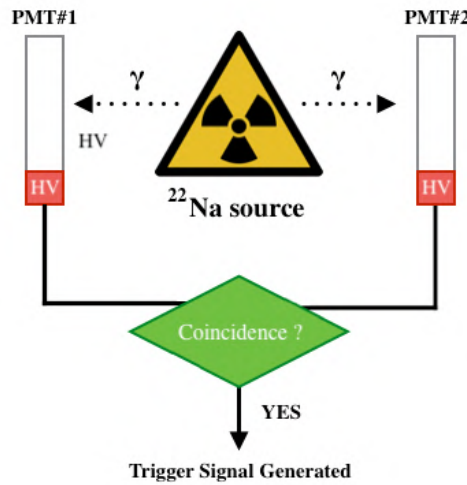


Figure 7.7: Workflow of the True Random Trigger. A trigger signal is generated if the two PMT⁴ signals are in coincidence

8 | Tracking detectors

The 2015 COMPASS spectrometer covers a large angular phase space from 25 mrad to 165 mrad in the LAS region and from 8 mrad to 45 mrad in the SAS region. This broad coverage is resulting from the combination of three tracking regions: Very Small Area Trackers (VSATs), Small Area Trackers (SATs), Large Area Trackers (LATs). These regions are discussed in Sec. 8.1, Sec. 8.2 and Sec. 8.3 respectively.

8.1 Very Small Area Trackers

In the Very Small Area Trackers (VSATs) region, the tracking is performed either by Scintillating Fiber (Sci-Fi) detectors, Silicon Microstrip detectors, Pixelized Micromesh gaseous structure (Micromegas) detectors or Pixel GEM detectors. Silicon detectors could not sustain long term radiation exposure using a high rate of hadron beam (10^8 hadrons per second) and were consequently removed from Drell-Yan setup to prevent anticipated aging.

³Random Trigger

Scintillating Fiber detectors, FI01, FI15, FI03, FI35, FI04 The Beam Telescope is composed of three scintillating fiber detectors, namely FI01, FI15, and FI03. They are made of the (X1, Y1), (U1, X1, Y1) and (U1, X1, Y1) coordinates, respectively. Additionally, FI04 is located in the LAS region near the micromegas detectors and composed of (X1, Y1, U1) coordinates. A single coordinate is made of the superposition of multiple staggered fiber layers, as shown in Fig. 8.1. The size of the active areas varies from $3.9 \times 3.9 \text{ cm}^2$ to $12.3 \times 12.3 \text{ cm}^2$. Spatial resolutions are either 130, 170, or $210 \mu\text{m}$ depending on the diameter of the fiber, which is 0.5, 0.75, and 1 mm, respectively. The timing resolution is about 400 ps. An example of the Sci-Fi efficiency 2015 (FI01X1) is shown in Fig. 8.2, and the full picture of the efficiency is shown in the Appendix I. Moreover, in 2015, FI03X1 and FI03U1 were slipped by 1.4 cm, which reduced the acceptance of the beam telescope due to a lack of redundancy. Consequently, the efficiency estimation coverage is limited as clearly visible in Fig. 8.2 for $Y > 1 \text{ cm}$.

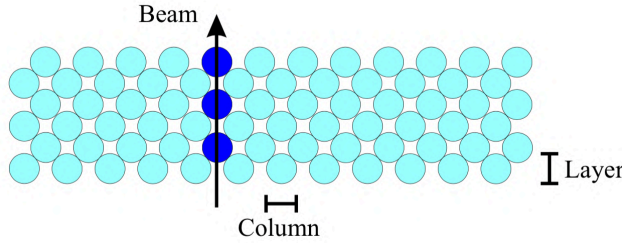


Figure 8.1: Illustration of the SciFi active area made of several layers of scintillating fibers. Either 8, 12 or 14 layers, depending on the station [87]

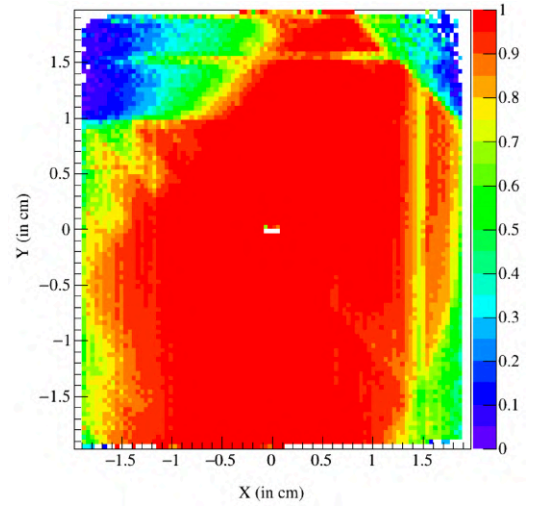


Figure 8.2: Efficiency of the FI01X1 plane : $\varepsilon(6\sigma)96.00\%$

The scintillating fiber detector, FI35, composed of the (U2, U1, V2, V1, X2, X1) coordinates, was placed between the upstream end-cap of the absorber and the hadron absorber (Fig. 6.1). The purpose of this detector was to improve the vertex resolution. However, it suffers losses from a very high occupancy due to particle radiation coming from the hadron absorber. Its use in the tracking is still under development.

Pixelized coverage of the new hybrid Micromegas stations. These detector stations are located after the absorber in the LAS region. The regular active area of the Micromegas detector is part of the SAT¹ region and is explained in the next section. However, the new pixelized area is part of VSAT² coverage. This sensitive pixel area is composed of pixels of $2.5 \times 0.4 \text{ mm}^2$ within a region of $25 \times 25 \text{ mm}^2$. Larger pixels have a size of $6.25 \times 0.4 \text{ mm}^2$ and cover a ring surface from 25 mm to 50 mm. The timing and spatial resolutions of the pixel region are 9 ns and $80 \mu\text{m}$, respectively.

¹Small Area Tracker

²Very Small Area Tracker

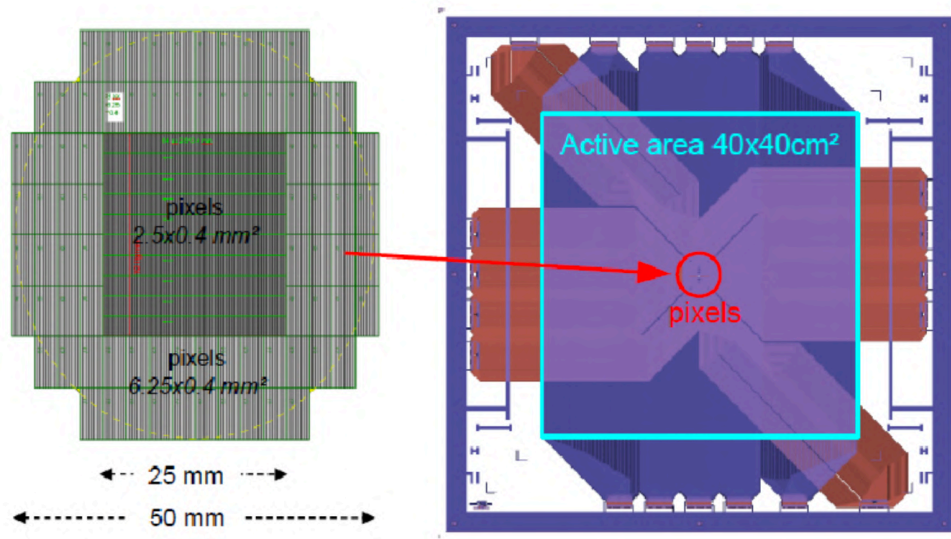


Figure 8.3: Design of the pixelized micromegas detectors

8.2 Small Area Trackers

The small Area Tracker region is composed of Micromegas detectors and Gas Electron Multiplier (GEM) detectors. These gaseous detectors intend to cover a region from 5 to 40 cm. The beam rate in this region is about 10^5 Hz.

Gas Electron Multiplier detectors, GM01 to GM11 and GP02, GP03. There are eleven GEM stations in the 2015 setup composed of four projection planes (U1, V1, X1, Y1) each. Besides, two Pixel GEMs, namely GP02 and GP03, are also used. Those detectors are evenly distributed throughout the spectrometer, starting from downstream of the SM1 magnet. A GEM detector is an assembly of three GEM foils. GEM foils are made up of $50\ \mu\text{m}$ polyimide foils coated on both sides with copper. During a standard run, the central region is neutralized to avoid a too high occupancy of the detector due to very low angle muons. A hole pattern is laser drilled with a density of 10^4 holes/ cm^2 [92]. The active area of GEM detectors is about $31 \times 31\ \text{cm}^2$.

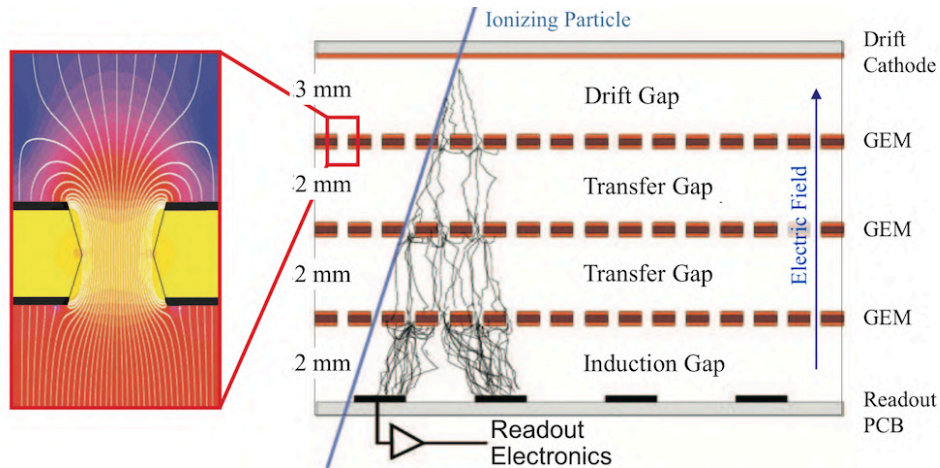


Figure 8.4: Diagram of the GEM amplification process. The left-hand side schematic is illustrating the typical electric field in a GEM hole.

The operating principle of GEM detectors is shown in Fig. 8.4. An incoming particle in the drift gap (also named conversion gap) is ionizing the gas mixture made of Ne/CF₄/C₂H₆ (80%/10%/10%). A drift field E_{drift} is applied to the cathode and initiate the drifting of the primary electrons. An electric potential, E_{GEM} , is applied to the GEM and generates an avalanche of electrons collected by the readout strips.

New Hybrid Pixelized Micromegas, MP01, MP02, MP03. There are three Micromegas stations, each of them composed of four projection planes. Those stations are located between the absorber and the SM1 magnet. The active area is split into two parts: the pixelized part introduced in the previous section, and the standard active area of a size of $40 \times 40 \text{ cm}^2$.

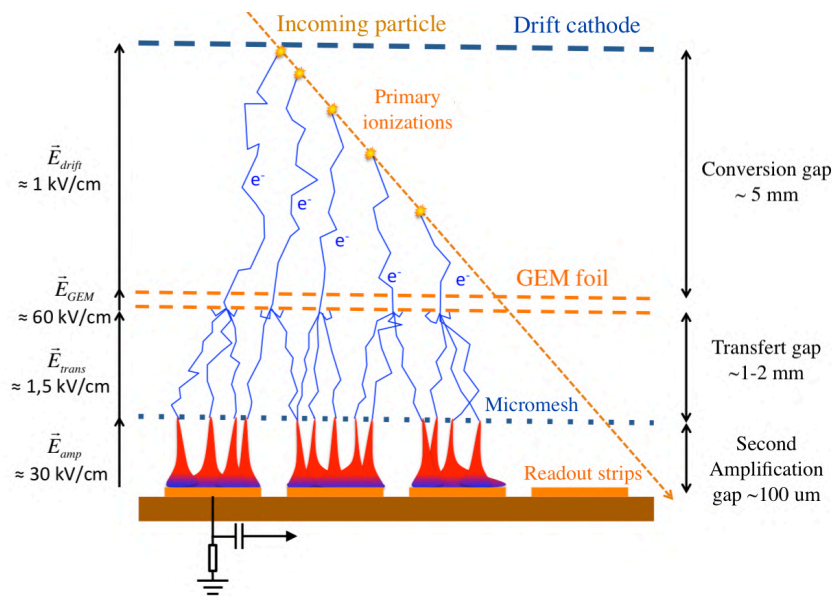


Figure 8.5: Schematic of the amplification process of the pixelized micromegas used at COMPASS (adapted from [93])

The operating principle of the new hybrid pixelized Micromegas detector is shown in Fig. 8.5. This hybrid technology is based on the combination of a metallic micromesh and an additional GEM foil. The GEM foil reduces the disruption probability rate during electron transfer. A gap space of $100 \mu\text{m}$ between the micromesh and the readout strips minimizes the transverse propagation of the final electron cascade and aims at the excellent spatial resolution of this technology. The timing and spatial resolutions of the strip part are about 9 ns and $110 \mu\text{m}$, respectively.

8.3 Large Area Trackers

The Large Area Trackers (LATs) region covers the outer region of the spectrometer. The LAT³ region includes detectors located both in the first and second stages of the spectrometer. The central part of LAT detectors are all neutralized; Consequently, the geometrical coverage is ensured by the VSAT and SAT detectors. This region uses five different types of drift chamber technologies and is described as following.

³Large Area Tracker

Drift Chambers, DC00, DC01, DC04, DC05. The 2015 setup combines four drift chambers. DC00 and DC01 are located upstream SM1 with an active area of $180 \times 127 \text{ cm}^2$. DC04 and DC05 are located downstream SM1 with a larger active area of $248 \times 208 \text{ cm}^2$.

A schematics of the operating principle is shown in Fig. 8.6. A DC detector is made of four double layers. The purpose of the double layer is to avoid tracking ambiguities. Each layer is made of an alternation of $20 \text{ }\mu\text{m}$ radius sensitive wires (anode) and $100 \text{ }\mu\text{m}$ radius field wires, equally distributed in space. These wires are enclosed in between two cathode foils, which are separated by 8 mm gas space. The center of these foils (30 cm diameter) are independent and supplied by a separate high-voltage to neutralize the center of the detector. The purpose of this dead-zone, also known as beam killer, is to lower the large amount of charges generated by muons at low angles. The spatial resolution of DC detectors is of the order of $300\text{--}400 \text{ }\mu\text{m}$. Fig. 8.7 shows a typical efficiency map of the DC04V1 detector in 2015. Strips at $X \simeq -45 \text{ cm}$ shows few inefficient wires due to frontend electronics. Two structural elements in diagonal (green bands in Fig. 8.7) are used to support wires. Finally, the beam killer is visible in the center of the detector.

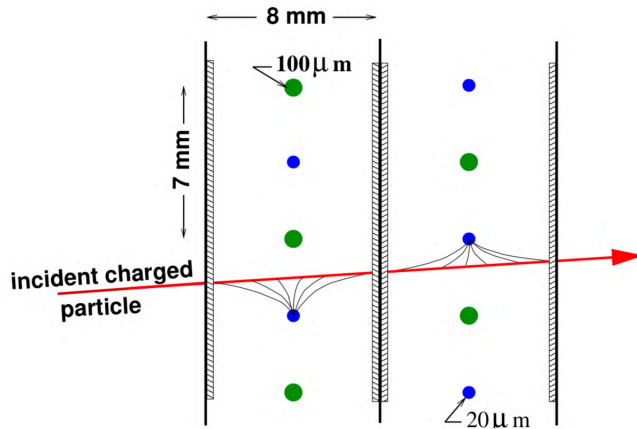


Figure 8.6: Schematic of the operating principle of the DCs [85]

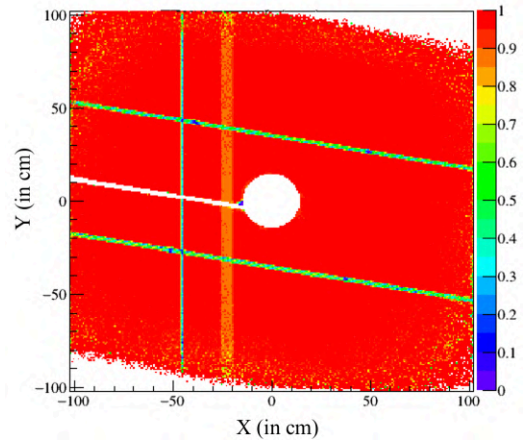


Figure 8.7: Efficiency of the DC04V1 plane : $\varepsilon(6\sigma) = 95.73\%$

Straw Chamber, ST03, ST05. Two straw detectors were in place in 2015, namely ST03⁴ and ST05. The ST05 detector, located in the SAS region, was not used for the tracking but remained in the spectrometer. ST03 is composed of six double layers. It is described in more detailed in Ch. III, including the calibration methods and the efficiency studies.

Multi-Wire Proportional Chamber, PA, PB, PS. There are 14 stations included in the tracking: six are in the LAS region and eight in the SAS region. They are three different types of technology, called type-A, type-A*, and type-B. Type A is composed of three projections (X, U, V). U- and V- views are rotated by $\pm 10^\circ$. Additionally, type A* is including an extra Y projection compared to type A. Type B is composed of an X projection coupled with either a U or V coordinate. Dead-zones in each of the detectors are about $16\text{--}22 \text{ mm}$ diameter. Besides the different projections, the difference between type A and B are the size of the active area, $178 \times 120 \text{ cm}^2$ and $178 \times 80 \text{ cm}^2$ respectively. The spatial resolution is about $600 \text{ }\mu\text{m}$.

⁴Straw Tube Detector

RichWall, RW RichWall detector is a tracking station downstream of the RICH composed of MDT⁵ tracker. A single MDT module is composed of eight aluminum combs covered with an inox layer and wrapped into a Noryl envelope of 1 mm. In the center of each module, a gold plated tungsten wire of 50 μm radius is used as the anode.

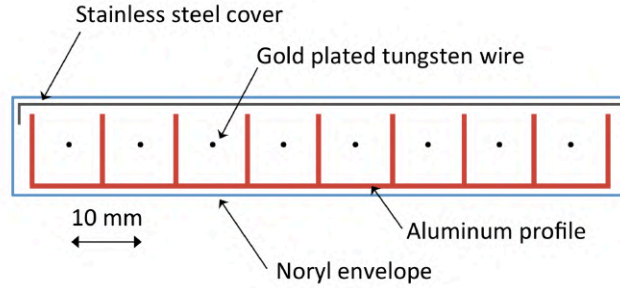


Figure 8.8: Sketch of a Mini Drift Tube module [87]

A Large Size Drift Chamber, W45. This detector consists of six stations, each made of a double projection. Each projection is a double layer covering an active area of $520 \times 260 \text{ cm}^2$, with a central dead-zone of either 50 cm or 100 cm diameter. Sensitive wires are spaced with a pitch of 4 cm. A typical spatial resolution was about 500-600 μm in 2015.

9 | Muon Identification

A more general description of particle identification, including hadron identification (from RICH-1 detector), is given in the COMPASS-II proposal [26]. However, the Drell-Yan analysis only relies on the identification of muons. In such a case, this task is achieved by using two Muon Walls (MW) stations. Those stations MW1 and MW2 are located in both LAS and SAS region, respectively.

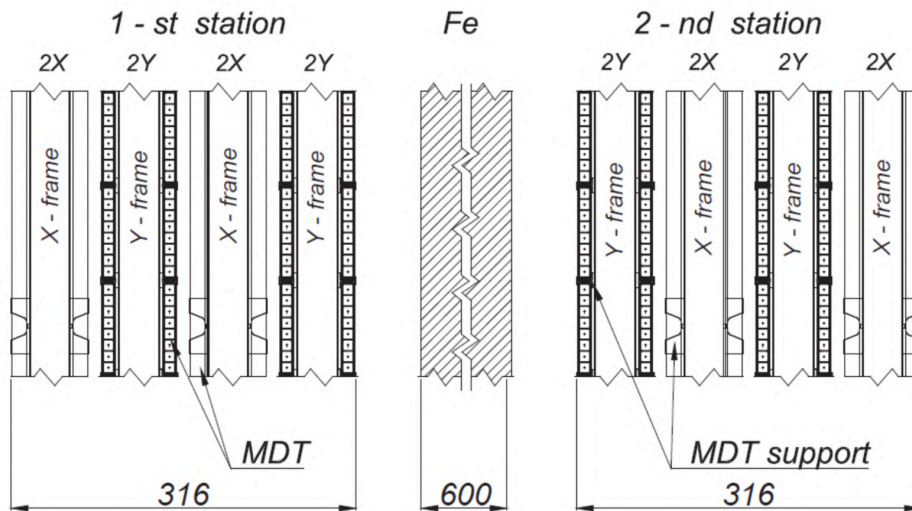


Figure 9.1: Schematic of the MW1 [86]

⁵Mini Drift Tubes

Muon Filters Absorbers, MF1, MF2 Three Muon Filters (MF) are used in the spectrometer to filter out hadrons and light particles. MF1 and MF3 are made of 60 cm of Iron, which has high stopping power. The MF2 is built around a concrete absorber of 2.4 m.

Muon Walls Detectors, MW1,MW2. Both consist of eight tracking planes upstream and eight planes downstream of the Muon Filters, MF1, and MF2s, respectively. MW1 and MW2 are acting in different locations. MW1 is dedicated to the LAS region and made of MDT trackers, as shown in Fig. 9.1, with an active area of $480 \times 410 \text{ cm}^2$ and a central hole of $140 \times 80 \text{ cm}^2$. Moreover, the MW2 acts in the SAS region and is composed of MDT trackers downstream and uses the W45 detector for upstream tracking.

10 | Data Acquisition System

10.1 Data Flow

The DAQ is a high-level system able to deal with a large amount of data coming out of detectors from the experimental hall. In 2015, the typical trigger rate during a normal run was about 30 kHz at high intensity. Table 10.1 shows the trigger table for a high intensity run in 2015 including pre-scaling. A division factor, called pre-scaling, is set to balance the load of the DAQ and only record relevant data. All dimuon triggers are pre-scaled to 1, and some triggers are disregarded when set to 0.

Table 10.1: Summary table of the 2015 trigger table. In this example, the *in* and *out* rates correspond to the first spill values of run 264738.

Trigger Name	Division Factor	In rate	Out rate
Dimuon Trigger MLAST	1	4081	4081
Single Muon Trigger MT	100	445615	4457
Dimuon Trigger OLAST	1	4912	4912
Single Muon Trigger OT	100	114239	1143
Calorimeter Trigger	0	3571205	0
Inner Veto	0	8895444	0
Beam Halo Trigger	0	1327070	0
Beam Trigger	35000	60224913	1722
Dimuon Trigger LLAST	1	98608	98608
Single Muon Trigger LAS	500	685091	1371
True Random	1	6426	6426
Noise Random	0	2534705	0

In 2015, a total of four readout engines (computers) were in charge of processing the high outgoing data flow and building the final raw signal. A simplified diagram of the 2015 DAQ data flow is shown in Fig. 10.1. Analog signals are collected by electronic front-end (FE) cards. Signals are digitized either on FE cards (TDC¹, F1², ADC³), or at the next stage in the HGeSiCa⁴, CATCH⁵, GANDALF⁶ cards.

¹Time-To-Digital Component

²Eight Channel Time-to-Digital Converter Chip for High Rate Experiments

³Analog-To-Digital Converter

⁴Hot GEM and Silicon Control and Acquisition

⁵COMPASS Accumulate, Transfer and Control Hardware

⁶Generic Advanced Numerical Device for Analog and Logic Functions

The digitized data is sent via SLink⁷ to the FPGA⁸ multiplexers. The multiplexed signal is sent to the readout engine before storage. For long term storage, data are then written on CASTOR⁹, a magnetic tape recorder at CERN.

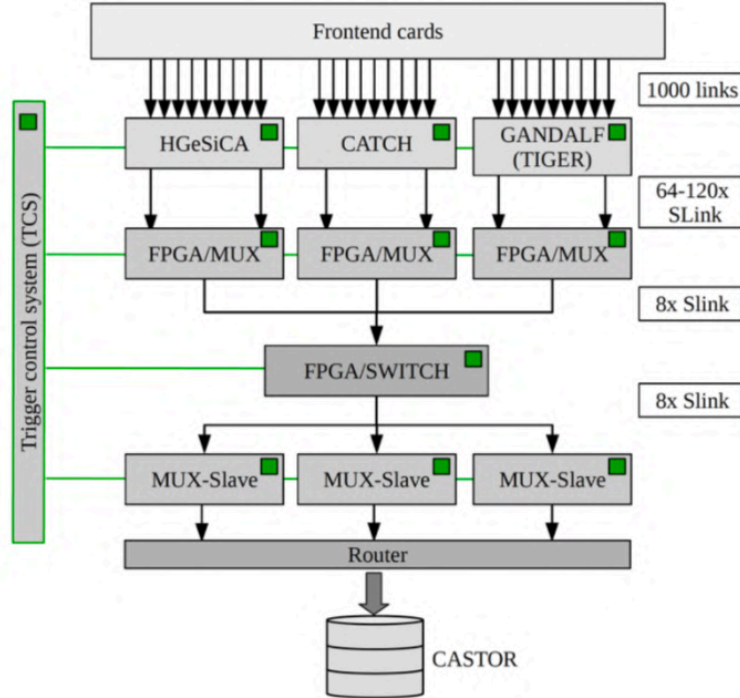


Figure 10.1: Schematic readout and data acquisition flow at the COMPASS experiment since 2015. The green boxes corresponds to the components that receive the trigger signal by the Time Control System (TCS) [94].

10.2 DAQ Scalars

The DAQ system reads counting information from NIM counters. A scaler counts the number of DAQ events between the BOS¹⁰ and EOS¹¹ signals. A non-exhaustive list of DAQ scalars is shown in Appendix A. Such additional information are highly useful for beam flux determination, as well as dead time estimation. In 2015, the main scalars used in the analysis are the RT scaler $N_{RT,attempted}$, and First Level Trigger (FLT) scaler $N_{FLT,attempted}$ for luminosity calculation.

- The RT scaler counts the expected random triggers before DAQ processing. The recorded RT are directly counted from uDST data.
- The FLT scaler counts all incoming triggers fired, both physics and RT events, before DAQ processing. The collected FLT are obtained from mDST data.

Additionally, a second scaler system, known as *Munich scalars*, is read out independently of the DAQ.

⁷CERN specification for an easy-to-use FIFO-like data-link

⁸Field Programmable Gate Array

⁹CERN Advanced STORage manager

¹⁰Begin-Of-Spill

¹¹End-Of-Spill

Chapter III

Straw Tube Detector

11 Operating Principle	54
11.1 Proportional chambers	54
11.2 Straw Tube Technology	56
11.2.1 Detector Structure	56
11.2.2 Gas Mixture	58
11.2.3 Front-End Electronics	58
12 Calibration and Characterization in 2015	58
12.1 Calibration Methods	58
12.1.1 Alignment and Residual Distributions	59
12.1.2 Relation $R(T)$	60
12.1.3 T_0 Calibration	60
12.1.4 Detector Time Gate	60
12.1.5 X-ray Correction	61
12.2 Results: Performance Studies	62
13 Results: Hardware upgrades in 2016-2017	62
13.1 Gas System Upgrade	62
13.2 Air Contamination Measurement	64
13.3 Gas Filter Refurbishing	64

The straw tube technology used at COMPASS detects outgoing muons among other particles in the Large Angle Spectrometer (LAS) region. During the COMPASS-I phase, the tracking was performed using the following straw detectors: ST02, ST03, ST04, ST05, ST06. ST04 and ST06 were removed in 2004. At the end of 2014, ST02 was also removed from the spectrometer and replaced by the DC05 detector [95]. Finally, the ST05 detector was not used in the tracking in 2015 and removed from the spectrometer after data taking. Consequently, only ST03 detector remains in the spectrometer since 2016.

The LMU Munich group was responsible for this technology until 2013. Pieces of knowledge related to this detector were about to be lost when the University of Illinois group joined COMPASS and became the main responsible in 2014. Part of this Ph.D. work consisted of relearning, maintaining and calibrating the ST03 detector from 2016 to 2018 in collaboration with the Joined Czech group from Prague.

This chapter describes to some extends the operating principle of proportional chambers, and introduces the specificities of the straw tube technology. The characterization of the detector in 2015 is presented, as well as the most important hardware upgrades performed in 2016 and 2017.

11 | Operating Principle

A gaseous detector is a detection technology able to track charged particles. These latter cross and ionize a gas volume along its path, resulting in the creation of ion-electron pairs to be collected by the detector electronics.

One century ago, Hans Geiger and Ernest Rutherford operated for the first time a gaseous detector [96]. Early gaseous detectors such as cloud chambers [97] or spark chambers [98] were used to measure the trajectory of charged particles with limited precision. In 1968, Georges Charpak and Fabio Sauli accomplished a groundbreaking achievement by building for the first time a Multi-Wire Proportional Chamber. Since this time, many other technologies, based on the same principle, were developed including straw tube detectors.

11.1 Proportional chambers

The working principle of gaseous detectors relies on particle ionization in a gas mixture by operating in the proportional regime. Fig. 11.1 is an illustrative diagram of the collected signal for different voltage regions and different α , β and γ radiations. The same proportional principle applies to muons detected in the COMPASS tracking chambers. The nature of proportional counting makes the amplification linear as a function of the applied voltage. In other words, the collected charge is proportional to the ion-electron pairs created by the incident radiation. Ionizing particles, crossing a gas volume inside the

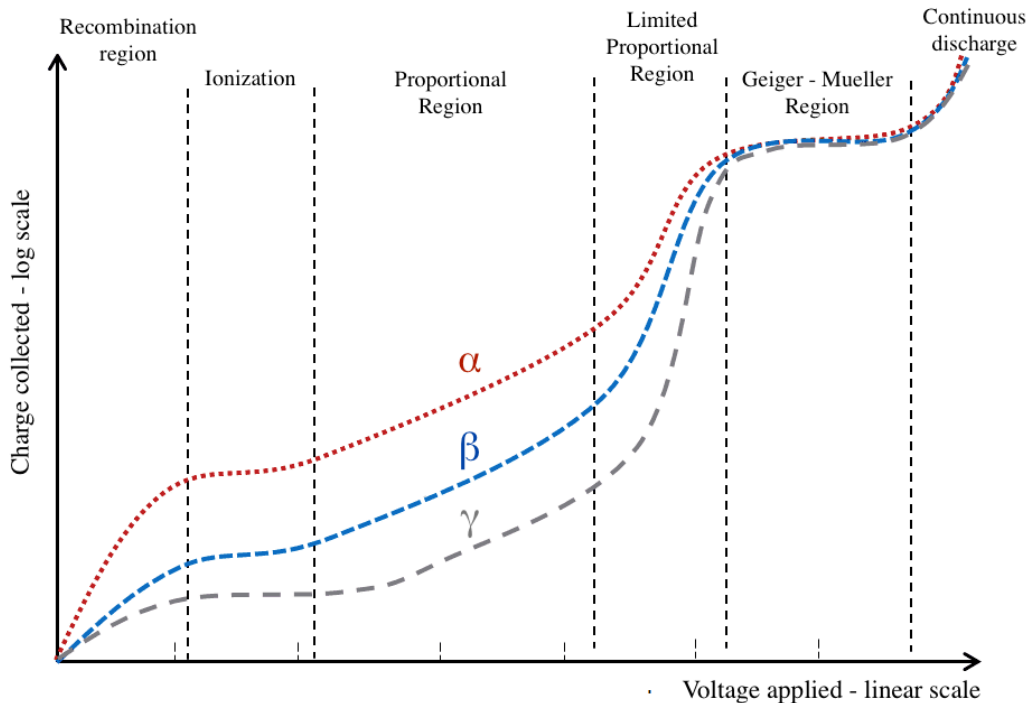


Figure 11.1: Operating regions of gaseous detectors [99]

chamber, create primary ion-electron pairs. Electrons and ions drift in opposite directions with different speeds when an electric field is applied between the cathode and the sense wire, as shown in Fig. 11.2. Under an intense electric field, the accelerated electrons also ionize the medium, creating an avalanche of ion-electron pairs, which are collected by the front-end electronics through the anode wire.

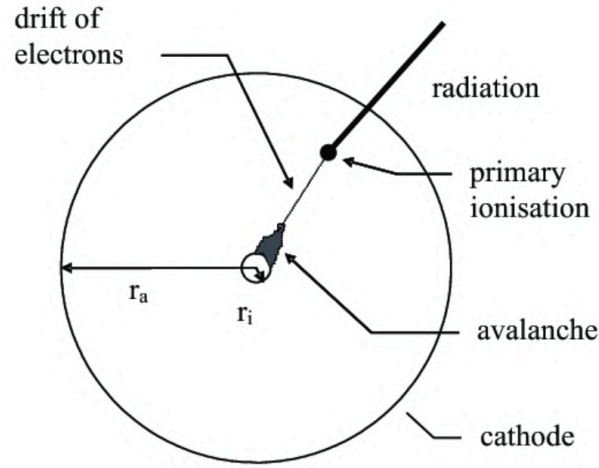


Figure 11.2: Principle of proportional counter [100]

In Fig. 11.3, the collected charge cannot only be attributed to the drift of the electrons which is of the order of few nanoseconds (in blue). The electron signal is too short compared to the integration time of the electronics. Consequently the collected signal is finally also related to the potential gradient of the electric field relative to the ion drifting (in red).

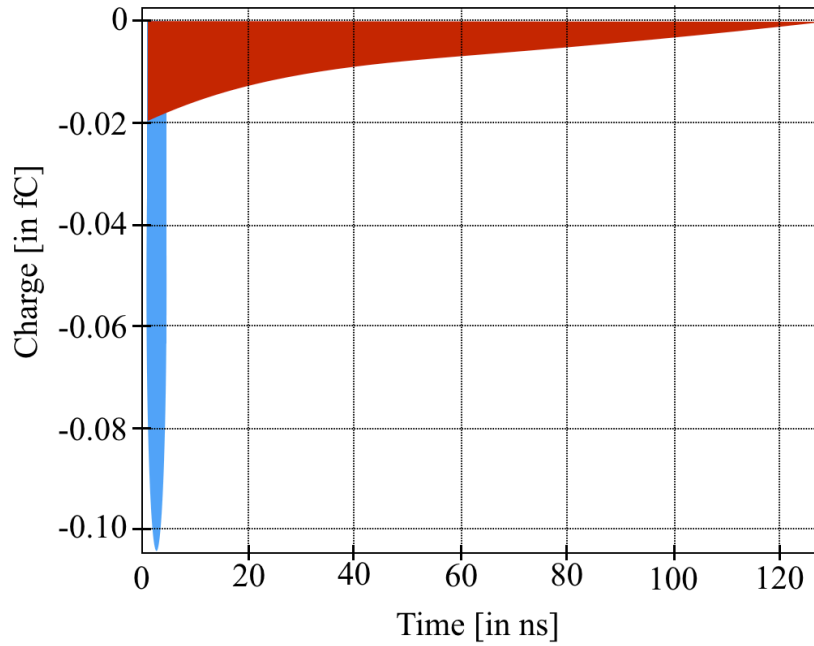


Figure 11.3: Collected charges as a function of time. The blue curve represents the signal induced by the electron drifting. This signal is in the order of few nanosecond. The red curve is the current induced by the displacement of ions toward the cathode

The wire position gives only an approximate position of the hit. Much better precision is achieved by measuring the drift time of the electron-ion pairs. The relation between the distance to the wire and the drift time is called $R(T)$ relation and described latter in Sec. 12.1. This relation converts the measured drift time into a drift distance and improves spatial resolution.

11.2 Straw Tube Technology

11.2.1 Detector Structure

Straw tubes. A single straw tube consists of an inner layer of Carbon loaded Kapton XC ($40\mu\text{m}$ thickness), a glue film ($7\mu\text{m}$ thickness), and an outer layer of aluminized Kapton ($12\mu\text{m}$ thickness) [101]. An illustration of a straw tube is shown in Fig. 11.4. Each cylindrical tube contains an anode wire to be connected to an electronic channel of the front-end cards. The inner layer of the tube acts as a cathode. This tube has a relatively high impedance and largely transparent to electromagnetic fields: Cross-talk, signal attenuation, and external noise sources are consequently reduced [101]. The thin anode wire, made of gold plated tungsten [101], has a diameter of $30\mu\text{m}$.

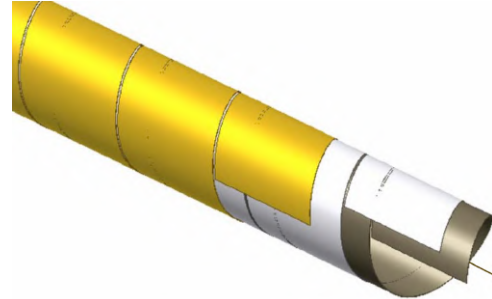


Figure 11.4: Illustration of a straw tube design

Double Layer Structure. A layer of straw tubes is glued with a second layer in a staggered arrangement, shifted by half a diameter, and fixed to an aluminum frame. The double-layer schematics is shown in Fig. 11.5. The main motivations of a double-layer design are to increase the detector acceptance and resolve the left-right ambiguity within a plan. A single layer is not able to distinguish whether the incoming charged particle crossed the detector on the left or right side of the wire.

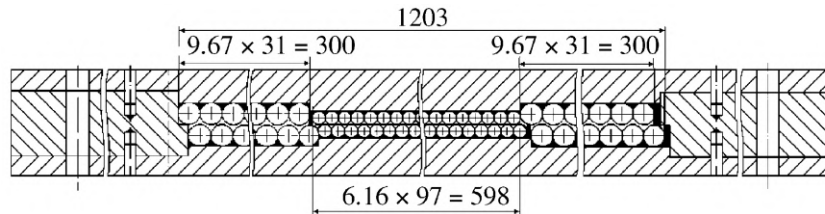


Figure 11.5: Illustration of a double-layer of the straw tube detector

Carbon strips and protective volumes. The double layers are held horizontal or vertical in a staggered arrangement using carbon strips, as shown in Fig. 11.6. This detector technology is sensitive to atmospheric conditions [102]. Therefore two protective enclosure volumes on either side of the detector are filled with Argon to keep double-layers air-proof and to reduce humidity within the straw.

Detector Structure. The sensitive area made of double layers, either X or Y-types, has a total size of either $280\text{ cm} \times 323\text{ cm}$ or $325\text{ cm} \times 272\text{ cm}$ respectively [101]. The active area is made of three sectors (a, b, c) of straw tubes with different diameters. (Fig. 11.6) The two *outer sectors a and c* are made of 31 tubes of 9.67 mm diameter. The *inner sector b* is composed of 97 tubes of 6.16 mm diameter. In 2015, electric fields applied to the cathode were respectively 1780 V for the 10 mm tubes and 1640 V for the 6 mm tubes. The purpose of smaller diameters in the central region is to support a larger rate of particles at a low angle. Additionally, the particle rate near the center of the detector is very high due to the beam and interacting particles at low angles. Consequently, a dead-zone of $20 \times 20\text{ cm}^2$ is located in the center of the detector to avoid a too large occupancy of the detector.

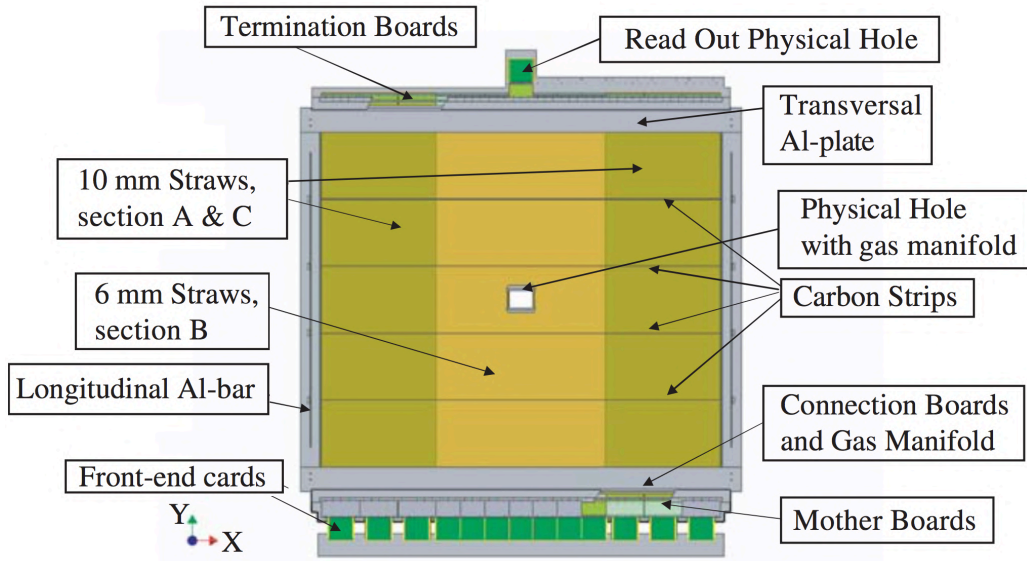


Figure 11.6: Schematic view of the X double-layer of a straw tube detector [87], including the electronic front-end in the bottom of the detector. A single read-out electronic card is used to collect the second half of the signal due to the physical hole.

At COMPASS in 2015, the last but not the least operated ST03 detector is composed of six double-layers (X1, Y1, U1, V1, Y2, X2), as shown in Fig. 11.7. The (U1, V1) views are inclined by $(-10^\circ, +10^\circ)$ respectively. The horizontal and inclined views are X-type straws, while the vertical planes are of Y-type straws. In the next pages, the naming of each view follows the pattern : ST03[xx][y][z], where [xx] corresponds to a detector view $X1..X2$, [y] corresponds to the upstream u or downstream d layer and [z] is the a, b, c sector of the corresponding detector plane.

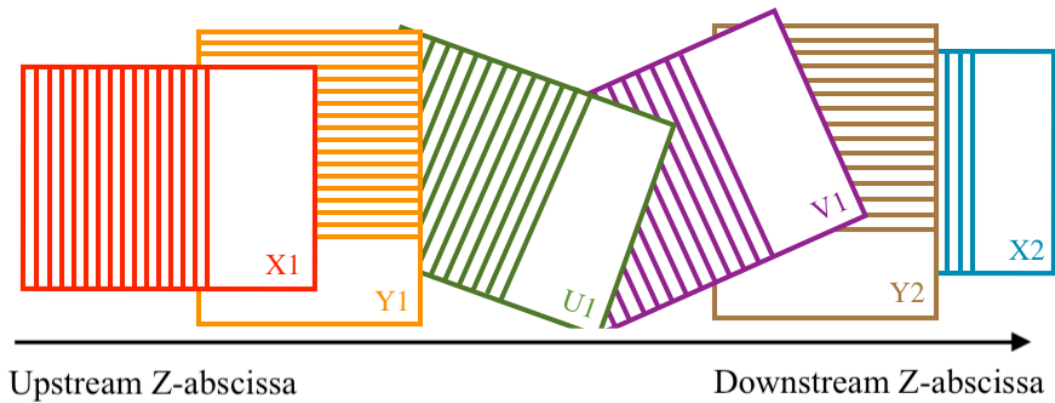


Figure 11.7: Illustration of the six double layers sequencing of the ST03 detector.

A detector measures at least the horizontal and vertical projected coordinates to determine the position of the particles. The additional views are used for the resolution of track combinatorial ambiguity. Indeed, it is crucial to have sufficient redundancies to avoid such ambiguities, but also to compensate detector inefficiencies. Fig. 11.8, 11.9 illustrates the tracking ambiguity due to low redundancy or high particle rate. In this case, as an example, the simultaneous detection of two true hits results in the detection of two additional ambiguities. This issue is addressed by increasing the redundancy and adding rotated coordinates such as (U1, V1).

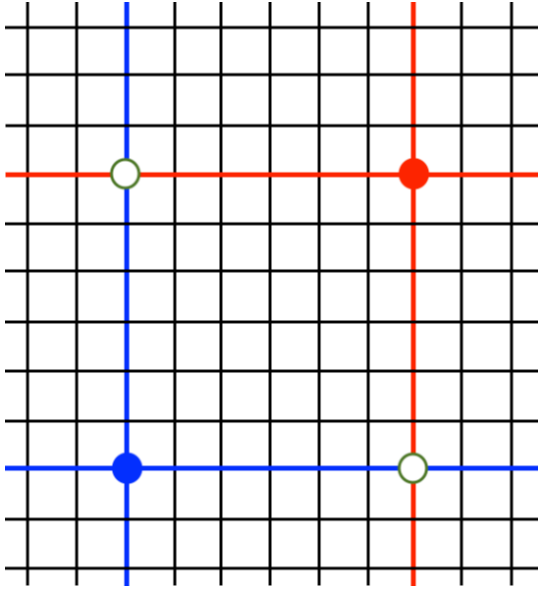


Figure 11.8: Illustration of the combinatorial ambiguity due to low redundancy in the tracking of one detector. Ambiguities are drawn with the white/green circles. True hits are blue and red circles

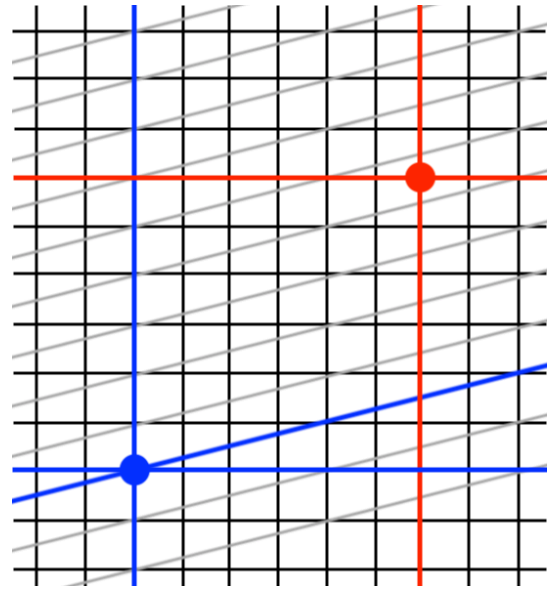


Figure 11.9: This combinatorial ambiguity is resolved by the additional coordinate (in gray) compared to the left-hand side plot.

11.2.2 Gas Mixture

The gas circuit is detailed in Appendix D. The gas mixture, tuned for hadron beam runs, is composed of Ar, CO₂ and CF₄ (80%/10%/10%) and circulates through each double layer. Argon gas is used for its signal amplification properties. CO₂ is a quencher to suppress electrical discharges in the tubes. Additionally, a third compound, CF₄, increases the drift velocity [103]. The total gas flow rate depends on the atmospheric pressure and the regulation speed of the gas recycling line.

11.2.3 Front-End Electronics

A single $\mathcal{F}1$ -TDC front-end board includes 64 readout channels [87]. Each board embeds eight $\mathcal{F}1$ chips for digitization and eight ASD-8 analog chips. The latter consists of a pre-amplifier, an amplifier, and discriminator chips. Thresholds are remotely controlled. There are 14 cards per view, including one extra card to connect the part of the detector separated by the central hole. The digitized signal is transmitted from $\mathcal{F}1$ -TDC cards to CATCH cards using the HOTLink interface with shielded ethernet cables.

12 | Calibration and Characterization in 2015

12.1 Calibration Methods

A detector calibration is an iterative procedure in order to optimize detector performances. These corrective parameters are the R(T) relation, the T₀-value and the x-ray calibration, described later. In 2015, the x-ray correction has been disregarded.

An initial alignment and calibrations are required to reconstruct the reference tracks using the rest

of the spectrometer. Those reference tracks are then compared with detector hits to determine ST03 efficiency. In 2015, the alignment was performed first using a muon beam at a lower intensity. In a second time, a hadron beam run at high intensity was used for each period throughout 2015.

12.1.1 Alignment and Residual Distributions

During the calibration procedure, the ST03 detector is removed from the tracking in order not to bias the reconstruction of the reference tracks. A residual distribution, $\Delta r = r_{\text{hit}} - r_{\text{trk}}$, is used to minimize the misalignment and misorientation of each detection plane in the spectrometer reference frame (Fig. 12.1). This distribution corresponds to the deviation of the hit position measured by the detector from the projected position of the reference track, as illustrated by Fig. 12.2. The full picture of the residual distributions after calibration is available in Appendix C.

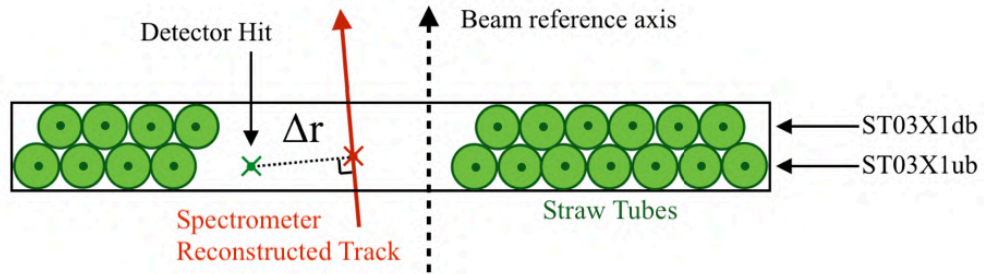


Figure 12.1: Sketch of top view of ST03X1, including an example of residual Δr . The red axis corresponds to the reference track reconstructed by the spectrometer but the ST03 detector

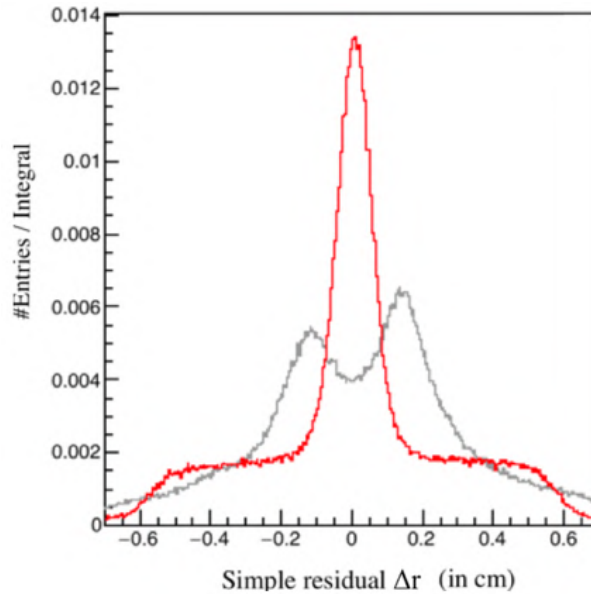


Figure 12.2: Example of simple residual of ST03Y2ub before (in grey) and after calibration and realignment (in red)

12.1.2 Relation $R(T)$

As explained in Sec. 11.1, the RT relation is one of the main characteristics of the straw tube chamber. This relation converts the drift time T to a drift distance R , as shown in Fig. 12.3. The two-arm shape from 10 ns to 60 ns is obtained whether the particle crosses to the left or right of the nearest wire. A fit in red is performed and corresponds to the RT relation used for the correction of the reconstructed data. The T_0 and ΔT will be discussed later in the next sections. The full picture of the $R(T)$ distributions is available in Appendix C.

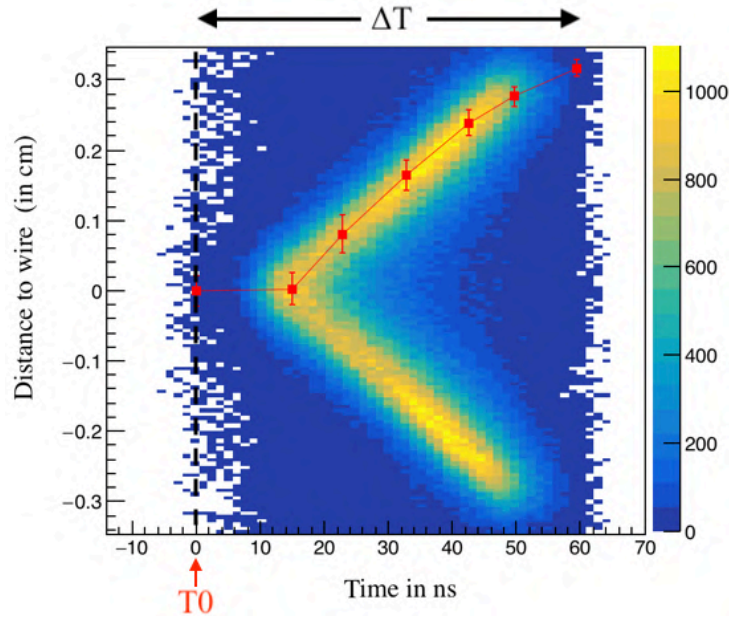


Figure 12.3: RT relation of the ST03Y2ub with calibration fit in red

12.1.3 T_0 Calibration

A typical hit timing is of the order of 1670 ns compared to this trigger reference time. Due to the electronics latency and the length of cables, the corresponding detector hit of the event has to be retrieved from the buffer of $\mathcal{F}1$ chip. Consequently, a reference value, known as T_0 -value, is adjusted to correct the timing of the hit. In previous example, a typical T_0 -value will be fine-tuned of the order of $T_0 \simeq -1600$ ns or -1660 ns to align the $R(T)$ relation in time as shown in Fig. 12.3. This time is negative because the trigger has fired in the past compared to the time the hits are collected.

12.1.4 Detector Time Gate

The drift velocity depends on parameters such as the electric field and the gas mixture used in the detector. A detector time gate ΔT is opened to select only the relevant hits. This time gate should not be too large to minimize noise hits. In Fig. 12.3, the hits correlated with the trigger are located between 0 and 60 ns as visible by the two-arm profile.

- A typical ΔT value for the central tubes is about 60 ns.
- The time gate is chosen proportionally to the diameter of the tubes. Consequently, the ΔT value for outer tubes is of the order of 90 ns.

12.1.5 X-ray Correction

Although straw tubes are constrained with carbon strips, the detector structure still suffers from atmospheric variations, especially the temperature. The precise positioning of the wire inside the tubes was last determined in 2005 using an x-ray gun [102]. The setup was composed of an x-ray gun and a CCD sensor, as shown in Fig. 12.4a. A typical picture is shown in Fig. 12.4b, where anode wires are visible in dark grey.

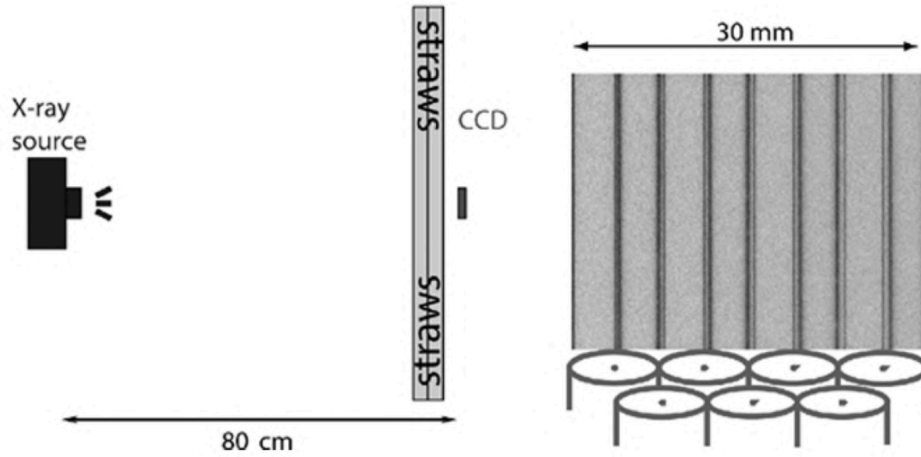


Figure 12.4: (a) Left: Sketch of the setup with an x-ray gun and the CCD sensor; (b) Right: Typical picture obtained with the CCD sensor

The measurement aimed to precisely determine the positioning of the wire in six different locations (at the edges of the detector and the four-carbon strips). However, no recent measurement had been performed since 2005. In consequence, the activation of this additional correction was worsening the situation. Fig. 12.5 illustrates the systematic deterioration of the resolution by applying the old x-ray correction, except for Y views, which remain almost constant. Consequently, this correction had finally been deactivated in 2015.

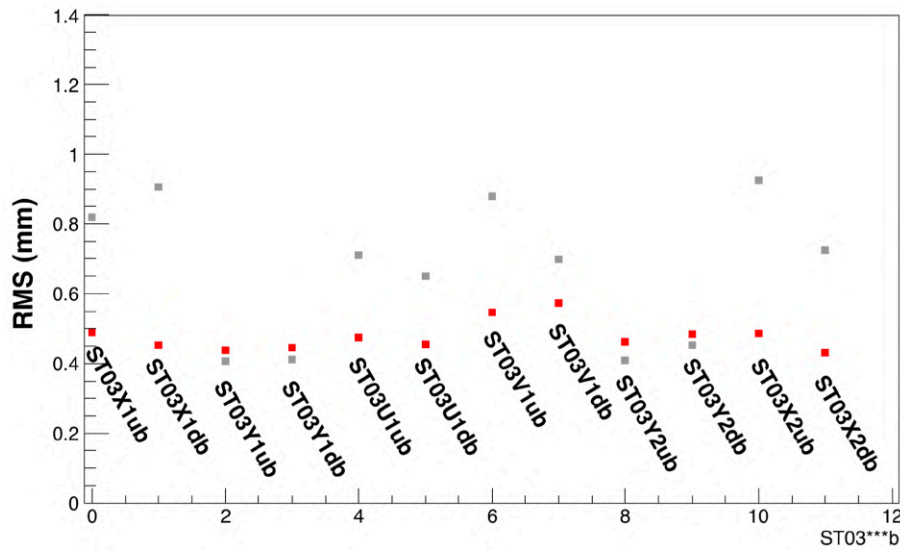


Figure 12.5: Comparison of the resolution between views with (in grey) and without (in red) the x-ray correction from the 2005 calibrations

12.2 Results: Performance Studies

The detector performances depend on beam conditions, detector calibrations, and alignment. In 2015, the gas mixture was modified to optimize the detector capability rate with an incoming hadron beam. The effect of the gas purity and the aging of the detector are discussed in Sec. 13. The performance study with 2015 data is performed at a nominal beam intensity of 10^8 hadrons per second as measured by the ion chamber at the entrance of the COMPASS hall.

Spatial resolution. An estimation of the spatial resolution has been performed, for each layer, by using a gaussian fit of the residual distribution. An example of fit is shown in Fig. 12.6. In 2015, the average resolution was about $450 \mu\text{m}$ using a hadron beam. In comparison, in the early year of operation (2002) of the ST03 chamber, the spatial resolution was estimated to be about $200 \mu\text{m}$ with a muon beam [101].

Efficiency plot. The average value of ST03 efficiency is about 93% in 2015. As an example, Fig. 12.7 shows the two-dimensional efficiency of the central region of ST03X1. Efficiency plots are computed for each plan by comparing the reference tracks to the number of expected hits. A full picture of the efficiency of ST03 is available in Appendix C. The dead zone in the center of the detector is visible. Moreover, the shadows of the four-carbon strips are visible in the figure at $Y_0 \simeq -80 \text{ cm}$, $Y_1 \simeq -30 \text{ cm}$, $Y_2 \simeq 30 \text{ cm}$, $Y_3 \simeq 80 \text{ cm}$. Additionally, the efficiency coverage is limited by collected muons.

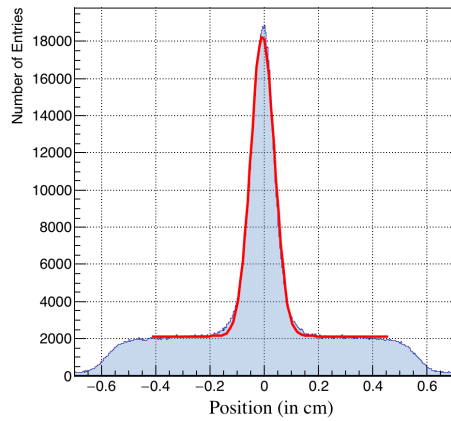


Figure 12.6: Resolution of the ST03X1ub view, $\sigma = 0.439 \text{ mm}$

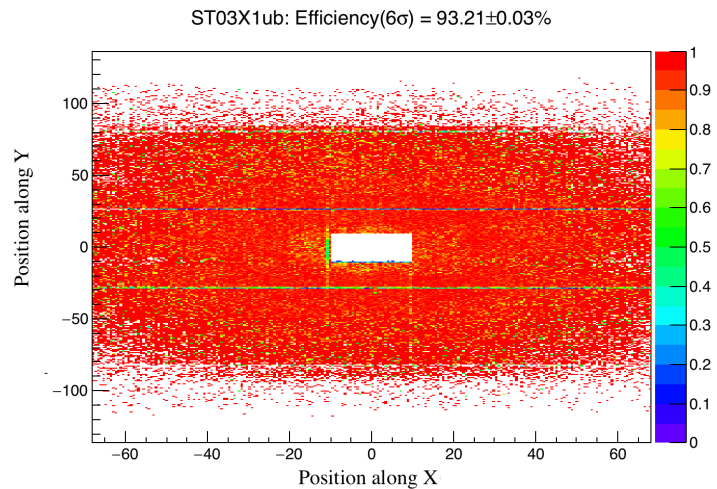


Figure 12.7: Efficiency of the ST03X1ub, $\varepsilon = 93.21 \pm 0.03\%$

13 | Results: Hardware upgrades in 2016-2017

13.1 Gas System Upgrade

The gas system is detailed in Appendix D. This gas system was commonly designed for a COMPASS apparatus including five straw detectors and also recycle a fraction of the gas input.

In 2016, the removal of ST05 straw detectors triggered some issues in the regulation of the gas flow in the gas recycling line. Therefore, the speed of the recycling pump had to be reduced based on the amount of gas returning from the last chamber. It is a matter of fact, that the outgoing flow changes based on the atmospheric pressure. The regulation of the pump was performed using an absolute pressure sensor based on a safe fixed pressure value based on the initial setup, which included five straw detectors. Consequently, it was observed that sizable atmospheric pressure variations turned the regulation pump out of its working range. This problem, observed in 2016, might have also slightly affected the global efficiency of the ST03 detector in 2015 for some periods of time.

Test of the gas regulation. The inadequate regulation system issue was confirmed during two periods of tests using only Argon gas, as shown in Fig. 13.1. The time scale to observe a reduction of the detector efficiency is about a few weeks, as shown in the second test period B.

- Test Period A: The regulation was manually performed daily, such that the gas injection was properly regulated (Fig. 13.1).
- Test Period B: The regulation was performed automatically based on the absolute pressure sensor. A failure of the regulation translates into a continuous decrease of the argon flow (Fig. 13.1, in green) over a month.

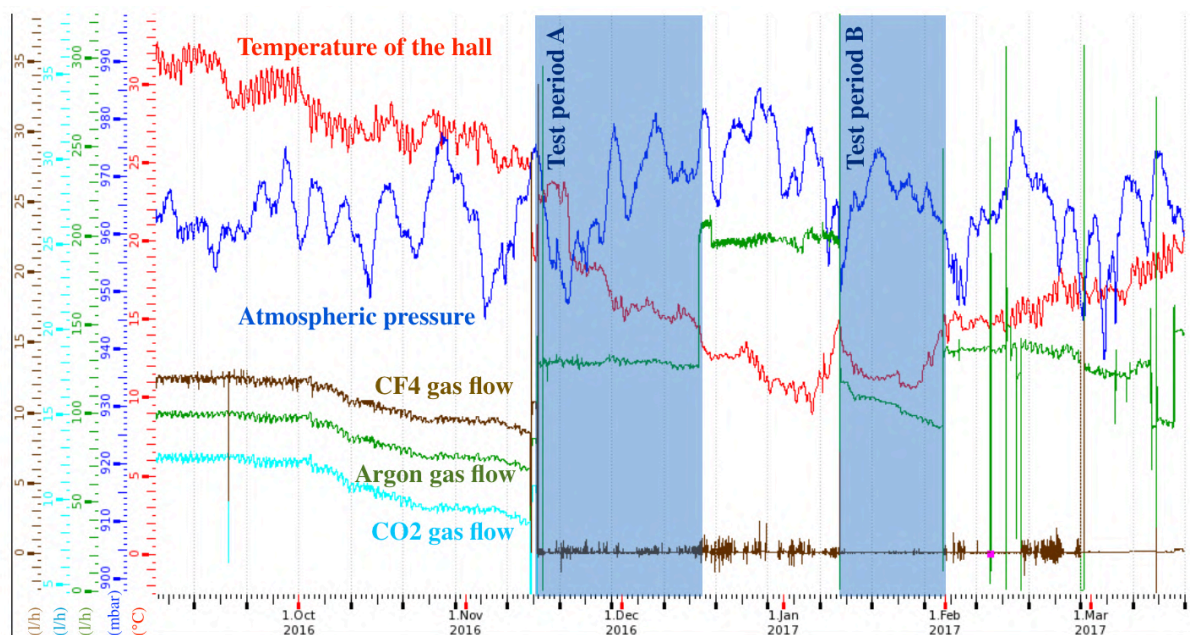


Figure 13.1: Test of the pump regulation. The failure in period B resulted in a global loss of efficiency of about 30% in the detector efficiency

The observation of the gas misregulation (Fig. 13.1, period B) is a confirmation of a contamination issue. It makes possible the under-pressure of the chamber depending on the atmospheric pressure variation, allowing water and oxygen from the environment to enter the chamber. Consequently, it is clear that safety bubblers injected air into the gas line.

Adopted Solution. The recycling gas system has been modified to address the misregulation by adding a differential pressure sensor. The atmospheric pressure was used as a reference pressure. Moreover, the speed of the compressor was also reduced. Additionally, the compressor regulation value was also added to the COMPASS monitoring system.

13.2 Air Contamination Measurement

Following the gas line upgrade, an extra gas sensor has been connected to the gas line. This extension takes a small fraction of recycled gas and measures the O_2 fraction in the gas. The digitized value was displayed in terms of part-per-millions volume (ppmV). 1000 ppmV corresponds to 0.1% of oxygen, so 0.5% of air. The lowest O_2 measured value was about 10 ppmV after flushing the detector for 16 hours.

13.3 Gas Filter Refurbishing

The gas circuit of the straw chamber was built with gas filters to reduce pollution and humidity in the gas circuit, especially in the recycling line. Running without gas filters results in accelerated aging of the straw tubes.

In an environment of a high radiation experiment, the fluorine element s, especially CF_4 , is radioactively activated and results in accelerated aging of the detector [104]. Additionally, the outgassing of some materials, as well as oxygen and organic radicals, can spread throughout the chamber. As the anode is made of gold plated tungsten, the former elements and the organic compounds can recombine with tungsten creating cracks in the wire structure [105]. Since 2016, gas filters have been regenerated every year with the setup in Fig. 13.2 and following the procedure described below :

- Day 1: The filters are placed in an oven at room temperature and flushed with pure argon to remove elements present in the filters. A few hours later, the oven is turned on at 200°C. The temperature allows cleaning more deeply the filter.
- Day 2: Switch to Arcal gas (mix of $Ar+H_2$). H_2 is the active component of the filter, which combines with the organic chain elements coming out from the detector.
- Day 5: Switch back to Argon
- Day 6: Stop the oven and reinstall filters in the gas line.



Figure 13.2: Two filters connected to a gas line and placed in the oven.

Chapter IV

First Level Data Production

14 COMPASS Software Chain	66
14.1 Data Decoding and Calibration Database	66
14.2 Data Reconstruction	67
14.3 Monte-Carlo Simulation	68
15 Petascale Computing Resources	69
15.1 A New COMPASS Production Workflow	69
15.2 The Blue Waters Facility	71
15.3 A New Perspective: Frontera Supercomputer	71
16 New Production Framework: ESCALADE	72
16.1 Analysis Purpose	72
16.2 Software Architecture	73
16.3 Functional Checks	74
17 Results: Official COMPASS Drell-Yan Productions	74
18 Results: Official Monte-Carlo Simulations	76

The first level of data production consists of processing raw binary files collected by the DAQ system and turn them into so-called Data Summary Tree (DST) files for further analysis. The creation of these files requires an intensive computing power to reconstruct tracks. Therefore, part of this Ph.D. work consisted of evaluating the performances of the Blue Waters Petascale Computing Center and assessing the compatibility of COMPASS software.

Moreover, a suitable data production model, as required by the COMPASS collaboration, must be continuously improved to meet the requirements of raw data processing for recent and future measurements. Therefore, productions also required to be precisely monitored under the supervision of a COMPASS production team at Blue Waters. Consequently, a new multi-platform production framework, described later and called ESCALADE, has been developed during this Ph.D. work for current and future large amount of data processing.

14 | COMPASS Software Chain

Three major software compose the COMPASS 2015 software chain: CORAL¹, PHAST² and TGEANT³. CORAL is the reconstruction software used at COMPASS, the bedrock of the software chain. The COMPASS analysis software, PHAST, is used to read reconstructed data files. Finally, TGEANT [106], a Geant4-based program for Monte-Carlo simulations, is used to determine detector acceptance in the analysis.

A diagram of the reconstruction chain is shown in Fig. 14.1. The reconstruction algorithm commonly processes real data or Monte-Carlo Simulation (MC) data. Only the first step is different because MC data require a digitization step.

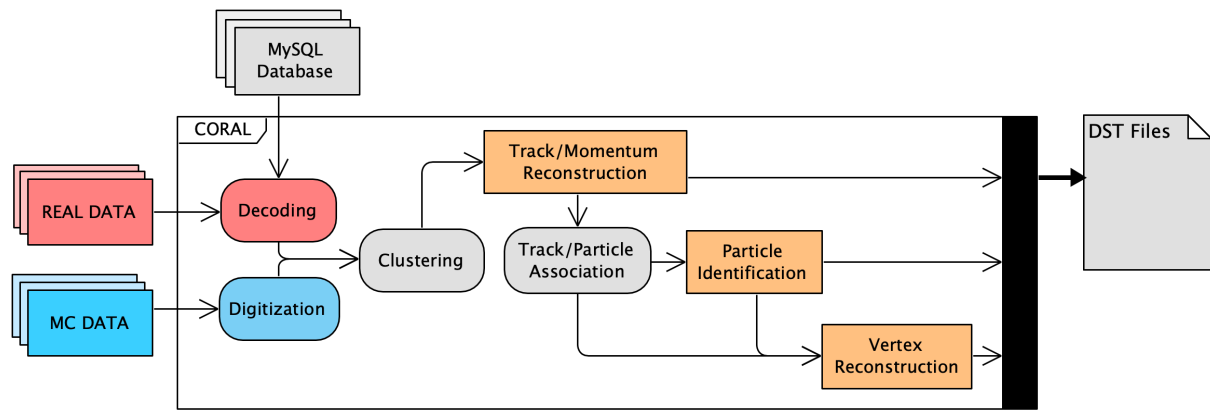


Figure 14.1: Data flow of the reconstruct software chain. Real and MC data are drawn in red and blue respectively. The orange blocks corresponds to the outgoing information

14.1 Data Decoding and Calibration Database

Collected data are encoded into binary files by the DAQ system during data taking. Those data are decoded during reconstruction. The decoding library is used to readback the hit information, also known as digits. The detector calibration is applied to each digit, to correct for time propagation of the collected signal. Calibrations are stored and synchronized in the master MySQL database located on the internal CERN network. Many replicas of the primary database are available over clusters used by COMPASS collaborators.

Reconstructed data are stored in a tree format, known as DST⁴ files. Tree files, including hits, are named Mega Data Summary Tree (MDST). The standard files are known as Mini Data Summary Tree (mDST), and skimmed files are named Micro Data Summary Tree (uDST). All these files are meant to be analyzed event-by-event using PHAST.

¹Compass Reconstruction AnaLysis software package

²PHysics Analysis Software Tool

³COMPASS Geant4-based Monte-Carlo program

⁴Data Summary Tree

14.2 Data Reconstruction

The first step of the reconstruction consists in gathering digit information into a hit, also known as a hit cluster. This step called clustering attributes time and position information to each corresponding set of hits. Additionally, the clustering takes into account digit amplitudes as the presence of the magnetic field results in an asymmetric signal amplitude deposited, as shown in Fig. 14.2.

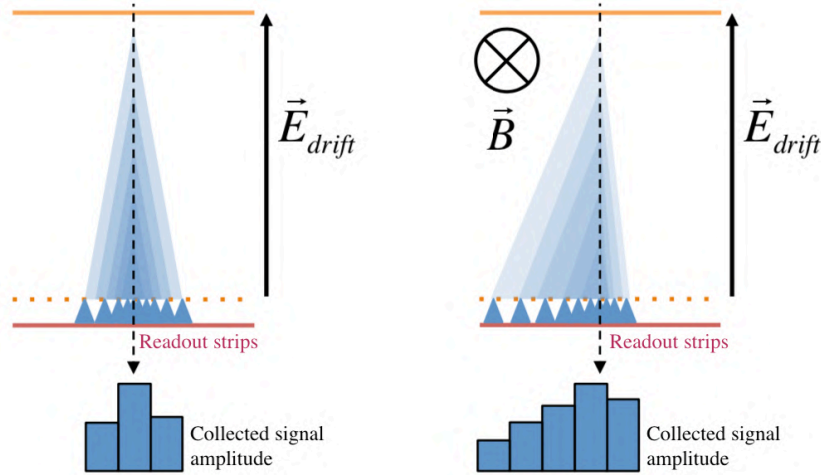


Figure 14.2: Left: Illustration of a symmetric signal amplitude in a pixel micromegas detector in a magnetic field-free region. The electric field, \vec{E}_{drift} , drifts the electron signal toward the readout strips [93]; Right: The asymmetric signal deposited in the Micromegas readout is due to the presence of a magnetic field. This is representative of the real case as these stations are located near SM1 magnet.

A Kalman Filter Algorithm [107, 108] is involved in both track and vertex reconstructions. This filter produces an estimate of an unknown quantity, by using partial measurements. At COMPASS, this parametrization is performed with six components: $(X, Y, P_X, P_Y, q|P|)$ as a function of the Z-abscissa, where q is the charge of the track. Additionally, this procedure accounts for statistical noise and various types of uncertainties. First, small pieces of tracks, also known as tracklets, are reconstructed in the magnetic field-free regions. These tracklets are bridged in the magnetic field region using a fitting procedure. Combined tracks resulting from this procedure are associated with a χ^2/NDF value, a momentum vector and the corresponding covariance matrix.

The vertex fit procedure relies on the track extrapolation from the first measured point to the target region for the outgoing particles and the last measured point for beam tracks. Vertices are fitted in the region where tracks intersect. A vertex is only called primary vertex if it is also associated with an incoming beam track. Track particles are identified using the number of radiation lengths, X/X_0 . A X/X_0 value greater than 30 corresponds to a particle that went through muon walls and is consequently tagged as a muon particle. Additionally, an energy loss correction is applied to the four-momentum vector of the extrapolated tracks based on the Geant4 geometry.

In 2015, a Drell-Yan primary vertex referred to a vertex with two outgoing muons and an incoming beam track. An example of reconstructed event is shown in Fig. 14.3. This figure shows the interaction of an incoming particle in the target region.

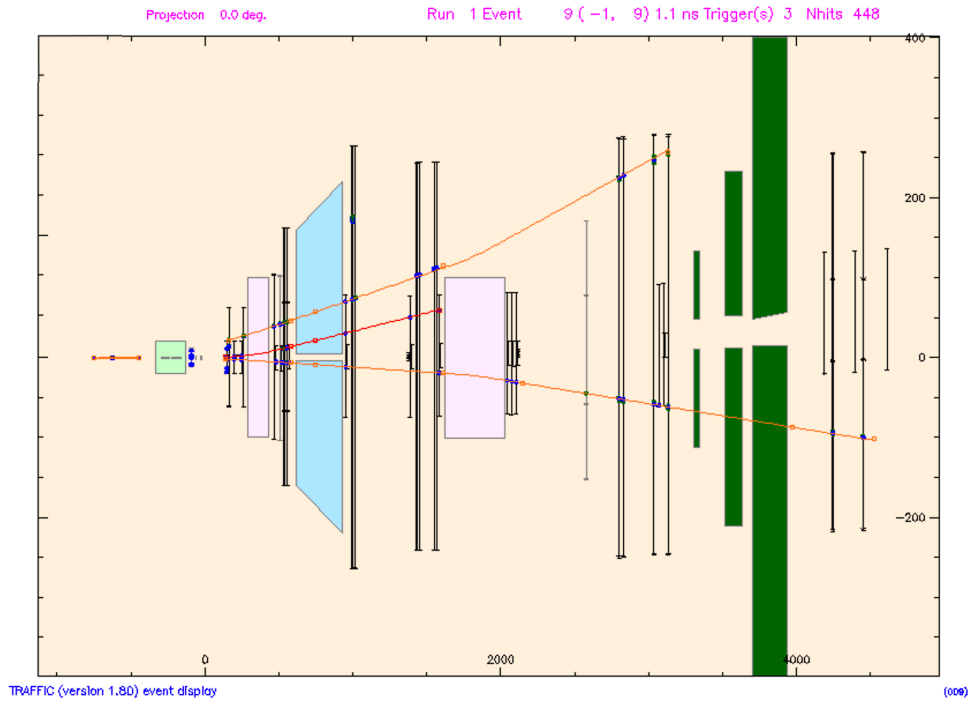


Figure 14.3: Example of event reconstruction with the COMPASS 2015 setup. This picture corresponds to the event display of Coral. All reconstructed tracks are drawn in red. The gold lines represent very well reconstructed MC tracks. The upstream block (in light green) corresponds to the PT cells. SM1 and SM2 magnets are represented in pink. The beam absorber is not represented in this picture.

14.3 Monte-Carlo Simulation

The TGEANT Monte-Carlo project is a Geant4-based program. As a standard Geant4 project, this simulation is split into four tasks: geometry description, particle propagation, physics interaction, and sensitive detector area definition. A visualization of the 2015 setup is shown in Fig. 14.4. The beam particle (in yellow) interacts with the material of the various targets and end up in the tungsten beam dump. Detector hits are drawn in red on the picture.

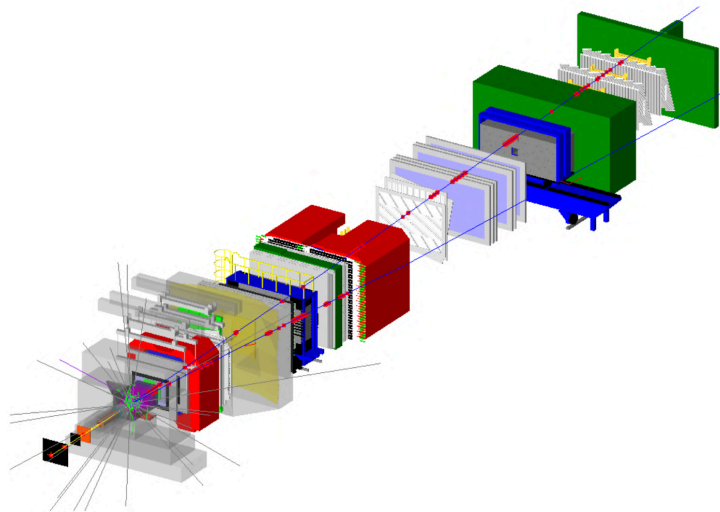


Figure 14.4: Visualisation of the COMPASS 2015 MC geometry and example of interactions involving a single pion beam particle. The red dots correspond to detector hits

At the origin of time, an initial beam particle is generated using a library of beam particles⁵. This so-called beam file is computed based on measured data at COMPASS and initiates the Geant4 beam particle gun. Such a technique aims to inject in the simulation a realistic beam of the M2 beam characteristics. Particle propagations are carried out by the Geant4 propagation algorithms, based on the known cross-section and the interaction length of the crossed materials. The higher the physics process probability is, the shorter the step length is defined. A step in Geant4 is an intermediate state, where an interaction point can possibly occur.

The TGEANT simulation embeds external High Energy Physics (HEP) event generators, such as Pythia6 [109] or Pythia8 [110]. When the first inelastic interaction of the beam particle occurs, the selected physics generator is called and returns the parametrization of each outgoing particle. A schematic of the vertex generation mechanism is shown in Fig. 14.5.

In 2015, either Pythia6 or Pythia8 event generators are used as a Drell-Yan event generator. The detailed Pythia8 configuration will be presented, and results will be compared with Pythia6 in Ch. 25.

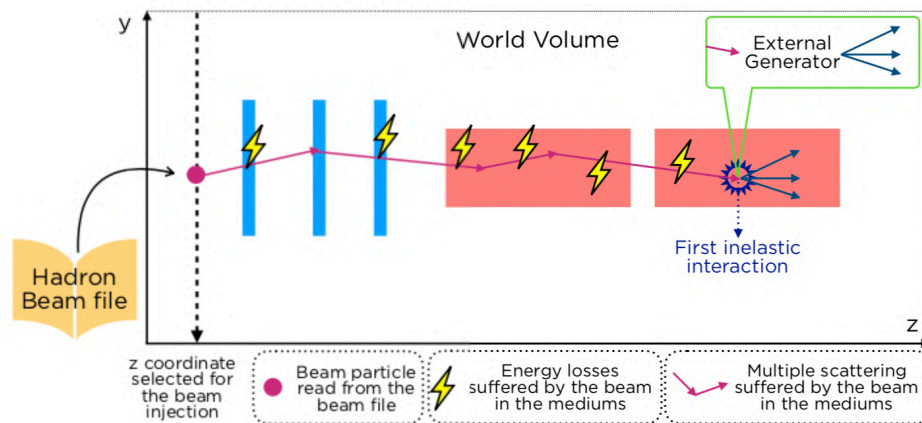


Figure 14.5: Schematic workflow of the new vertex generation mechanism for DY [111].

The generated MC information, such as the true vertex position and the incoming and outgoing tracks information, is forwarded to the reconstruction software. The detector responses, both resolutions, and efficiencies, are introduced during MC data reconstruction. At this step, MC hits are replaced with smeared hits or disregarded based on the detector efficiency maps, before proceeding with the standard reconstruction procedure as real data.

15 | Petascale Computing Resources

15.1 A New COMPASS Production Workflow

In perspective of the three forthcoming data taking (2016, 2017, and 2018), as well as the several MC simulation campaigns, the COMPASS computing resources had to be upgraded [112]. A proposal [113] to use the Blue Waters, a petascale computing facility, was approved in May 2016. The exploratory allocation was granted from May to December 2016 to verify the software compatibility, evaluate the

⁵An entry of the beam library is composed of the position in the transverse plane (X-Y), its slope in the (X-Z) and (Y-Z) planes and its energy-momentum vector

performance gain and time processing of raw data reconstruction at a large scale. The success of this testing period [114] finally led to a reliable production workflow, as described in Fig. 15.1. This production workflow was found to be an excellent balance between the required usage of the LXPLUS computing facility at CERN and the newly introduced Blue Waters supercomputer. The large amount of resources available at Blue Waters gave the possibility to carry out up to 75% of the MC productions and 67% of collected data reconstructions.

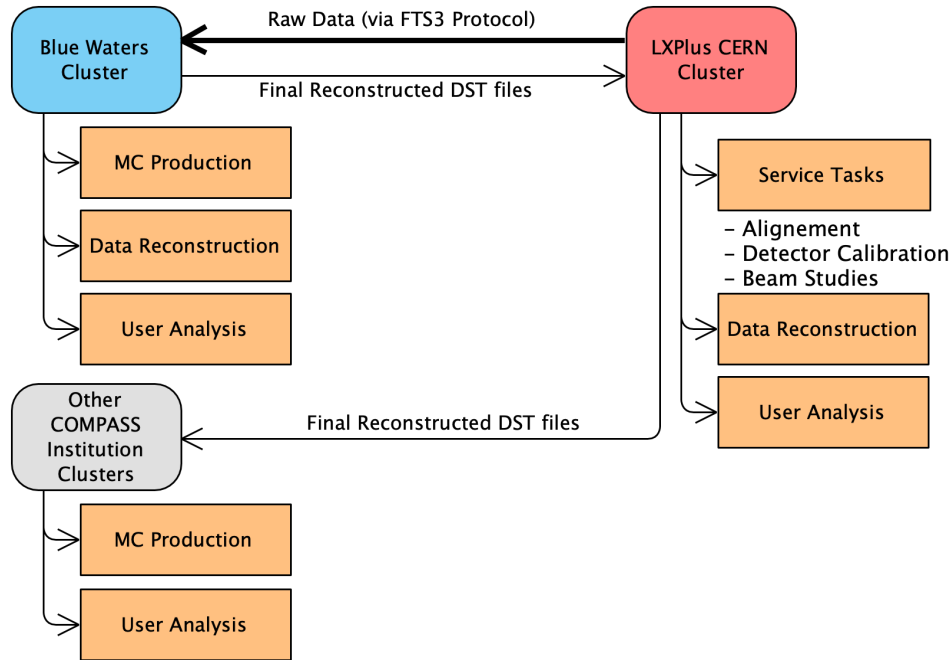


Figure 15.1: Diagram of the COMPASS new large-scale production scheme including the Blue Waters facility [114]

A total of six allocations ensured the stability of this production model over the last four years. The timeline is shown in Fig. 15.2. The node-hour unit used is an arbitrary time unit, explained latter in the next Sec. 15.2. The first five allocations were granted at BlueWaters by the NSF¹ (US). Additionally, a new allocation is in full swing in a different NSF-funded petascale computing system, namely Frontera, to ensure the continuity of the COMPASS production model.

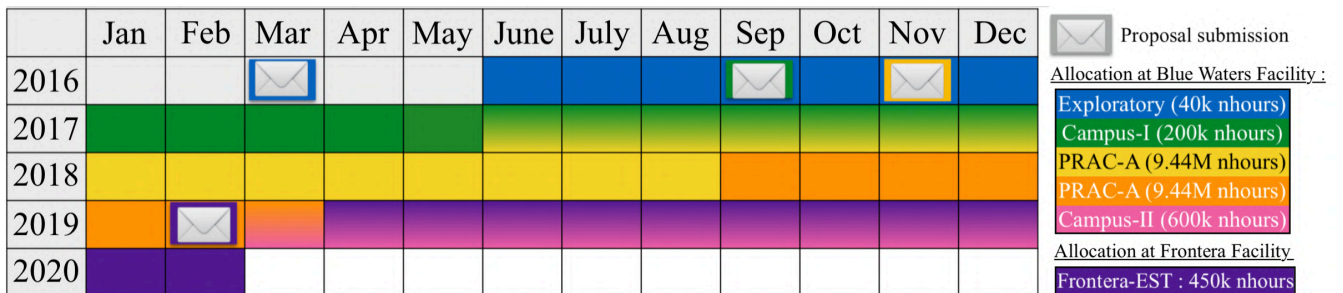


Figure 15.2: Timeline of the Blue Waters allocations granted from 2016 to 2019.

¹National Science Foundation (United States of America)

15.2 The Blue Waters Facility

The Blue Waters supercomputer is an NSF-funded petascale computing facility. This HPC² center is hosted by the NCSA³. It is known to be one of the most powerful computing centers on a university campus. This cluster is using Cray XE6/XK7 nodes. It consists of 22,500 XE6 nodes and 4200 XK7 nodes. The technical characteristics of the traditionally used XE6 compute nodes are shown in Fig. 15.3. A single XE6 dual-socket node employs 2 AMD Interlagos processors, composed by 16 cores each, and 64GB of physical memory. The Blue Waters system takes advantage of the Cray Gemini interconnect, which implements a 3D torus topology (Fig. 15.4) to minimize communication overhead between nodes. Also, the TORQUE⁴ workload manager is used as a job scheduler.

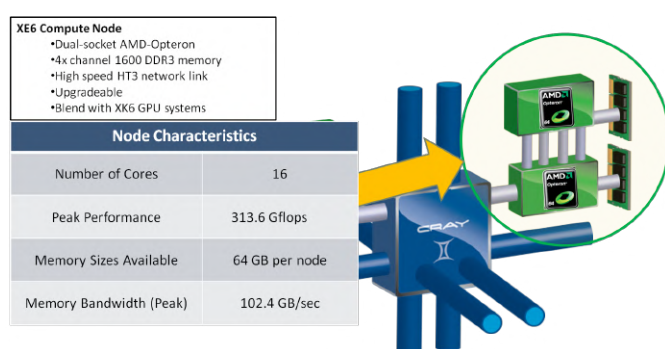


Figure 15.3: Technical specs of a XE6 compute node. XE6 are the most common nodes available at Blue Waters. Frontera-EST (Frontera Early Science Team) is a project allocation located TACC, also granted by NFS, see Sec. 15.3

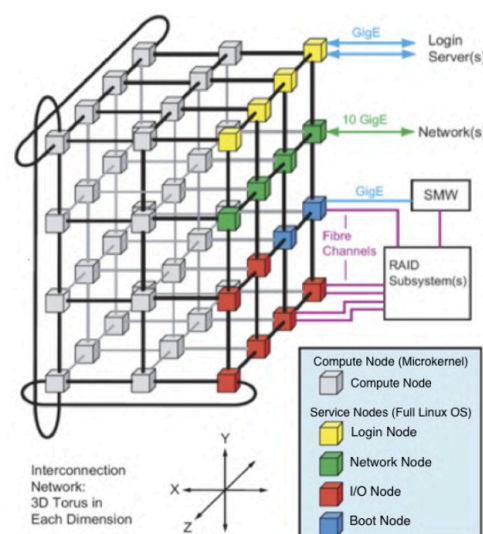


Figure 15.4: Simplified view of the Cray Gemini interconnect as employed at Blue Waters.

The COMPASS awarded allocation is in units of node-hours. One node-hour depends on the hardware used. Furthermore, the COMPASS workflow only uses XE6 nodes. Consequently, the charged node-hour is optimized to take advantage of the 32 cores, in the limit of the 64GB memory per node.

15.3 A New Perspective: Frontera Supercomputer

In the prevision of the Blue Waters decommissioning, a new NSF-funded petascale computing system has been deployed at TACC⁵. This HPC system is powered by Sky Lake Intel processors, interconnected by a Mellanox Infiniband HDR and HDR-100 interconnect (Fig. 15.5). The computing resources are charged in terms of node-hours. However, the unit cannot be compared with the Blue Waters facility, due to differences in the hardware resources. An initial number of 8008 nodes of 56 CPUs is available, to be upgraded during the 2019 commissioning. A peak node performance can go up to 4.8 Tflops, which is fourteen times faster compared to the Blue Water facility, which reaches up to 313.6 Gflops per compute node. The SLURM⁶ workload manager is used as a job scheduler.

²High Performance Computing

³National Center for Supercomputing Applications

⁴Terascale Open-source Resource and QUEue Manager

⁵Texas Advanced Computing Center

⁶Simple Linux Utility for Resource Management

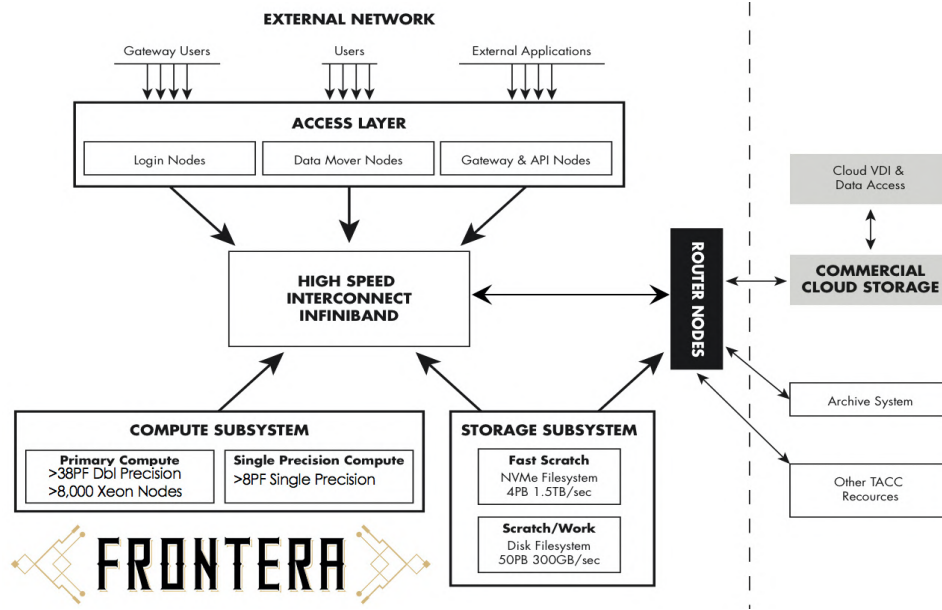


Figure 15.5: Hardware and software overview of the Frontera Facility [115]

16 | New Production Framework: ESCALADE

16.1 Analysis Purpose

A production framework, ESCALADE¹, was developed in C/C++, Python, and shell scripts and finally used as official data production software for the COMPASS collaboration. In this context, a production tool is an automated program, which is responsible for processing a large amount of input data with specific software. It performs all the necessary checks to ensure the integrity of the final results. Several official COMPASS productions were achieved over three years from 2016 using this workflow such as Drell-Yan 2015 (slot-1) and 2018 (test-1 and test-2) data productions, as well as many Monte-Carlo productions.

Drell-Yan 2015 is approximately about 4 TB mDST data. This multi-purpose framework was initially designed to process and to ensure all ingredients involved in the evaluation of the Drell-Yan cross-section were properly analyzed as many times as required: Data reduction, event selection, beam flux determination, as well as the multi-dimension acceptance correction.

The operating principle is split into four parts:

- Lookup for the path of a dataset and prepare a standard production directory.
- Submit jobs on a batch grid.
- Verify outgoing logfiles and resubmit the failing jobs.
- Certify and archive a data production to be used for physics analysis.

A typical size of a production was initially about few terabytes. It was able to handle up to 512 input files within a single production directory. This software was upgraded during summer 2018 to handle

¹univErSity of illinois urbana-ChAmpaign and cea-sacaLAy proDuction softwarE

larger scale productions with a scalable input structure. Additionally, this upgrade also included a job production verifier running on the batch, a cyclic redundancy check to prevent later file corruption, and a multi-pilot structure, as explained in Sec. 16.2.

16.2 Software Architecture

This software framework relies on a simple architecture introduced in Fig. 16.1. It includes XML configuration files to define all production settings and various parallel productions.

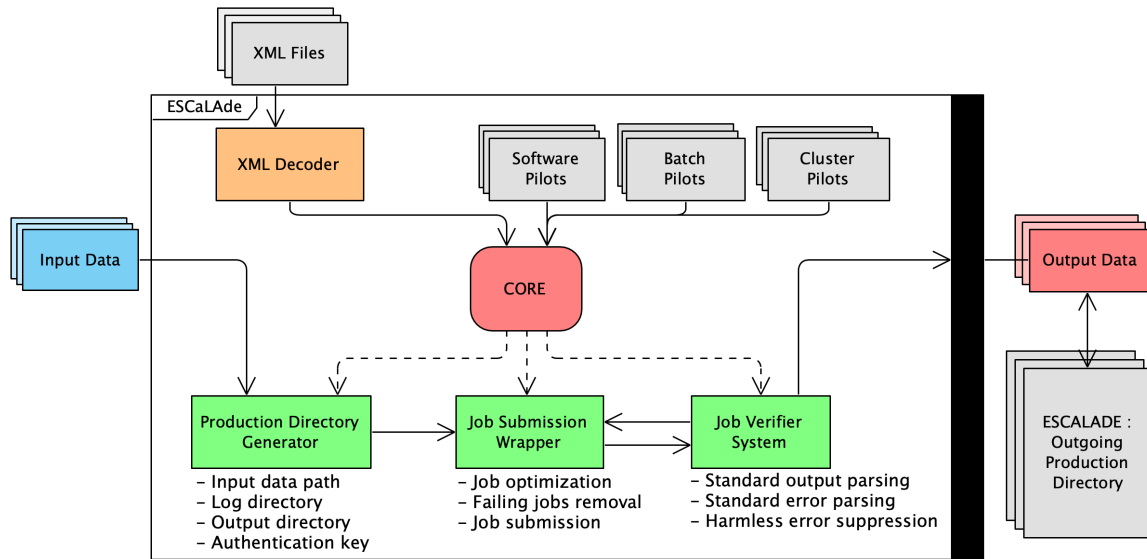


Figure 16.1: Diagram of the ESCALADE architecture. The outgoing files are the processed outgoing data and an outgoing archive to keep track of the production

The pilot architecture is separated into cluster, batch, and software pilots. Each pilot is independent and gives the knowledge to run software on a specific type of batch and some environment variables dedicated to the corresponding cluster. Such a structure aims to increase the versatility and to facilitate the deployment on multiple clusters. However, software pilots can also be restricted to a specific type of batch or cluster for job optimization reasons.

The XML file structure is minimized and expanded at the running time, as shown in Fig. 16.2. Each production can be divided and also subdivided into steps. A software pilot is specified at each step.

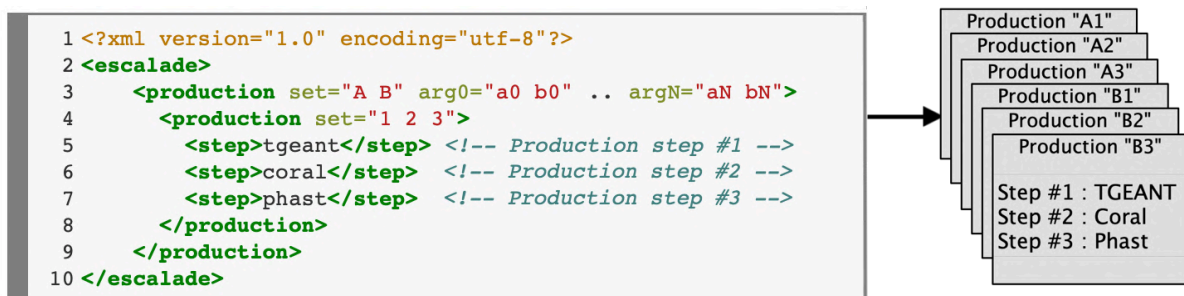


Figure 16.2: Structure of an XML configuration file.

A typical production directory is organized into four parts: an input directory, a logging directory, and an output directory. Moreover, the input directory contains slots of 512 text files each to avoid directory overload. Each single text file includes the data paths to process. The large output file size sometimes requires to locate the output directory in different disk spaces. In such cases, a unique authentication key is generated to keep track of the output directory.

The job verifier system is used to ensure the integrity of the production. It implements a logging analyzer, logging files parser, and mismatching detection between input and a possible missing output or logging files. This module is tuned on a pilot basis using database files to separate harmless and striking error messages. Harmless error messages are detected and removed using a suppression file.

16.3 Functional Checks

A second production software, PanDA² initially designed for the Atlas collaboration, has been adapted by the COMPASS PanDA team to be used with COMPASS software in the CERN cluster.

A cross-check campaign has been carried out during Summer 2018 to ensure the validity of both COMPASS production software, PanDA at CERN, and ESCALADE at Blue Waters. It consisted of processing the first level production using a common dataset and comparing results between ESCALADE and the PanDA production system. This sanity test was successful and learnful, because it allowed to fix both issues on COMPASS PanDA pilots and helped to prepare a complete database file for the job verifier system of ESCALADE, based on the knowledge of the COMPASS PanDA team.

17 | Results: Official COMPASS Drell-Yan Productions

Three large-scale productions were recently produced at Blue Waters using ESCALADE: the 2015 data reproduction (slot-1), the first production of the newly collected 2018 data (test-1), and a second test production (test-2) of the 2018 data.

- The 2015 data are divided into nine periods, from W07 to W15. A total of 771,115 raw files (818.11 TB) were processed in parallel to reduce the processing time to eight hours, which corresponds to the time required to process a single file. Table 17.1 gives the detailed values period by period (W13, W14, W15 were produced at CERN with the PanDA production system).
- The 2018 data are split into nine periods from P00 to P08, which corresponds to a total of 1,538,488 raw files (1,642.68 TB). Table 17.2 shows the detailed values period by period.

Both Drell-Yan productions were done using a custom software/batch pilot, as shown in Fig. 17.1. The job dispatching requires one master node and involves an MPI¹ program, named Parallel-Command-Processing (PCP). The master node manages up to 96 nodes per job. The size of a single period remained quite large to fit into one single production. Consequently, each period was subdivided into sub-production of 3072 raw files each to reduce the risk of failure and balance the sequential workload of the job verifier.

²Production and Distributed Analysis System

¹Message Passing Interface

Real data reconstruction requires the use of a database, and each XE6 node is composed of 32 CPUs. Consequently, each node is separated into 1 database instance and 31 CORAL instances. Therefore, each CORAL instance only sent requests to its local database to avoid unnecessary communications between nodes².

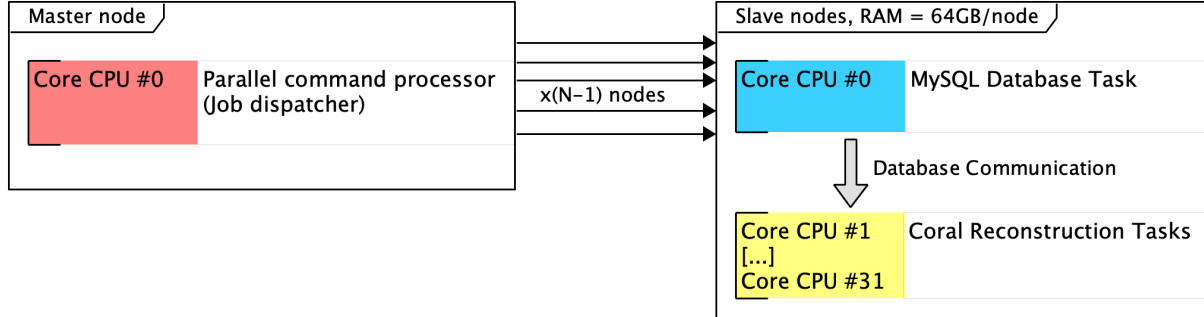


Figure 17.1: Job optimization of a typical CORAL production.

Table 17.1: Summary table of the 2015 data (slot-1).

Name	Period	#Runs	#Spills	Raw Files	mDST Files	μ DST Files	μ DST #Events
W07	Jul 9 - Jul 22	284	29,963	103.63 TB	30.05 TB	2.13 TB	125,272,736 evts
W08	Jul 23 - Aug 5	332	28,692	104.10 TB	30.42 TB	2.27 TB	137,793,896 evts
W09	Aug 6 - Aug 26	269	29,112	111.79 TB	28.65 TB	2.23 TB	127,552,707 evts
W10	Aug 26 - Sep 9	396	30,504	84.63 TB	28.97 TB	2.29 TB	154,507,311 evts
W11	Sep 11 - Sep 30	460	47,285	137.61 TB	44.25 TB	3.53 TB	201,808,645 evts
W12	Sep 30 - Oct 14	356	39,049	95.71 TB	32.24 TB	2.82 TB	166,446,997 evts
W13	Oct 15 - Oct 28	315	34,194	83.82 TB	30.46 TB	2.44 TB	144,314,906 evts
W14	Oct 28 - Nov 8	241	24,739	57.33 TB	20.76 TB	1.66 TB	110,144,684 evts
W15	Nov 9 - Nov 16	106	12,850	39.49 TB	11.34 TB	0.92 TB	54,286,239 evts
2015	—	2,758	276,388	0.81 PB	257.14 TB	20.29 TB	1,222,128,121 evts

Table 17.2: Summary table of the 2018 data (test-2)

Name	Period	#Runs	#Spills	Raw Files	mDST Files	μ DST Files
P00	May 16 - Jun 13	371	55,794	330.12 TB	24.30 TB	3.32 TB
P01	Jun 21 - Jul 3	286	34,255	127.25 TB	14.87 TB	1.90 TB
P02	Jul 6 - Jul 31	450	64,966	253.74 TB	24.14 TB	3.18 TB
P03	Aug 1 - Aug 15	337	48,826	177.59 TB	20.76 TB	2.62 TB
P04	Aug 16 - Sep 5	369	47,498	183.46 TB	17.24 TB	2.25 TB
P05	Sep 5 - Sep 17	188	28,491	111.02 TB	10.22 TB	1.33 TB
P06	Sep 20 - Oct 1	256	37,179	124.46 TB	12.21 TB	1.63 TB
P07	Oct 3 - Oct 30	488	62,721	251.59 TB	21.53 TB	2.85 TB
P08	Nov 1 - Nov 12	170	22,551	83.45 TB	7.69 TB	1.00 TB
2018	—	2,915	402,281	1.64 PB	152.96 TB	20.08 TB

²The technical name of this option is called *commtransparent*

18 | Results: Official Monte-Carlo Simulations

A first large-scale MC production of the 2015 MC was performed in Spring 2018. The following physics processes were produced using TGEANT with the Pythia8 generator: Drell-Yan, J/ψ , ψ' , Open-Charm and Upsilon production. The Pythia8 configuration is presented later in Sec. 25.2. A total of approximately 200M events per physics process were generated. The purpose of this production was to carry a large sample of MC data for multi-dimensional acceptance.

A second MC campaign, including both 2015 and 2018 simulations, was recently carried out and still under study. It includes the most recent technical updates at the simulation level, such as 2D-detector and trigger efficiencies.

All MC productions were following the same job pattern, as shown in Fig. 18.1. MC productions, both generation and reconstruction, do not require the use of a calibration database. Consequently, job optimization is highly simplified. It was possible to run both software in a row. A MC job is composed of a master node and each slave node is in charge of running 32 TGEANT instances followed by 32 CORAL reconstruction instances.

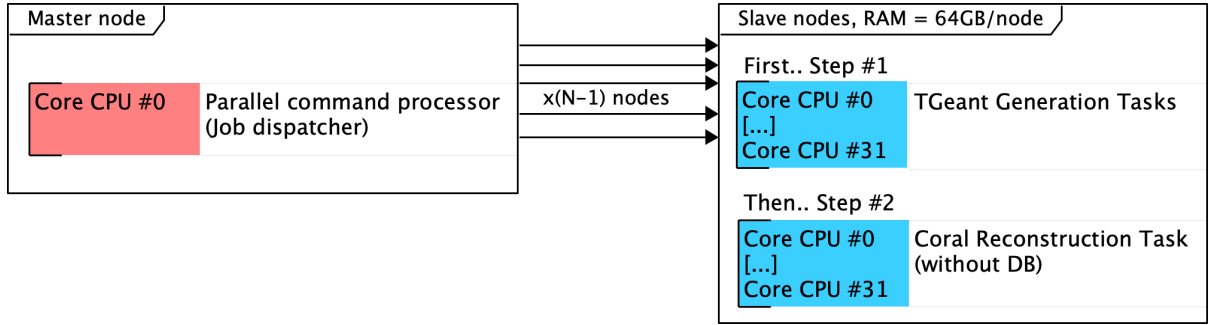


Figure 18.1: Job optimization of a typical MC production.

Table 18.1: Summary table of the 2015/2018 MC generated data produced at Blue Waters

Physics Process	#Events Generated		
	Campaign #1, 2015 MC	Campaign #2, 2015 MC	Campaign #2, 2018 MC
DY ($2 < M_{\mu\mu}/(\text{GeV}/c^2) < 3.8$)	211 200 000 evts	32 000 000 evts	32 000 000 evts
DY ($3.8 < M_{\mu\mu}/(\text{GeV}/c^2) < 8.5$)	211 200 000 evts	192 000 000 evts	192 000 000 evts
Open-Charm	211 200 000 evts	32 000 000 evts	32 000 000 evts
Resonance J/Ψ	211 200 000 evts	32 000 000 evts	32 000 000 evts
Resonance Ψ'	211 200 000 evts	32 000 000 evts	32 000 000 evts
Resonance Υ	211 200 000 evts	32 000 000 evts	32 000 000 evts

Chapter V

Luminosity Measurement in 2015

19 Introduction to Fixed Target Luminosity	78
19.1 Instantaneous Pion-Nucleon Luminosity, L	78
19.2 The Integrated Luminosity, \mathcal{L}	79
20 Transverse Nucleon Density	79
20.1 Nuclear Target Densities	80
20.2 Polarized-Target Nucleon Densities	80
20.2.1 Packing Factor, P_F	80
20.2.2 Component Fractions	82
20.2.3 Target Fiducial Volume	83
20.2.4 Isotopic Composition of the 2015 PT targets	84
20.2.5 Temperature Dependence	85
20.2.6 Summary Table	86
21 Beam Flux	87
21.1 Ionization Chamber Flux	87
21.2 Absolute Flux Estimation	88
21.2.1 Beam Track Reconstruction	89
21.2.2 Beam Meantime	90
21.2.3 Time in Spill Range	92
21.3 Beam Attenuation	93
21.3.1 Mean Free Path of a Pion	93
21.3.2 Cross Cell Selection	94
21.3.3 Flux Attenuation as a function of Z_{vtx}	94
21.4 Data Inhibition	97
21.4.1 DAQ Lifetime	98
21.4.2 VETO Lifetime	99
22 Stability Studies	102
22.1 Apparatus Stability	102
22.1.1 Spill by Spill Analysis	102
22.1.2 Run by Run Analysis	102
22.2 Beam Flux Stability	104
22.2.1 Bad Spill List	104
22.2.2 Period by Period Analysis	106
22.3 Uncorrelated Background Events	108
22.3.1 Contextualization	108
22.3.2 Beam Structure Study	109
23 Results: Systematic Uncertainties, Summary, Figure of Merit	111

This chapter is dedicated to the evaluation of the luminosity in 2015 at COMPASS. The luminosity is a crucial ingredient in the determination of absolute cross-section at $\sqrt{s} = 18.9$ GeV. This chapter also provides an estimation of the systematic uncertainties related to the luminosity. Qualitative analysis of both beam and apparatus stability are also presented.

19 | Introduction to Fixed Target Luminosity

Keys to access the world of the *infinitely small* are given by measuring a quantity known as the *interacting cross-section* σ . This quantity is defined as the probability for an incident beam particle to scatter off a target particle.

In a particle physics experiment, there are two performance parameters, which are essential in the determination of this cross-section. The first is the *beam energy*, also related to the center-of-mass energy in fixed target experiment by the relation $\sqrt{s} \simeq \sqrt{2P_b m_p}$, where P_b is the beam momentum and $m_p \simeq 0.938 \text{ GeV}/c^2$ is the proton mass. At COMPASS, for an hadron beam of $190 \text{ GeV}/c$, the center of mass energy is $\sqrt{s} = 18.90 \text{ GeV}$. Finally, the second quantity is the number of *useful* interactions, also known as number of *events*. Therefore, the capability of a setup to produce events and consequently to measure a cross-section is given by the *luminosity* L , which is defined as follows:

$$\frac{dN_{\mu\mu}}{dt} = \sigma \times L \quad (19.1)$$

where $N_{\mu\mu}$ is the number of dimuon events (for Drell-Yan process: two muons in the final state)

$dN_{\mu\mu}/dt$ refers to the dimuon rate

L is the instantaneous pion-nucleon luminosity [$\text{cm}^{-2}\text{s}^{-1}$]

19.1 Instantaneous Pion-Nucleon Luminosity, L

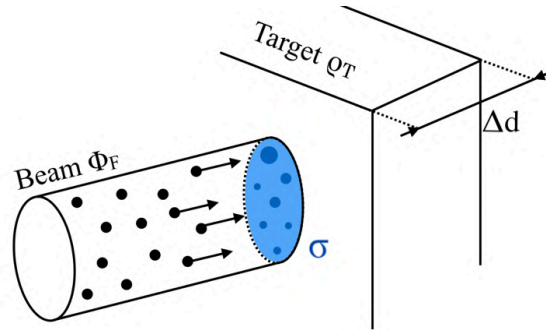


Figure 19.1: Illustration of an incident beam crossing a layer Δd of target material. The blue region represents the cross-section σ .

Fig. 19.1 illustrates the production cross-section of an incoming beam flux Φ_F colliding with a target material ρ_T . In this context, the instantaneous pion-nucleon luminosity L is defined as the product of the transverse nucleon density ρ_T , and the instantaneous beam flux Φ_F . Therefore, the dimension of the luminosity L is [$\text{cm}^{-2}\text{s}^{-1}$], also known as [$b^{-1}\text{s}^{-1}$].

$$L(t) = \rho_T \times \Phi_F(t) \quad (19.2)$$

where Φ_F is the instantaneous flux [s^{-1}]

ρ_T is the transverse nucleon density [cm^{-2}]

t refers to the time in the spill [s]

Additionally, the total number of nucleons in the target, also known as number of diffusion centers, is assumed to be constant during the whole data taking year.

19.2 The Integrated Luminosity, \mathcal{L}

The Drell-Yan dimuon pair production at high mass is a rare process. As an example, a Drell-Yan interaction between a pion and a deuterium target π^-D is about 150 pb. Consequently, it is more appropriate to determine an integrated number of dimuon events over longer period of time. The beam luminosity will be consequently integrated over the same sensitive time, *i.e.* over spills and time in the spill and excluding data acquisition dead times. Thus, Eq. 19.2 turns into Eq. 19.3, where \mathcal{L} corresponds to the integrated luminosity, and its dimension refers to $[\text{cm}^{-2}]$.

$$\mathcal{L} = \varrho_T \times \mathcal{F} \quad (19.3)$$

By extension, \mathcal{F} corresponds to a number of incident beam particles, where the integrated beam flux is defined as: $\mathcal{F} = \sum_{\text{spill}} \int_{T_0}^{T_1} \Phi_F(t) dt$, where T_0 and T_1 refer to the beginning and end of time, respectively.

20 | Transverse Nucleon Density

The transverse nucleon density ϱ_T , also known as target areal density, corresponds to the total number of diffusion centers in the target per unit of area $[\text{nucleon}/\text{cm}^2]$. This density is expressed as a transverse density to simplify the analysis and fix the effective radius at the last stage of the analysis. The total number of nucleons N_T in a target is expressed as :

$$N_T = \left[\frac{V \times \rho \times N_A}{M_A} \right] \times A \quad (20.1)$$

where ρ refers to the material density $[\text{g}.\text{cm}^{-3}]$

V is the total volume of the target $[\text{cm}^3]$

$N_A = 6.022140857 \times 10^{23}$, the Avogadro number $[\text{mol}^{-1}]$

M_A is the molar mass of a nucleus A $[\text{g}.\text{mol}^{-1}]$

A is the number of nucleons

The differential surface is defined as $dS = 2\pi R dR$ for cylindrical targets. Therefore, the density ϱ_T for a target of length L given by the relation :

$$\varrho_T = \frac{N_T}{\pi R^2} = \left[\frac{L \times \rho \times N_A}{M_A} \right] \times A \quad (20.2)$$

In fine, each of the four targets shown in Fig. 20.1 are associated with their corresponding density, denoted $\varrho_{T, \text{cell1}}$, $\varrho_{T, \text{cell2}}$, $\varrho_{T, \text{Al}}$ and $\varrho_{T, \text{W}}$ respectively. Target dimensions were given in Fig. 6.1 in Ch. II.

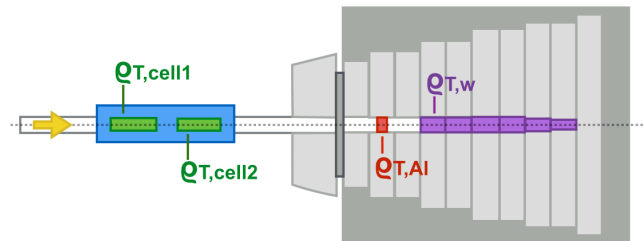


Figure 20.1: Simplified target 2015 setup composed of the PT Cell 1, PT Cell 2, the Aluminum target and a Tungsten plug. Only the first 10 cm of tungsten are considered as a target.

20.1 Nuclear Target Densities

The simple case of solid targets is first presented. In the case of the COMPASS aluminum and tungsten targets, the transverse dimensions of the targets are larger than the beam (halo of the beam neglected). The aluminum target is made of pure ^{27}Al elements. The tungsten is made of a specific material containing 99.5% of the ^{184}W isotope and composed of other stable tungsten isotopes ^{182}W , ^{183}W , ^{185}W . The modification of the cross-section due to the 0.5% remaining isotopes is neglected.

Summary Table. The values used in the analysis are given in Tab. 27.2. In the case of a solid target, Eq. 20.2 can be used to determine the target areal density of each nuclear target.

$$\varrho_T^{Al} = \frac{L \times \rho_W \times N_A}{M(Al)} \times A_{Al} \qquad \varrho_T^W = \frac{L \times \rho_W \times N_A}{M(W)} \times A_W \quad (20.3)$$

Table 20.1: Summary table of nucleon density for the 2015 nuclear targets; The systematic uncertainties are small and consequently neglected.

Properties	Aluminum	Tungsten
A	27	184
M (g/mol)	26.98	183.84
ρ (g.cm $^{-3}$)	2.70	19.30
Length, L (cm)	7	10
ϱ_T (cm $^{-2}$)	1.1386×10^{25}	2.3266×10^{26}

20.2 Polarized-Target Nucleon Densities

The COMPASS polarized targets, previously introduced as hybrid targets in Ch. II, require a special treatment compared to solid nuclear targets. Indeed, from an experimental point of view, the precise determination of the cross-section is challenging, because of the composite nature of the target (bead irregularities, shapes, sizes,...). Moreover, it is impossible to experimentally distinguish dimuons originating from the interaction with solid NH_3 beads or the liquid helium (LHe).

20.2.1 Packing Factor, P_F

The NH_3 beads do not fit the entire volume of the target holder, because of its irregular shapes. Consequently, at the end of the 2015 run, the composition of each PT cell is obtained by determining the packing factor. The packing factor, P_F , is the volume ratio between the volume occupied by the solid ammonia and the total volume of the target cell. This quantity is dimensionless [Ø].

$$P_F = \frac{V_{\text{NH}_3}}{V_{\text{Cell}}} = \frac{1}{V_{\text{Cell}}} \frac{m_{\text{NH}_3}}{\rho_{\text{NH}_3}} \quad (20.4)$$

where m_{NH_3} refers to the measured mass of NH_3 [g]

ρ_{NH_3} is the NH_3 density [g.cm $^{-3}$]

$V_{\text{Cell}} = L \times \pi R^2 = 691.15 \text{ cm}^3$, is the volume of the cell [cm 3]

The target material is obtained by weighting the solid-state NH_3 beads (Fig. 20.2a) in socks by using the experimental setup, Fig. 20.2b. This measurement is performed in a nitrogen gas volume (2) at 80 K due to the evaporation of liquid nitrogen (1). The buoyancy of the LN2 is taken into account in the final weight, as suggested by the target group. The target material is collected into a sock (2) and weighted using a digital balance (4). The temperature is measured with a pt100 platinum thermometer (3).

A summary table of the measurement is given in Tab. 20.2. At low temperature, the ammonia density considered is $\rho_{\text{NH}_3} = 0.853 \pm 0.031 \text{ g/cm}^3$. This value has been measured in the past by the SMC collaboration [116, 117]. The packing factor in 2015 for the two PT cells is estimated as follows :

$$\begin{cases} P_{F1} &= 56.57\% \pm 2.41\% \\ P_{F2} &= 47.97\% \pm 2.05\% \end{cases} \quad (20.5)$$

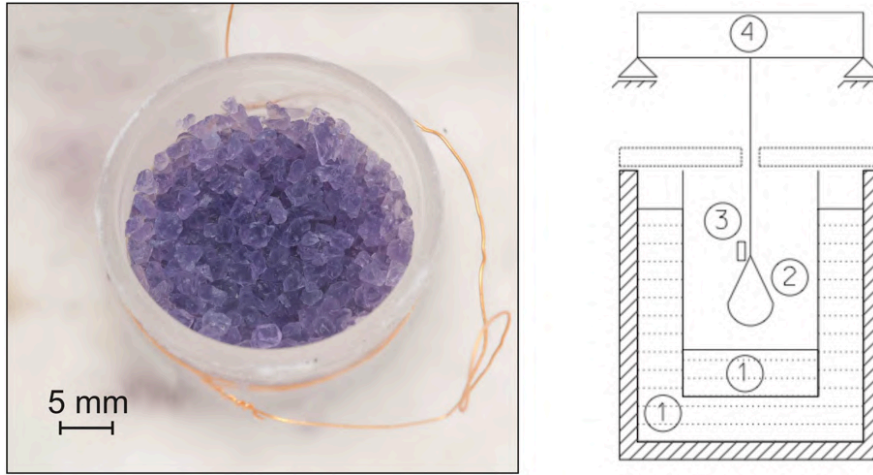


Figure 20.2: (a) Left: Picture of the NH_3 crystals one week after irradiation [118]. The size of solid NH_3 crystals is about 2-4 mm. (b) Right: Diagram of the target weighting setup.

Table 20.2: Summary table of the 2015 target material measured by the COMPASS target group after the data taking [119]. An additional 0.4 g systematic uncertainty is added to each sock due to material lost. The measurement is separated into four socks due to the limited size of the weighting setup

	PT Cell 1	PT Cell 1	PT Cell 2	PT Cell 2
	Sock #1	Sock #2	Sock #3	Sock #4
NH3 material [g]	155.8 ± 0.1	185.4 ± 0.1	128.1 ± 0.1	162.0 ± 0.1
sock [g]	2.7 ± 0.2	3.2 ± 0.2	2.9 ± 0.2	2.6 ± 0.2
label [g]	0.7 ± 0.1	0.7 ± 0.1	0.7 ± 0.1	0.7 ± 0.1
Sensor pt100 [g]	0.2 ± 0.1	0.2 ± 0.1	0.2 ± 0.1	0.2 ± 0.1
Polyamide + Copper wire	neglected	neglected	neglected	neglected
LN2 buoyancy [g]	-0.5 ± 0.0	-0.6 ± 0.0	-0.4 ± 0.0	-0.6 ± 0.0
net [g]	152.7 ± 0.9	181.9 ± 0.9	124.7 ± 0.9	159.1 ± 0.9

20.2.2 Component Fractions

In this section, the component fractions are defined to simplify the definition of mixtures and to associate their variables such as the molar mass, the density or the molar volume (molarity) to their elementary compounds.

In a stable mixture of compounds, the mass fraction w_i , the molar fraction x_i , and the volume fraction ϕ_i of the i -th compound are defined in Eq. 20.6. In these equations, the volume V_i refers to the volume of the i -th compound prior mixing.

$$\left\{ \begin{array}{lcl} w_i & = & \frac{m_i}{m_{\text{mix}}} \quad ; \quad \text{with} \quad \sum_i w_i = 1 \\ x_i & = & \frac{n_i}{n_{\text{mix}}} \quad ; \quad \text{with} \quad \sum_i x_i = 1 \\ \phi_i & = & \frac{V_i}{\sum_j V_j} \quad ; \quad \text{with} \quad \sum_i \phi_i = 1 \end{array} \right. \quad (20.6)$$

In the case of the polarizable target, the two-compound mixture is supposed homogeneously distributed, although the target is composed of irregular NH_3 beads and LHe. This mixture is stable, therefore the following relation is also assumed : $n_{\text{mix}} = n_{\text{NH}_3} + n_{\text{LHe}}$. Finally, the LHe is assumed to fill the remaining space in the target cell, such that $V_{\text{mix}} = V_{\text{Cell}} = V_{\text{NH}_3} + V_{\text{LHe}}$; This assumption is further discussed in Sec. 20.2.5. These considerations lead to the definition of the following relations between the component fractions as given in Eq. 20.7. Owning of a mixture made of only two compounds, the notation w_i , x_i and ϕ_i is simplified and will always refer to the NH_3 fraction.

$$w = \frac{m_{\text{NH}_3}}{m_{\text{mix}}} \left(= \frac{\rho_{\text{NH}_3}}{\rho_{\text{mix}}} P_F \right) \quad x = \frac{n_{\text{NH}_3}}{n_{\text{mix}}} \left(= \frac{M_{\text{mix}}}{M_{\text{NH}_3}} w \right) \quad \phi = P_F = \frac{V_{\text{NH}_3}}{V_{\text{mix}}} \left(= \frac{V_{m,\text{mix}}}{V_{m,\text{NH}_3}} x \right) \quad (20.7)$$

Under these assumptions, the relation between the mixture and its elementary compounds are defined in Eq. 20.8 and easily derived from the relation, $m_{\text{mix}} = m_{\text{NH}_3} + m_{\text{LHe}}$. The definition of the mean free path for a mixture is defined and eventually discussed later in the Sec. 21.3.1.

$$\left\{ \begin{array}{lcl} m_{\text{mix}} & = & m_{\text{NH}_3} + m_{\text{LHe}} \\ M_{\text{mix}} & = & M_{\text{NH}_3} \times x + M_{\text{LHe}} \times (1 - x) \\ \rho_{\text{mix}} & = & \rho_{\text{NH}_3} \times P_F + \rho_{\text{LHe}} \times (1 - P_F) \\ V_{m,\text{mix}} & = & V_{m,\text{NH}_3} \times P_F + V_{m,\text{LHe}} \times (1 - P_F) \end{array} \right. \quad (20.8)$$

where M is the molar mass of the corresponding compound [g/mol]

V_m refers to the molarity of the corresponding compound [mol.cm^{-3}]

Consequently, the definition of the component fractions as a function of LHe and NH_3 quantities is naturally derived as shown in Eq. 20.9.

$$w = \left[1 + \frac{(1 - P_F)}{P_F} \times \frac{\rho_{\text{LHe}}}{\rho_{\text{NH}_3}} \right]^{-1} \quad x = \left[1 + \frac{(1 - w)}{w} \times \frac{M_{\text{NH}_3}}{M_{\text{LHe}}} \right]^{-1} \quad P_F = \left[1 + \frac{(1 - x)}{x} \times \frac{V_{m,\text{LHe}}}{V_{m,\text{NH}_3}} \right]^{-1} \quad (20.9)$$

20.2.3 Target Fiducial Volume

As a matter of fact, the polarized targets cannot fully be filled due to the shape of the NH_3 beads. Consequently, the target fiducial volume refers to the effective volume occupied by the polarizable NH_3 . The concept of Random Close Packing (RCP) is a coefficient that describes the volume occupied by a compound when randomly packed. This coefficient consequently gives an educated guess of the packing factor measurement reliability. From literature [120], the structure of the NH_3 beads is similar to a cubic lattice. Thus, typical compactness of material is between $\sim 47 - 53\%$.

However, getting such good compactness is a challenging task. The simulation (Fig. 20.3) was designed by the COMPASS target group to demonstrate the difficulty of filling the target. This toy MC simulation illustrates the volume occupied by the NH_3 beads of variable sizes (with spherical shape). This figure shows some possible NH_3 arrangements for a given packing factor value. As an example, the configuration $P_F = 47.60\%$, might reflect a situation with some unfilled space in the top of the cell.

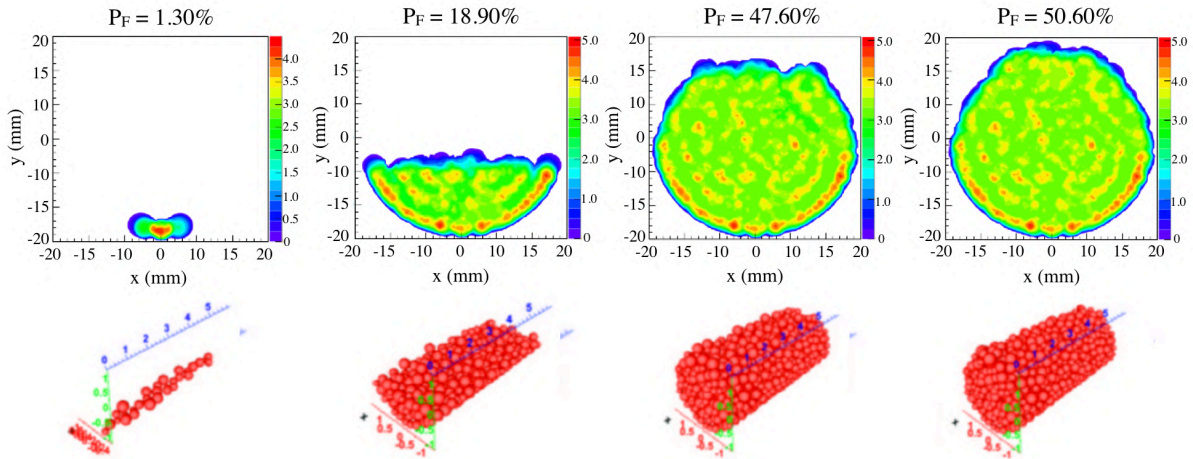


Figure 20.3: From left to right: illustration of the target filling as a function of the packing factor P_F . In this simulation, spherical beads of NH_3 between 2 mm and 4 mm radius are assumed.

In Fig. 20.4, the beam tracks projected upstream of each target are renormalized by the flux. On the left side of each track projection, the boundary of the target holder (2 cm radius) is visible. The right side of the circle is not visible, but it gives an approximative positioning of the target. A grey reticle is drawn to highlight the theoretical positioning of targets centered around 0. The red reticle gives the estimated positioning of the target in Fig. 20.4. The shift along X is expected because of the steering of the beam, previously discussed in the Sec. 6 of Ch. II. However, the second cell presents some peculiar profile. The red reticle, matching with the target holder, shows some slight shift about 2 mm compared to the central reticle in gray.

A dark blue hole in the top right of each profile is visible, but not due to the filling of the targets. This anomaly, also seen in the aluminum and tungsten targets, will be further discussed in Sec. 24.3.4 of Ch. VI. Consequently, at this stage of the analysis, there is no clear evidence of a significant target filling issue, but a systematic uncertainty will be estimated in Sec. 26 in Ch. VI, by comparing the ratio of cross-sections between the first and the second cell. Additionally, an excess of dimuon is due to nearby materials around the target and minimized by applying a radial cut below 1.9 cm on the vertex position.

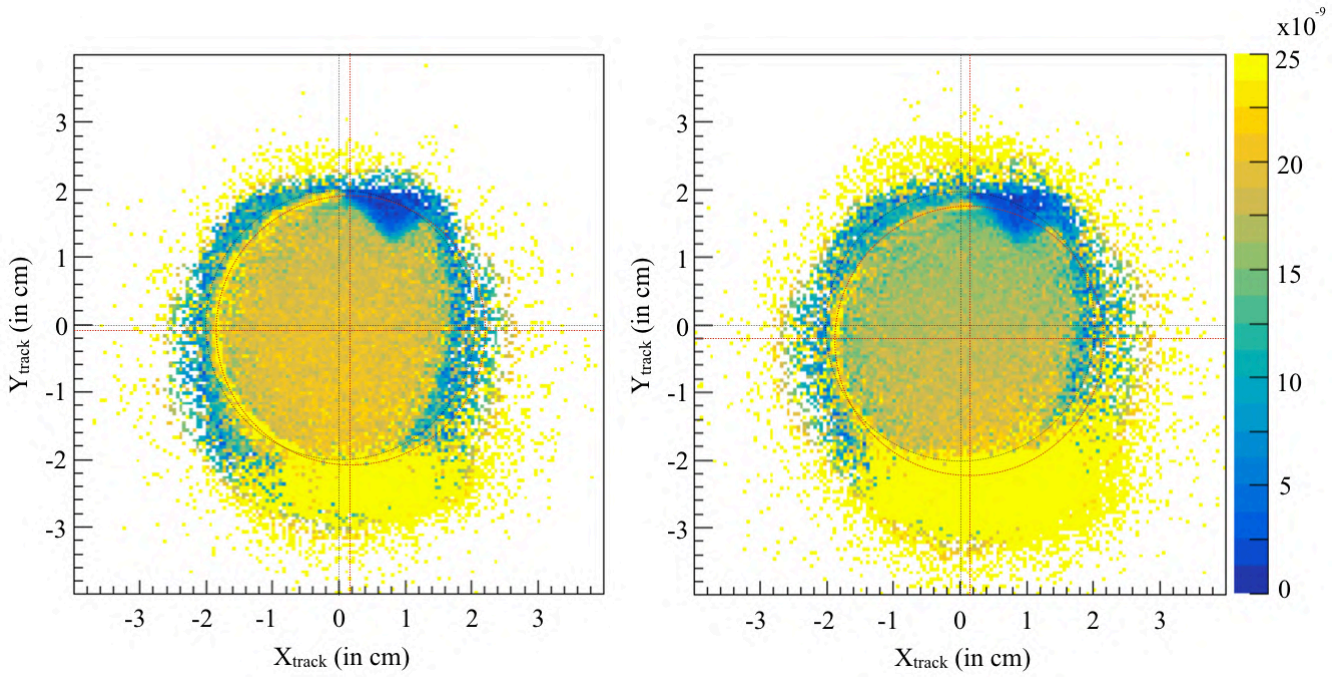


Figure 20.4: Transverse yield $N_{\text{beam}}/\mathcal{F}$, expressed as the ratio between beam tracks of Drell-Yan events and the beam flux \mathcal{F} computed in bins of X and Y. The gray reticle represent the theoretical positioning of the target. The red reticle represent the measured positioning; (a) Left: Upstream PT cell 1; (b) Right: Downstream PT cell 2.

20.2.4 Isotopic Composition of the 2015 PT targets

The composition of PT targets in 2015 will be evaluated by taking into account both NH_3 and LHe amounts of material, and their isotopic composition. Amounts of material are given in Tab. 20.3 and obtained from the target material measurement Tab. 20.2. Additionally, the amount of LHe material is calculated using the relation :

$$n_{\text{mix}} = \frac{n_{\text{LHe}}}{(1-x)} = \frac{n_{\text{NH}_3}}{x}$$

The natural abundance for hydrogen is 99.9885% of protons and 0.0115% of deuterons, nitrogen is 99.632% of ^{14}N and 0.368% of ^{15}N . The ^4He mole fraction in the target cryostat is estimated by the target group about 91%.

Table 20.3: Summary table of the isotopic composition of the 2015 PT material

Isotope	PT Cell 1 [mol]	PT Cell 2 [mol]
Proton (99.9885%)	58.934 ± 0.317	49.974 ± 0.317
Deuteron (0.0115%)	0.007 ± 0.001	0.006 ± 0.001
Nitrogen-14 (99.632%)	19.574 ± 0.106	16.599 ± 0.106
Nitrogen-15 (0.368%)	0.072 ± 0.001	0.061 ± 0.001
Helium-4 (91.059%)	9.579 ± 0.070	11.492 ± 0.083
Helium-3 (8.941%)	0.941 ± 0.006	1.128 ± 0.008

20.2.5 Temperature Dependence

In order to achieve 70% polarization of protons in the NH_3 target cells, the PT cryostat operates at very low temperatures, as introduced in Sec. 6. Consequently, at such low temperature, some properties of the material may change. In the literature [121], the helium density is well determined : $\rho_{\text{LHe}} = 0.1451 \text{ g/cm}^3$. However, the ammonia density, shown in Fig. 20.5 is poorly known at very low temperature. Indeed, few values have been measured, and the closest to the working temperature is Adeva 1998 [116] at 77 K. At such temperature and pressure conditions, the NH_3 beads remain solid. There is no transition phase below 77 K. Therefore, the NH_3 density is reasonably extended to the cryostat temperature.

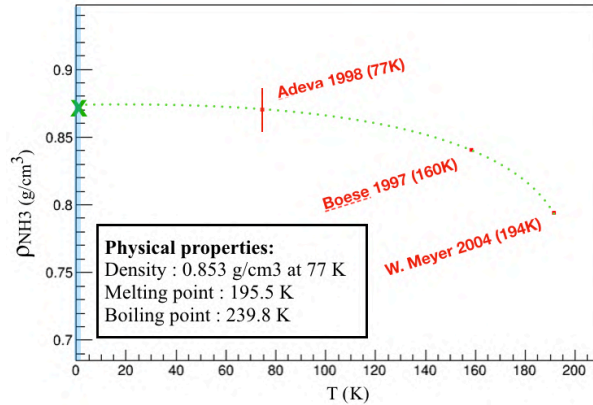


Figure 20.5: The NH_3 density as a function of the temperature. In red, the measured values of NH_3 density. The blue area is the region of interest of the COMPASS data taking.

In frozen spin configuration, the temperature decreases below 60 mK. This temperature is even lower than superconducting magnets at LHC. A superfluid transition of ^4He into He-II takes place below the lambda point at $T_\lambda \simeq 2.1768 \text{ K}$ as illustrated in Fig. 20.6.

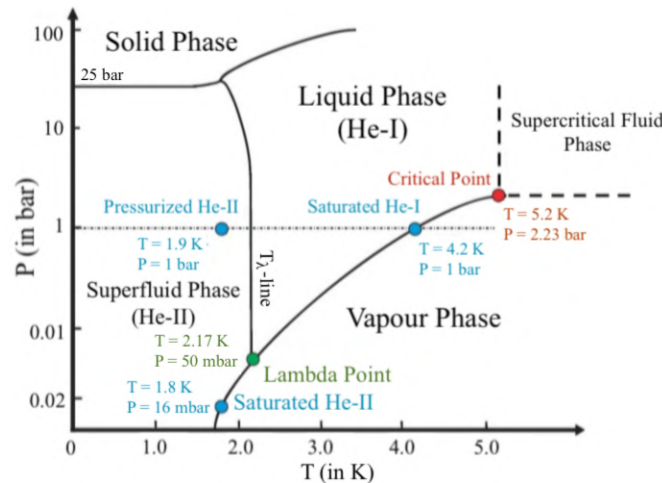


Figure 20.6: Helium-4 phase diagram [122]

In the cryostat, the pressure is given by the ^3He vapor at saturated vapor pressure. The LHe is composed of a mixture between liquid ^3He and He-II. In the literature [121], the He-II is the notation of the superfluid ^4He , also known as the *second sound* of the ^4He in analogy to the wave motion in the air. The *second sound* is a known quantum phenomenon [121], where the heat transfer propagates such as wave-like motion. Additionally, the He-II has the highest thermal conductivity of any known material. Its density denoted ρ , is described in the literature using a two-fluid model. The density is written $\rho = \rho_S + \rho_N$, where ρ_S is the density of the superfluid phase, which has no viscosity or entropy.

The density of the normal phase is denoted ρ_N . In this model, the normal component is progressively replaced by the superfluid component toward lower temperatures, as shown in Fig. 20.7. Consequently, there is no discontinuity in the apparent density $\rho \simeq 0.1451 \text{ g/cm}^3$.

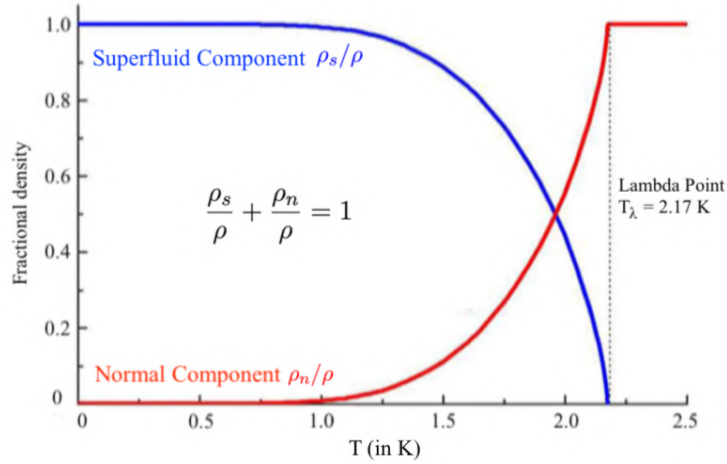


Figure 20.7: Temperature dependence of the normal and superfluid phase diagram of ^4He [123]

The superfluid properties of ^4He absorbed in porous media are discussed in various papers [120]. Consequently, the NH_3 beads might appear to be porous in the scope of the ^4He . The relation $V_{\text{mix}} = V_{\text{Cell}} = V_{\text{NH}_3} + V_{\text{LHe}}$ would not longer be conserved. This effect is expected to be small, because of the ^4He cross-section, but it can be estimated by considering $V_{\text{mix}} = V_{\text{NH}_3} + V_{\text{Cell}}$.

20.2.6 Summary Table

The detailed values used in the analysis are shown in Tab. 20.4. The values for the first and second cell are obtained using the mixed formula, Eq. 20.8. In this motion, special care has been taken to express this equation in terms of the amount of each material $n_{\text{NH}_3}, n_{\text{He}_3}, n_{\text{He}_4}$ due to the hybrid nature of the PT targets.

$$\varrho_T^{\text{cell}} = \frac{(N_{T,\text{NH}_3} + N_{T,\text{LHe}})}{\pi R^2} = \frac{N_A}{\pi R^2} \times [n_{\text{NH}_3} A_{\text{NH}_3} + n_{\text{He}_3} A_{\text{He}_3} + n_{\text{He}_4} A_{\text{He}_4}] \quad (20.10)$$

where n_i refers to the amount of material the i -th compound in the target [mol]

A_i is the atomic weight of the i -th nucleus in the target nucleus [uma]

Table 20.4: Summary table for the 2015 PT material; The systematic uncertainties are small and consequently neglected.

Properties	LHe	NH ₃	PT Cell 1	PT Cell 2
m [g]	–	–	334.6 ± 1.8	282.8 ± 1.8
M [g.mol ⁻¹]	3.91	17.03	12.43 ± 0.02	11.35 ± 0.02
ρ [g.cm ⁻³]	0.1451	0.853 ± 0.036	0.5438 ± 0.0040	0.4821 ± 0.0036
Length, L [cm]	–	–	55	55
Fraction P_F	–	–	0.5677 ± 0.0242	0.4814 ± 0.0205
Fraction w	–	–	0.8904 ± 0.0055	0.8517 ± 0.0055
Fraction x	–	–	0.6513 ± 0.0014	0.5690 ± 0.0015
ϱ_T [cm ⁻²]	–	–	$(2.3217 \pm 0.0085) \times 10^{25}$	$(2.0235 \pm 0.00849) \times 10^{25}$

21 | Beam Flux

In the evaluation of the cross-section, the renormalization of the collected data by the incoming beam particle flux going through the fiducial volume of the targets is a crucial step. A precise determination of the 2015 beam rate through the targets is performed in this section. The attenuation factor due to the material budget crossed by the beam is also presented. Finally, an additional term due to the limited capability of the DAQ to record data is estimated.

21.1 Ionization Chamber Flux

The ionization chamber, namely *ion2 chamber* in the experimental hall, is located upstream of the COMPASS apparatus and monitors the rough intensity. The incident radiation causes the gas to ionize and create ion-electron pairs [88]. Moreover, this device is independent of the COMPASS DAQ system and has a large acceptance which makes it an excellent upper limit reference to estimate the intensity of the incoming beam flux. An estimation of the flux is given in Fig. 21.1 using Eq. 21.1.

$$\mathcal{F}_{\text{ion2}} = \beta \times N_{\text{ion2}}, \text{ with } \beta = \begin{cases} 7400 \pm 370, & \text{for a } \mu^- \text{ beam} \\ 5300 \pm 265, & \text{for a } \pi^- \text{ beam} \end{cases} \quad (21.1)$$

The β calibration numbers, provided by the EN/EA¹ department at CERN, depends on the beam nature and material budget. By considering a negatively charged π beam, the average integrated flux in 2015 is about 3.90×10^8 hadrons/spill. This flux is estimated with an uncertainty of $\pm 5\%$.

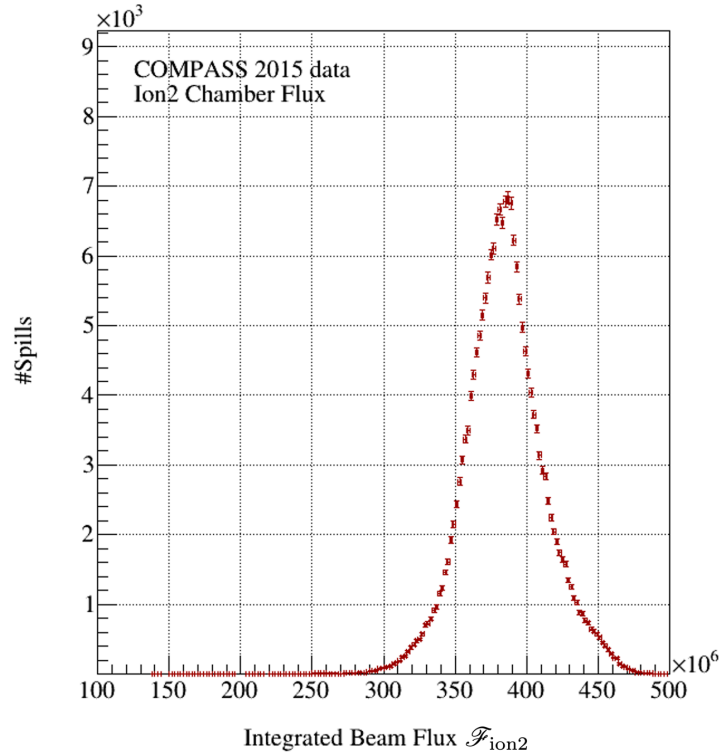


Figure 21.1: Distribution of beam flux per spill given by the ion2 chamber for a hadron beam calibration using COMPASS 2015 data. Flux is integrated over time in the spill [1s; 5.6s].

¹Engineering Group responsible for CERN's Experimental Areas

21.2 Absolute Flux Estimation

The ion2 chamber flux provides a rough estimate of the incoming beam rate entering the COMPASS area. However, this flux is not representative of the effective number of beam particles going through the targets. Consequently, the COMPASS beam telescope station is used to measure a precise flux. The retained beam tracks will be subjected to selection criteria in time and space as well as the Drell-Yan event selection in order to renormalize by the number of incoming beams.

In this analysis, only Random Trigger (RT) events are considered to ensure an unbiased estimation of the flux. The absolute beam flux \mathcal{F} integrated over time and spills, analogous to a number of beam particles, is defined as follows :

$$\mathcal{F} = \sum_i^{\text{\#spill}} \frac{1}{\Delta t} \frac{N_{\text{beam},i}}{N_{\text{RT},i}} \Delta T_{\text{spill}} \quad (21.2)$$

where $N_{i,\text{RT}}$ is the number of random trigger recorded in the i -th spill

$N_{\text{beam},i}$ is the total number of reconstructed beam tracks in the fiducial volume of the target

ΔT_{spill} is the width of the considered time in the spill range

Δt is the beam meantime width

In this chapter, the absolute beam flux is estimated using a radial cut of 1.9 cm on the beam tracks. This radial cut is used to select the fiducial volume of the target and gives an overview of the beam stability, but it might also be changed later in the analysis. Fig. 21.2 shows the comparison of the ion2 chamber flux with the beam telescope flux restricted to the transverse fiducial volume of the target, which is consequently lower. The details of the flux measurement are given in the next sections.

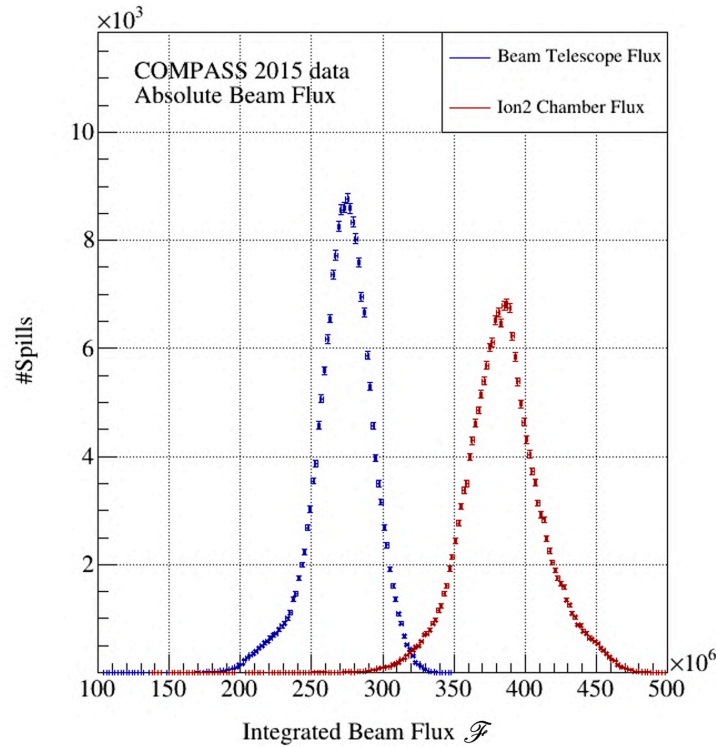


Figure 21.2: Distribution of 2015 absolute beam flux estimated with the ion2 chamber in red (no radial cut) and with the COMPASS beam telescope in blue (with a radial cut of $R < 1.9$ cm).

21.2.1 Beam Track Reconstruction

The beam track reconstruction is a two-step process using the hits found in the beam telescope stations, as illustrated in Fig. 21.3. The space track can be decomposed into X- and Y- projections. Each of the beam track is associated with an XY position, a timing value, a momentum vector, and a χ^2 value of the fit. In 2015, a beam track is reconstructed, when at least 6 hits are found in the space track, and at least 2 hits per X-, Y- projections. At most 3 common hits may be used in two different space tracks. Consequently, these reconstructed tracks are usually good quality tracks.

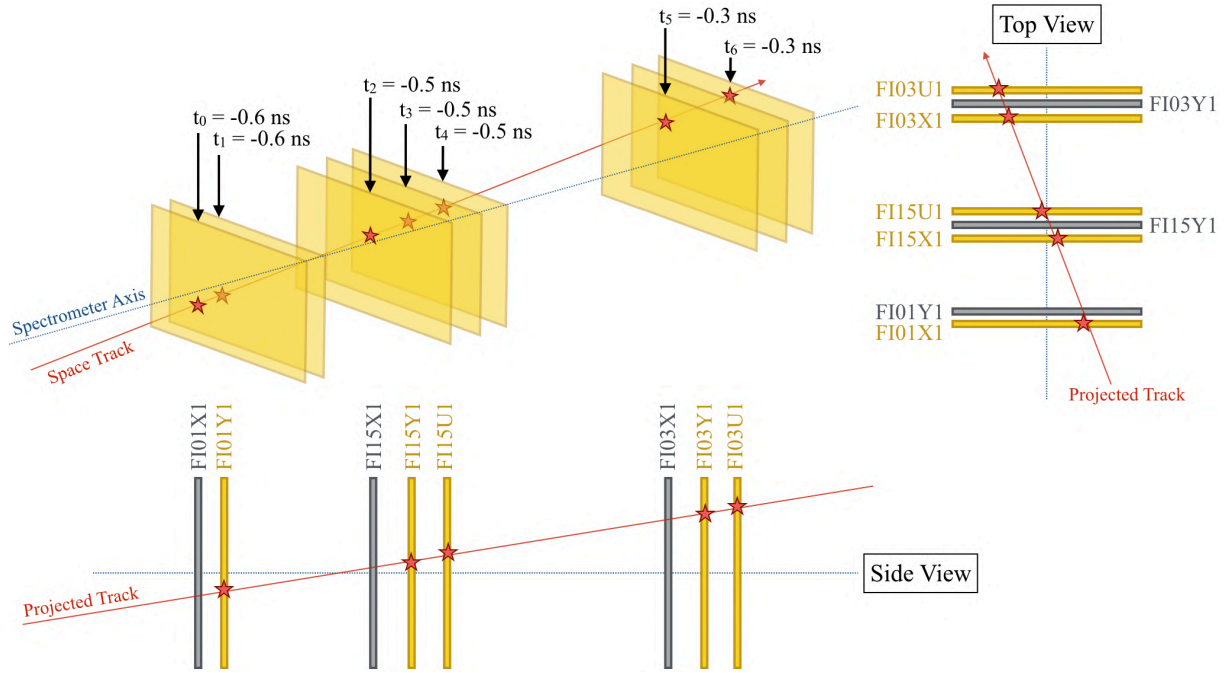


Figure 21.3: Illustration of beam track reconstruction, based on the X (top view) and Y projections (side view). Stars in the picture represents hits in the Sci-Fi detectors. The timing of hits are shown and denoted t_i . Detectors in gray are the views orthogonal to the corresponding projections.

In 2015, the number of tracks for RT trigger is shown in Fig. 21.4. There are about 1500 to 1700 reconstructed beam tracks per spill, when applying a radial cut at $R < 1.9$ cm and a beam timing cut -3 ns $< \Delta t < 3$ ns (introduced in Sec. 21.2.2). The number of reconstructed tracks varies with the intensity (*e.g.* lower intensity from spill 0 to 20), the stability of the apparatus (*e.g.* spill #29, #82, #150), and the random trigger rate.

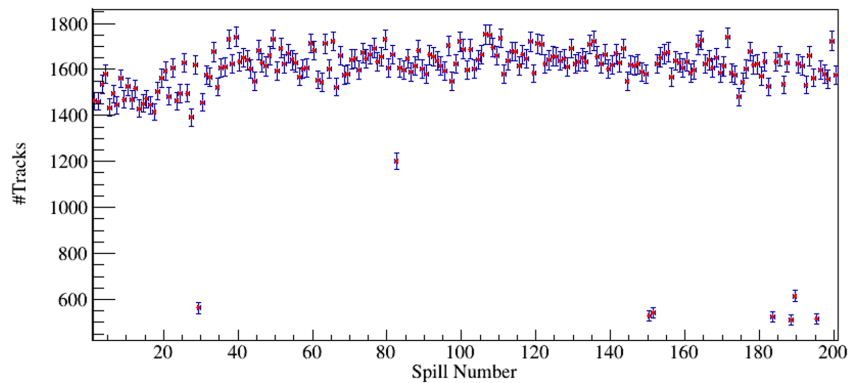


Figure 21.4: Distribution of the number of tracks as a function of the spill number for a typical high intensity run.

The beam tracks are required to cross the target fiducial volume by extrapolating them. Thus, a track is considered as valid if, by extrapolation, it crosses the target entirely from the upstream to the downstream surface. The principle of the radial selection is shown in Fig. 21.5.

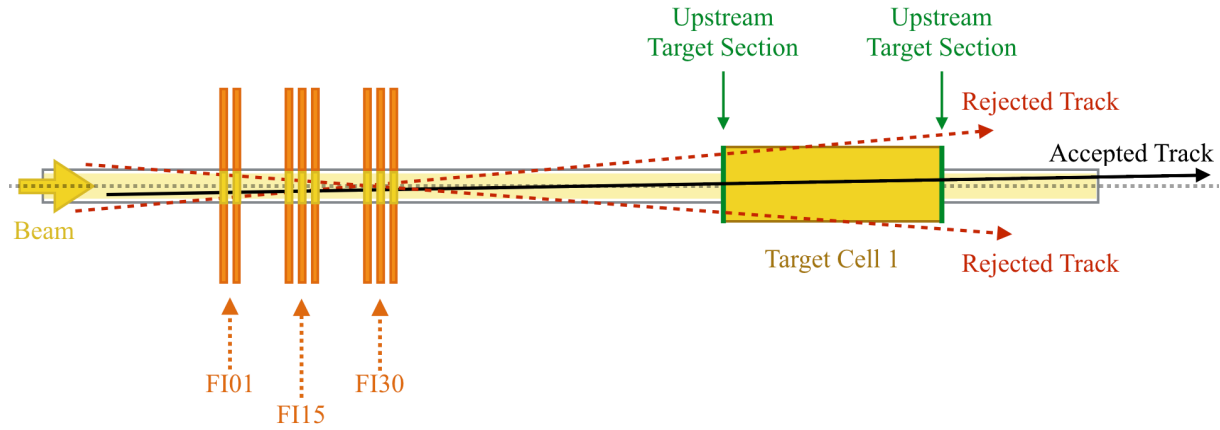


Figure 21.5: Illustration of the beam telescope and some typical examples of accepted and rejected tracks

The flux distribution, shown in Fig. 21.6, is estimated target by target and remains smooth both in the low intensity and high intensity regions. In 2017, the beam track reconstruction algorithm was improved, and a new reproduction of the data occurred in 2018. The comparison of the previous and the improved algorithm is shown in Appendix E.

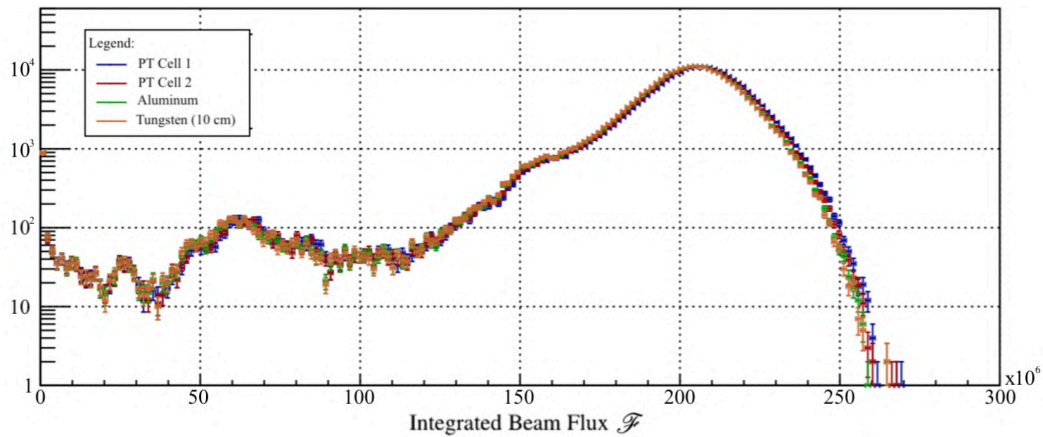


Figure 21.6: Flux distribution target by target using the COMPASS 2015 data. It shows a stable flux as a function of the target, which means a rather focused beam

21.2.2 Beam Meantime

The meantime of a beam track is defined as the average time of its hits in the beam telescope stations. The origin of time is given by the trigger time. The track timing is defined based on the timing of the collected hits within the selected time range. Taking the illustration in Fig. 21.3, the meantime of the track is $\langle t \rangle = -0.47$ ns.

A typical beam meantime profile is shown in Fig. 21.7. A time gate selection cut is applied at the reconstruction level for each Sci-Fi projection. In 2015, this time gate was $[-6$ ns; 6 ns] limiting the width of the RT beam meantime (in red) in Fig. 21.7. This beam time profile shows a flat distribution around

the origin of time and two shoulders at -5 ns and 5 ns. Additionally, this edge effect is also introduced by the time gate selection in the reconstruction.

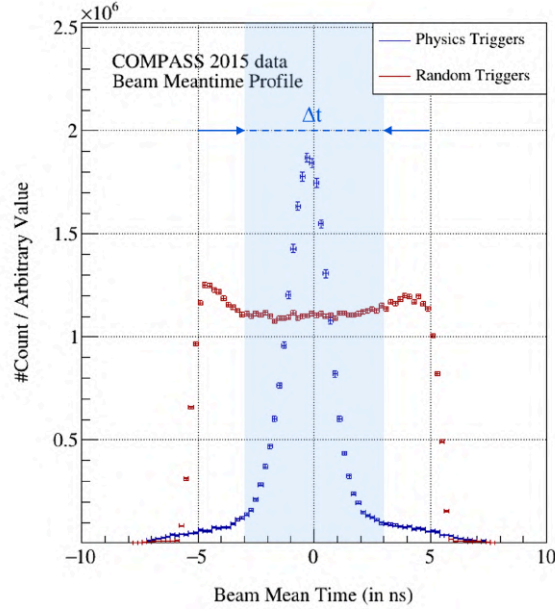


Figure 21.7: Distribution of the hit timing of beam tracks in 2015, for physics trigger in blue and RT events in red (the renormalization value is arbitrary)

The beam mean time width, Δt , is chosen based on a tradeoff between maximizing the number of events and minimizing the systematic uncertainty in both physics and RT events. The beam meantime profile must contain the correlated data peak, as shown in Fig. 21.7 (blue band). The flux remains stable for width up to 6 ns, as shown in Fig. 21.8b. Moreover, the integrated flux varies at most from 45% with and without Δt selection. Consequently, the Δt is adjusted within the range $[-3 \text{ ns}; 3 \text{ ns}]$, as highlighted by the blue band in Fig. 21.7b. In this case, the systematic uncertainty is minimized, smaller than 1%, and consequently neglected.

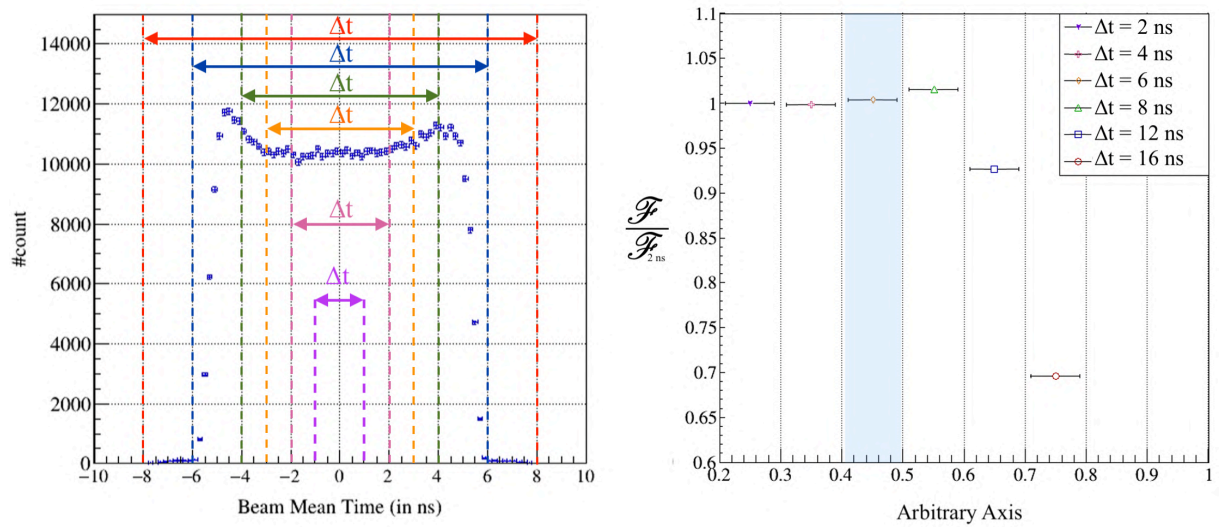


Figure 21.8: (a) Left: Distribution of the beam mean time for RT events and different Δt selections. (b) Right: The integrated flux corresponding to the various Δt cuts (integrated over the run, and renormalized by the case $\Delta t = 2 \text{ ns}$).

21.2.3 Time in Spill Range

A correct selection of time in the spill range is important to avoid a miscalculation of the flux. In Fig. 21.9a, the physics trigger profile is starting later than the random trigger. Indeed, physics triggers are subjected to the VETO signal unlike random trigger events (Ch. II, Sec. 7.4).

Therefore, the time in spill range ΔT is selected regarding to the profile of both physics and random trigger events. In Fig. 21.9a, the decrease of reconstructed tracks for RT events (in red) is related to an increase of the DAQ load, as explained in Sec. 21.4. Finally, the beam extraction stops after 5.6 s.

The yield $N_{\mu\mu}/\mathcal{F}$ remains constant because the Drell-Yan production rate varies proportionally to the effective flux. The influence of the time in spill gate ΔT selection is tested using three different time in spill lengths (Fig. 21.9b). No systematic effect is observed for these three sets of ΔT , which confirms the absence of systematic effect in the evaluation of the flux or the reconstruction efficiency due to the variation of intensity. Moreover, in this figure, the evaluation of the cross-section appears to be invariant of the time in the spill. Consequently, the time in spill selection, ΔT , is chosen within the range [1.0 s; 5.6 s] and the systematic uncertainty is neglected.

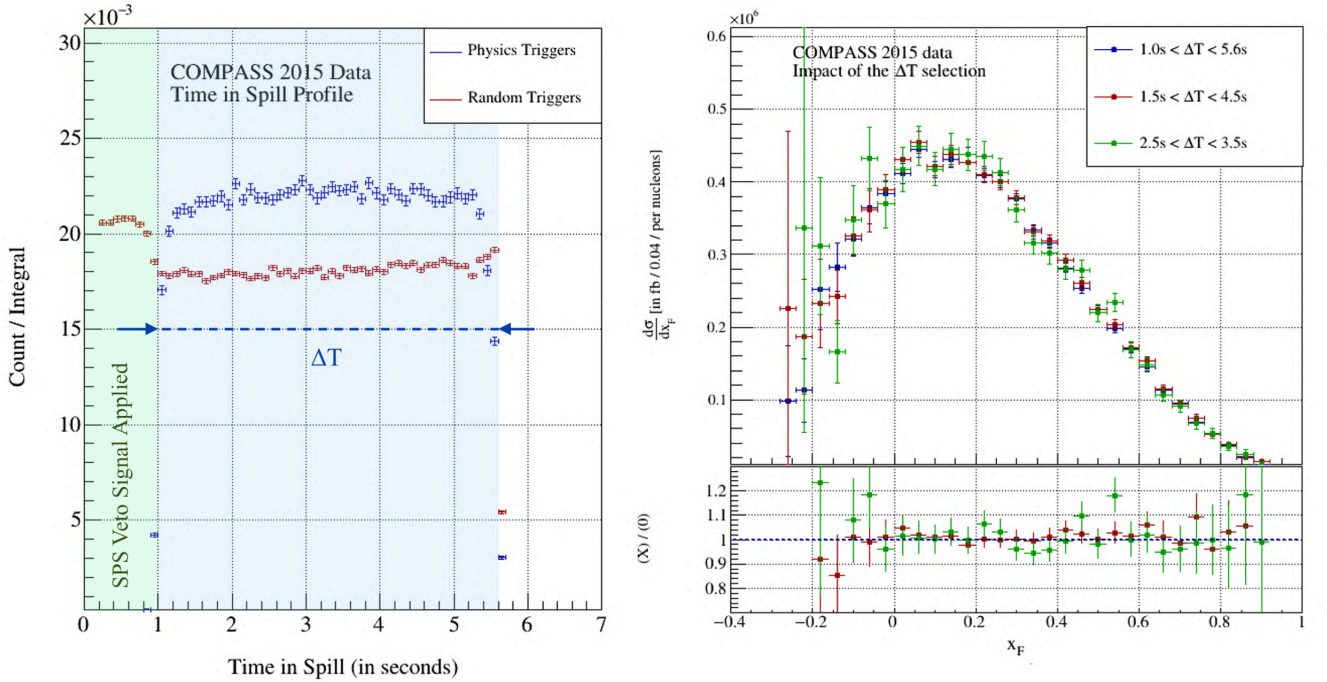


Figure 21.9: (a) Left: Distribution of time in spill using random triggers in red and physics triggers in blue; (b) Right: Differential cross-section $d\sigma/dx_F$, as a function of x_F , for different time in spill selection, ΔT . The selection $1.0 \text{ s} < T < 5.6 \text{ s}$ is used as a reference for comparison purpose in the ratio plots.

21.3 Beam Attenuation

As previously introduced, the beam may cross a large amount of material budget before reaching a specific target. This significantly reduces the beam intensity and requires to be corrected by taking into account the beam attenuation in the flux calculation.

21.3.1 Mean Free Path of a Pion

First, the mean free path is the average length before undergoing an interaction in a medium. This length is defined in Eq. 21.3 in terms of [cm].

$$\frac{1}{\lambda(E)} = n\sigma(Z, E) \quad (21.3)$$

where $\lambda(E)$ is the mean free path and depends on the energy E of the beam [cm]

$\sigma(Z, E)$ is the total cross-section per atom of the process for a given element [cm²]

$n = \rho \frac{N_A}{M}$ refers to the total number of atoms per volume [cm⁻³]

The mean free path λ depends on the budget material crossed by the beam particle. Consequently, an *invariant* length, denoted $\tilde{\lambda}$, is often preferred, because of its independence with the material density. It is defined as $\tilde{\lambda} = \rho \times \lambda$, and is expressed in terms of [g.cm⁻²].

The mean free path may either be defined as a nuclear collision length, λ_T , or a nuclear interaction length, λ_I , depending on the type of reactions considered. On the one hand, the collision length includes elastic, quasi-inelastic, and inelastic interactions. On the other hand, the nuclear interaction refers to inelastic interactions only. Consequently, the collision length is always smaller than the nuclear interaction length. The nuclear interaction length used to estimate the attenuation of a pion beam at 190 GeV/c², is reasonably independent of the beam momentum, as shown in Fig. 21.10.

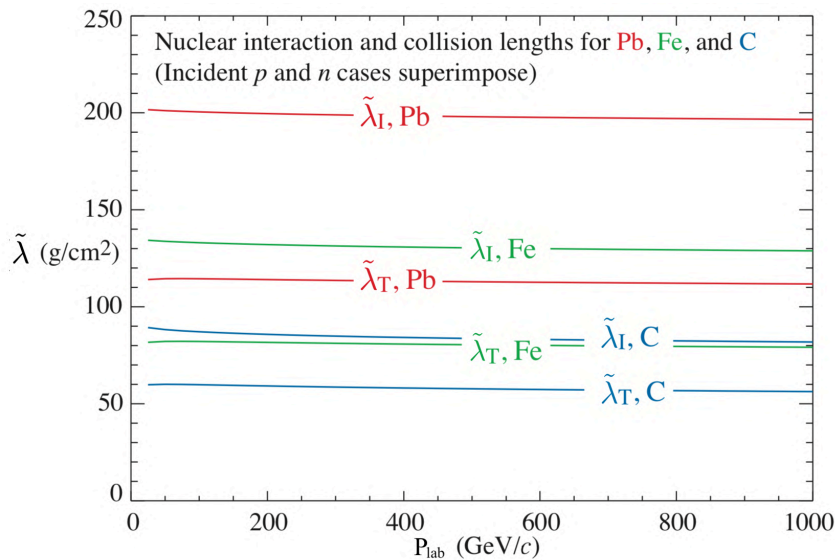


Figure 21.10: Nuclear interaction and collision lengths as a function of P_{lab} and different type of targets. This dependence is eventually considered as negligible [124].

Along the line of mix quantities, previously defined in Sec. 20.2.2, the mix length, λ_{mix} for different compounds follow the relation :

$$\frac{1}{\lambda_{\text{mix}}} = \sum_i n_i \phi_i \sigma_i \quad (21.4)$$

where $n_i = \frac{\rho_i \mathcal{N}_A}{M}$ refers to the total number of atoms per volume of the i-th compound [cm^{-3}]
 ϕ_i is the volume fraction of the i-th compound
 $\sum_i n_i \phi_i \sigma_i$ is also known as the *macroscopic cross-section* in the literature [125]

In the case of the PT targets, the expression of the mix invariant length $\tilde{\lambda}_{\text{mix}}$ is derived from Eq. 21.4 and simplified using the relation $[\rho_{\text{NH}_3} P_F = \rho_{\text{mix}} w]$ and $[\rho_{\text{LHe}}(1 - P_F) = \rho_{\text{mix}}(1 - w)]$. Consequently, the final expression becomes:

$$\frac{1}{\lambda_{\text{mix}}} = \frac{P_F}{\lambda_{\text{NH}_3}} + \frac{(1 - P_F)}{\lambda_{\text{LHe}}} \implies \frac{1}{\tilde{\lambda}_{\text{mix}}} = \frac{w}{\tilde{\lambda}_{\text{NH}_3}} + \frac{(1 - w)}{\tilde{\lambda}_{\text{LHe}}} \quad (21.5)$$

21.3.2 Cross Cell Selection

An additional beam selection is applied by extrapolation of the beam tracks, as illustrated in Fig. 21.11. This selection ensures that the beam track went through all upstream targets to properly account for beam attenuation.

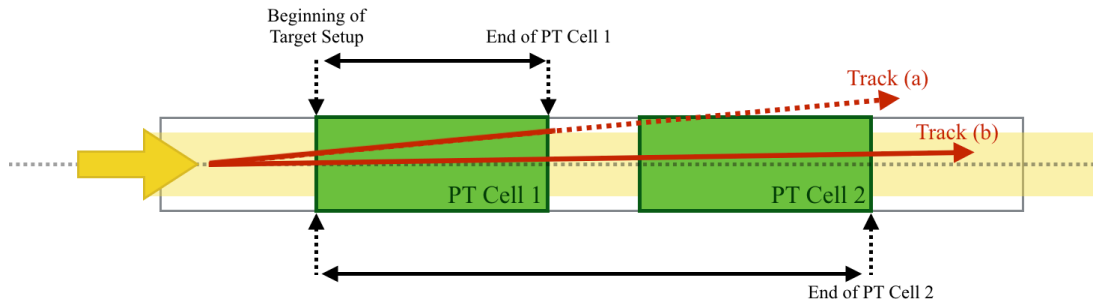


Figure 21.11: Illustration of the cross target selection. Only tracks crossing previous targets are considered.

As an example in this figure, the track (a) is rejected in the event selection for the second PT cell but remains valid for the first PT cell. At the opposite track (b) is selected for both targets as it goes through the entire target setup. The same logic applies to the aluminum target as well as the tungsten target.

21.3.3 Flux Attenuation as a function of Z_{vtx}

A first beam attenuation is estimated based on a simple absorption model using the interaction length of each target material. A set of coefficients a_k is computed using Eq. 21.6. These attenuation coefficients, a_k , are computed target by target and shown in Fig. 21.12.

$$\begin{cases} a_0 = 100\%, & \text{for } n = 0 \\ a_n = \prod_{k=1}^n \exp\left(-\frac{\rho_k \times L_k}{\lambda_{\text{int},k}}\right), & \forall n > 0 \end{cases} \quad (21.6)$$

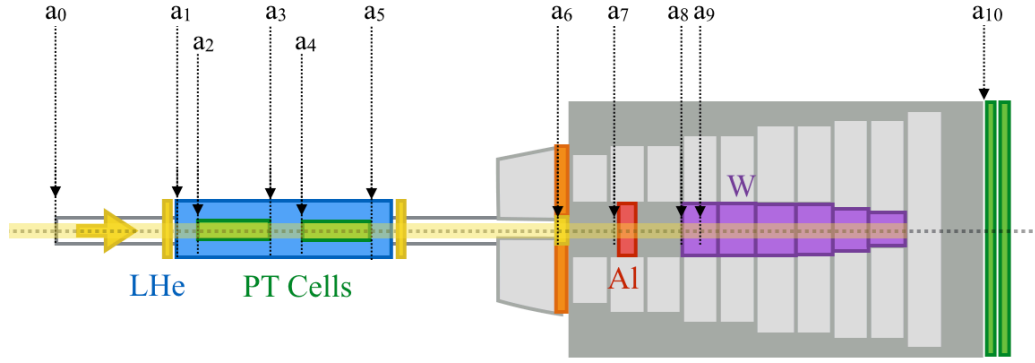


Figure 21.12: Simplified 2015 target setup including the location of the a_i absorption coefficients.

The computed value of the coefficients are given in Tab. 21.1 at the various positions denoted a_i . In a second step, the coefficients are derived in a continuous way along Z . This flux attenuation is computed using the COMPASS 2015 MC geometry. The MC attenuation obtained (Fig. 21.13), accounts for the material budget crossed by the beam and the positioning of each target material.

In Fig. 21.13a, The flux absorption is compared between the MC approach and the simple calculation in the ratio plot. In the simple model, some materials were missing in the total budget, such as the FI35 contribution at $Z_{vtx} \simeq -100$ cm or the radiation shielding attenuation at $Z_{vtx} \simeq -148$ cm.

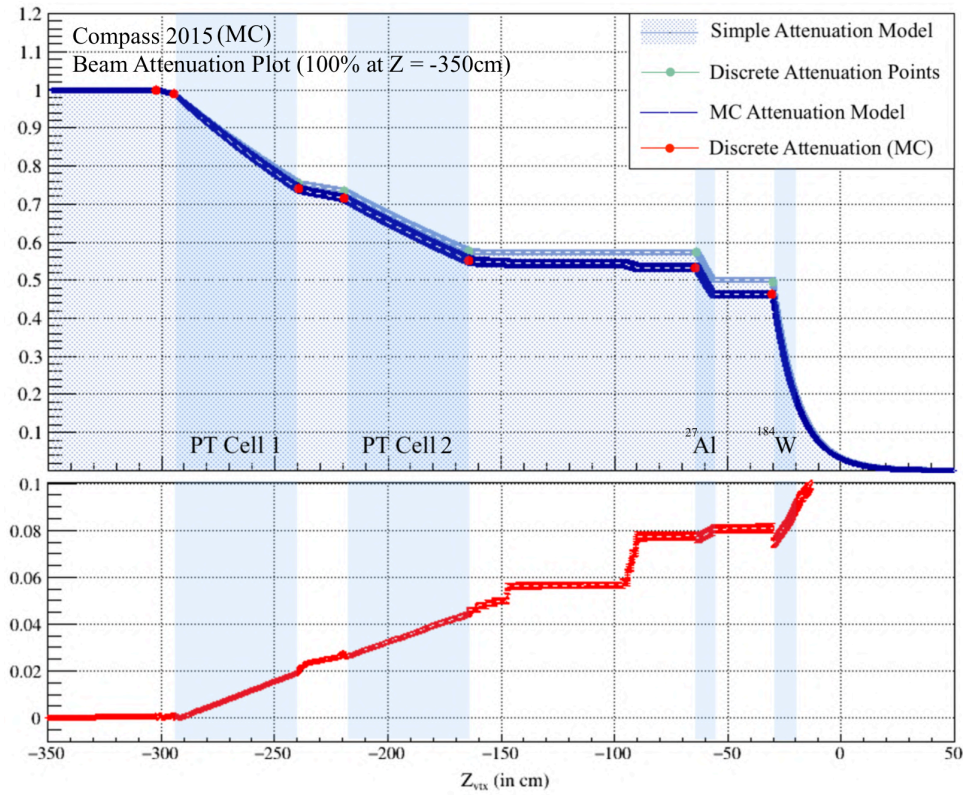


Figure 21.13: (a) Top: Attenuation of the incoming beam flux as a function of Z_{vtx} . The light blue curve corresponds to the naive calculation. The dark blue curve shows the attenuation computed using MC simulation. The green and red points are the intensity at the entrance of some a_k positions for the simple and MC attenuation model, respectively. Finally, the blue band refers to the targets; (b) Bottom: Ratio between the simple method and the MC approach

The initial intensity of the beam is set at 100% after the beam telescope station at $Z = -350$ cm. The overall agreement between naive attenuation and MC attenuation is quite reasonable, but still shows some systematic differences. However, it remains compatible with the pion interaction length of each material within 2%, which sums up target after target. Consequently, a systematic up to 2%, 3%, 3% and 4% will be quoted for the PT cell 1, PT cell 2, aluminum, and tungsten, respectively.

In Fig. 21.13b, slopes between targets in the ratio plot are slightly different. This discrepancy is considered in the analysis as a systematic uncertainty in the method and would deserve further studies. The MC approach will be used for the cross-section evaluation as it accounts for a more accurate geometry.

Table 21.1: Summary table of the material absorption estimated from MC simulation. These coefficients take into account the uncertainty on the packing factors and the NH_3 density.

	Coefficient a_n	
	Simple Approach	MC Approach
Begin of the Target Setup	$a_0 = 100\%$	$a'_0 = 100\%$
Upstream LHe	$a_1 = 100\% \pm 0.00\%$	$a'_1 = 100\% \pm 0.00\%$
PT Cell 1	$a_2 = 98.89\% \pm 0.00\%$	$a'_2 = 98.82\% \pm 0.07\%$
Mid-range LHe	$a_3 = 75.41\% \pm 0.01\%$	$a'_3 = 73.96\% \pm 0.90\%$
PT Cell 2	$a_4 = 73.43\% \pm 0.66\%$	$a'_4 = 71.49\% \pm 0.89\%$
Downstream LHe	$a_5 = 57.69\% \pm 0.64\%$	$a'_5 = 55.26\% \pm 1.12\%$
Sci-Fi FI35	$a_6 = 57.42\% \pm 0.68\%$	$a'_6 = 54.29\% \pm 0.94\%$
Aluminum	$a_7 = 57.42\% \pm 0.68\%$	$a'_7 = 53.28\% \pm 1.08\%$
Tungsten #1	$a_8 = 49.59\% \pm 0.58\%$	$a'_8 = 46.17\% \pm 0.38\%$
Tungsten #2 (After 10 cm)	$a_9 = 20.53\% \pm 0.24\%$	$a'_9 = 18.83\% \pm 0.38\%$
End of Absorber	$a_{10} = 0.00\%$	$a'_{10} = 0.00\%$

21.4 Data Inhibition

The DAQ system may inhibit data recording in two different ways introducing either a busy or a VETO signal. The busy signal introduces regulation of the data rate; and the VETO signal rejects ambiguous events (bad geometry track, coincidence with beam halo,...). Dimuon pairs selected in a physics analysis are subjected to these inhibitions, while for flux calculation, RT is not subjected to VETO signal. Additionally, once this additional factor is taken into account in the absolute flux, the flux is often renamed effective flux.

The first DAQ inhibition results in the introduction of a DAQ deadtime. The generation of a dynamic busy signal is led by the three cases defined as follows:

- **Case (1)** : 2 consecutive triggers result in $4\ \mu\text{s}$ delay
(DAQ rate will be limited to $\sim 500\text{kHz}$)
- **Case (2)** : 3 consecutive triggers result in $30\ \mu\text{s}$ delay
(DAQ rate will be limited to $\sim 100\text{kHz}$)
- **Case (3)** : 10 consecutive triggers result in $250\ \mu\text{s}$ delay
(DAQ rate will be limited to $\sim 40\text{kHz}$)

In practice, this inhibition is due to the rate limitation of the hardware front-end. Each front-end electronics has its proper readout time. In 2015, the overall spectrometer acquisition system was imposed by the readout of the APV electronics.

Along the same line, the VETO inhibition is set when a track fire the VETO system. Additionally, some vetoed events were given as examples in Sec. 7.3, Ch. II. Figure 21.14 shows the evolution of the percentage of VETO and DAQ inhibition as a function of the ion2 chamber flux. At high intensity, both VETO and DAQ deadtimes show a linear trend. The shape of the DAQ deadtime at low intensity is more complex because of the dynamic signal introduced in the DAQ.

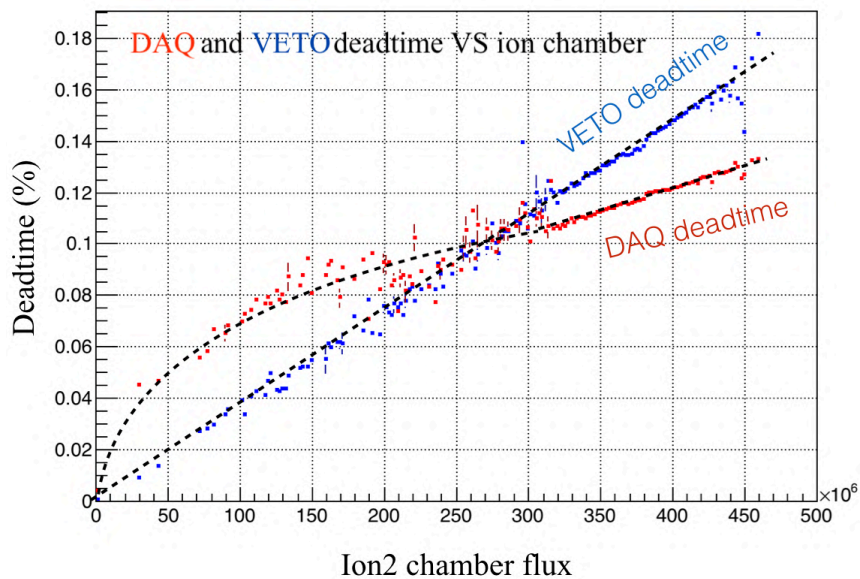


Figure 21.14: Profile of the DAQ and VETO deadtimes as a function of the flux intensity. The nominal intensity for physics data taking corresponds to an ion2 chamber flux between $3 \cdot 10^8$ and $4.5 \cdot 10^8$ hadrons per spill.

In the analysis, RT events are corrected for both DAQ and VETO inhibitions by applying a coefficient in the flux calculation, as illustrated in Eq. 21.7. These coefficients refer to lifetime (LT), and related with the deadtime by the simple relation: $LT = 1 - DT$. The absolute flux is consequently substituted in the following by the so-called effective flux. In the final analysis, this correction will result in a ratio $N_{\mu\mu}/\mathcal{F}_{\text{eff}}$ free of DAQ and VETO dependences. The VETO lifetime depends on the physics trigger considered in the analysis.

$$\mathcal{F}_{\text{abs}} \longrightarrow \mathcal{F}_{\text{eff}} = LT_{\text{RT,DAQ}} \times LT_{\text{VETO}}^{\varphi} \times \mathcal{F}_{\text{abs}} \quad (21.7)$$

21.4.1 DAQ Lifetime

The DAQ inhibition does not depend on the trigger choice. Therefore a unique value for the DAQ deadtime is determined to correct the cross-section estimation. The LT is calculated using either RT or FLT² scalers in Eq. 21.8. Additionally, technical information about the 2015 scalers are provided in Appendix A.

$$\left\{ \begin{array}{l} LT_{\text{RT,DAQ}} = 1 - DT_{\text{RT,DAQ}}, \text{ with } DT_{\text{RT,DAQ}} = 1 - \frac{N_{\text{RT,recorded}}}{N_{\text{RT,attempted}}} \\ LT_{\text{FLT,DAQ}} = 1 - DT_{\text{FLT,DAQ}}, \text{ with } DT_{\text{FLT,DAQ}} = 1 - \frac{N_{\text{FLT,recorded}}}{N_{\text{FLT,attempted}}} \end{array} \right. \quad (21.8)$$

where $N_{\text{RT,recorded}}$ is the number of RT triggers effectively recorded by the DAQ.system

$N_{\text{RT,attempted}}$ is the number of RT triggers attempted to be recorded.

$N_{\text{FLT,recorded}}$ is the number of FLT triggers effectively recorded.

$N_{\text{FLT,attempted}}$ is the number of FLT triggers attempted to be recorded.

The DAQ lifetime measured from the FLT scalers and the RT scalers is shown in Fig. 21.15. In both cases, the average is in the order of 88-89%.

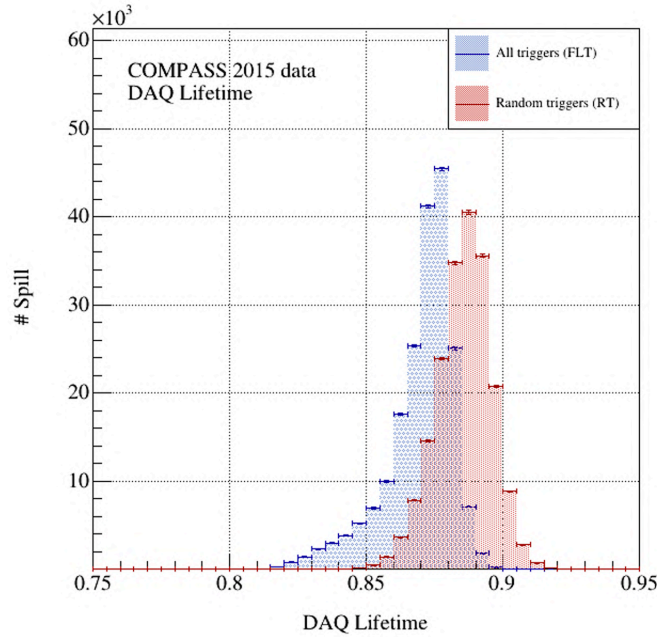


Figure 21.15: DAQ lifetime distribution over 2015 data estimated from both FLT trigger scalers (in blue) and RT (in red) trigger scalers.

²First Level Trigger

The asymmetric tail results mainly from a variation of the beam intensity. In 2015, a beam extraction problem originating from a faulty quadrupole in the SPS beamline was found to be the reason for bad beam extraction and, consequently, various DAQ crashes or rapid increase of the DAQ deadtime. Finally, the unexpected difference between the FLT and RT is reported as an additional 1% systematic uncertainty from the difference between the two DAQ lifetimes, and the RT deadtime will be used in the analysis.

21.4.2 VETO Lifetime

The VETO lifetime is a more complex quantity to evaluate because of its trigger dependence. The triggers used in the analysis were introduced in Sec. 7.2. These are the dimuon triggers because the process of interest has two outgoing muons in the final state. A first formula of the VETO lifetime for RT is given in Eq. 21.9.

$$LT_{RT,VETO} = \frac{N_{RT,attempted+veto}}{N_{RT,attempted}} \quad (21.9)$$

where $N_{RT,attempted+veto}$ is the RT trigger rate with VETO signal applied

$N_{RT,attempted}$ is the RT trigger rate attempted

In 2015, hardware limitations prevented to measure the veto deadtimes simultaneously of the normal data taking. Therefore, decisive information, to estimate the VETO deadtime trigger for each dimuon trigger, were absent in 2015. However, in 2018 a measurement of the VETO lifetime for LAST \otimes LAST, OT \otimes LAST, MT \otimes LAST triggers was performed regularly, in the perspective of recovering, by extrapolation, the 2015 VETO lifetime.

Many possibilities were attempted to fix the 2015 estimation of cross-section using the 2018 measurement. The two main ideas were the following :

- A first method consists in reconstructing dimuon trigger signals at the software level based on hits in the hodoscopes using RT events. The time width of a RT event is about 350 ns. The coincidence between RT events and dimuon triggers was expected to be large over 2015 data. Therefore, the 2018 measurement was an opportune sample to validate the procedure and account for fake-positive triggers compared to the hardware trigger signals. This method has been implemented and tested on a small sample for the FPGA based LAS \otimes LAS in the CORAL reconstruction software, with special care to mimic the trigger delays properly as in hardware modules. Trigger signals were successfully reconstructed in 98% of the cases. However, this method requires a better timing calibration of the trigger hodoscopes in the reconstruction software to be applied at a large scale in the analysis. Additional studies were also required to implement OT \otimes LAST and MT \otimes LAST triggers.
- A second method, namely delayed VETO method, relies on the extrapolation of the measurements from 2018 to 2015 of the VETO deadtime. It assumes the trigger hardware modifications (optimization of trigger time gates, few slab replacements) between 2015 and 2018 as negligible. This method was chosen as the best quick-fix method to have a good estimate of VETO deadtime.

Delayed VETO method for the estimation of the VETO lifetime. In this method, the response of the COMPASS VETO system is modified by adding a time delay to the VETO signal. The real data trigger rate in 2018 was measured for both VETO OFF and ON, knowing that the VETO signal is shifted by a specific value. During the measurement in 2018, the delay of the VETO signal V_{tot} for LAST \otimes LAST, OT \otimes LAST and MT \otimes LAST was set to +100ns, +60ns and +60ns respectively. Eq. 21.10 gives the definition of the VETO lifetime for a given physics trigger φ .

$$LT_{VETO}^{\varphi} = \frac{N_{veto-delayed}^{\varphi}}{N_{veto-off}^{\varphi}} \quad (21.10)$$

where $N_{veto-delayed}^{\varphi}$ corresponds to the φ trigger rate with VETO applied
 $N_{veto-off}^{\varphi}$ corresponds to the number of trigger φ without VETO applied

Figure 21.16a illustrates the dependence of the VETO deadtime as a function of the ion2 chamber flux. The linear trend of the fitting functions highlights the scaling effect and a small flux dependence at high intensity for the selected trigger. Moreover, Fig. 21.16b shows the deadtime ratios for each dimuon trigger with respect to the VETO deadtime from RT scalars. The 2018 VETO deadtime from RT is estimated at 17% within $\Delta T = [1s; 5.6s]$. Distributions are fitted with a Gaussian form to obtain the mean value.

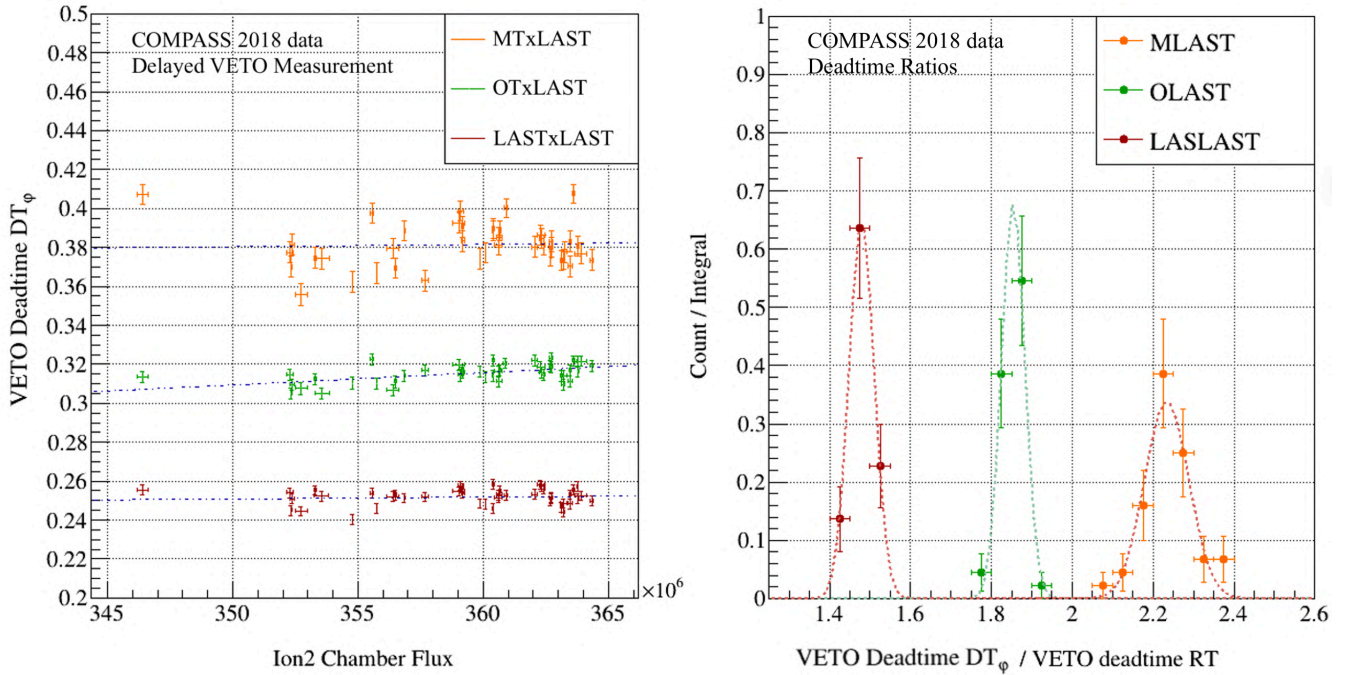


Figure 21.16: (a) Left: The 2018 VETO deadtime distributions for dimuon triggers as a function of the ion2 chamber flux; (b) Right: The VETO deadtimes renormalized by the VETO deadtime from RT.

Extrapolation of the 2018 measurement to 2015 data. The extrapolation from 2018 to 2015 relies on the assumption that the fine tuning of the trigger time gate in 2018 is negligible. Consequently, the extrapolation is performed using the following formula :

$$LT_{VETO,2015}^{\varphi} = 1 - \frac{DT_{VETO,2018}^{\varphi}}{DT_{RT,VETO,2018}} \times DT_{RT,VETO,2015} \quad (21.11)$$

Figure 21.17 shows the obtained VETO lifetime from the extrapolation of the 2018 measurement. The difference between RT and dimuon triggers is significant but expected, as dimuon triggers results from the combination of two single trigger signals within a limited time gate defined by the dimuon trigger logic.

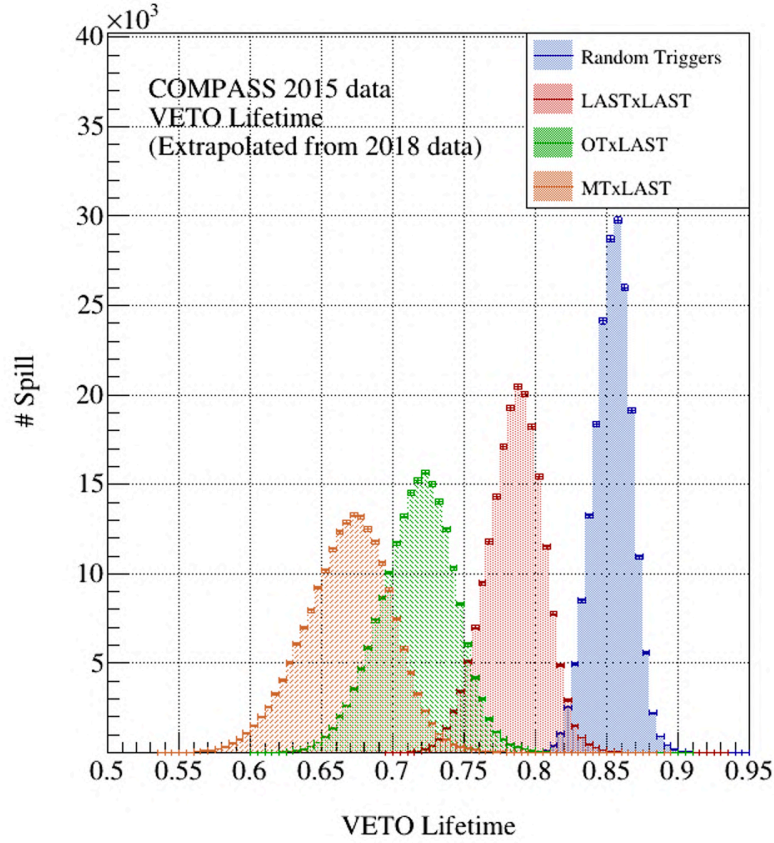


Figure 21.17: The spill by spill VETO lifetime distribution (in blue) of the 2015 RT data is obtained from Munich Scaler database. Other 2015 VETO lifetimes for dimuon triggers are obtained from the extrapolation of the 2018 deadtime measurement (red, green, orange).

22 | Stability Studies

The stability studies aim to minimize systematic uncertainties induced by the instability of the spectrometer and consequently simplify data analysis by rejecting bad spills and runs, based on the beam quality and spectrometer stability. A list of bad spills will be determined and used in the analysis. The detailed table of the remaining Drell-Yan events after applying this bad spill list is also given in Tab. 22.2.

22.1 Apparatus Stability

22.1.1 Spill by Spill Analysis

The apparatus stability is determined on a spill-by-spill basis using numerous macro-variables. These variables are assumed to remain constant over time if the spectrometer is in good working conditions. The list of macro-variables is defined as follows:

- Number of beam particles / Number of events
- Number of beam particles / Number of primary vertices
- Number of hits per beam track / Number of beam particles
- Number of primary vertices / Number of events
- Number of outgoing tracks / Number of events
- Number of outgoing particles / Number of events
- Number of outgoing particles in a primary vertex / Number of primary vertices
- Number of outgoing particles in a primary vertex / Number of events
- Number of hits in outgoing particles / Number of outgoing particles
- Number of μ^+ tracks / Number of events
- Number of μ^+ tracks in a primary vertex / Number of events
- Number of μ^- tracks / Number of events
- Number of μ^- tracks in a primary vertex / Number of events
- Number of outgoing particles / Number of outgoing particles
- Number of all vertices / Number of all vertices
- Trigger rates (MT \otimes LAST, OT \otimes LAST, LAST \otimes LAST)

In Fig. 22.1, macro-variables as a function of the spill illustrate the stability of three 2015 periods, namely W07, W13, W15. As an example, the beginning of the W13 period was particularly unstable, based on these macro-variables. Additionally, W15 period was the most stable period in terms of spectrometer stability.

22.1.2 Run by Run Analysis

A run by run analysis is also performed based on the control of a relevant kinematic variables ($M_{\mu\mu}$, x_F , x_π , x_N , q_T , P_{μ^-} , P_{μ^+} , P_π , P_N , X_{vtx} , Y_{vtx} , Z_{vtx}). The stability of the distributions are compared over the time using an Unbinned Kolmogorov Test. Tab. 22.1 illustrates the impact of the stability selection

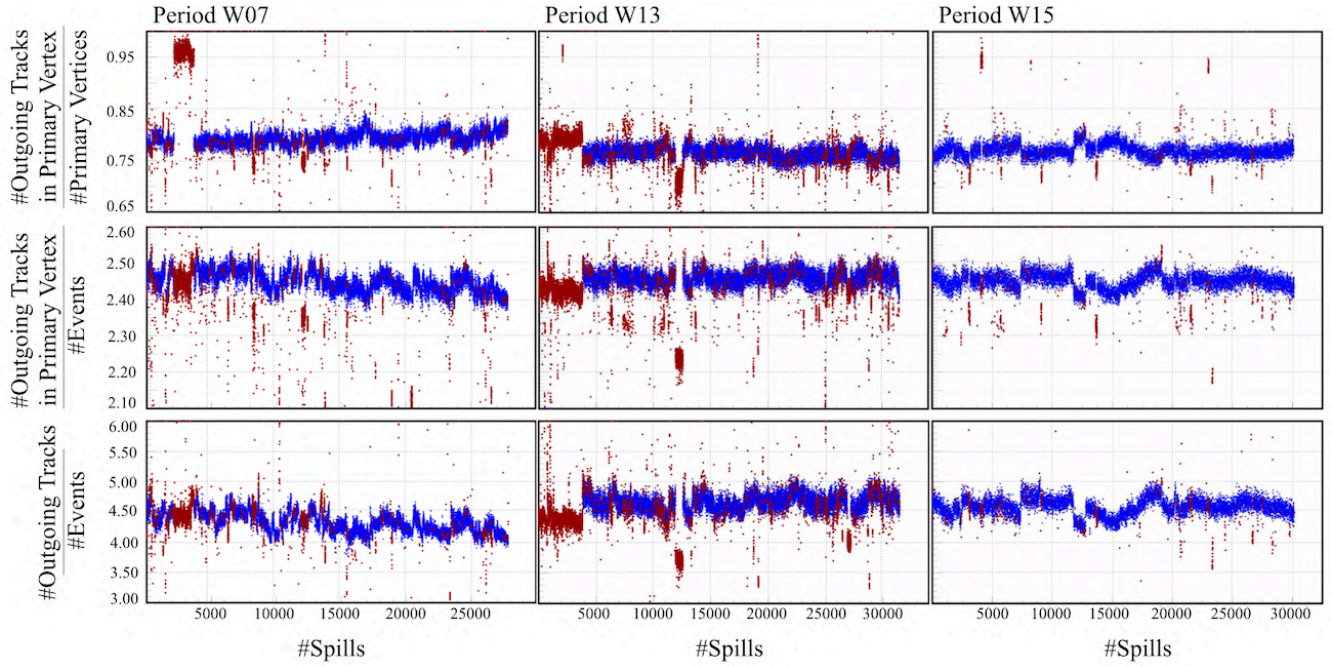


Figure 22.1: Example of three macro-variable distribution VS spill for three periods of data taking. Spills tagged as bad are marked in red.

period by period that will be applied later in the cross-section extraction analysis. More details on the apparatus stability study can be found in the release note [126].

Table 22.1: Apparatus stability study in 2015. Rejection rate of the apparatus quality selection for a given dimuon events selection.

	Number of Selected Dimuon Events (Event ratio compared without list applied)			
Period	No List Applied	Bad Spills	Bad Runs	Combined Suppression
W07	10645 evts (100%)	10113 (95.00%)	9272 evts (87.10%)	8755 evts (82.22%)
W08	10342 evts (100%)	9307 evts (89.99%)	9084 evts (87.83%)	8057 evts (77.90%)
W09	10869 evts (100%)	10212 evts (93.95%)	9596 evts (88.29%)	8965 evts (82.48%)
W10	11495 evts (100%)	10611 evts (92.31%)	10190 evts (88.65%)	9337 evts (81.23%)
W11	17300 evts (100%)	16806 evts (97.14%)	13186 evts (76.22%)	12787 evts (73.91%)
W12	13321 evts (100%)	12391 evts (93.02%)	12327 evts (92.54%)	11408 evts (85.64%)
W13	11572 evts (100%)	10836 evts (93.64%)	9589 evts (82.86%)	8984 evts (77.64%)
W14	7310 evts (100%)	6852 evts (93.73%)	7005 evts (95.83%)	6555 evts (89.67%)
W15	4306 evts (100%)	4203 evts (97.61%)	4251 evts (98.72%)	4148 evts (96.33%)
Total	97160 evts (100%)	91331 evts (94.00%)	84500 evts (86.97%)	78996 evts (81.31%)

22.2 Beam Flux Stability

22.2.1 Bad Spill List

Scaler Stability. The scalers involved in this analysis are the N_{RT} scalers, and the number of beam tracks N_{beam} . The stability of these parameters is directly related to the stability of the beam flux and the DAQ system. In the beam flux stability, the apparatus stability list is applied to overcome the problems already solved by the previous studies. As example, the improvement thanks to the stability selection is clearly visible in the low intensity region $N_{beam} < 1000$ and $N_{RT,recorded} > 4000$ in Fig. 22.2. In the same figure, the comparison of the left and right plot shows the difference before and after applying the apparatus stability selection. Additionally, spills with less than 50 beam tracks or $N_{RT,recorded} < 50$ events are disregarded (red bands in the figures).

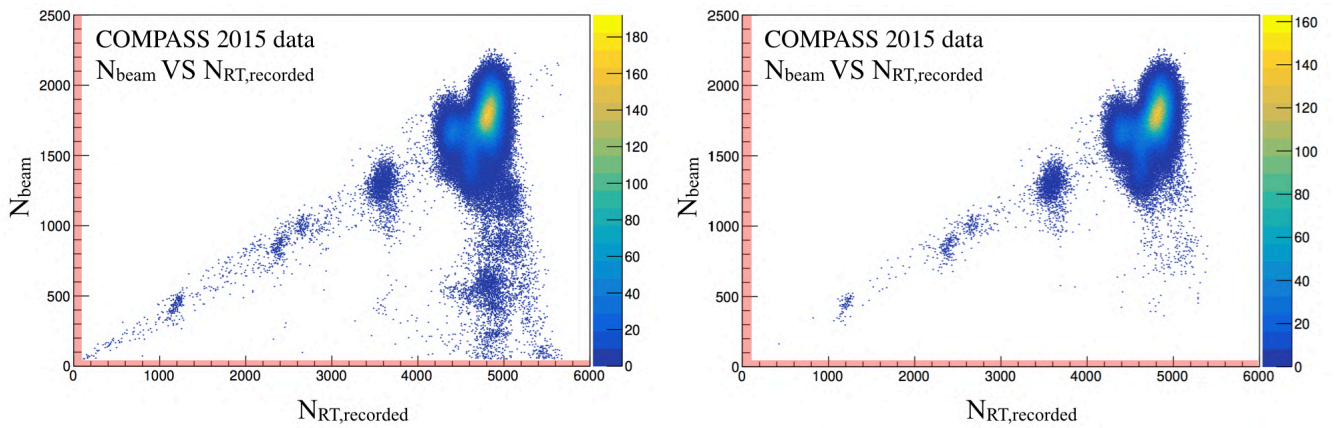


Figure 22.2: (a) Left: Spill distribution before apparatus stability selection, as a function of the number of beam from RT and the number of RT event in the spill ; (b) Right: Spill distribution after apparatus stability selection. The red bands are the rejected regions because of too low scaler or beam track rate

In Fig. 22.2b, the scalars show unexpected features, the presence of few local spots ($N_{RT,recorded} \sim 1200, 2500$ and 3500) seems to be correlated with a common DAQ effect, as both scalars are affected in the same way. This linear trend will be a further study using the DAQ deadtime information. In the region $4000 < N_{RT,recorded} < 5000$, various trends can be observed. This distribution was produced period by period to disentangle the structure, and find the origin of each effect.

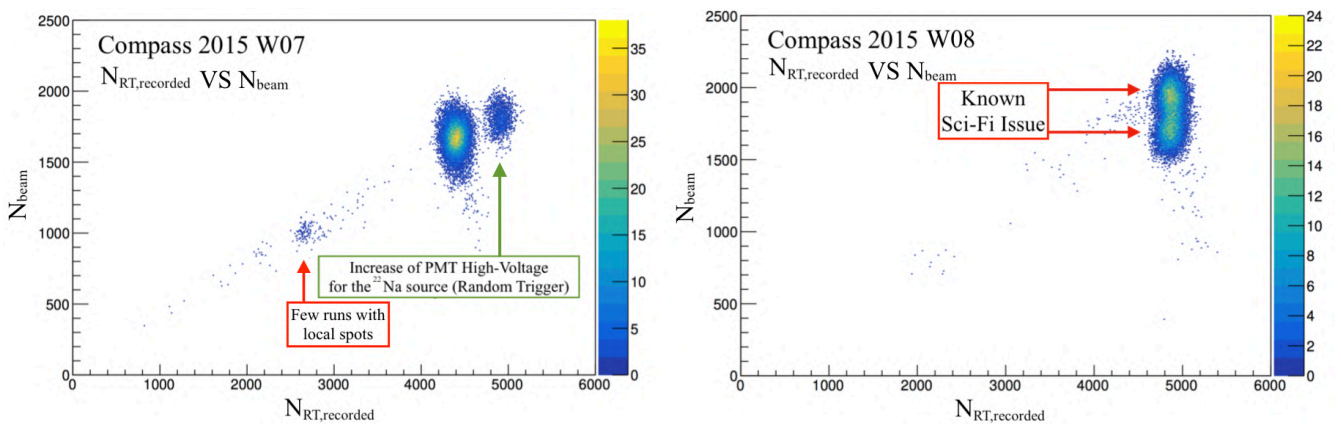


Figure 22.3: Spill distribution as a function of N_{beam} and $N_{RT,recorded}$ for W07 (left) and W08 periods (right)

In Fig. 22.3, the distribution of the W07 period shows a main spot at $N_{\text{RT,recorded}} \simeq 4500$. The local spot at $N_{\text{RT,recorded}} \simeq 5000$ corresponds to an increase of the PMT High-Voltage of the ^{22}Na source at the end of the period. In W08, an issue with the beam telescope station occurred and resulted in a decrease in the number of beam tracks. However, this effect cancels out in comparison to the physics events. Indeed, the reduced efficiency of the beam reconstruction affects both the physics data and flux measurement similarly, as discussed later in Ch. VI. Consequently, these data are kept in the analysis.

DAQ Stability. In Fig. 22.2, a clear linear trend is visible for $N_{\text{RT,recorded}} < 4000$. This effect can be isolated by looking at the correlation between DAQ deadtime from FLT and RT, as shown in Fig. 22.4. This correlation plot will be used to reject problematic spills outside of the blue band. The topology of these local spots were found to originate either of the two following hardware issues: some runs ending prematurely (Fig. 22.5a) or faulty NIM module issues (Fig. 22.5b).

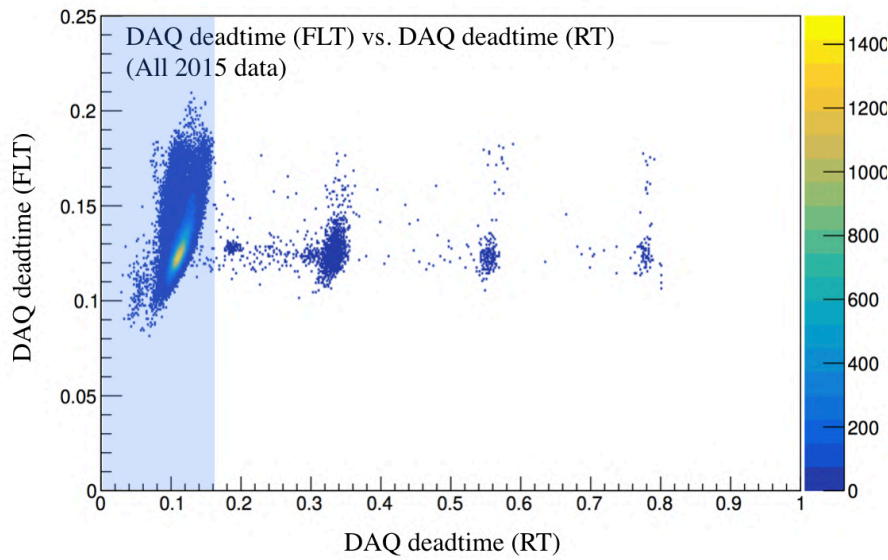


Figure 22.4: Correlation between DAQ deadtime from FLT and RT. This figure shows local spots at 32%, 55% and 78% to be disregarded. The blue band corresponds to a stable DAQ

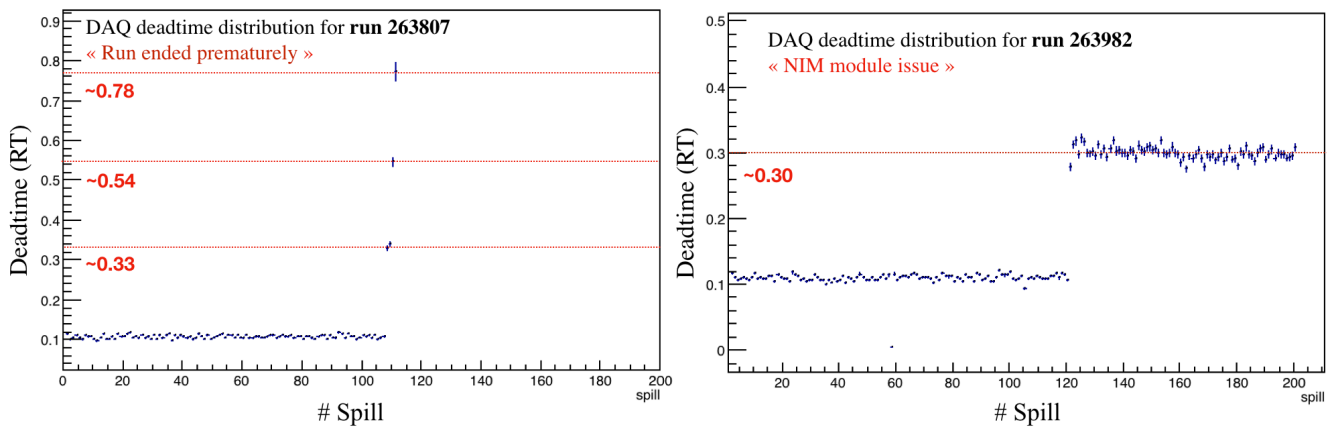


Figure 22.5: (a) Left: DAQ Deadtime as a function of the spill number (run 263807). An increase of the DAQ deadtime occurred due to a crash of the DAQ system. Data remained collected, however flux scalers were stacked; (b) Right: DAQ Deadtime as a function of the spill number (run 263982). A sudden increase of the DAQ deadtime is visible. This issue was identified as a dysfunctional NIM module in the DAQ chain.

22.2.2 Period by Period Analysis

The final flux distributions, period by period, are shown in Fig. 22.6. These distributions are compared with and without stability selections. These quality selections have an overall impact in low and high flux regions. In particular, the low tail below 1.50×10^8 is significantly reduced by accounting for the beam and apparatus stability. Additionally, the most stable periods in 2015 were W11, W12, and W13. Other periods present some double peaks distribution characteristic of unstable beam quality.

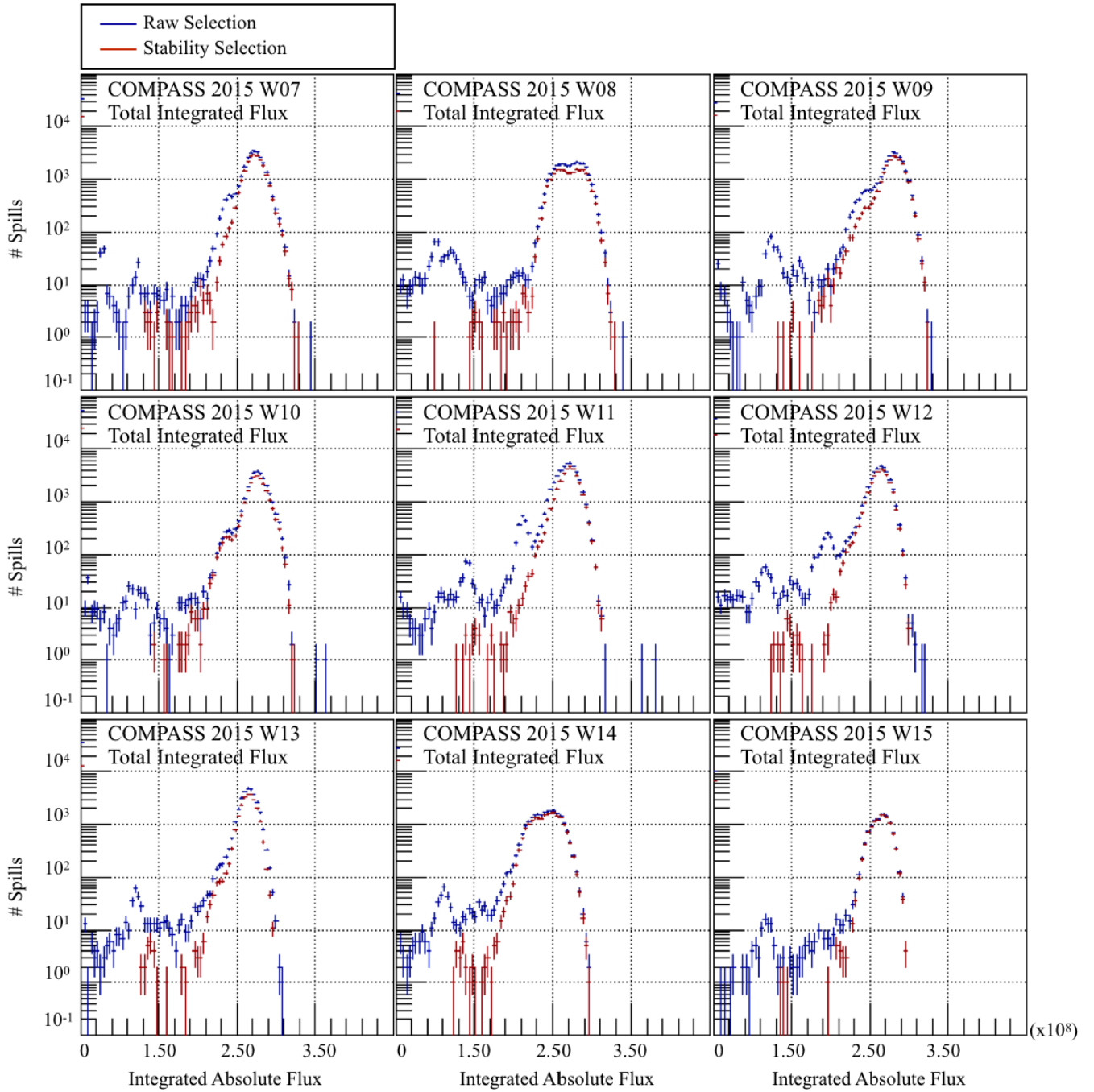


Figure 22.6: Overview of the flux stability, period by period, with (in red) and without (in blue) bad spill selection

Summary table and final flux distributions. The impact of the stability selection is integrated over 2015 and shown for beam flux in Fig. 22.7a. The impact of the beam stability in the cross-section as a function of the x_F is highlighted in Fig. 22.7b. Finally, Tab. 22.2 illustrates the impact of the selection, with the apparatus stability, beam stability, and both combined with respect to the initial number of selected events.

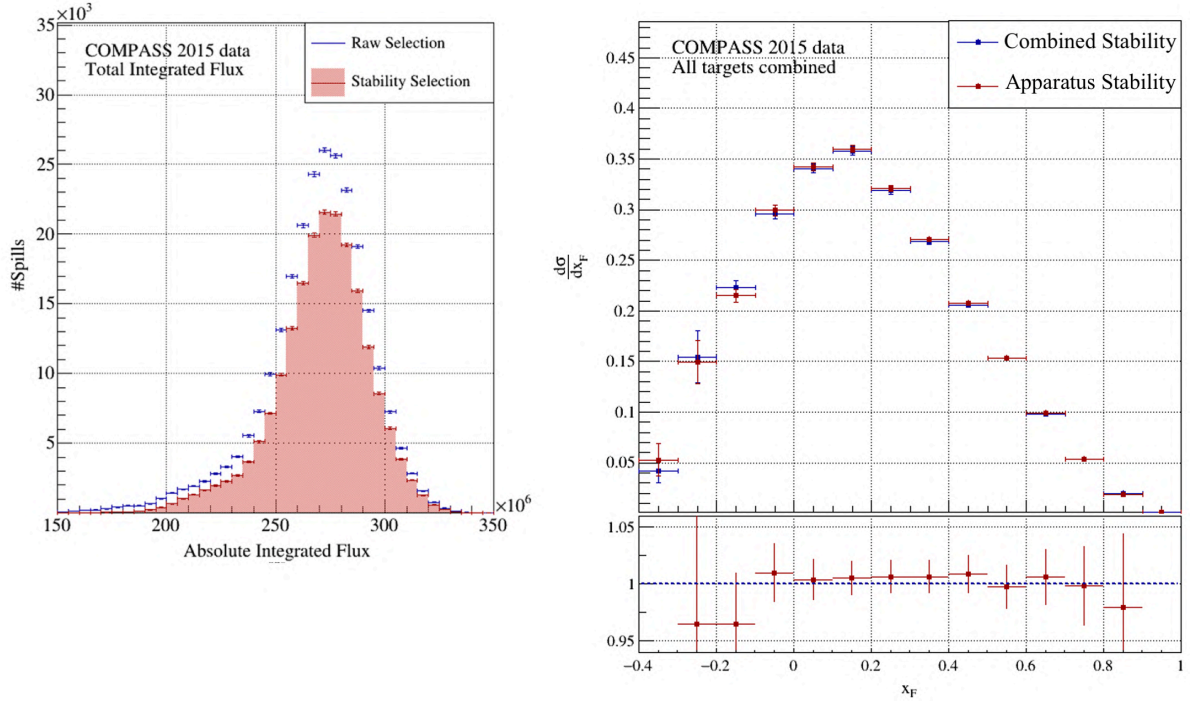


Figure 22.7: (a) Left: Absolute Integrated Flux distribution with (in red) and without (in blue) stability selection; (b) Right: Impact of the stability selection on the differential cross-section $d\sigma/dx_F$ as a function of x_F

Table 22.2: Summary table of stability studies in 2015 for a given dimuon events selection.

	Number of Selected Dimuon Events (Event ratio compared without list applied)			
Period	No List Applied	Beam Stability	Apparatus Stability	Combined Stability
W07	10645 evts (100%)	10253 evts (96.32%)	8755 evts (82.22%)	8496 evts (79.81%)
W08	10342 evts (100%)	10336 evts (99.94%)	8057 evts (77.90%)	8053 evts (77.87%)
W09	10869 evts (100%)	10808 evts (99.44%)	8965 evts (82.48%)	8914 evts (82.01%)
W10	11495 evts (100%)	11455 evts (99.65%)	9337 evts (81.23%)	9315 evts (81.03%)
W11	17300 evts (100%)	17236 evts (99.63%)	12787 evts (73.91%)	12751 evts (73.71%)
W12	13321 evts (100%)	13301 evts (99.85%)	11408 evts (85.64%)	11397 evts (85.55%)
W13	11572 evts (100%)	11534 evts (99.67%)	8984 evts (77.64%)	8951 evts (77.35%)
W14	7310 evts (100%)	7293 evts (99.76%)	6555 evts (89.67%)	6542 evts (89.49%)
W15	4306 evts (100%)	4297 evts (99.79%)	4148 evts (96.33%)	4141 evts (96.16%)
Total	97160 evts (100%)	96513 evts (99.33%)	78996 (81.31%)	78560 evts (80.85%)

22.3 Uncorrelated Background Events

22.3.1 Contextualization

A background increase on many detectors appeared at the end of the 2015 data taking and mainly affected the W14 period, as visible in Fig. 22.8a. It resulted in an increase of the DAQ deadtime due to the larger amount of background; this effect is illustrated in Fig. 22.8b. Following this study, a systematic uncertainty of 2-4% is added in the cross-section evaluation, depending on the kinematics.

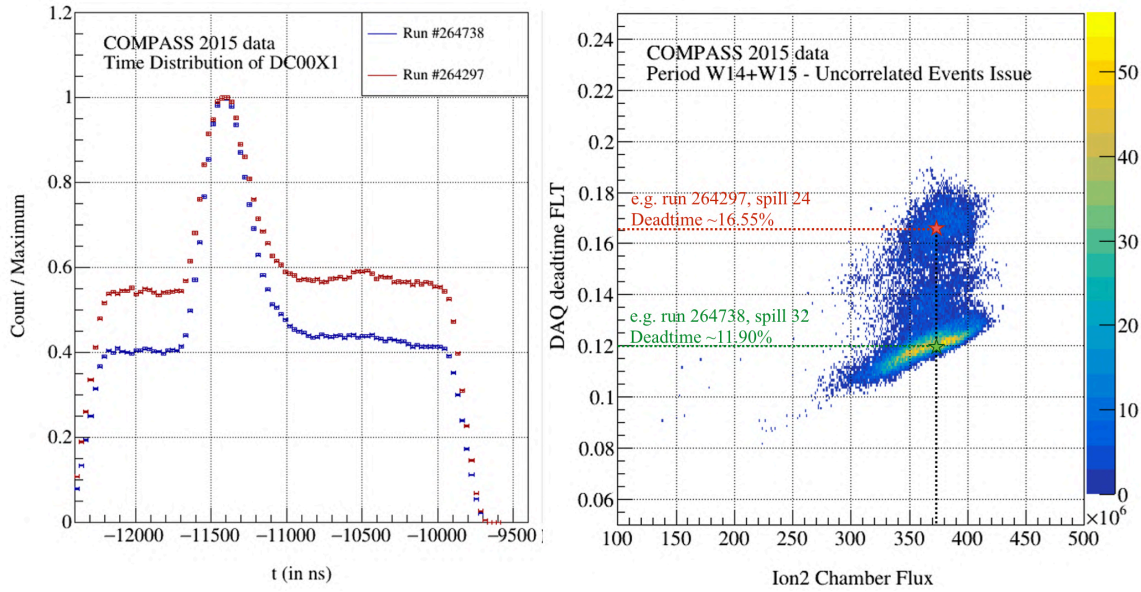


Figure 22.8: (a) Left: Illustration of the uncorrelated background in the time spectrum of the DC00X1 view; (b) Right: Distribution of the DAQ deadtime from FLT vs the ion2 chamber flux.

This increased background was thought to originate from a bad debunching. Consequently, the first step was to find the proper observable sensitive to beam debunching. The ion2 chamber scaler N_{ion2} , which is directly correlated to the beam, was found to be the most relevant, as shown in Fig. 22.9. Many trials were attempted to remove this uncorrelated background. Therefore, the most promising is introduced in the following.

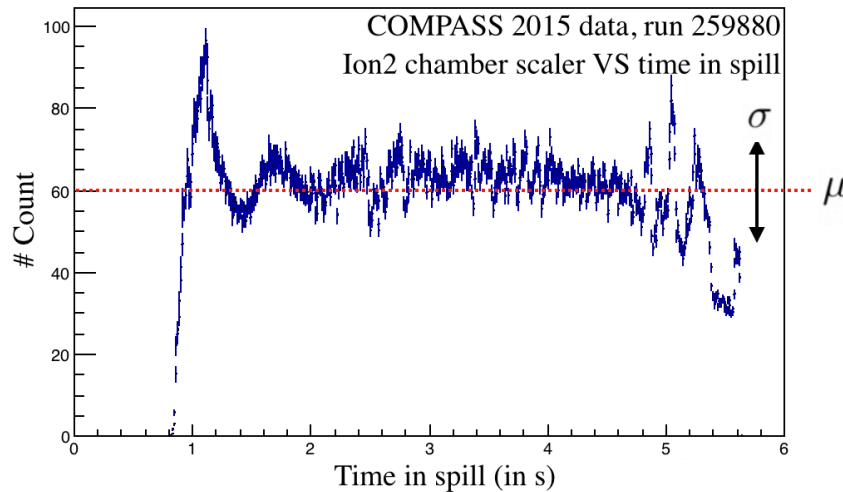


Figure 22.9: Example of the ion2 chamber flux profile (non-exhaustive) as a function of the time in spill (one single run, RT events)

22.3.2 Beam Structure Study

Fluctuations of the beam intensity in the cross-section are accounted by the flux correction. However, a quantification of the bad beam debunching is attempted using the variability of the distribution compared to the mean value. This quantity is introduced as the duty factor $d_f[T_0; T_1]$ in Eq. 22.1. The duty factor is defined in the range $[0;1]$. In case of a constant distribution, the duty factor becomes $d_f[T_0; T_1] = 1$.

$$d_f[T_0; T_1] = \frac{\langle n \rangle^2}{\langle n^2 \rangle} = \frac{\mu^2}{\mu^2 + \sigma^2} \quad (22.1)$$

where T_0, T_1 are the begin and end of spill respectively [s]

n is the number of event in a bin

μ is the mean of the distribution

σ is the standard deviation

Figure 22.10 shows the stability distribution of the duty factor as a function of the 2015 periods. It is clear the W07, W08, and W14 periods were especially unstable during the data taking. Unfortunately, there is no clear separation between ill and good spills. However, to evaluate the systematic error induced by the uncorrelated background, a duty factor restriction is temporarily applied in the analysis, $d_f[T_0; T_1] > 0.78$.

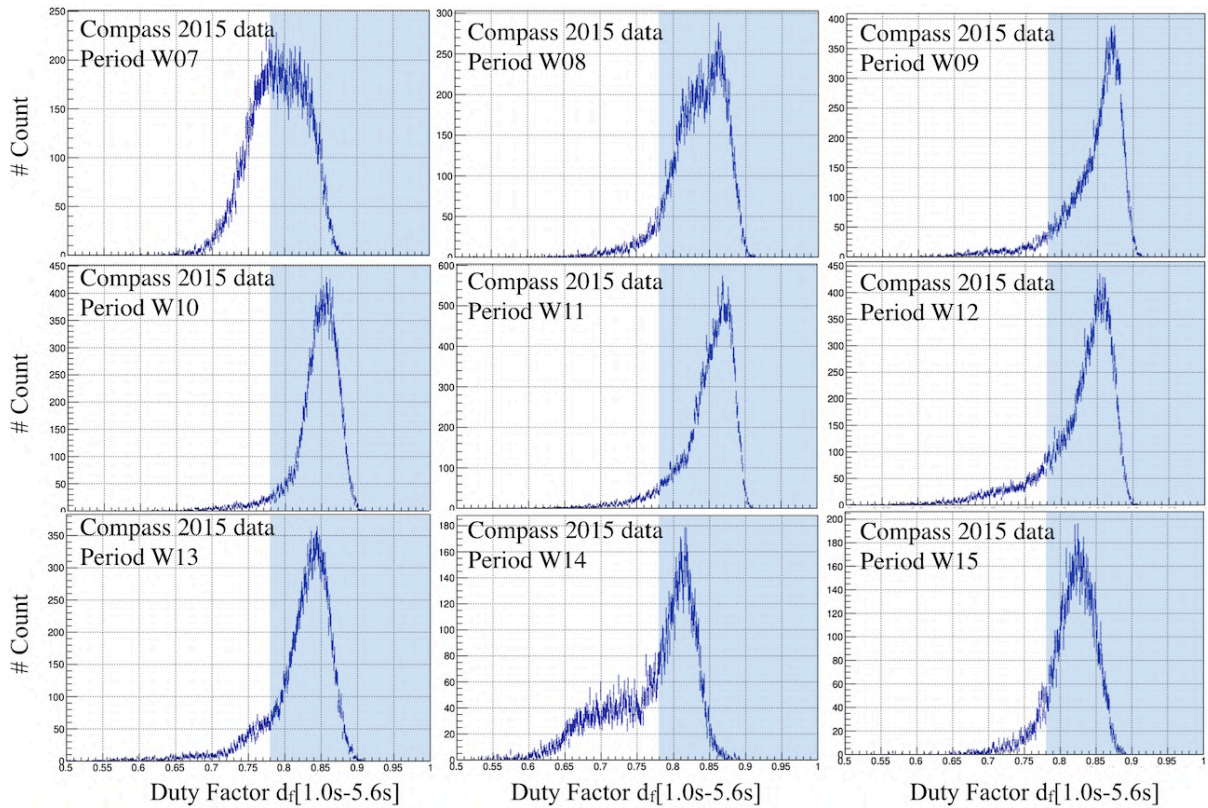


Figure 22.10: Distribution of the duty factor over 2015 data, sorted period by period. The blue band is the restricted area where beam fluctuations are minimized

The application of the duty factor cut removes most of the problematic spills, as shown in Fig. 22.11, but also rejects a significant amount of relevant statistics in the analysis. The impact at the level of

the cross-section is estimated in Fig. 22.12. The ratio plot highlights a modification of the cross-section distribution of about 4% at high x_F in the worst case. As no clear solution was found to reduce this background, the duty factor is applied in the limit of the beam stability studies. A systematic uncertainty of 2-4% will be quoted in the stability of the flux.

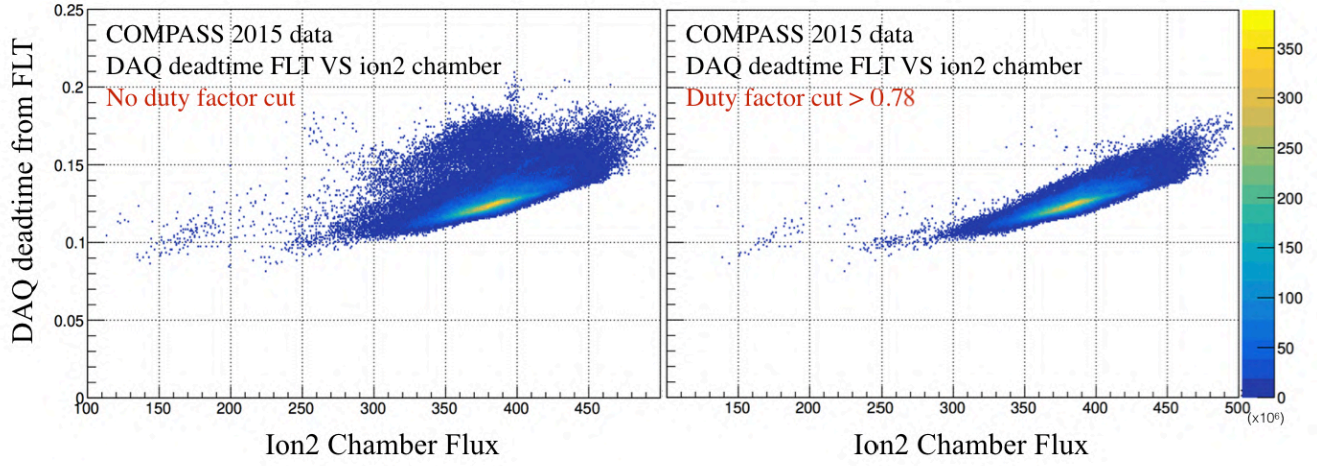


Figure 22.11: Comparison between the DAQ deadtime as a function of the ion2 chamber flux before (left) and after (right) applying the duty factor

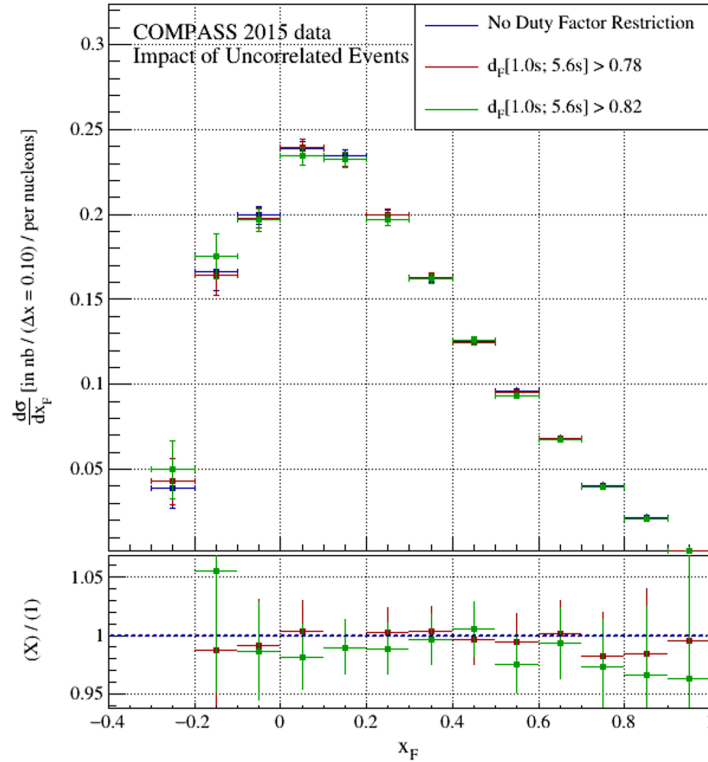


Figure 22.12: Cross-section as a function of x_F for several cuts on the duty factor

23 | Results: Systematic Uncertainties, Summary, Figure of Merit

The total uncertainty on the final cross-section is defined as the quadratic sum of the systematic uncertainties and the statistic uncertainty :

$$\sigma_{\text{tot}}^2 = (\sigma_{\text{sys.}}^2) + (\sigma_{\text{stat.}}^2) \quad (23.1)$$

The summary list of the systematic uncertainties attributed to the flux estimation is detailed in Tab. 23.1 and summarized as follows:

- **Packing Factor Measurement:** A systematic value is quoted to account for possible loss of material during the measurement.
- **DAQ Deadtime:** A systematic uncertainty due to the difference of deadtime extraction between the RT method and the FLT method is quoted.
- **Uncorrelated Background Events:** A difference in the final cross-section was observed from the too strict rejection of the combinatorial background using the duty factor.
- **Beam Contamination:** This systematic uncertainty was previously introduced in Tab. 5.1 (Sec. 5, Ch. II). This systematic refers to the percentage of impurity compared to the π^- contribution, as measured by Atherton et al. [89]. Finally, the contamination of a 190-GeV π^- beam is expected to be about 3% from this table.
- **Beam Absorption:** The beam absorption is estimated with both the MC approach and the naive calculation. This estimation shows a slope target by target, which differs by 2%, 2%, 0.5%, 2% for each target, respectively. These uncertainties are squared-summed as a function of Z_{vtx} and taken into account in the systematic uncertainty table.

Table 23.1: Summary table of the systematic uncertainties associated to the luminosity in 2015

	Uncertainty σ_i target by target			
Systematic uncertainties	PT Cell 1	PT Cell 2	Al	W (10 cm)
Packing Factor Measurement	0.5%	0.5%	–	–
DAQ Deadtime	1%			
Uncorrelated Background Events	4%			
Pion Beam Contamination	5%			
Beam Absorption	2%	3%	3%	4%
Total uncertainty	7%	7%	7%	8%

This chapter introduced the method used to compute the COMPASS 2015 flux and target density. Various selections, tests and systematic studies were performed and led to the determination of the integrated luminosity of each target (including flux attenuation and data inhibition) over 1808 non-empty runs (203 095 spills) :

- PT Cell 1: $\mathcal{L}_1 = 0.7646 \text{ fb}^{-1}$
- PT Cell 2: $\mathcal{L}_2 = 0.4868 \text{ fb}^{-1}$
- Aluminum: $\mathcal{L}_3 = 0.2134 \text{ fb}^{-1}$
- Tungsten (First 10 cm): $\mathcal{L}_4 = 1.8951 \text{ fb}^{-1}$

These values may also be converted in terms of instantaneous luminosities:

- PT Cell 1: $L_1 = 0.8184 \times 10^{-6} \text{ fb}^{-1}/\text{s}$
- PT Cell 2: $L_2 = 0.5211 \times 10^{-6} \text{ fb}^{-1}/\text{s}$
- Aluminum: $L_3 = 0.2284 \times 10^{-6} \text{ fb}^{-1}/\text{s}$
- Tungsten (First 10 cm): $L_4 = 1.3395 \times 10^{-6} \text{ fb}^{-1}/\text{s}$

The figure of merit (Fig. 23.1) shows the total integrated pion-nucleon luminosity recorded for each COMPASS 2015 target as a function of the period. These distributions account for deadtimes, beam attenuation and stability selection.

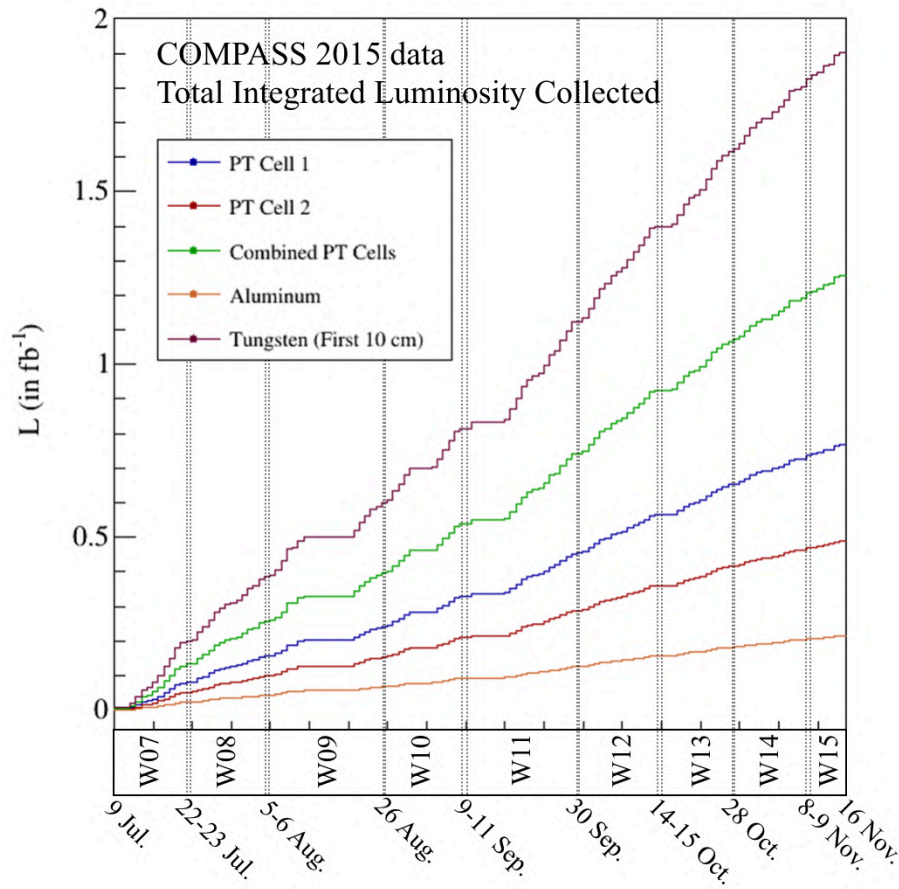


Figure 23.1: Total Integrated Pion-Nucleon Luminosity Collected for COMPASS targets in 2015

Chapter VI

Measurement of Drell-Yan Cross-Sections

24 Presentation of the 2015 Data Set	114
24.1 Data Taking Conditions	114
24.2 Event Selection	115
24.3 Additional Studies	119
24.3.1 Period Compatibility	119
24.3.2 Dimuon Data Yield	119
24.3.3 Combinatorial Background Estimation	121
24.3.4 Target Tomography and Beam Positioning	122
24.4 Drell-Yan Kinematic Distributions	124
25 Acceptance Correction	126
25.1 Introduction	126
25.2 Event Generation	127
25.3 Spectrometer Acceptance	130
25.3.1 Geometrical Acceptance	130
25.3.2 Event Migration and Detector Inefficiencies	131
25.3.3 Trigger System Efficiency	134
25.3.4 Overcorrection of the Beam Telescope Acceptance	137
25.4 Multi-Dimensional Acceptance	138
25.5 Model-Dependent Uncertainties	141
26 Introduction to the Absolute Drell-Yan Cross-Sections	145
26.1 The Drell-Yan Cross-Section Per Nucleon	145
26.2 Perturbative QCD Predictions at NNLO	145
26.2.1 Parton Level Monte Carlo, DYNNLO	145
26.2.2 Drell-Yan Predictions at COMPASS energy ($\sqrt{s} = 18.90$ GeV)	146
26.3 Discussion on the Single Differential Cross-Sections $d\sigma/dx_F$	149
26.4 Summary of the Final Uncertainties	150
27 Results: Extraction of the Drell-Yan 2015 Cross-Sections	151
27.1 Study of the Double Differential Drell-Yan Cross-Sections	151
27.1.1 Comparison with E615 data and DYNNLO simulation	151
27.1.2 Cross-Section $d^2\sigma/d\sqrt{\tau}dx_F$ in the COMPASS Kinematic Range	155
27.1.3 Summary Table	156
27.2 A-Dependence in Pion-Nucleus Interactions	158
27.2.1 Evaluation of the α parameter	158
27.2.2 Summary Table	160
27.3 Drell-Yan Cross-Sections at High- q_T	161
27.3.1 Transverse Momentum Distributions	161
27.3.2 The <i>Kaplan Form</i> : <i>Ad-Hoc</i> Fitting Function	161
27.3.3 Studies as a function of x_F , $M_{\mu\mu}$, \sqrt{s}	162
27.3.4 Invariant Cross-Sections at High- q_T , $Ed^3\sigma/dq^3$	164
27.3.5 Summary Table	166
27.4 Invariant Double Drell-Yan Cross-Sections $M^2 d^2\sigma/dx_1 dx_2$	168
27.4.1 Motivations	168

24 | Presentation of the 2015 Data Set

The 2015 data set used in the analysis corresponds to the nine periods introduced in Ch. IV and tagged as slot-1 (s1) production. Previous large scale test productions were named t1, t2, t3 productions. In comparison with last test productions, several improvements were made in the s1 production: the beam track reconstruction algorithm was improved (Appendix E), and the alignment of the spectrometer was updated.

24.1 Data Taking Conditions

The 2015 Polarized Drell-Yan data taking took place between July 8th and November 12th. This data taking follows the 2014 pilot Drell-Yan run, which was dedicated to the commissioning of the spectrometer and the data acquisition system.

In 2015, data were collected for the first time using two transversely polarized targets to measure transverse spin asymmetries, such as the Sivers asymmetry. The data taking was relatively stable. Although, such a high intensity hadron beam about 6×10^7 hadrons/s was used for the first time during a full data taking year. Finally, a new large area drift chamber detector, namely DC05, was placed in the spectrometer downstream of SM1. This detector was used to improve the reconstruction in the SAS region. Tab. 24.1 shows the data taking partitioned into periods and sub-periods of alternated polarization.

Table 24.1: Summary of the 2015 data (slot-1), including the spin polarization information. A vertical arrows $\uparrow\downarrow$ illustrate the orientation of the proton spin for each cell respectively.

Period	Subperiod	Date	Run Numbers	Polarization
W07	SP1	Jul 9 - Jul 15	259363 - 259677	$\downarrow\uparrow$
W07	SP2	Jul 15 - Jul 22	259744 - 260016	$\uparrow\downarrow$
W08	SP1	Jul 23 - Jul 29	260074 - 260264	$\uparrow\downarrow$
W08	SP2	Jul 29 - Aug 5	260317 - 260565	$\downarrow\uparrow$
W09	SP1	Aug 6 - Aug 12	260627 - 260852	$\downarrow\uparrow$
W09	SP2	Aug 12 - Aug 26	260895 - 261496	$\uparrow\downarrow$
W10	SP1	Aug 26 - Sep 1	261515 - 261761	$\uparrow\downarrow$
W10	SP2	Sep 4 - Sep 9	261970 - 262221	$\downarrow\uparrow$
W11	SP1	Sep 11 - Sep 22	262370 - 262772	$\downarrow\uparrow$
W11	SP2	Sep 23 - Sep 30	262831 - 263090	$\uparrow\downarrow$
W12	SP1	Sep 30 - Oct 7	263143 - 263347	$\uparrow\downarrow$
W12	SP2	Oct 8 - Oct 14	263386 - 263603	$\downarrow\uparrow$
W13	SP1	Oct 15 - Oct 21	263655 - 263853	$\downarrow\uparrow$
W13	SP2	Oct 22 - Oct 28	263926 - 264134	$\uparrow\downarrow$
W14	SP1	Oct 28 - Nov 2	264170 - 264330	$\uparrow\downarrow$
W14	SP2	Nov 4 - Nov 8	264429 - 264562	$\downarrow\uparrow$
W15	SP1	Nov 9 - Nov 11	264619 - 264672	$\downarrow\uparrow$
W15	SP2	Nov 12 - Nov 16	264736 - 264857	$\uparrow\downarrow$

24.2 Event Selection

For the purpose of the Drell-Yan process study, the initial data set requires to be reduced due to the large amount of reconstructed events, but also filtered out to only select the relevant pairs for the final analysis.

24.2.1 Data Reduction

First, the large number of 2015 reconstructed events in the mDST, which also includes single muon tracks, has to be reduced to spare computing resources. Consequently, only events fulfilling the following criteria are kept in the analysis:

- All events with at least one muon pair ($X/X_0 > 15$) attached to a vertex, regardless of their charges.
- All true random trigger events.

The purpose of these criteria is to keep only events, which might be potentially tagged as a Drell-Yan event latter in the analysis. As an example, all events with only single muon tracks are consequently removed. However, some specific triggers are also kept to perform flux analysis.

This reduction step considerably shrinks the amount of data and consequently reduces the computing time. Following this step, the events are stored into a file called μ DSTs. A complete table of the μ DST reduction was shown in Tab. 17.1 in Ch. IV.

24.2.2 Trigger Selection

The detection of muon pairs is performed using the LAST \otimes LAST and OT \otimes LAST triggers. The MT \otimes LAST flag is not required in this analysis due to the significant contamination of the trigger with high momentum muons, originating from the decay of π^- and K^- composing the hadron beam. However, one can note that the MT \otimes LAST events are not vetoed either.

24.2.3 Primary Vertex Selection

The primary vertex is defined by an incoming beam track with at least one outgoing muon pair. Each event contains a so-called, Best Primary Vertex (BPV), which is defined as follows :

- The vertex with the highest outgoing track multiplicity, after removal of the beam decay muons, is considered as the best.
- In case of multiple primary vertices with the same multiplicity, only the primary vertex containing the muons firing hodoscopes is considered.
- Finally, in case of ambiguity, space and time χ^2 attached to the vertex are computed. The smallest reduced χ^2 is then used as the best primary vertex to resolve the ambiguity.

A combinatorial approach is performed to define the candidate pairs to be used in the dimuon event selection. Among the combination of all muons with common primary vertex, the pairs with the best primary vertex are first selected. If it is not included in the list of common primary vertex, the vertex with the reduced χ^2 closest to one is selected. Its attached muon pairs are then tagged as candidate pairs.

24.2.4 Final Dimuon Event Selection

A dimuon event selection is applied following the triggers and vertex pre-selection. This event selection has been determined and tested over several months using both test productions and the most recent slot-1 production. The candidate muons are required to fulfill the Drell-Yan quality selection in Tab. 24.2.

Table 24.2: The selection criteria of dimuons for dy2015 slot-1 production.

Initial Pre-Selections
Dimuon Trigger Selection : LASTxLAST or LASTxOT
Best Primary Vertex Selection
Oppositely Charged Muon Pairs
Drell-Yan Event Selection
(1) Dimuon mass $M_{\mu\mu}$ must be in the High Mass Drell-Yan (HMDY): $4.3 < M_{\mu\mu}/(\text{GeV}/c^2) < 8.5$
(2) The first measured point of each muon must be upstream of SM1 : $Z_{\text{first}} < 300 \text{ cm}$
(3) The last measured point of each muon must be downstream MF1 : $Z_{\text{last}} > 1500 \text{ cm}$
(4) Time difference between muons must be between $\pm 5 \text{ ns}$: $ t_{\mu^-} - t_{\mu^+} < 5 \text{ ns}$.
(5) Muon track χ^2 must be below 10 to ensure good track reconstructions : $\chi^2_{\text{track}}/n.d.f. \leq 10$
(6) Trigger validation (pointing to hodoscope).
(7) ($0 < x_\pi < 1$), ($0 < x_N < 1$) to be restricted within their physical range and $(-0.2 < x_F < 0.9)$ due to limited acceptance.
(8) Good spill selection: Beam and Apparatus stability list
(9) Time in the spill selection : $1 \text{ s} < t_{\text{spill}} < 5.6 \text{ s}$
(10) Beam meantime restriction: $ t_{\text{beam}} < 3 \text{ ns}$
(11) Beam-muon tracks correlation: $ t_{\text{beam}} - t_{\mu\pm} < 2 \text{ ns}$
(12) Beam decay muon rejection: ($ P _{\mu\pm} > 7$ and $ P _{\mu+} < 180 - P _{\mu-}$) and $0.2 \times \theta_{\mu+} < \theta_{\mu-} < 5.0 \times \theta_{\mu+}$)
Target Selection
Only for PT Cell 1:
(13) A selection on the Z position of the vertex : $-294.5 < Z_{\text{vtx}}/(\text{cm}) < -239.3$
(14) Radial vertex selection : $R_{\text{vtx}} < 1.7 \text{ cm}$
(15) Cross the full upstream target setup (for attenuation purpose)
Only for PT Cell 2:
(13) $-219.5 < Z_{\text{vtx}}/(\text{cm}) < -164.3$
(14) $R_{\text{vtx}} < 1.7 \text{ cm}$
(15) Cross the full upstream target setup
Only for Aluminum target :
(13) $-63.5 < Z_{\text{vtx}}/(\text{cm}) < -56.5$
(14) $R_{\text{vtx}} < 1.7 \text{ cm}$
(15) Cross the full upstream target setup
Only for Tungsten target :
(13) $-30.0 < Z_{\text{vtx}}/(\text{cm}) < -20.0$ (for 10 cm) or $-30.0 < Z_{\text{vtx}}/(\text{cm}) < -10.0$ (for 20 cm)
(14) $R_{\text{vtx}} < 1.7 \text{ cm}$
(15) Cross the full upstream target setup

Further details for some selection criteria, defined in Tab. 24.2, are given hereafter :

- **Criterion (1)** : A dimuon mass $M_{\mu\mu}$ restriction is applied to keep, almost background free, dimuons originating from the Drell-Yan process. The precise mass range has been determined according to the contamination of all competing dimuon processes in Sec. 25.5.2.
- **Criterion (6)** : The trigger validation is a necessary check to ensure that the selected muon pair by combination has fired the expected dimuon trigger. First, it consists of extrapolating the muon tracks at the location of the fired hodoscopes and in verifying these tracks are within their acceptances.
- **Criterion (7)** : The x_1 and x_2 variables are restricted within their physical range. For some events, x_1 and x_2 values were found outside of this range due to large reconstruction uncertainty. These events were rejected. The x_F variable is restricted within -0.2 and 0.9 because of acceptance coverage. This acceptance restriction is discussed later in Sec. 25.4.
- **Criterion (8)** : The good spill selection refers to the beam and apparatus stability list defined in Sec. 22 of the luminosity chapter.
- **Criterion (11)** : An additional time restriction between beam track and muon tracks is applied to the Drell-Yan event selection. This selection criterion reduces the mis-association between muons and uncorrelated beam tracks. Fig. 24.1 highlights the time correlation between muons and beam tracks. An uncorrelated background is visible and is rejected by applying this criterion. Additionally, one can note that such uncorrelated beam tracks are symptomatic of an additional dimuon background; this background is interpreted and reduced by criterion (12).

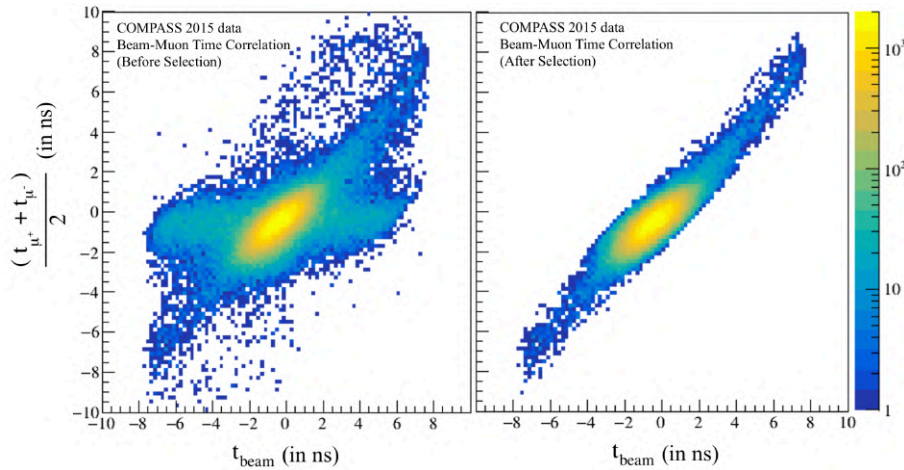


Figure 24.1: Time correlation between beam and muon tracks. This figure shows uncorrelated beam tracks associated with muon pairs before (left) and after (right) event rejection.

- **Criterion (12)** : The purpose of this selection criterion is to reject muons originating from the expected beam decay $\pi^- \rightarrow \mu^- \bar{\nu}_\mu$ as visible in Fig. 24.2 at large P_{μ^-} momentum (inclusive trigger). The momentum cut is not enough to remove this contamination. Consequently, a cut on the polar angle is also applied. The background due to beam decay muons contaminates mainly the MT \otimes LAST dimuon trigger (Fig. 24.3c). However, this selection is also applied to other dimuon triggers. Especially the OT \otimes LAST trigger owing of the overlap with MT \otimes LAST trigger.

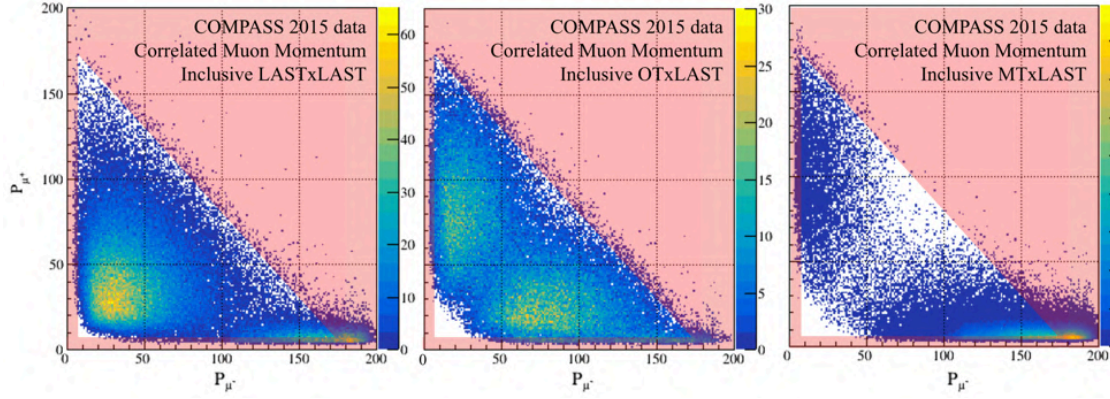


Figure 24.2: The red bands are the region rejected by the beam decay muon criterion; (a) Left: Distribution of correlated muon momenta for inclusive LAST \otimes LAST trigger; (b) Middle: Distribution of muon momenta for inclusive OT \otimes LAST trigger; (c) Right: Distribution of muon momenta for inclusive MT \otimes LAST and LAST \otimes LAST triggers

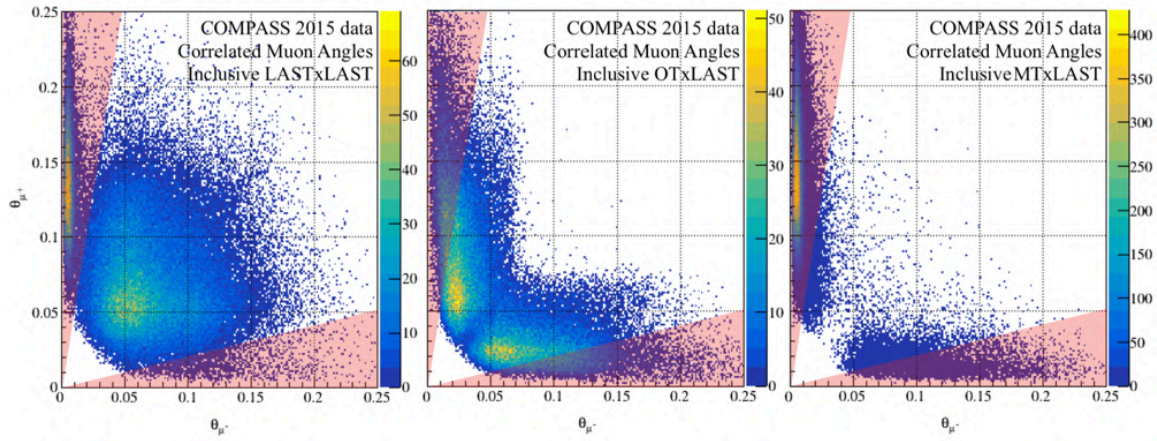


Figure 24.3: (a) Left: Correlated polar angle distribution of muons for inclusive LAST \otimes LAST trigger; (b) Middle: Correlated polar angle distribution of muons for inclusive OT \otimes LAST trigger; (c) Right: Correlated polar angle distribution of muons for inclusive MT \otimes LAST trigger

- **Criterion (14)** : A radial cut $R_{\text{vtx}} < 1.7$ cm is applied on the vertex distribution to only select events originating from the corresponding target region. Although the expected radius of the PT target is 1.9 cm, the choice of the cut is discussed in Sec. 24.3.4 to reduce systematic effects.
- **Criterion (15)** : A radial cut is also applied on the extrapolated beam tracks $R_{\text{trk}} < 1.7$ cm to the downstream face of the target. This radial cut ensures the beam track fully crossed the upstream targets and lost an energy corresponding to the attenuation profile determined in the MC.

Applying these selection criteria, the final dimuon pairs accounted in the physics analysis is given for each target in Tab. 24.3. Additionally, the precise number of dimuon pair selected is detailed step by step in Appendix F.

Table 24.3: Final statistics for each target after applying quality Drell-Yan pair selection

Target	$4.3 < M_{\mu\mu}/(\text{GeV}/c^2) < 8.5$
Polarized Target Cell 1	17,689 events
Polarized Target Cell 2	14,373 events
Aluminum	2,410 events
Tungsten – 10 cm	17,891 events

24.3 Additional Studies

Some additional studies using the Drell-Yan 2015 data are presented in this section to demonstrate the need of some previously introduced selection criteria, but also to verify the reliability of some corrective factors that will be used in the evaluation of the cross-section.

24.3.1 Period Compatibility

A check is performed to verify the compatibility between periods. This test consists of comparing the shape of distributions between periods of 2015 data, including the stability selection presented in Sec. 22, Ch. V. In this case, all Drell-Yan muon pairs originating from all targets in the range $4.3 < M_{\mu\mu}/(\text{GeV}/c^2) < 8.5$ are considered. Each distribution is normalized by its integral, and each bin is considered as a random variable X_n . The mean μ and the standard deviation σ associated to X_n are computed and the pull distribution defined as $Z_n = \frac{X_n - \mu}{\sigma}$. The central limit theorem ensures the Z_n variable tends towards a normal distribution, such as : $\lim_{n \rightarrow +\infty} Z_n = \mathcal{N}(0, 1)$.

Consequently, this verification led to the fit of the distributions presented in Fig. 24.4. This fit is performed using a single Gaussian shape, and the resulting mean and standard deviation of each variable are given in the figure. In this selected set of variables, each pull distribution is centered around zero, and the sigma of the pull distribution is close to one, in the limit of the 2015 statistics. Therefore, 2015 data are compatible between each period and will be combined on a yearly basis in the following.

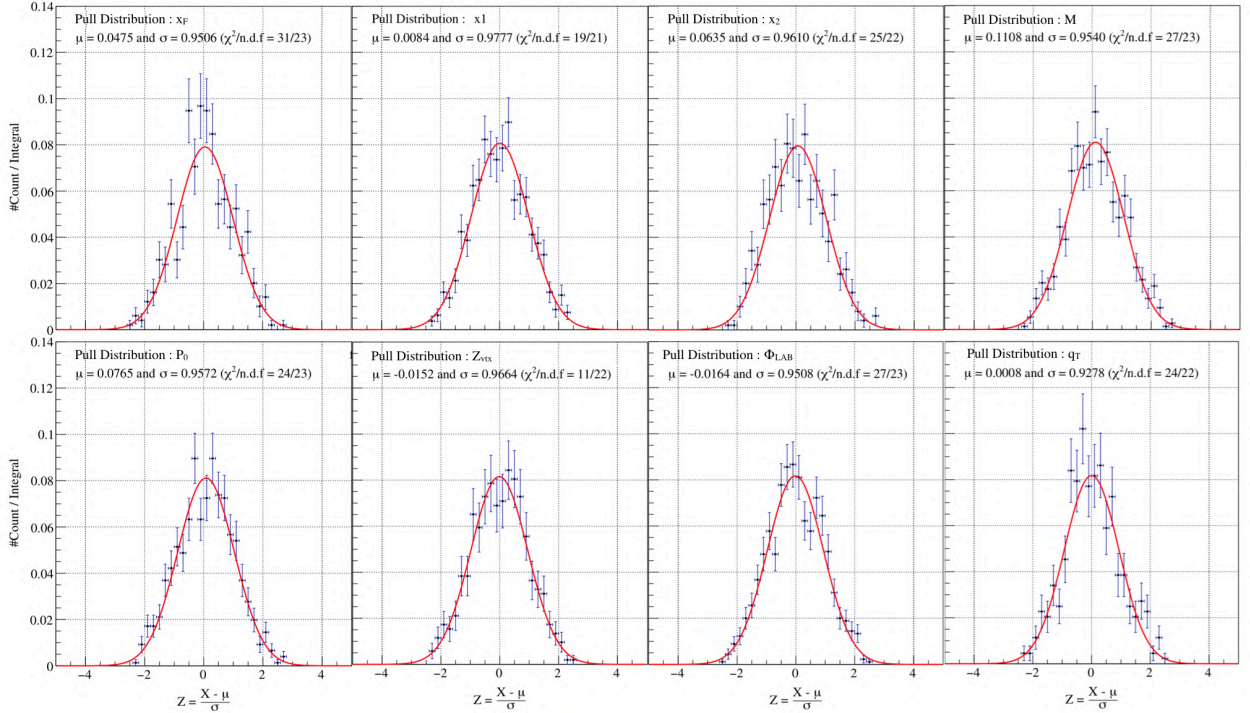


Figure 24.4: Pull distributions of the main variables x_F, x_1, x_2, M (dimuon mass), P_0 (μ^- momentum), Z_{vtx} , Φ_{LAB} and q_T ; The distribution are fit with a single Gaussian (in red). The parameters μ, σ of the Gaussian fit as well as the reduced χ^2 values are provided in the title of each plot.

24.3.2 Dimuon Data Yield

The dimuon data are renormalized by the beam flux determined in Ch. V to demonstrate the reliability of the flux extraction. In order to increase the statistics, the mass selection is relaxed to select any event with a dimuon mass larger than 2 GeV/c^2 . The selected dimuon data are shown in the top panel (Fig. 24.5a) as a function of the spill number. The resulting yield is computed on a spill by spill basis.

Three specific runs, namely 264466 (W14), 264467 (W14), 264738 (W15) have been selected to illustrate the impact of this correction. These three *golden runs* have been selected because of their specific beam flux profiles as shown in Fig. 24.5b:

- Run 264466 is a low intensity run with an average intensity of 1.8×10^8 hadrons per spill.
- Run 264467 shows a fluctuating intensity due to beam extraction issue from spill #290 to #310.
- Run 264738 is a typical high intensity run with an average intensity of 2.7×10^8 hadrons per spill.

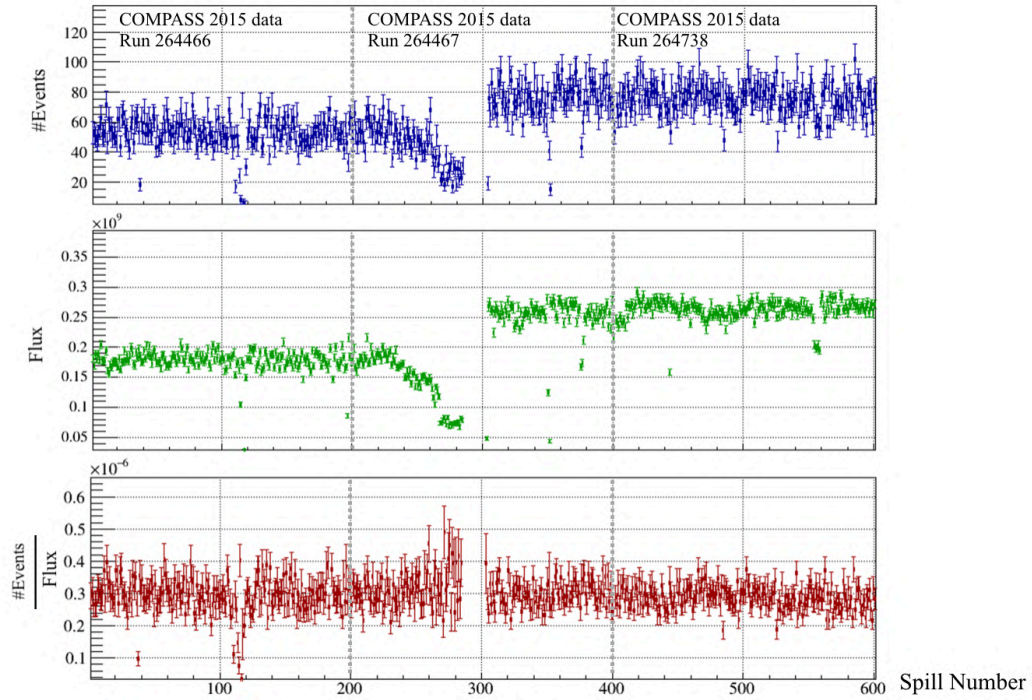


Figure 24.5: Resulting yield of data for three different runs in 2015. (a) Top: Dimuon events with a relaxed mass selection applied ($M_{\mu\mu} > 2 \text{ GeV}/c^2$); (b) Middle: Integrated flux over time in the spill as a function of the spill number; (c) Bottom: Yield of data, the flux dependence cancels out in the ratio.

A satisfying normalization is obtained in the bottom panel of Fig. 24.5c, especially for the run 264467, where the reduction of events can be explained by the variation of flux. Few spills with a low yield remain in the figure (spill #110, #113, #114, #116 in run 264466). However, these latter were identified as problematic due to the stability of the apparatus and consequently rejected from the analysis. Finally, the distribution is stable and shows a constant profile, also confirmed by the pull distribution Fig. 24.6.

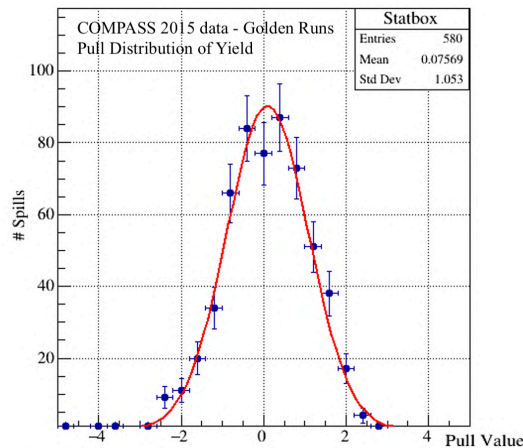


Figure 24.6: Pull distribution of the data yield for the three golden runs

24.3.3 Combinatorial Background Estimation

The total number of collected dimuon event $\langle N_{\mu^+\mu^-}^{\text{tot}} \rangle$ in the analysis has several origins. Muon pairs may originate from a dimuon production process $\langle N_{\mu^+\mu^-}^{\text{sig}} \rangle$, such as the Drell-Yan process, charmonium resonance, open-charm decay, or bottomonium resonance. However, an additional combinatorial background (CBKG) $\langle N_{\mu^+\mu^-}^{\text{cbkg}} \rangle$ of dimuon tracks can originate from combinations with uncorrelated single muons. As an example, these single muons may find their origin in π or K decays, or fake-positive reconstructed muons.

$$\langle N_{\mu^+\mu^-}^{\text{tot}} \rangle = \langle N_{\mu^+\mu^-}^{\text{sig}} \rangle + \langle N_{\mu^+\mu^-}^{\text{cbkg}} \rangle$$

The opposite sign combinatorial background $N_{\mu^+\mu^-}^{\text{cbkg}}$ can be determined, by assuming a symmetric acceptance in the detection of μ^+ and μ^- . The combinatorial background and its uncertainty is given by the following relations (details in Appendix H):

$$N_{\mu^+\mu^-}^{\text{cbkg}} = 2\sqrt{N_{\mu^+\mu^+}N_{\mu^-\mu^-}}$$

$$\Delta N_{\mu^+\mu^-}^{\text{cbkg}} = \sqrt{N_{\mu^+\mu^+} + N_{\mu^-\mu^-}}$$

From an experimental point of view, a method to obtain a symmetric acceptance is to apply the "image cut" requirement. It involves swapping the charge sign of each muon, and verifying the pairs are still in the acceptance of the fired hodoscope after extrapolation. The dimuon mass spectrum from 2 to 14 GeV/c^2 is shown after applying the image cut in Fig. 24.7. The combinatorial distribution decreases with the dimuon mass. This contamination from a combinatorial background in the HMDY¹ region is evaluated by about 0.11% of the total collected signal.

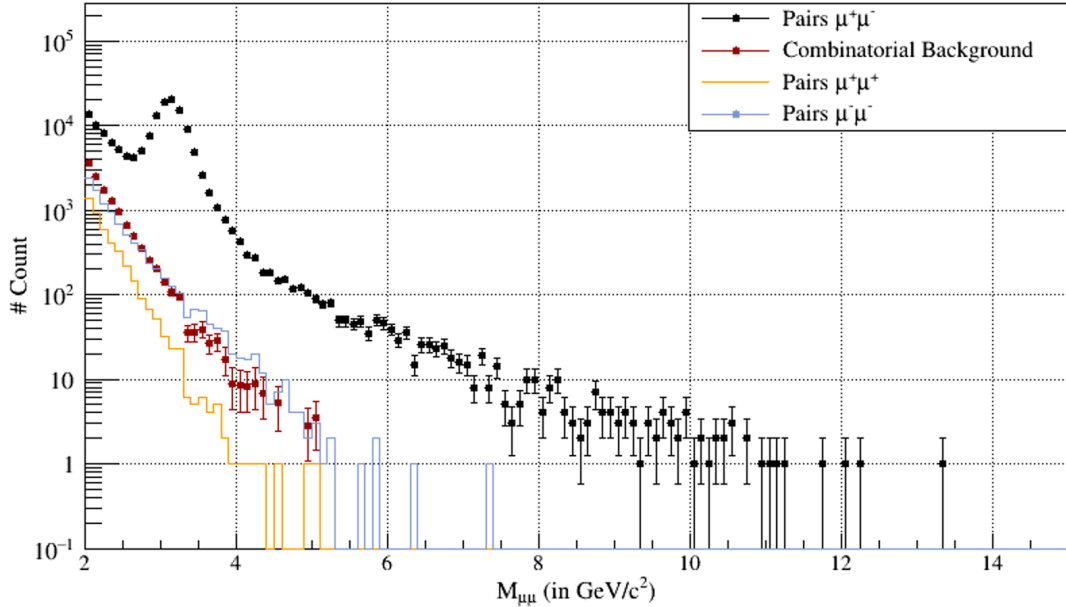


Figure 24.7: Dimuon mass spectrum for the combined PT cells from 2 GeV/c^2 for $\mu^-\mu^-$, $\mu^+\mu^+$ and $\mu^+\mu^-$ pairs and including the evaluating $N_{\mu^+\mu^-}^{\text{cbkg}}$ combinatorial background. The image cut is applied in this figure.

¹High Mass Drell-Yan

24.3.4 Target Tomography and Beam Positioning

The tomography of the target provides essential information about the quality of the selected dimuon events. This analysis consists of studying the transverse beam profile to different Z positions. These Z-abscissa refer to the upstream and downstream locations of each target, as shown in Fig. 24.8.

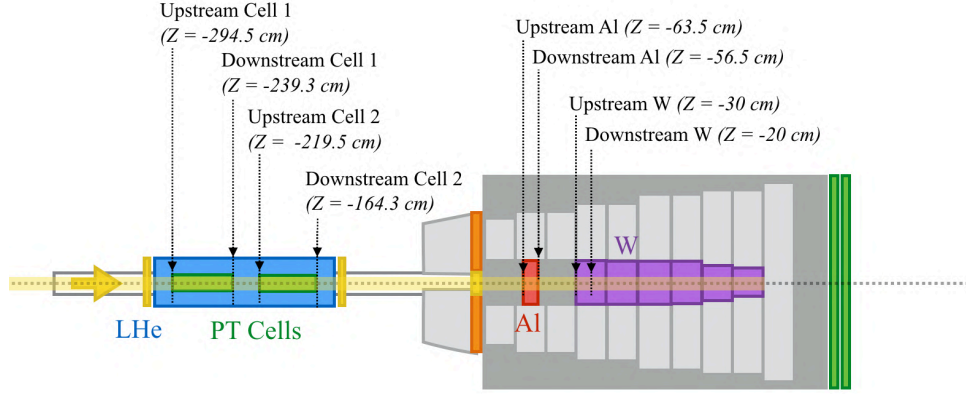


Figure 24.8: Illustration of the reference positions used for the tomography of the COMPASS target setup

The study of the target tomography is performed using a larger dimuon data sample made of muon pairs originating from the best primary vertex with a mass $M_{\mu\mu}$ larger than $3.0 \text{ GeV}/c^2$. All selection criteria introduced in Tab. 24.2 are applied, except the mass selection, the target selection, and the kinematic cuts. The beam tracks N_{track} attached to vertices are normalized by the real incoming flux \mathcal{F} , as estimated from Ch. V. This yield is computed in bins of X_{trk} and Y_{trk} to apply the proper correction and possibly highlight some contamination from the neighboring materials.

The aluminum and tungsten targets are a simple solid cylinder of material with a diameter larger than the beam size. Consequently, the positioning of the beam does not play a major role. Nonetheless, this is different for the hybrid targets, because the PT cells are about 2.0 cm radius, including the target holder, and 1.9 cm radius without. Although the beam radius has been enlarged to avoid overheating of the PT cells in 2015, it is still comparable to the target radius.

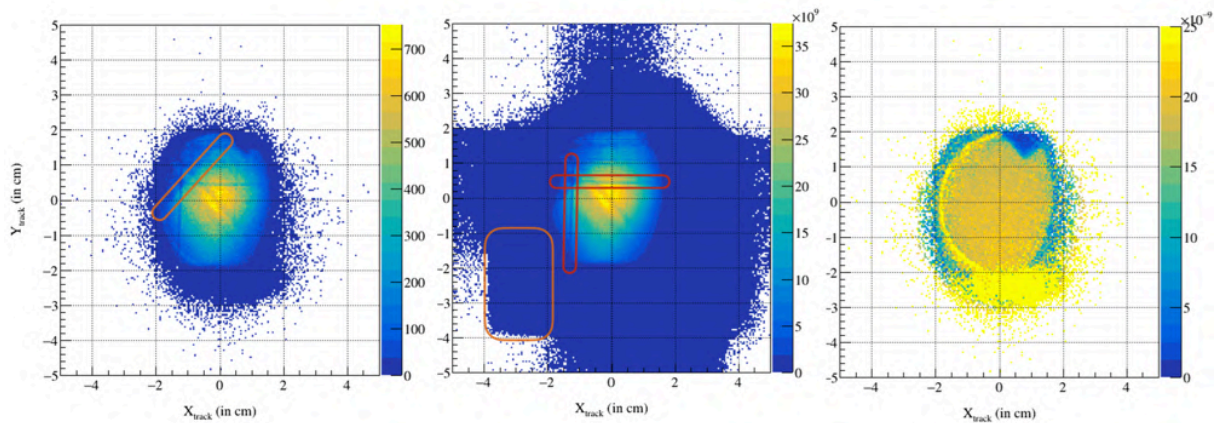


Figure 24.9: (a) Left: Number of beam tracks N_{track} , as a function of X_{track} and Y_{track} positioning, after extrapolation of the beam tracks to the upstream position of PT Cell 1; (b) Center: Flux profile \mathcal{F} ; (c) Right: Target yield $N_{\text{track}}/\mathcal{F}$; The limits of the acceptance of FI03 views are highlighted in orange and inefficient strips is highlighted in red

In Fig. 24.9, both (a) and (b) show vertical and horizontal lines, which are the signature of beam telescope inefficiencies (one is highlighted in red). Some of the physical edges of FI03 planes are visible

in orange. An example of the target yield is shown in Fig. 24.9c. Finally, a complete picture of the COMPASS 2015 target setup is shown in Fig. 24.10. This figure can be decomposed into the left-hand side, which shows the data yield without radial cut on the vertex position, and the right-hand side, which includes a radial cut ($R_{\text{vtx}} < 1.9$ cm) to match the theoretical position of the targets. Each couple of plot refers to the upstream and downstream projection of the beam tracks. Moreover, the *target axis* in the picture shows the yield as a function of each target.

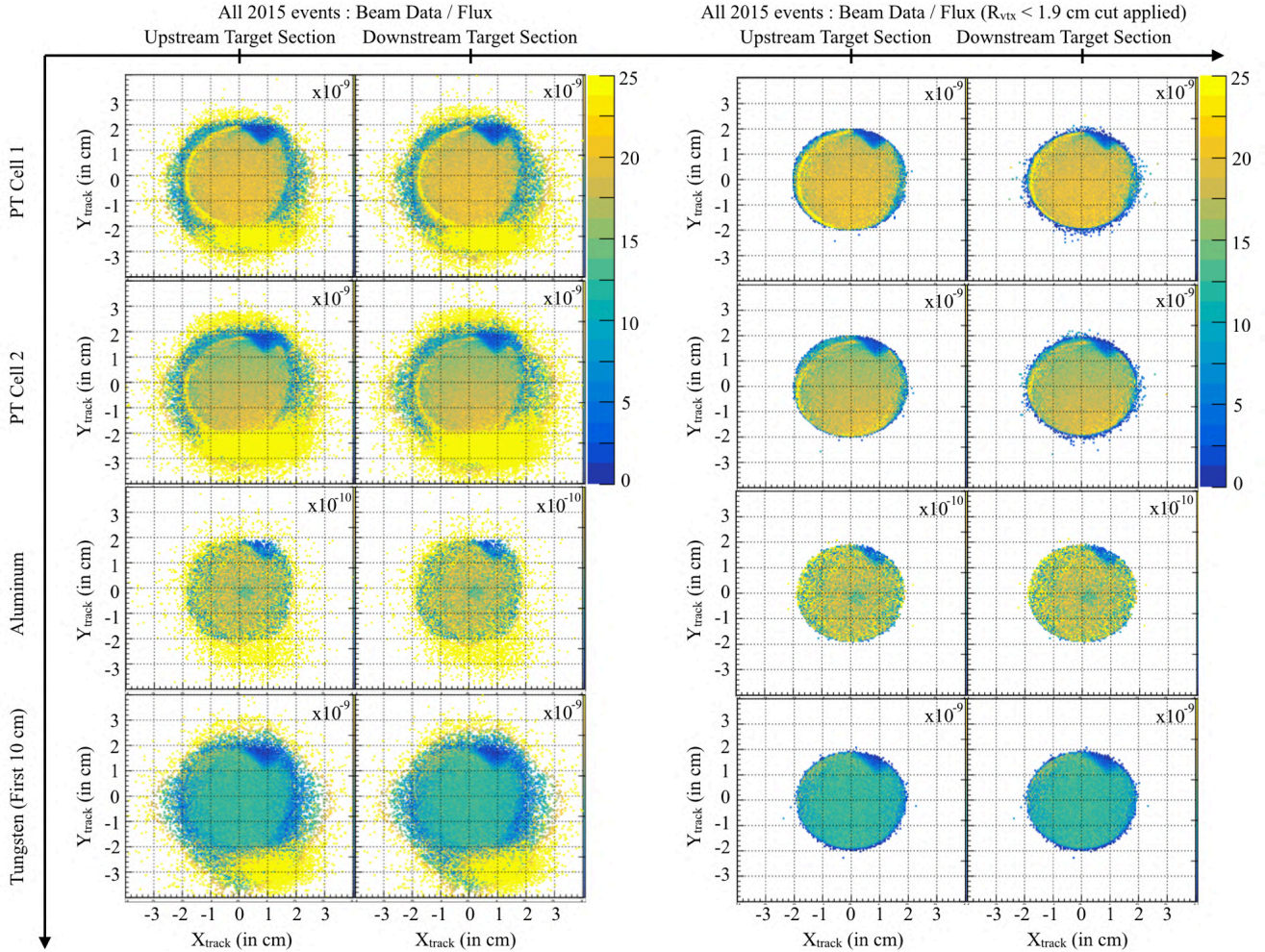


Figure 24.10: Complete overview of the target setup tomography with and without radial cut on the vertex position ($R_{\text{vtx}} < 1.9$ cm)

A possible target filling issue was already introduced in Sec. 20.2.3, Ch. V. However, the full picture of the target tomography confirms in the limit of the apparatus resolution, no clear evidence of a target filling issue.

Also, the dark blue spots cannot be tagged as missing material in the cells, as also visible in ^{27}Al and ^{184}W . Additionally, the limit of the target holder is visible in the picture of the PT cells in light yellow on the left side of the targets. Consequently, the contamination of these elements is evaluated by applying a tighter radial cut in the target selection. The impact of this new selection are presented in Fig. 24.11. Finally, the impact of the radial cut in the cross-section highlights an overall systematic effect of about 1% for the cells, as shown in their corresponding ratio plots. Therefore, a radial cut of 1.7 cm is chosen to reduce edge effects, and a systematic uncertainty about 2% will be quoted in the analysis.

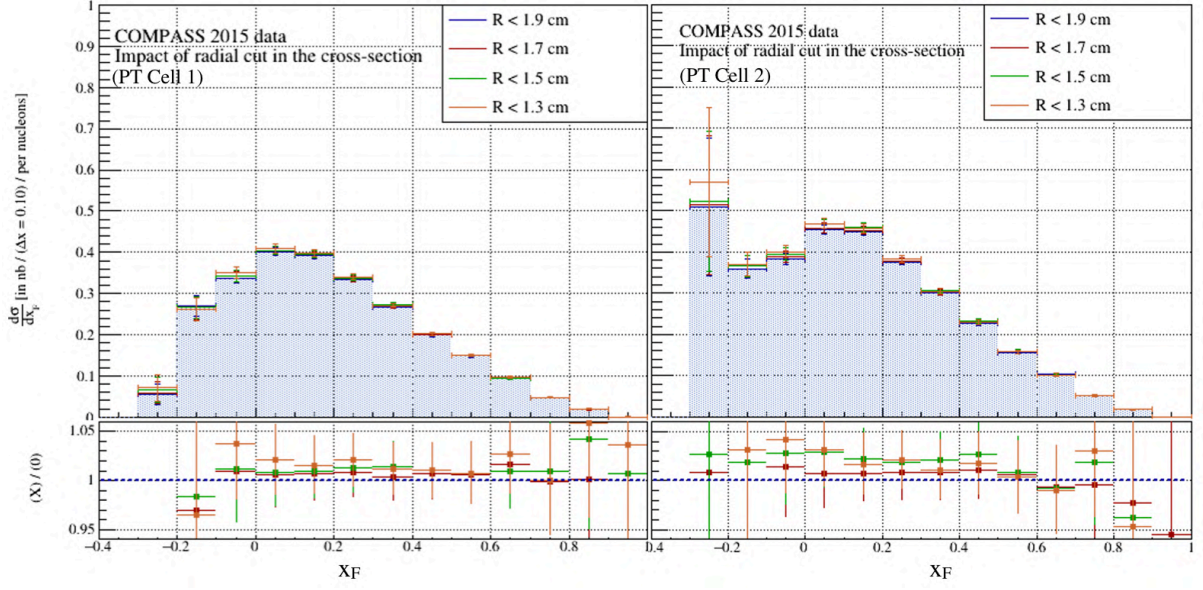


Figure 24.11: Differential Drell-Yan cross-section for cell 1 (left) and cell 2 (right) vs x_F , in the mass range $4.3 < M_{\mu\mu}/(\text{GeV}/c^2) < 8.5$, for several cuts on the target radius ranging from 1.3 cm to 1.9 cm; The ratio plots shows the comparisons with the radial cut of 1.9 cm.

24.4 Drell-Yan Kinematic Distributions

The kinematic region probed by the Drell-Yan 2015 data is shown in Fig. 24.12 (left) as a function of the x_1 and x_2 variables. This distribution presents a wide distribution between 0.1 and 1 for the x_1 variable, which gives the opportunity to study the internal structure of the beam PDF, as previously discussed in Ch. I. This variable is anti-correlated with x_2 : a large x_2 corresponds to the low x_1 region and vice-versa. In Fig. 24.12 (right), the region probed in Q^2 is shown as a function of x_2 . The lower mass region related to the study of the J/Ψ is also shown and probes a lower x_2 region compared to the high-mass Drell-Yan.

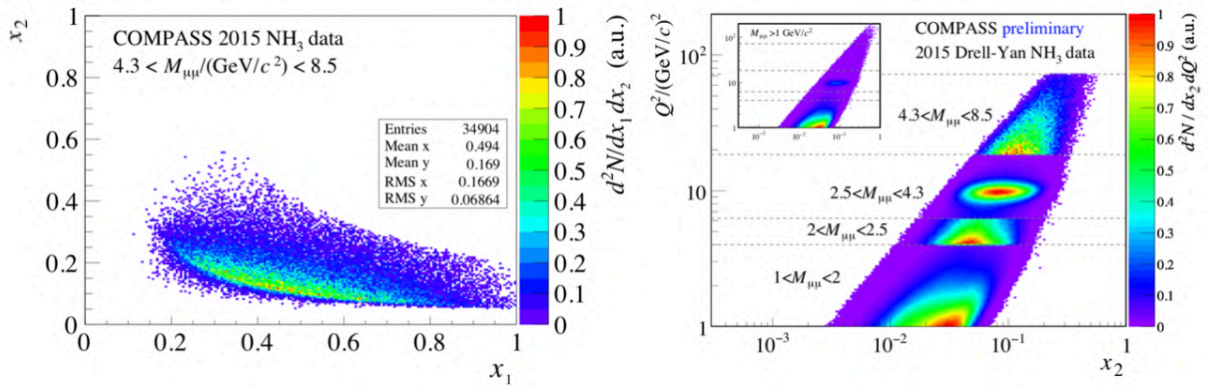


Figure 24.12: Overview of the Drell-Yan kinematic distributions from the COMPASS 2015 data as a function of x_1 and x_2 (left) and as a function of x_2 and Q^2 (right)

Finally, Fig. 24.13 presented hereafter shows the kinematic distributions of the four different targets. All targets are shown with a mass cut between $4.3 \text{ GeV}/c^2$ and $8.5 \text{ GeV}/c^2$. Moreover, the Z_{vtx} distribution in Fig. 24.13a is a representation of the raw rate of events along the beam propagation axis. A decrease of the intensity due to absorption results in a drop of the event rate from the first to the second cell. Despite this attenuation of the beam, the tungsten induces a much larger rate compared to other targets. A complete picture of the correlation between variables is also shown in Fig. 24.14.

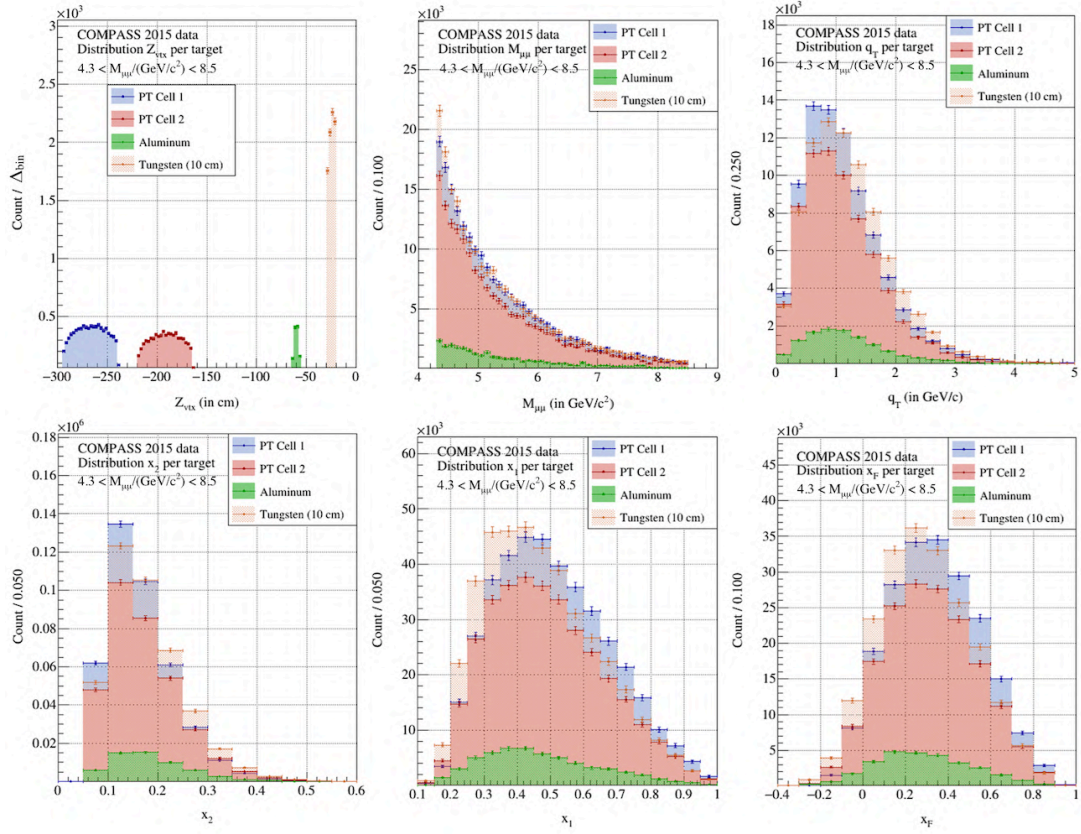


Figure 24.13: Overview of the Drell-Yan kinematic distributions from the COMPASS 2015 data.

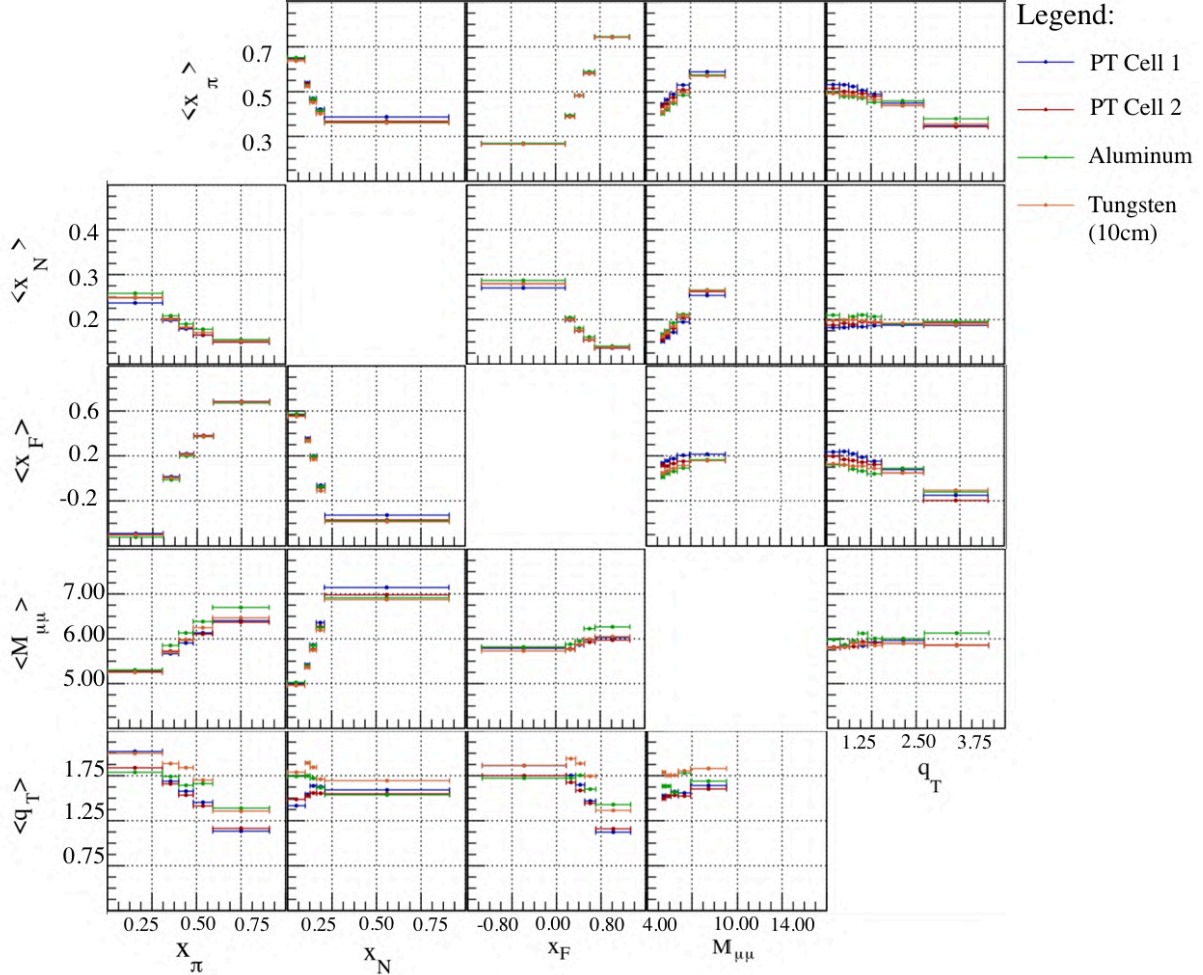


Figure 24.14: Overview of the correlation between reconstructed kinematic variables.

25 | Acceptance Correction

25.1 Introduction

The determination of the acceptance correction factor ε is an important step in the determination of the cross-section. The final corrective factor ε can be subdivided into two terms: a geometrical acceptance term \mathcal{A} and a second term related to detector efficiency. Using this acceptance factor, the experimental data are corrected for the following effects:

- The geometrical acceptance of the spectrometer (tracking detectors and triggers)
- Hardware inefficiencies of tracking detector and trigger system.
- Inefficiencies of the COMPASS tracking software and mis-associations of vertices to a muon pairs.
- Event migration effects due to the finite precision of the spectrometer reconstruction

The corrective factor ε is determined using a MC simulation of the experiment as follows. The π^- beam particles are parametrized (momentum, energy, position) thanks to a TGEANT beam file (Sec. 14.3, Ch. IV). The generated beam track is propagated through the setup until it reaches its interaction point in a target. An event generator, namely Pythia8 [110] in 2015, is called to obtain the parameters of the two outgoing muons. In practice, the geometrical acceptance and all of detector biases are simultaneously determined for practical reasons. Indeed, generated dimuon tracks are reconstructed with CORAL and analyzed by following the same procedure and selection criteria as the real data. Finally, the acceptance correction used in the analysis is obtained using a modified bin-by-bin method and defined for the i -th bin as shown in Eq. 25.3. A simple example of this acceptance correction and its impact in the cross-section evaluation is shown in Fig. 25.1. This example illustrates how reconstructed data are transformed into the generated kinematic space by dividing them by the acceptance factor.

$$\varepsilon_i = \frac{N_{i,MC}^{\text{rec}}}{N_{i,MC}^{\text{gen}}} \quad (25.1)$$

where N_{MC}^{gen} refers to the number of generated events in a bin i

N_{MC}^{rec} is the number of reconstructed events expressed in the reconstructed phase space.

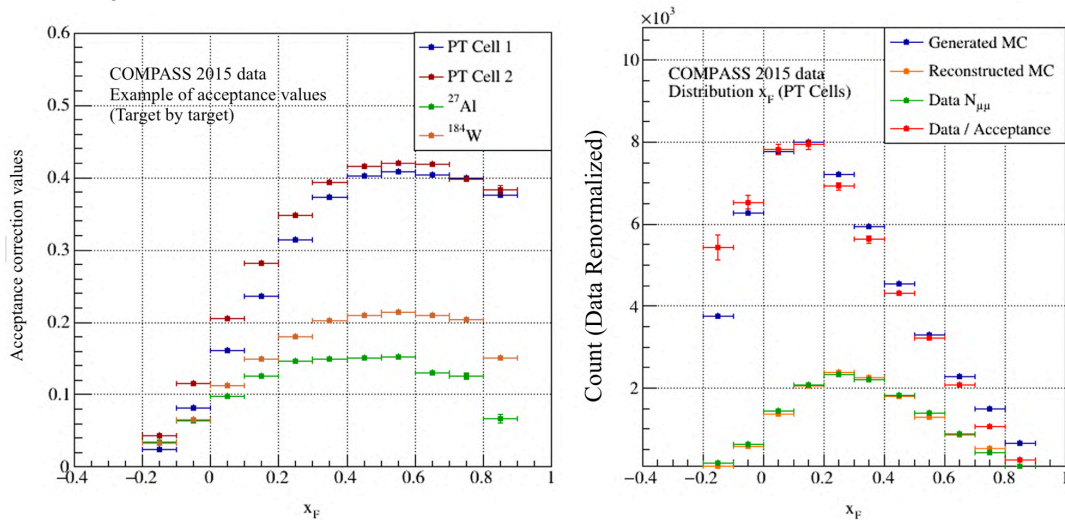


Figure 25.1: (a) Left: Example of acceptance correction for each target (including detector 2D efficiency maps and recent trigger efficiency); (b) Right: Impact of the correction using COMPASS MC and 2015 data as a function of x_F ; 2015 data with and without acceptance correction are normalized by the integral of generated and reconstructed MC events, respectively

The essential feature of this method consists of splitting all generated and reconstructed events into separated trees to account for event migration. This method presents some approximations in the determination of the acceptance compared to unfolding techniques but remains valid when both generated events $N_{\text{MC}}^{\text{gen}}$ and reconstructed $N_{\text{MC}}^{\text{rec}}$ are subjected to the same geometrical and kinematic selection :

- **Target cuts:** The primary vertex is selected within the fiducial volume of the targets.
- **Cross the full upstream target setup:** The extrapolated beam track must cross the previous target cells to apply the beam absorption correction
- **All kinematical cuts:** $(-1 < x_F < 1)$, $(0 < x_\pi < 1)$ and $(0 < x_N < 1)$, $M \in [4.3; 8.5]$ GeV/c², and the beam decay muon rejection. In consequence, these kinematical cuts also have to be applied to all theoretical calculations to be compared with the extracted data.

Based on this short introduction to the acceptance calculation, a detailed presentation of the methodology of the acceptance correction will be shown in the following. It includes event generation, comparisons between reconstructed MC and 2015 data, and an evaluation of systematic uncertainties. The multi-dimensional correction technique, for the extraction of the double and triple differential cross-sections, is also presented.

25.2 Event Generation

The inelastic collision in MC simulation can be restricted to a specific physics process using an event generator. In 2015, the event generator describing dimuon processes was the Pythia8 generator [110]. Pythia8 is used primarily to generate Drell-Yan from the interaction between an incoming π^- at 190 GeV/c on a nucleon target. However, it can also be configured to generate the J/Ψ , Ψ' , Open-Charm and Upsilon contribution for background contamination studies in the mass range $M_{\mu\mu}$ between 2 and 8.5 GeV/c².

The calculation of the acceptance is only performed based on the generation of the Drell-Yan process at high-mass. The Pythia8 parameters are tuned as described in Tab 25.1.

The momentum distribution of the positive muons from MC simulation for each target is compared to real data in Fig. 25.2. A satisfactory agreement between the two distributions is found. Consequently, this gives some confidence in the correct modeling of the apparatus in the limit of the physics model used.

However, a perfect agreement between kinematical variables of the 2015 data and the MC simulation is not mandatory to extract the relevant acceptance. This is especially true when the correlation between variables is not very well known, which are the reasons for collecting new data. Finally, only a sufficiently large phase space coverage is required to describe the kinematic region probed by the spectrometer and not fall into a zero in the acceptance for a given bin.

The q_T distribution and its correlation with other variables in Drell-Yan is not very well known. Therefore, as an example to ensure a sufficiently large phase space in q_T , a tuning of its distribution is obtained by tuning the primordial k_T of the partons. The k_T is defined as the transverse momentum distributions using the k_x and k_y , component, respectively. These distributions are assumed Gaussian and the k_T width is adjusted using the following formula :

$$\sigma = \frac{\sigma_{\text{soft}} Q_{\text{half}} + \sigma_{\text{hard}} Q}{Q_{\text{half}} + Q} \times \frac{m}{m + m_{\text{half}} y_{\text{damp}}} \quad (25.2)$$

Table 25.1: Pythia8 configuration for 2015 MC acceptance

Pythia8 PDF settings	
Beam π^- PDF	LHAPDF6:GRVPI1
Nucleon PDF	LHAPDF6:NNPDF23_nlo_as_0119
Pythia8 radiation settings	
Initial State Radiation	ON
Final State Radiation	ON
Multiple Parton Interactions	ON
Pythia8 kT tuning	
BeamRemnants:halfScaleForKT	$Q_{\text{half}} = 2.0$
BeamRemnants:halfMassForKT	$m_{\text{half}} = 4.0$
BeamRemnants:primordialKTsoft	$\sigma_{\text{soft}} = 1.1$
BeamRemnants:primordialKThard	$\sigma_{\text{hard}} = 1.8$

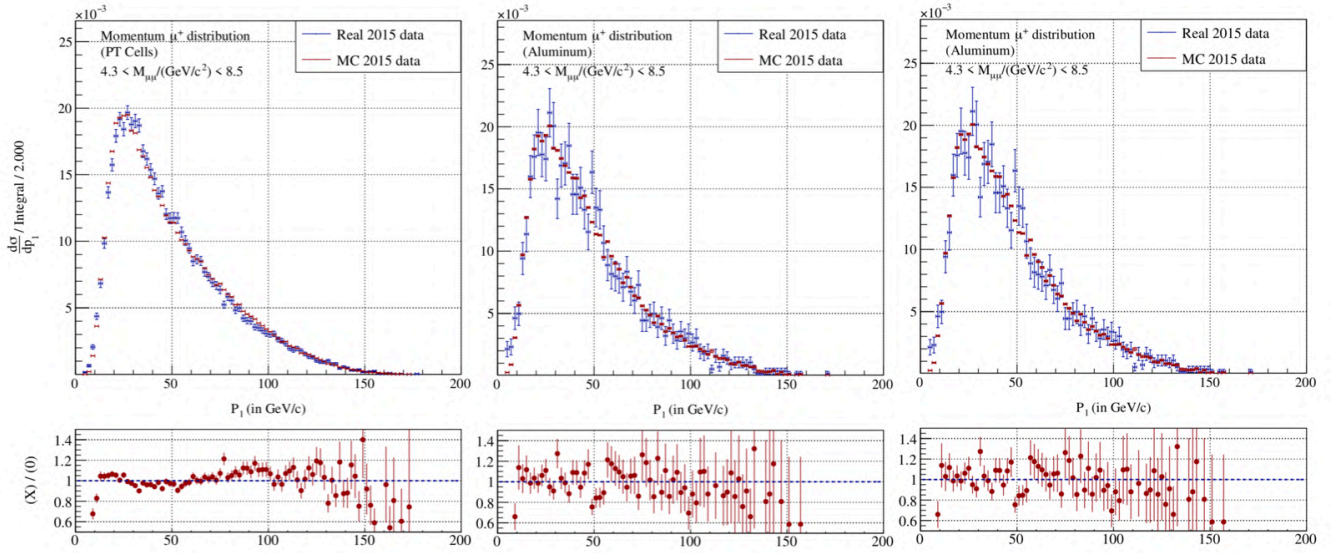


Figure 25.2: Reconstructed MC yield as a function of muon momentum (in red) and compared with the 2015 data (in blue)

where Q refers to the energy scale of the central process.

m is the mass of the system.

Q_{half} is the half-way point between hard and soft interactions.

m_{half} is the half-way point between low-mass and high-mass.

σ_{soft} is the width of the primordial k_T of the parton in the soft-interaction limit.

σ_{hard} is the width of the primordial k_T of the parton in the hard-interaction limit.

y_{damp} is a purely technical dampening factor for better convergence of the kinematics construction.

(parameter neglected, set to 1)

The comparison of such advanced kinematic distributions, as shown in Fig. 25.3 is mainly meant to verify the proper description of the experimental apparatus in the simulation: detector positioning, detector description.

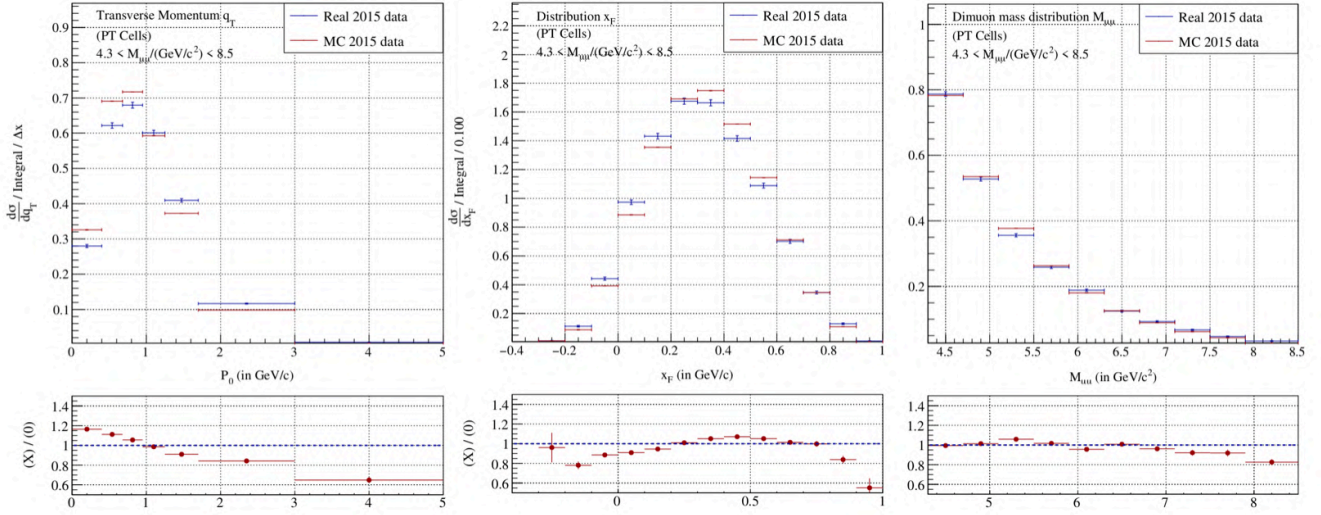


Figure 25.3: Reconstructed MC yield as a function of q_T , x_F and $M_{\mu\mu}$ (in red) and compared with the 2015 data (combined PT cell in blue)

Finally, although the acceptance might be defined regardless of the physics, the event generation is optimized based on the already existing production cross-section models for computer resource purposes. By convention, the statistics of the MC is often required to be at least ten times larger than the collected data.

25.3 Spectrometer Acceptance

25.3.1 Geometrical Acceptance

The geometrical acceptance (Fig. 25.4) is determined in the generated kinematic space. In this space, the geometrical acceptance for the i -th bin, Eq. 25.3 only includes geometrical coverage without migration effect. The migration effect is canceled as the number of reconstructed events $N_{MC}^{\text{rec,gen}}$ are counted and expressed in the kinematic phase space of the generated events.

$$A_i = \frac{N_{i,MC}^{\text{rec,gen}}}{N_{i,MC}^{\text{gen}}} \quad (25.3)$$

where N_{MC}^{gen} refers to the number of generated event in a bin i

$N_{MC}^{\text{rec,gen}}$ is the number of reconstructed pairs expressed in the generated phase space.

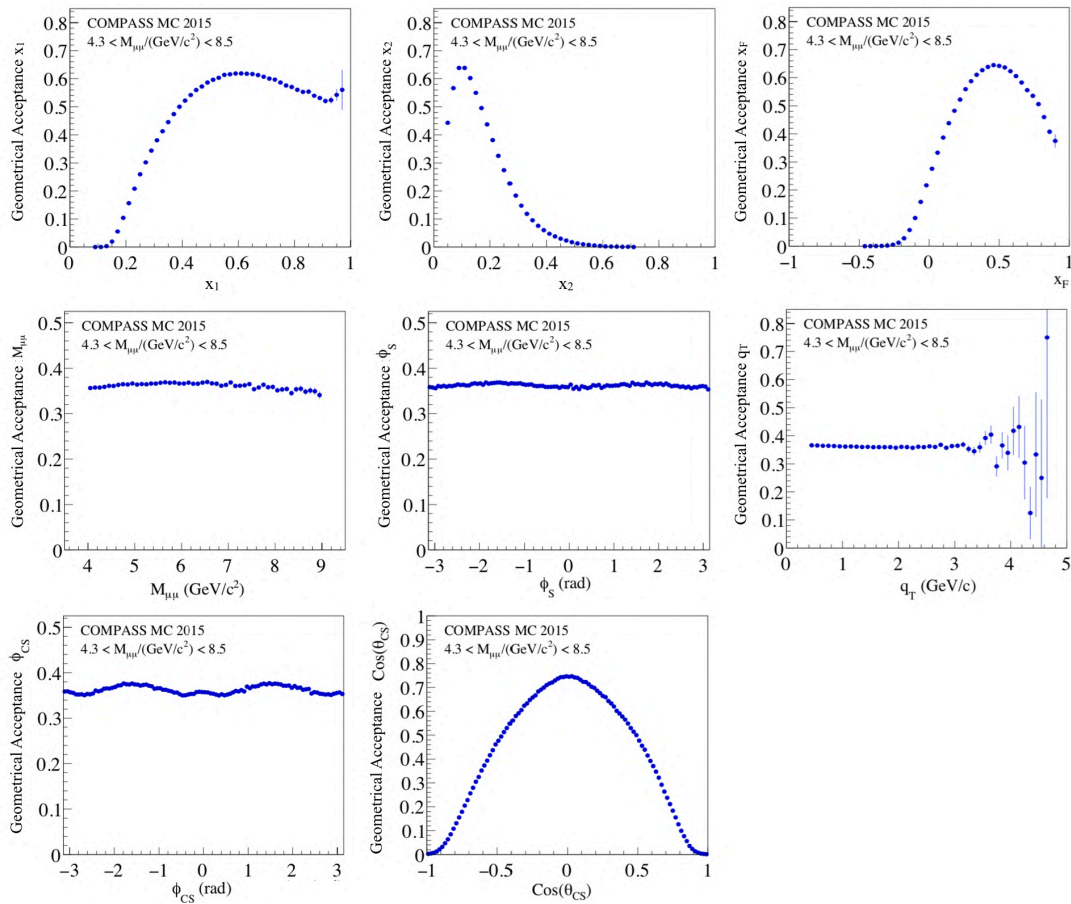


Figure 25.4: True geometrical acceptances (NH₃ targets) illustrating the expected coverage (no migration) [127]

In Fig. 25.4, the geometrical acceptance is shown as a function of the main kinematic variables. These plots illustrate the acceptance covered by the COMPASS apparatus in terms of x_1 , x_2 , x_F , $M_{\mu\mu}$, ϕ_S , q_T , ϕ_{CS} , $\cos(\theta_{CS})$. The large x_F acceptance and the geometrical acceptance of the x_2 distributions allows measuring the effect of nuclear medium with an incoming π^- beam. Moreover, the x_1 distribution allows probing a wide range in x in the structure of the π^- . Finally, the large range in q_T acceptance gives also the opportunity to study the dependence of the dimuon mass or x_F variables as a function of the dimuon transverse momentum.

25.3.2 Event Migration and Detector Inefficiencies

Bias in the reconstructed data might be induced by various factors: detector performances, detector positioning, event selection, and track reconstruction algorithms. First, the *event migration* is induced by the limited resolution of detectors, which lead to a kinematic smearing of reconstructed quantities compared to the generated information. Second, the detector inefficiency might result in a generated event that cannot be reconstructed. These effects play a role in the amplitude of the reconstructed signal or in other words in a reduction of the acceptance coverage.

Consequently, the MC simulation of the apparatus has to be compared to real data to ensure the accurate description of the apparatus. As an example, the muon angular distributions between real data and MC are compared in Fig. 25.5. In the limit of the collected statistics in 2015, Fig. 25.5a seems to show some inefficient spots, which have to be included in the MC simulation. Consequently, the muon angular distribution (Fig. 25.5b) is adjusted by including a detector 2D efficiency map to reproduce the real data better.

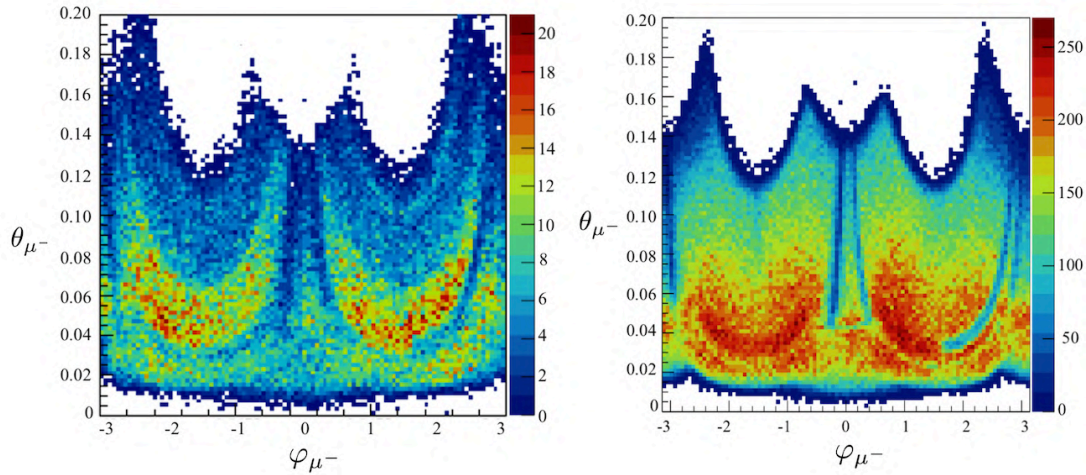


Figure 25.5: (a) Left: Angular distribution of the μ^- in the 2015 data. This profile shows some inefficient regions (in dark blue); (b) Right: The corrected MC profile after tuning of the detection efficiency. The MC data better describes the corresponding 2015 data on the left.

The characterization of the kinematic smearing is performed by computing the spectrometer resolution. In the following resolution analysis, a true MC event is required to be associated with a selected reconstructed Drell-Yan pair. The situation when a single generated event leads to two reconstructed dimuon events is disregarded. In comparison to the real data this case was not observed and at most a single muon pair is found for each selected trigger event.

In this case, a direct correlation is performed between the generated pairs and their reconstructed pairs to evaluate the migration effects. Therefore, a residual distribution (Eq. 25.4) is computed and fitted using either a simple or double Gaussian to estimate the resolution of any kinematic variable.

$$\Delta X = X_R - X_G \quad (25.4)$$

where X_G refers to the generated value of an observable X

X_R is the reconstructed value associated to X_G

Fig. 25.6 shows the residual plot of the dimuon mass $M_{\mu\mu}$ and the Z_{vtx} position. The residual distributions are fitted using a double Gaussian. The leading signal (in green) is used to extract the resolution of the variable. A tail Gaussian (in blue) is used to describe the background induced by the mis-associations between generated and reconstructed pairs. The Z_{vtx} distribution suffers from the description of the multiple scattering in the tungsten. The asymmetry and the shift of the residual distributions toward the positive $\Delta Z_{\text{vtx}} > 0$ values highlight a possible bias in the tracking algorithm. In other words, the generated tracks tend to be reconstructed about 1.5 cm upstream. An improved model would require further studies to better account for the energy loss in the nuclear medium. Consequently, the effect of this MC bias is minimized by choosing a larger binning to compensate for the smearing effect.

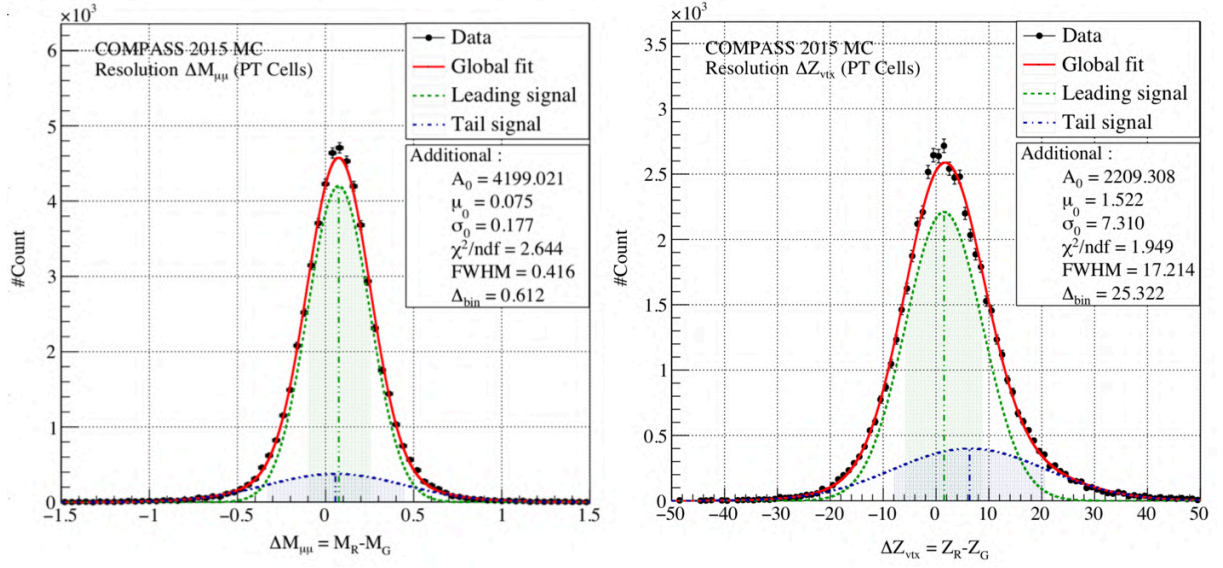


Figure 25.6: (a) Left: Residual distribution of the dimuon mass for the combined PT cells. (b) Residual distribution of the Z_{vtx} distribution for the combined PT cells.

The choice of the bin size is driven by various factors to avoid discrete effects due to statistical fluctuations and the smearing effect due to the finite detector resolution. Each bin of a histogram is considered as a uniform distribution. Consequently, the standard deviation of this distribution σ_{uniform} should not be larger than the estimated resolution of σ_0 . This consideration leads to Eq. 25.5.

$$\sigma_{\text{uniform}}^2 = \frac{\Delta_{\text{bin}}^2}{12} \gtrsim \sigma_0^2 \quad \Rightarrow \quad \Delta_{\text{bin}} \gtrsim \sigma_0 \sqrt{12} \quad (25.5)$$

where Δ_X refers to bin width of the observable X

σ_0 is the standard deviation of the leading signal

A summary table (Tab. 25.2) gives the detailed resolution values of the main kinematic variables as a function of the target. Further resolution plots are shown in Appendix G. Finally, the binning of the kinematic distribution will be established based on this resolution study in the limit of the statistical accuracy.

All resolutions are worsening by going through cells, but the Z_{vtx} . Indeed, the Z_{vtx} is improved by going closer to the tracking station, except in the tungsten because of multiple scattering. The intersect of muon pair with the beam is better defined as the acceptance is larger. Therefore, for a muon pair at a given opening angle, $\Delta\theta = |\theta_{\mu^-} - \theta_{\mu^+}|$, the fit of the vertex is improved. This feature is more precisely confirmed in Fig. 25.7b, which shows the evolution of the resolution as a function of Z_{vtx} .

Table 25.2: Summary of the kinematic resolutions for the different targets evaluated in the high-mass Drell-Yan region

Kin. Variable	PT Cells		Aluminum		Tungsten (10 cm)	
	σ_0	Δ_{bin}	σ_0	Δ_{bin}	σ_0	Δ_{bin}
$M_{\mu\mu}$ [GeV/c ²]	0.176	0.608	0.221	0.767	0.401	1.389
x_1 [\emptyset]	0.011	0.036	0.011	0.038	0.012	0.043
x_2 [\emptyset]	0.008	0.027	0.013	0.047	0.019	0.065
x_F [\emptyset]	0.015	0.051	0.017	0.060	0.027	0.094
q_T [GeV/c]	0.112	0.389	0.209	0.723	0.296	1.026
φ_{LAB} [mrad]	0.136	0.473	0.370	1.282	0.765	2.650
$\cos\theta_{\text{CS}}$ [mrad]	0.016	0.054	0.028	0.099	0.045	0.157
φ_{CS} [mrad]	0.095	0.329	0.179	0.619	0.225	0.781
X_{vtx} [mm]	0.25	0.88	0.36	1.24	0.41	1.42
Y_{vtx} [mm]	0.23	0.78	0.35	1.20	0.40	1.38
Z_{vtx} [cm]	7.310	25.322	2.571	8.907	3.234	11.202

The resolution of some variables is correlated with other kinematic variables. This correlation is illustrated in Fig. 25.7 where the resolution of the azimuthal angle improves with the dimuon transverse momentum q_T . For instance, a cut in q_T can be beneficial for an analysis of the angular distribution. However, no correlations were found with the variables of interest discussed in the scope of cross-section analysis.

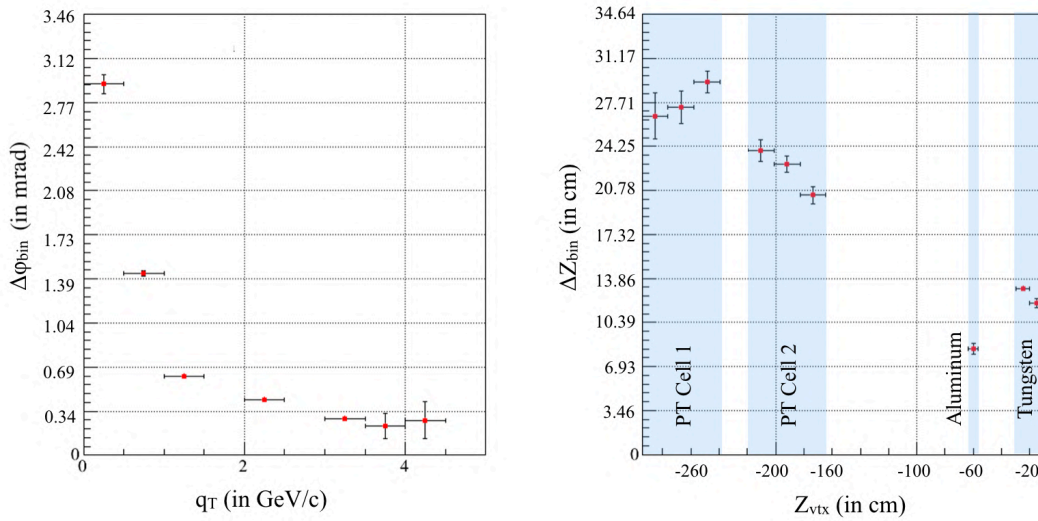


Figure 25.7: (a) Left: Correlation of the φ_{LAB} resolution VS the transverse dimuon momentum q_T ; (b) Right: Evolution of the Z_{vtx} resolution as a function of Z_{vtx}

25.3.3 Trigger System Efficiency

The efficiency of the trigger system can be decomposed into two parts: the hodoscope efficiency and the coincidence matrix efficiency. This correction has been recently implemented in MC and is taken into account in the analysis through the acceptance correction.

$$\varepsilon_{\text{tot}} = \varepsilon_{\text{hodo.}} \times \varepsilon_{\text{coinc.}}$$

The hodoscope efficiency $\varepsilon_{\text{hodo.}}$ is directly related to the hardware efficiency of the hodoscope slabs, while the matrix efficiency $\varepsilon_{\text{coinc.}}$ refers to the efficiency of the coincidence system (hardware modules, cable connections,..) between two detection planes (e.g., HG01Y1 and HG02Y1/2).

Hodoscope Efficiency. In 2015, the trigger efficiency was determined using special runs taken by the trigger group and dedicated to this task. In these special runs, in addition to single muon triggers, a so-called calorimeter trigger was used. This trigger has the advantage of covering the entire kinematic region covered by the LAST, the OT, and the MT triggers. As it is an independent trigger, it gives an unbiased sample of events from which the efficiency of the hodoscopes can be determined. Consequently, the hodoscope efficiency is computed as follows:

$$\varepsilon_{\text{hodoscope}} = \frac{N_{\text{track,hit}}}{N_{\text{track}}}$$

where N_{track} is the total number of tracks crossing the slabs of the hodoscope.

$N_{\text{track,hit}}$ refers the number of tracks crossing the hodoscope with an associated hit.

A first look at the impact of this efficiency correction is performed using the dimuon data selected in the physics analysis. Figure 25.8 shows a spatial distribution of extrapolated tracks at the location of the hodoscopes. It illustrates the situation before trigger efficiency correction for each of the trigger hodoscopes involved in the analysis. Some inefficient regions are clearly visible in each hodoscope.

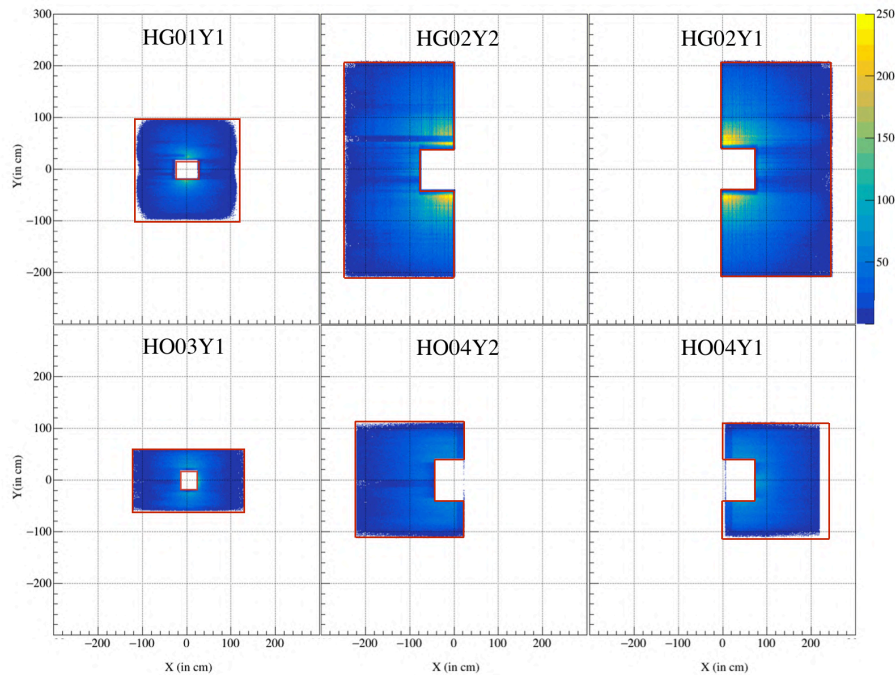


Figure 25.8: Extrapolation of the dimuon tracks to the Z-abscissa corresponding to each hodoscope; Red lines are the theoretical shape of the hodoscopes (HO04Y2 and HO04Y1 presents some overlap around zero which is expected from the design of the spectrometer).

In the case of dimuon tracks, an important remark must be emphasized. Dimuon tracks in the analysis are obtained from the combination of two single muon triggers, either $\text{LAST} \otimes \text{LAST}$ or $\text{OT} \otimes \text{LAST}$. Moreover, each single muon hodoscope relies on a set of two slabs due to coincidence purposes. Consequently, each event is convoluted with the efficiency of 4 hodoscope slabs and the efficiency of 2 trigger coincidence matrix pixels. An example using the HG02Y1 hodoscope is shown in Fig. 25.9. This hodoscope presents an inefficient region in its central slabs before applying slab efficiency corrections (left), which is corrected after efficiency corrections (right). Consequently, it illustrates the positive impact of this first correction step.

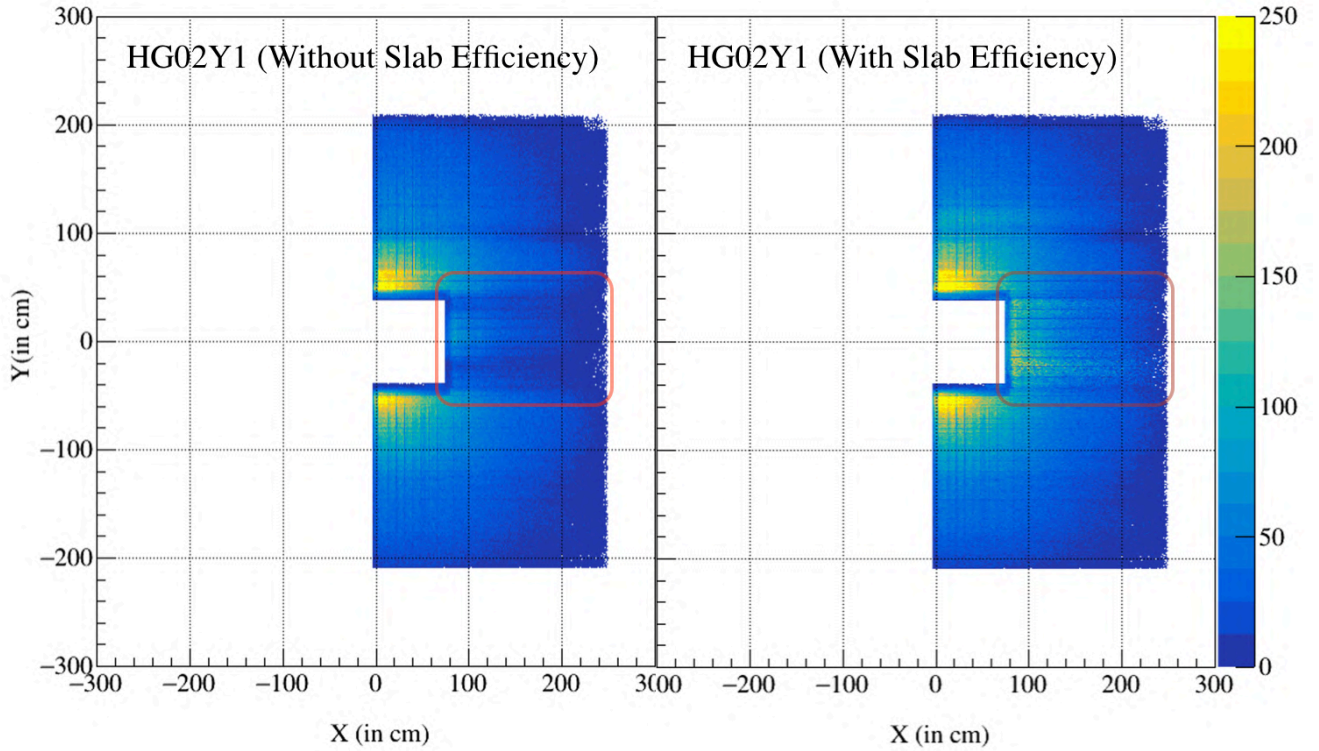


Figure 25.9: (a) Left: Track distribution extrapolated at the Z-abscissa of the HG02Y1 hodoscope, before slab efficiency correction; (b) Right: Extrapolated track distributions at the Z-abscissa of the HG02Y1 hodoscope; A red square in the picture highlights the positive impact of the correction in the central slabs

Trigger Matrix Efficiency. Traditionally, the hodoscope coincidence is performed based on a trigger matrix pattern as discussed in Sec. 7.1, Ch. II. A coincidence pixel is triggered when the slab numbers between HG01 and HG02 or HO04 and HO3 are in coincidence and in the accepted pattern for the corresponding trigger. However, this coincidence pattern might not be fired due to signal transmission, or specific timing of the signal. Consequently, the coincidence matrix efficiency has to be taken into account in the extraction of the cross-section.

This additional correction is estimated based on hits in the hodoscopes by selecting inclusive calorimeter triggers and does not rely on tracking information. For an expected trigger, hits in the corresponding hodoscopes are combined offline to verify the compatibility of this list with the trigger matrix pattern. The online trigger signal is then computed and compared to provide an efficiency value for a given pair of slabs. Fig. 25.10 shows the three matrix patterns used for the coincidence in the HG and HO hodoscopes.

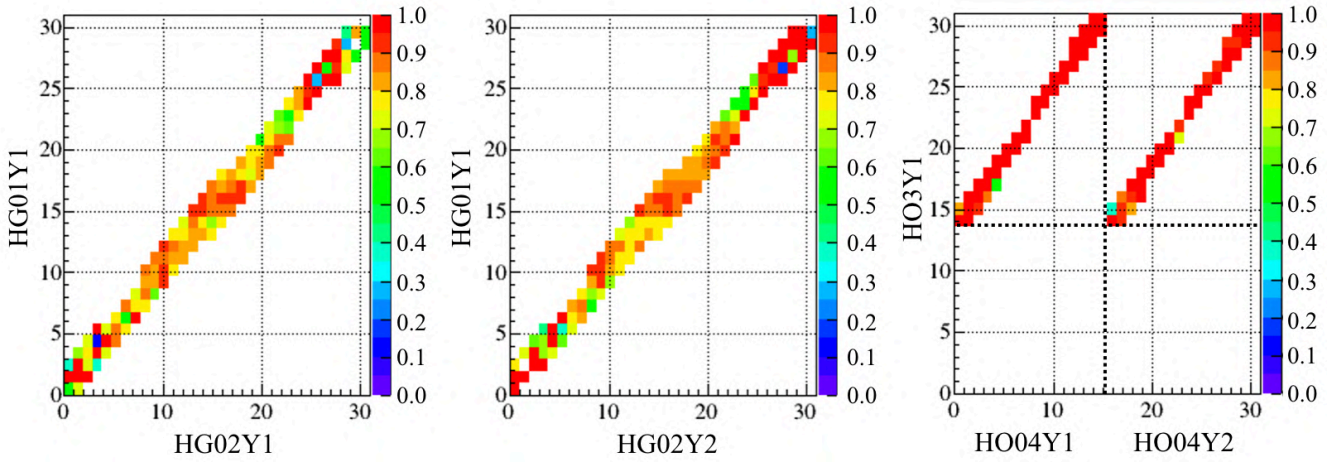


Figure 25.10: The efficiency of the trigger matrix pattern used for the HG and HO hodoscopes. The x and y axis refer to the slab number of the corresponding hodoscope plane

The impact of this correction in the cross-section is expected to be rather large because of the low trigger efficiency values measured in 2015. The implementation of the first evaluation of the trigger efficiency for 2015 was performed during summer 2019 and it remains under verification. Fig. 25.11 shows the impact of the trigger efficiency at the level of the acceptance correction. This correction has a considerable impact on the acceptance of many variables, such as x_F , which shows an overall reduction of acceptance.

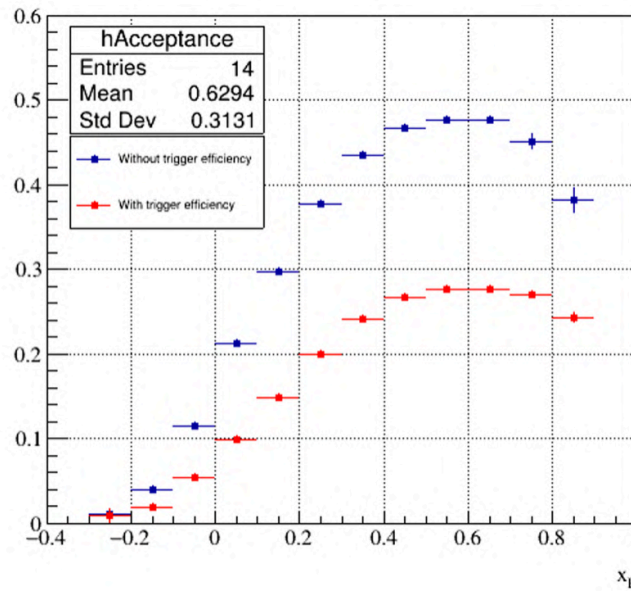


Figure 25.11: Example of the relative acceptance modification with (red) and without (blue) trigger efficiency implementation as a function of x_F . This correction represents a reduction of 40% in the initial acceptance. Moreover, this plot is not meant to be used as a reference for cross-section and final acceptance estimation.

25.3.4 Overcorrection of the Beam Telescope Acceptance

Although the acceptance correction is meant to correct for detector inefficiencies and geometrical acceptance, the beam telescope correction presents some specificities due to the flux correction. Indeed, as previously discussed in Ch. V, beam tracks are reconstructed in physics analysis and flux analysis (Fig. 25.12) based on the same telescope acceptance and inefficiencies.

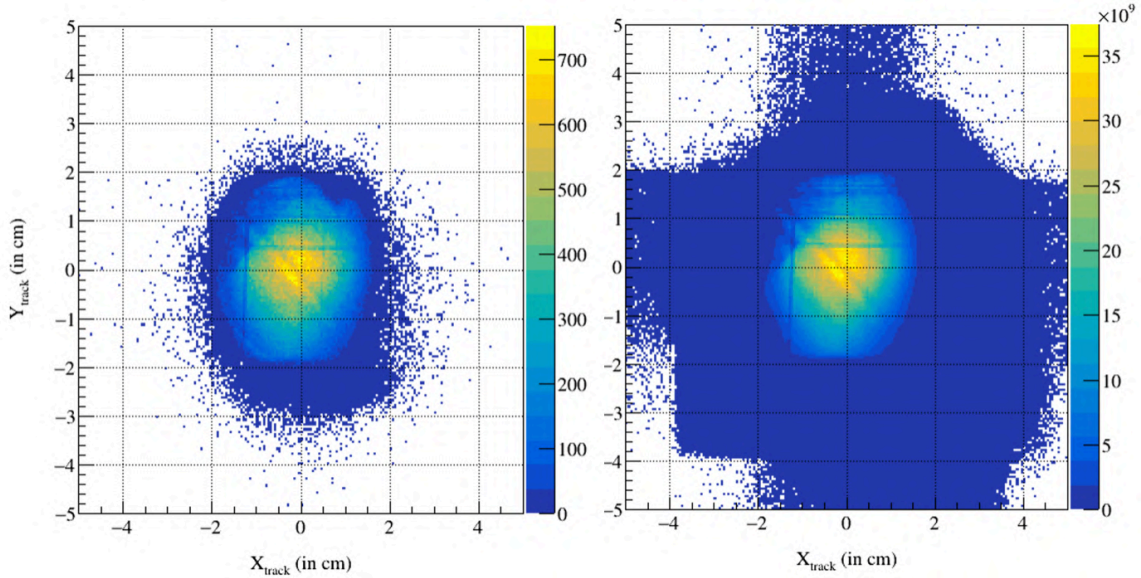


Figure 25.12: (a) Left: Typical profile of the beam telescope, projected to the upstream abscissa of the PT cell 1. This profile shows vertical and horizontal lines which refer to inefficiency of the Sci-Fi detectors; (b) Right: The profile of the beam computed from the flux analysis introduced in Ch. V

Consequently, the acceptance of the beam telescope is already corrected for and should not be included in the MC simulation. Only generated events with a reconstructed beam track satisfying the selection criteria are considered. After this selection, the beam telescope profile does not show any more evidence of inefficiencies, and consequently, the acceptance effect is only accounted for in the flux correction.

25.4 Multi-Dimensional Acceptance

The Drell-Yan process can be generated at leading order and described with a set of two variables, e.g. $(\sqrt{\tau}, x_F)$. However, the production model of the q_T distribution is described using an empirical tuning of the primordial k_T of partons. Consequently, the q_T variable and its correlation with other variables is not very well known theoretically.

Consequently, a multi-dimensional acceptance is computed bin-by-bin and an increase of the dimensionality should favor a reduction of its model dependence in the limit of the available statistics. The acceptance correction for the i -th kinematic bin b_i , spanning a Drell-Yan phase space denoted PS of N dimensions, is defined in Eq. 25.6.

$$\varepsilon_i(b_i) = \frac{N_{i,MC}^{\text{rec}}}{N_{i,MC}^{\text{gen}}} \quad \forall b_i = (x_{1,i}, \dots, x_{N,i}) \in \text{PS} \quad (25.6)$$

where N_{MC}^{gen} refers to the number of generated events for a generated kinematic bin i

N_{MC}^{rec} is the number of reconstructed events for a reconstructed phase space.

Such PS is made of a finite number of kinematic bins. The set of parameters $(x_{1,i}, \dots, x_{k,i})$ refers to a possible set of kinematic variables. Therefore, a possible combination for the x_i parameters might be defined as an example for $N = 3$, by $(x_1, \dots, x_3) = (M_{\mu\mu}, x_F, q_T)$. Figure 25.13 illustrates a case for a 3x3 binning, which shows a direct comparison between reconstructed 2015 data and MC expressed as a function of x_F for several bins of $(M_{\mu\mu}, q_T)$. The corresponding ratio plots are shown in Fig. 25.14.

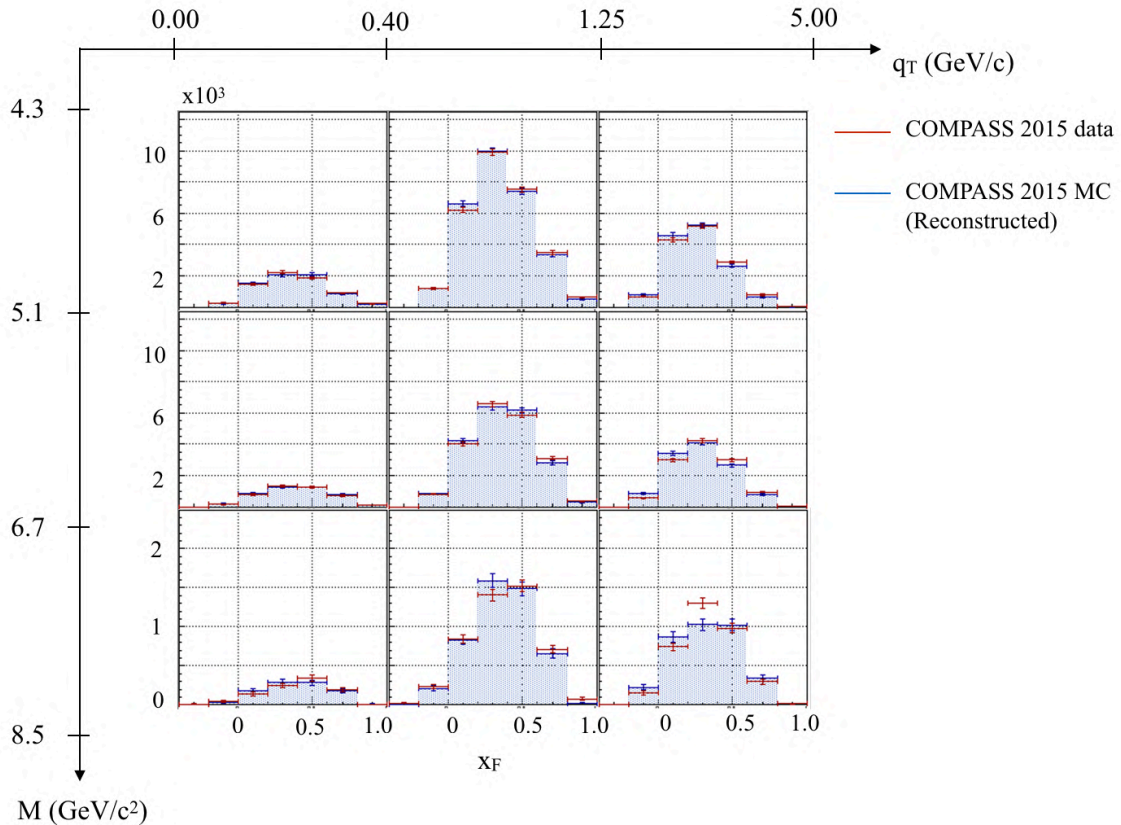


Figure 25.13: Comparison between reconstructed data from COMPASS 2015 (PT Cell 1) and COMPASS MC for various bins in $(M_{\mu\mu}, q_T)$. The MC data are rescaled based on 2015 data integral

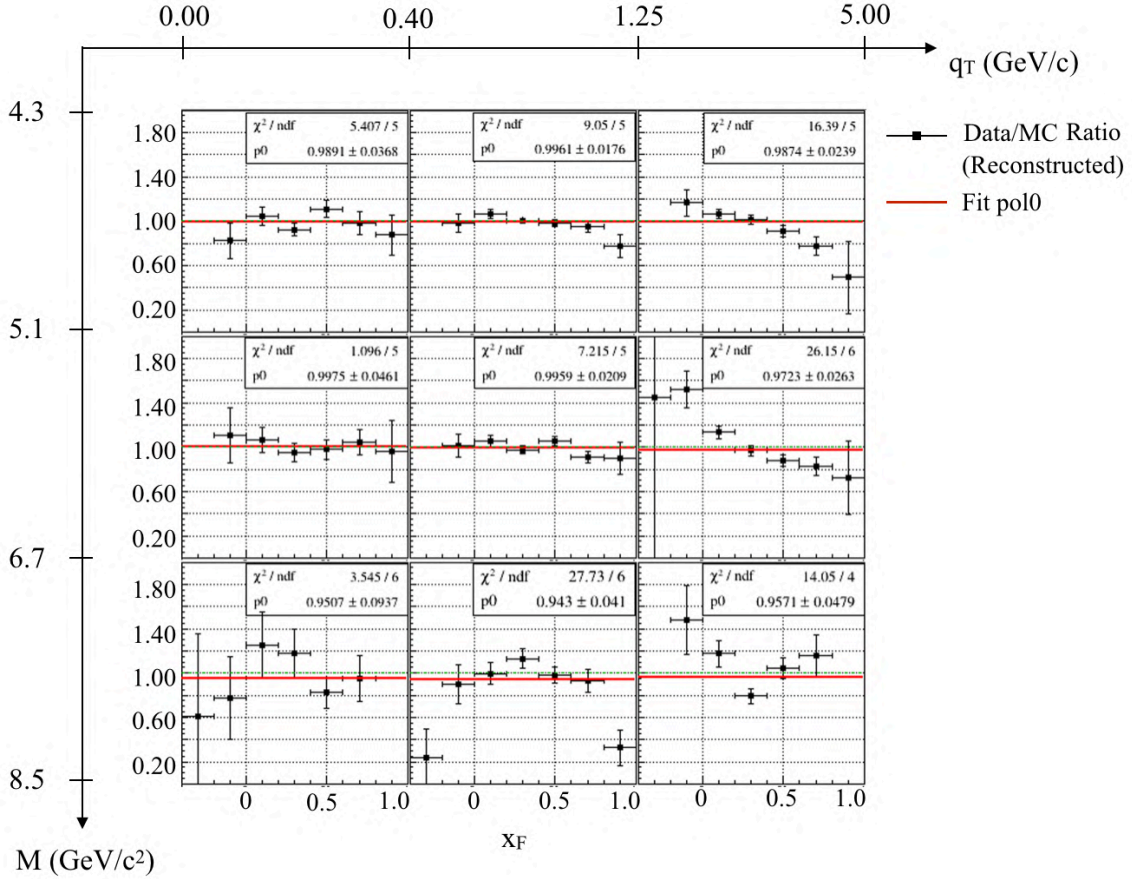


Figure 25.14: Ratio plot between the reconstructed MC and the 2015 data (PT Cell 1). These plots highlight some differences in the correlations between MC and 2015 data at high q_T

Requirements for Multi-Dimensional Corrections. A good agreement between reconstructed MC and 2015 data is not mandatory. Indeed, the generation of a flat MC distribution would allow computing a reasonable acceptance if the MC geometry properly describes the real situation. However, the comparison of reconstructed distributions between real data and MC would not be possible. The agreement between 2015 data and MC is mainly used with 1D distributions (e.g., momentum distributions, angles, energy distributions, target positioning) to find inconsistencies in the description of the apparatus, as we expect the physics model to reproduce reasonably the reality. Moreover, the choice of using a physics generator instead of flat MC is driven by a computing resource argument, because we expect to probe preferentially the region of the spectrometer explored by the reconstructed data.

Therefore, the requirement for multi-dimensional studies will be to generate and reconstruct MC data over a phase space, at least as large as the collected physics data. This would ensure the proper correction in acceptance of the corresponding kinematic region in the 2015 data. Consequently, it is important to verify bin-by-bin the correct definition of the acceptance values to avoid loss of data. In Fig. 25.15, the acceptance distributions are compared with the real data phase space as a function of $(M_{\mu\mu}, x_F, q_T)$. The importance of this comparison is emphasized with the behaviors of few x_F bins, such as $[-0.4; -0.2]$ and $[0.9; 1.0]$. These bins showed a too low acceptance value and were consequently rejected of the analysis. This rejection will also be confirmed in the following discussion.

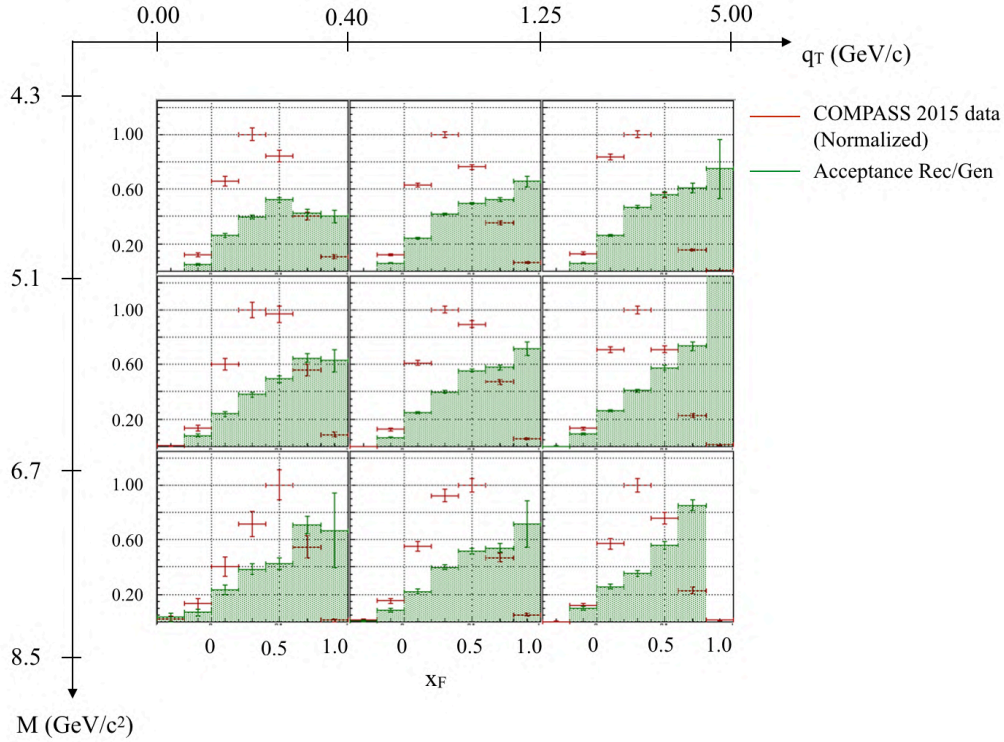


Figure 25.15: Acceptance correction for PT Cell 1 (in green) for the simple case as a function of $(M_{\mu\mu}, x_F, q_T)$. The reconstructed data (PT Cell 1) are shown in red to check the phase space coverage

Multi-Dimensional Acceptance Test. The multi-dimension acceptance calculation is tested by comparing cross-sections using various acceptance corrections. As an example, Fig. 25.16a shows the evolution of the mean acceptance per bin of x_F as a function of 3 different acceptances : $A(Z_{\text{vtx}}, x_F)$, $A(Z_{\text{vtx}}, x_F, M)$, $A(Z_{\text{vtx}}, x_F, M, q_T)$. The ratio plot highlights an increase of the acceptance at high- x_F compared to the initial acceptance correction.

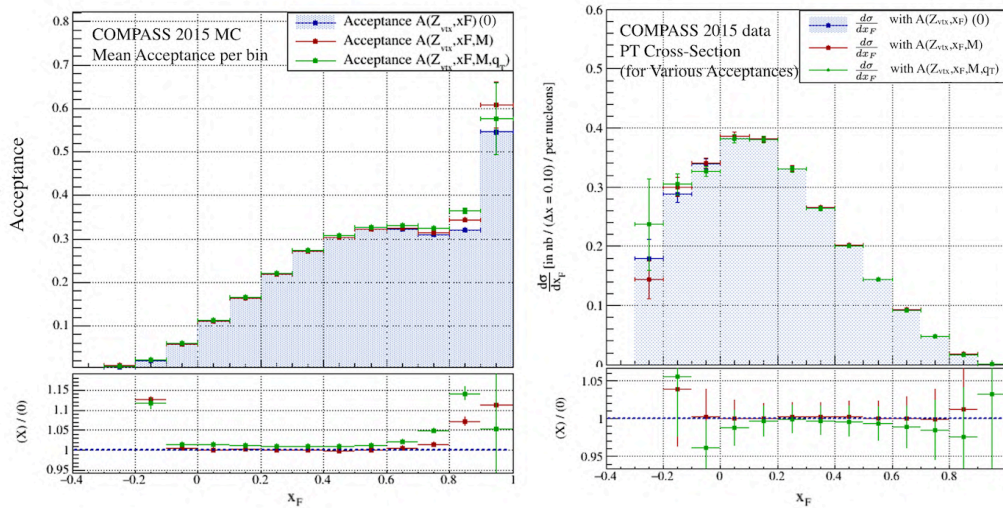


Figure 25.16: (a) Left: Comparison of the acceptance as a function of x_F ; (b) Right: Comparison of a single differential cross-section as a function of x_F to test the impact of the dimensionality

Such a study is also meant to verify the stability of the acceptance calculation. Therefore, the large x_F bin $[0.9;1.0]$ shows a large variation under this test, including a large uncertainty and will consequently be rejected from the analysis.

In Fig. 25.17, the integrated simple, double and triple differential cross-sections were also evaluated using their 1D-, 2D-, 3D- acceptance corrections, respectively. The integrated double and triple differential cross-sections highlight the dependence of the Drell-Yan process in terms of M and x_F . The increase of 3% of the integrated cross-section compared to the single differential cross-section $d\sigma/dM$ shows an insufficient acceptance correction, when the results are shown as a function of the M only.

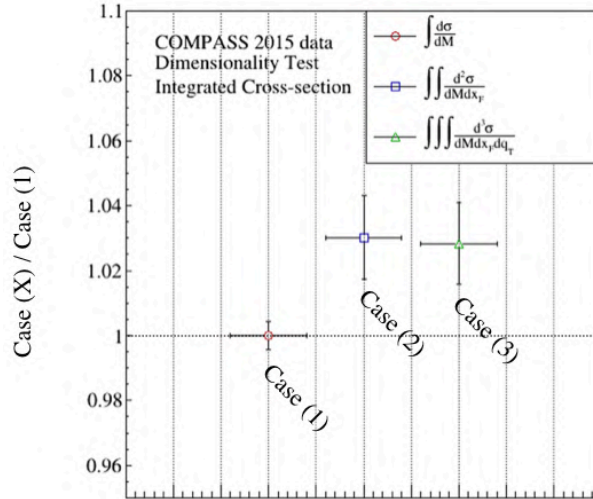


Figure 25.17: Comparison of the total integrated cross-section computed from the simple, double and triple differential cross-sections

25.5 Model-Dependent Uncertainties

25.5.1 Generator Model Uncertainty

A systematic uncertainty introduced by choice of the event generator has been evaluated by comparing two event generators using a similar amount of data. The Pythia8 generator foreseen to be used in the computation of the 2015 MC acceptance has been compared with Pythia6 [109] based on the same configuration. Data were compared based on the same reconstruction configuration and software.

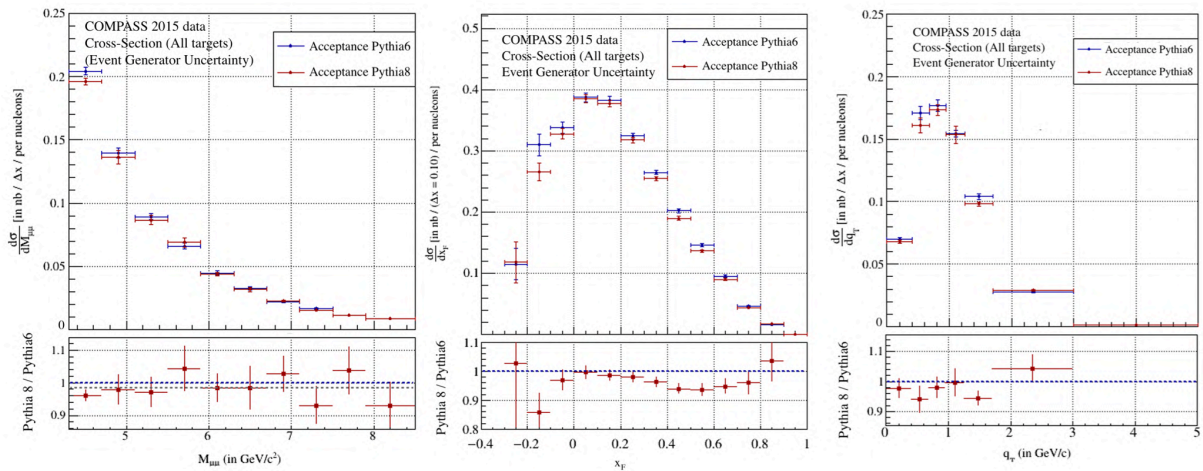


Figure 25.18: Comparison of single differential cross-sections as a function of $M_{\mu\mu}$, x_F , q_T using an acceptance computed either with Pythia6 or Pythia8

In Fig. 25.18, single differential cross-sections are corrected for acceptances estimated by two different

event generators. The acceptance correction is computed using the following variables $(M_{\mu\mu}, x_F, q_T)$. These figures are used to evaluate the uncertainty due to the choice of the physics generator. The mass and the q_T distributions present some compatible fluctuations, although a possible normalization is not excluded. However, the cross-section, as a function of x_F shows a clear dependence on the generator. This model dependence is used to assess a systematic uncertainty bin-by-bin in the evaluation of the cross-section, which is estimated on average to be about 5%.

25.5.2 Data Contamination

A fit of the mass spectrum is performed to correct dimuon data by removing the background events coming from other processes with a muon pair in the final state. The purpose of this study is to estimate via a MC method background events and consequently also estimate latter the impact of background subtraction along with other kinematic variables. Consequently, the corrected number of events N_{DY} in the analysis would be defined as :

$$N_{\text{DY}} = N_{\mu\mu} - N_{\text{bkg}} \quad (25.7)$$

At this stage, this background subtraction method is not applied, and only an estimate of the overall systematic uncertainty is provided depending on the target cells. Fig. 25.19 provides an example of the fit performed over the different targets.

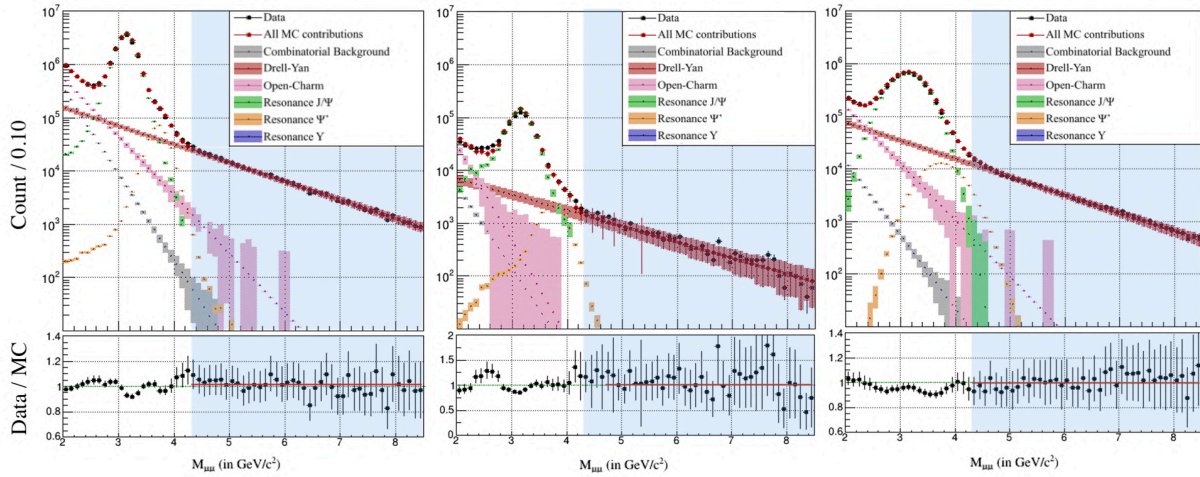


Figure 25.19: Decomposition of the dimuon mass spectrum for PT cells (left), aluminum (middle) and tungsten (right). The region of interest for Drell-Yan physics analysis is marked with a blue band

At first, only the combinatorial background is computed (as introduced in the Sec. 24.3.3). This background is fixed compared to the dimuon data. In a second time, each contribution is generated using the Pythia8 generator. The fitting procedure consists of rescaling each contribution to describe the 2015 mass spectrum, as follows :

- The Drell-Yan contribution is generated in the MC in two parts, namely low mass and high mass ranges, for computing reasons. These contributions are then combined and rescaled based on the background-free range from 4.5 GeV/c² to 8.5 GeV/c².
- Consequently, the open-charm process remains the only free continuum in the fit. This continuum is extrapolated using an exponential decrease from 2 GeV to 6 GeV to avoid discrete effects due to the limited statistics at large mass.
- Additionally, the J/Ψ , Ψ' , and Υ amplitudes remain three free parameters in the fit.

Mass Spectrum for PT Targets. In Fig. 25.19 (left), the smearing of dimuon resonances might be underestimated as revealed by the bad description of the resonances between 2.5 GeV and 4 GeV. In the region between 4.3 GeV and 8.5 GeV, the background is estimated about 3% as given in Tab. 25.3.

Table 25.3: Summary table of the dimuon spectrum for PT cells to estimate the background contamination to the Drell-Yan process

Mass Range	J/ Ψ	Psi'	Open-Charm	CBKG	Υ	Drell-Yan	Total Bkg.
4.00 GeV - 8.50 GeV	1.04%	4.24%	3.32%	0.13%	0.00%	91.26%	8.74%
4.10 GeV - 8.50 GeV	0.32%	1.84%	2.91%	0.10%	0.00%	94.83%	5.17%
4.20 GeV - 8.50 GeV	0.00%	0.80%	2.50%	0.08%	0.00%	96.62%	3.38%
4.30 GeV - 8.50 GeV	0.00%	0.35%	2.13%	0.06%	0.00%	97.46%	2.54%
4.40 GeV - 8.50 GeV	0.00%	0.16%	1.80%	0.05%	0.00%	97.99%	2.01%
4.50 GeV - 8.50 GeV	0.00%	0.08%	1.53%	0.03%	0.00%	98.35%	1.65%
4.60 GeV - 8.50 GeV	0.00%	0.05%	1.29%	0.03%	0.00%	98.63%	1.37%
4.70 GeV - 8.50 GeV	0.00%	0.03%	1.09%	0.02%	0.00%	98.86%	1.14%
4.80 GeV - 8.50 GeV	0.00%	0.02%	0.92%	0.01%	0.00%	99.04%	0.96%

Mass Spectrum for the Al target. In Fig. 25.19 (middle), the smearing of the resonant processes between 2.5 GeV and 4 GeV is also not very well described for the aluminum compared to the PT cells. Moreover, the mass distribution around 2 GeV/c² is not perfectly fitted and might require some improvements. However, in the region between 4.3 GeV/c² and 8.5 GeV/c², the background is estimated to be about 1% as given in Tab. 25.4.

Table 25.4: Summary table of the dimuon spectrum for Al target to estimate the background contamination to the Drell-Yan process

Mass Range	J/ Ψ	Psi'	Open-Charm	CBKG	Υ	Drell-Yan	Total Bkg.
4.00 GeV - 8.50 GeV	2.98%	5.68%	0.06%	0.04%	0.00%	91.23%	8.77%
4.10 GeV - 8.50 GeV	0.00%	2.93%	0.05%	0.03%	0.00%	96.99%	3.01%
4.20 GeV - 8.50 GeV	0.00%	1.36%	0.04%	0.02%	0.00%	98.58%	1.42%
4.30 GeV - 8.50 GeV	0.00%	0.57%	0.03%	0.02%	0.00%	99.39%	0.61%
4.40 GeV - 8.50 GeV	0.00%	0.23%	0.02%	0.01%	0.00%	99.74%	0.26%
4.50 GeV - 8.50 GeV	0.00%	0.09%	0.01%	0.01%	0.00%	99.89%	0.11%
4.60 GeV - 8.50 GeV	0.00%	0.00%	0.01%	0.01%	0.00%	99.98%	0.02%
4.70 GeV - 8.50 GeV	0.00%	0.00%	0.01%	0.01%	0.00%	99.99%	0.01%
4.80 GeV - 8.50 GeV	0.00%	0.00%	0.00%	0.00%	0.00%	99.99%	0.01%

Mass Spectrum for the W target. Finally, Fig. 25.19 (right) presents some differences in terms of resolution compared to the previous targets. Consequently, in this range the background is estimated to

be about 5% as given in Tab. 25.5.

Table 25.5: Summary table of the dimuon spectrum for W cells to estimate the background contamination to the Drell-Yan process

Mass Range	J/ Ψ	Psi'	Open-Charm	CBKG	Υ	Drell-Yan	Total Bkg.
4.00 GeV - 8.50 GeV	5.88%	11.73%	1.79%	0.03%	0.00%	80.57%	19.43%
4.10 GeV - 8.50 GeV	2.44%	9.37%	1.63%	0.02%	0.00%	86.54%	13.46%
4.20 GeV - 8.50 GeV	0.90%	6.90%	1.45%	0.02%	0.00%	90.73%	9.27%
4.30 GeV - 8.50 GeV	0.30%	4.73%	1.27%	0.02%	0.00%	93.69%	6.31%
4.40 GeV - 8.50 GeV	0.09%	3.02%	1.10%	0.01%	0.00%	95.78%	4.22%
4.50 GeV - 8.50 GeV	0.02%	1.80%	0.95%	0.01%	0.00%	97.22%	2.78%
4.60 GeV - 8.50 GeV	0.01%	1.00%	0.81%	0.01%	0.00%	98.17%	1.83%
4.70 GeV - 8.50 GeV	0.00%	0.52%	0.69%	0.01%	0.00%	98.78%	1.22%
4.80 GeV - 8.50 GeV	0.00%	0.26%	0.59%	0.01%	0.00%	99.15%	0.85%

26 | Introduction to the Absolute Drell-Yan Cross-Sections

This section aims to introduce the final observables in perspective to complete the methodology of cross-section evaluation. The final and complete table of the uncertainties will also be presented at the end of this section.

The measurement of the absolute differential Drell-Yan cross-section is presented using the event selection, previously introduced in Sec. 24.2, in the mass range $4.3 < M_{\mu\mu}/(\text{GeV}/c^2) < 8.5$. The selected dimuon pairs originate from the interaction of a 190 GeV/c hadron beam mainly made of π^- either with the PT cell 1, PT cell 2, aluminum, or tungsten (10 cm) targets. These cross-sections will be compared later to the already published data, but also with predictions of Drell-Yan cross-sections.

26.1 The Drell-Yan Cross-Section Per Nucleon

The absolute Drell-Yan cross-section is either defined in terms of cross-section per nucleus or cross-section per nucleon. The cross-section per nucleon is often preferred to facilitate the comparison between targets and different experiments. Moreover, the production cross-section per nucleon is expected to be in the same order of magnitude regardless of the target, except for effects induced by the structure of nucleus (e.g., nuclear effects) which are of a higher order.

The definition of the Drell-Yan cross-section per nucleon σ_{nucleon} and per nucleus σ_{nucleus} are given in Eq. 26.1. Ingredients presented in this equation were introduced in this Ph.D. work earlier.

$$\sigma_{\text{nucleon}} = \frac{1}{\varepsilon} \times \frac{N_{\mu\mu}}{\mathcal{L}} \quad \sigma_{\text{nucleus}} = A \times \sigma_{\text{nucleon}} \quad (26.1)$$

where

- σ_{nucleon} (or also simply written σ) refers to the cross-section per nucleon.
- σ_{nucleus} (or also written σ_A) is the cross-section per nucleus.
- $N_{\mu\mu}$ is the total number of reconstructed pairs.
- ε refers to the convoluted acceptance correction
(geometrical acceptance ε_{acc} and spectrometer efficiency ε_{eff})
- $\mathcal{L} = \mathcal{F}_{\text{eff}} \times \varrho_T$ is the total effective pion-nucleon luminosity integrated over the sensitive time of the analysis (e.g. selected run, period, year).
- $\mathcal{F}_{\text{eff}}, \varrho_T$ are the effective flux, the transverse nucleon density, respectively.
- A is the number of nucleons for a given nucleus.

26.2 Perturbative QCD Predictions at NNLO

The cross-section aims to be compared with the theory. Consequently, the purpose of this section is to provide a first estimation of the expected cross-section to be measured using COMPASS data.

26.2.1 Parton Level Monte Carlo, DYNNLO

Perturbative QCD calculations at NNLO are performed using the DYNNLO program [128] to predict Drell-Yan cross-section at COMPASS energy, namely $\sqrt{s} = 18.9$ GeV. This program was initially written for vector boson production at hadron colliders for pp and $p\bar{p}$ reactions. The DYNNLO program does not

account for the resummation of the logarithmically-enhanced contributions of small dimuon transverse momentum q_T beyond leading log. Consequently, the dimuon transverse momentum q_T is not well described and only x_F and $M_{\mu\mu}$ dependencies will be studied.

Subsequently, DYNNLO was modified to compute Drell-Yan π^-p and π^-n cross-sections using separate beam and target PDF sets and including a π^- beam. These PDF sets are obtained from the LHAPDF6 library and shown in Fig. 26.1.

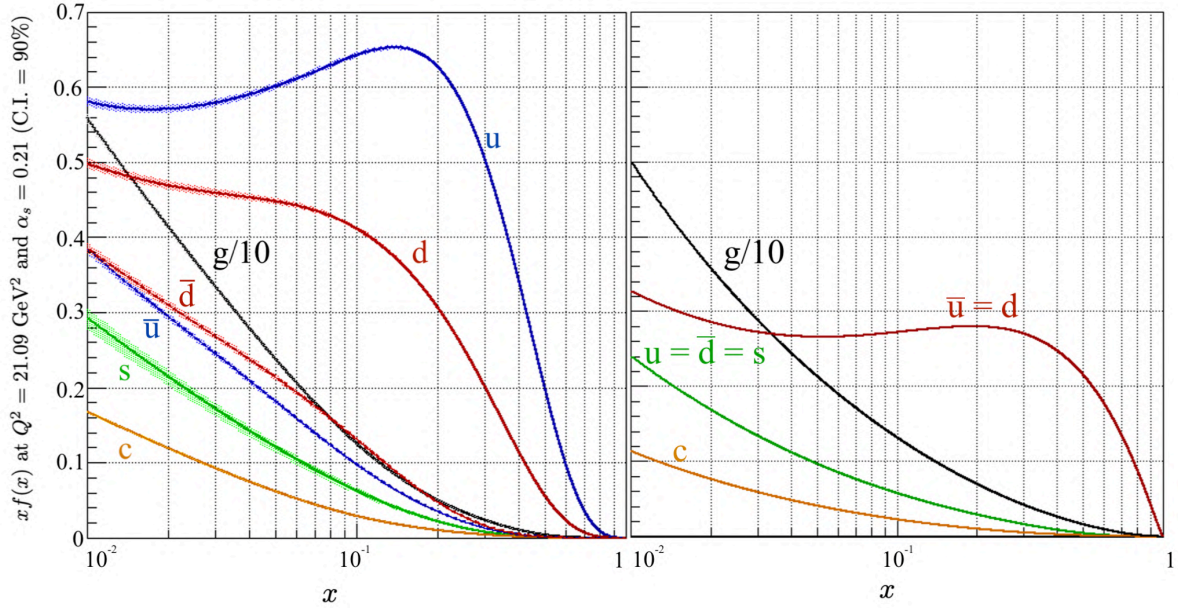


Figure 26.1: The PDF sets are evolved at $Q^2 = \langle M_{\mu\mu} \rangle^2$, where $\langle M_{\mu\mu} \rangle$ is the COMPASS average dimuon mass in the high mass region at $\sqrt{s} = 18.90$ GeV; Left: The CT14NNLO [129] quark PDF in the proton; Right: The GRVPI1 [81] quark PDF in the π^-

CT14NNLO is used to parametrize the proton PDF, as shown in Fig. 26.1 (left). Error bands are determined using the hessian error matrix [130] and the central PDF value as a reference. The parametrization of the pion PDF uses GRVPI1 PDF set. The PDF sets for π^- are limited and in LHAPDF only GRVPI0 at LO¹, GRVPI1 at NLO² are available. The PDF order consistency has been verified and the effect in the cross-section prediction small. Mainly only the DYNNLO calculation order matters.

No uncertainty estimation on the pion PDF is provided in this prediction. However, the first MC global QCD analysis of the pion parton distributions (JAM18 [78]) was published in 2018 and could be used in the future to provide a first estimation of uncertainties on the pion quark PDFs.

26.2.2 Drell-Yan Predictions at COMPASS energy ($\sqrt{s} = 18.90$ GeV)

The modifications made in DYNNLO require to be verified. Therefore, the first step consists of comparing the expected Drell-Yan calculation with some already published cross-section results. This comparison is done using the E615 Drell-Yan π^-W cross-section at 252 GeV ($\sqrt{s} = 21.7$ GeV) [45] in bins of $\sqrt{\tau}$ and x_F and will be extended in a second time to COMPASS energy.

¹Leading Order

²Next-to-Leading Order

Test of the modification using E615 data. At $\sqrt{s} = 21.7$ GeV, the E615 results are reproduced using the target isospin mixing. In this section, the nuclear effects are considered as negligible. These effects are expected to be important at large x_F and small x_2 . The contribution to the total cross-section of the individual $\pi^- p$ or $\pi^- n$ cross-sections are weighted by the fractions denoted $P(p)$ and $P(n)$ (Eq. 26.2), respectively. Z , N refer to the number of protons and neutrons and A the number of nucleons in the considered target.

$$P(p) = \frac{Z}{A} \quad P(n) = \frac{N}{A} \quad (26.2)$$

In fine, the probability values for ^{184}W are denoted $P(p) \simeq 0.402$ and $P(n) \simeq 0.598$ respectively. Fig. 26.2 shows the double differential cross-section as a function of x_F per bin of $\sqrt{\tau}$ in the range $[0.185; 0.392]$. This double differential cross-section computed at NNLO accuracy (in red) are in reasonably good agreement with E615 data in terms of global renormalization and make the proof of the modification, because pion PDF were fitted based on E615. Cross-sections for larger $\sqrt{\tau}$ values are shown and commented in the Appendix J.

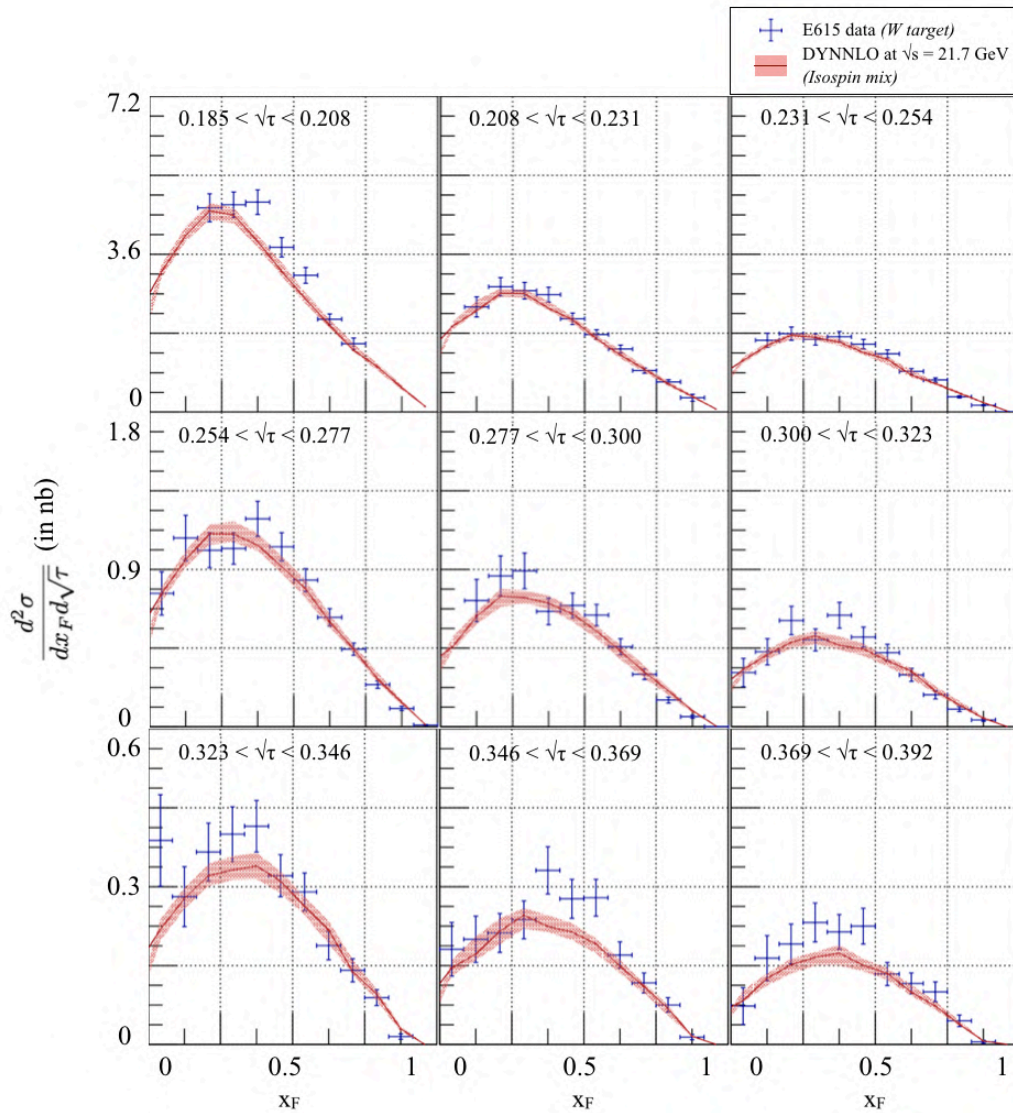


Figure 26.2: Comparison between E615 cross-section per bin of $\sqrt{\tau}$ and x_F with DYNLO calculation

Extrapolation of Drell-Yan Prediction at COMPASS Energy ($\sqrt{s} = 18.9$ GeV) Following the validation of the DYNNLO modification, a prediction of the cross-section using COMPASS data was made. In the case of a hybrid target, the proton and neutron fraction in the nucleus is modified as shown in Eq. 26.3. These formula are also compatible with solid case ($n_i = 1$), where the *microscopic cross-section* terms $\sum_i n_i \sigma_i$ just cancel.

$$P(p) = \frac{\left(\sum_i n_i \sigma_i \frac{Z_i}{A_i} \right)}{\left(\sum_i n_i \sigma_i \right)} \quad P(n) = \frac{\left(\sum_i n_i \sigma_i \frac{N_i}{A_i} \right)}{\left(\sum_i n_i \sigma_i \right)} \quad (26.3)$$

where n_i is the molar fraction of the i-th compound in the hybrid target.

σ_i refers to the cross-section of the i-th compound of atomic mass A

$\sum_i n_i \sigma_i$ is known as the *microscopic cross-section* in the literature [131]

Finally, values in Tab. 27.2 are used to obtain a prediction of the cross-section $\pi^- A$ for each target of the COMPASS setup based on the combination of $\sigma(\pi^- p)$ and $\sigma(\pi^- n)$ cross-sections using DYNNLO³.

Table 26.1: Summary of the proton/neutron probability for the COMPASS 2015 targets.

Properties	PT Cell 1	PT Cell 2	Aluminum ²⁷ Al	Tungsten ¹⁸⁴ W
P(p)	0.580	0.577	0.481	0.402
P(n)	0.420	0.423	0.519	0.598

The predictions for the PT cells, ²⁷Al and ¹⁸⁴W targets at COMPASS energy using isospin mixing of the πp and πn cross-section are presented in Fig. 26.3. The main purpose of this figure is to evaluate the absolute scale between targets at NNLO. These distributions highlight the decrease of the cross-section as a function of the increase of N/A simply because $\sigma(\pi^- p) > \sigma(\pi^- n)$. An order of magnitude is given in average as follows :

$$\frac{\sigma_{\text{Cell 2}}}{\sigma_{\text{Cell 1}}} \simeq 1.00 \quad \frac{\sigma_{\text{Al}}}{\sigma_{\text{Cell 1}}} \simeq 0.94 \quad \frac{\sigma_{\text{W}}}{\sigma_{\text{Cell 1}}} \simeq 0.89 \quad \frac{\sigma_{\text{W}}}{\sigma_{\text{Al}}} \simeq 0.95$$

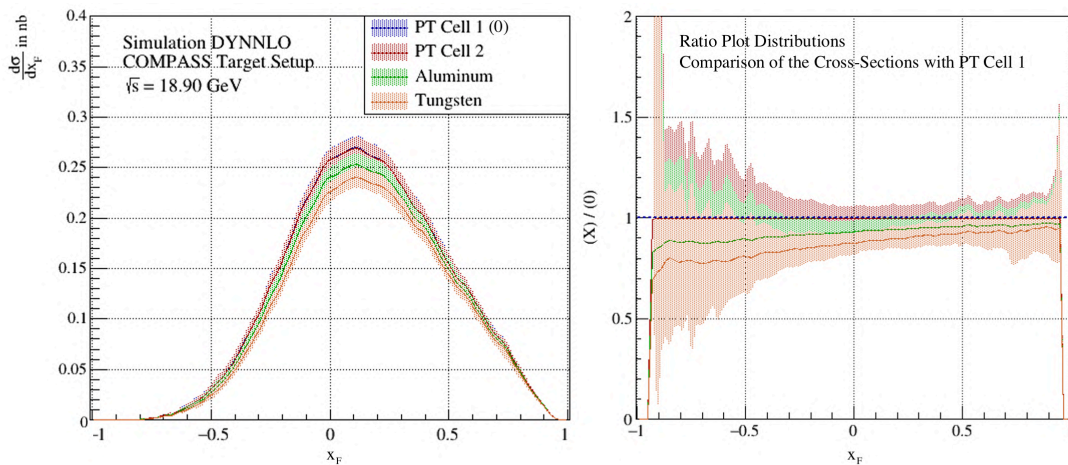


Figure 26.3: (a) Left: Prediction of Drell-Yan cross-section per nucleon for COMPASS 2015 setup integrated over $M \in [4.3 - 8.5]$ GeV/c² using GRVPI1xCT14NNLO at NNLO; (b) Right: Drell-Yan cross-section ratio compared with the PT cell 1

³Parton Level MC Simulation of vector boson cross-section production

26.3 Discussion on the Single Differential Cross-Sections $d\sigma/dx_F$

Although, the Drell-Yan cross-section was introduced and parametrized by only two parameters, often chosen as $(\sqrt{\tau}, x_F)$, the purpose of studying the integrated single differential cross-section is to have a first overview of the cross-section evaluated in this Ph.D. thesis using COMPASS data.

The acceptance correction used in this Ph.D. work includes the recent improvements in geometry description and 2D efficiency of detectors. Moreover, it is computed and applied to the extracted cross-section as a function of the following parameters $(Z_{vtx}, \sqrt{\tau}, x_F, q_T)$ with $4 \times 5 \times 11 \times 7$ bins as shown in Tab. 26.2. The binning is chosen in the limit of the COMPASS 2015 statistics. Additionally, it is also guided by the conclusions of the resolution studies, performed in Sec. 25.3.2.

Table 26.2: Summary of the binning chosen for the computation of the single differential cross-section extraction; The binning in mass just highlights a correspondence with $\sqrt{\tau}$ at $\sqrt{s} = 18.9$ GeV

Variable	Binning							
Z_{vtx} [cm]	[-294.5; -239.3]		[-219.5; -164.3]		[-63.5; -56.5]		[-30; -20]	
x_F	-0.20	-0.10	0.00	...	0.60	0.70	0.80	0.90
q_T [GeV/c]	0.00	0.40	0.68	0.95	1.25	1.70	3.00	5.00
$\sqrt{\tau}$	0.228	0.270	0.312	0.354	0.396	0.450	—	—
$M_{\mu\mu}$ [GeV/c ²]	4.30	5.10	5.90	6.70	7.50	8.50	—	—

The extraction of the simple differential Drell-Yan cross-section $\frac{d\sigma}{dx_F}$ for each target in the high mass region, $4.3 < M_{\mu\mu}/(\text{GeV}/c^2) < 8.5$, is shown in Fig. 26.4 and compared with NNLO predictions.

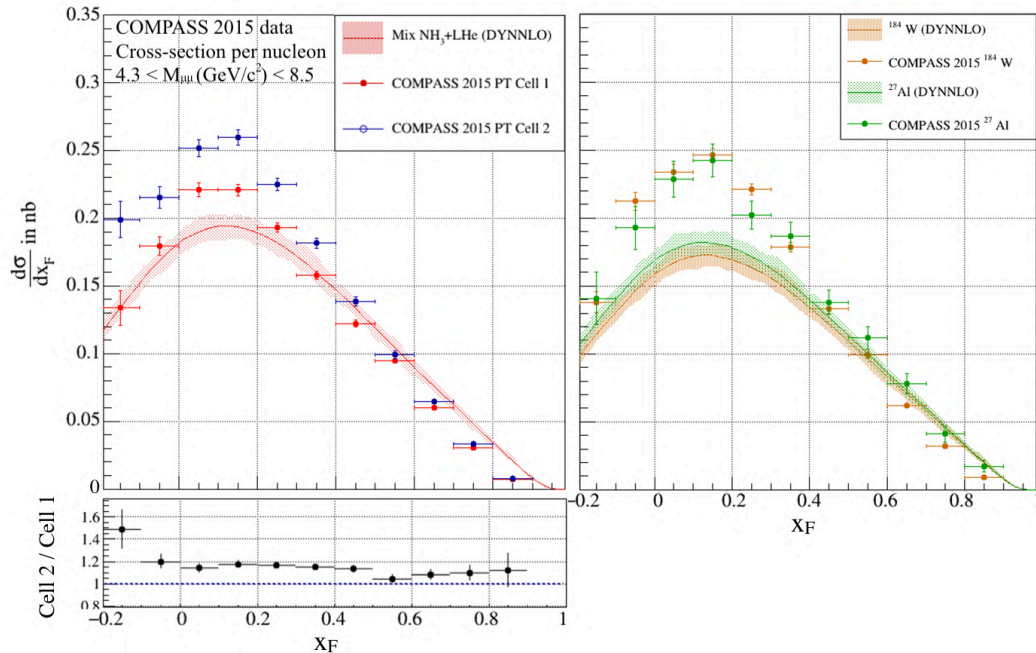


Figure 26.4: (a) Left: Hybrid target (PT Cells) cross-sections compared with their corresponding DYNNLO prediction; (b) Right: Comparison of the nuclear targets, namely ^{27}Al , ^{184}W (First 10 cm) with DYNNLO simulations

Discussion about the results on PT cells. In Fig. 26.4a, PT cells are compared to each other in the ratio plot. As a first observation, the cross-section per nucleon for the first PT cell appears to

be lower compared to the second cell. This difference in the cross-section highlights a discrepancy of about 15% on average. In spite of the target topology study in Sec. 24.3.4, the clear observation of this discrepancy might find an explanation in the difficulty of filling the hybrid targets. Assuming that the first target is fully filled, a difference in weight about 50 g between the two cells refers to 1 mm of missing material along the top of the 55 mm long target. Consequently, the resolution along Z most likely limited the tomography study. However, the assumption of the target homogeneity has a strong impact on the overall renormalization. A possible confirmation of this problem and further information might be obtained based on the analysis of the 2018 data and would then be corrected in the 2015 data. At this stage of the analysis only, an additional uncertainty of 15% is attributed to the second PT cell density.

As a second observation in Fig. 26.4a, the first cell is in better agreement compared to the second cell regarding the DYNNLO predictions. However, the first cell shows a higher cross-section at $x_F = 0.1$. This increase has been attributed to dimuon background contamination, which is already accounted in the list of the systematic uncertainty and will be consequently discussed later as a function of the double differential cross-section in Sec.27.1.

Discussion about the results on nuclear targets. In Fig. 26.4b, the results of the ^{27}Al and ^{184}W cross-sections are compared in three different ways. First, the comparison relatively to each other shows a reasonably good agreement for each data point. Moreover, these measured cross-sections are now compared with their DYNNLO prediction at $\sqrt{s} = 18.9$ GeV, respectively. These calculations predict a larger cross-section per nucleon for ^{27}Al compared to ^{184}W . However, these data seem to exhibit this feature only in the high x_F region, compared to ^{184}W cross-section.

Second comparison, the absolute renormalization of both nuclear targets appears to be larger than expected compared to the calculation. This discrepancy might partially find an origin in the flux normalization, and more precisely, beam absorption. This correction might require to include pion re-interaction effects (secondary Drell-Yan events) to extract a more accurate absolute cross-section value and shape for the distribution. This discrepancy will mainly be attributed to the dimuon background contamination. However, this global renormalization will also be discussed later, as a function of the double differential cross-section in Sec.27.1.

Finally, the last possible comparison would be with PT Cell1, which is an A -dependent result. This comparison is limited by its systematic uncertainty due to beam absorption. Indeed, the beam crosses a large material budget, after the PT Cell 1, before reaching the nuclear targets. This results in an approximative control of the beam intensity, which is insufficient to perform an A -dependence study. However, this systematic reduces in the case of the comparison between ^{27}Al and ^{184}W . Indeed, in this case, as there is no material between ^{27}Al and ^{184}W , the uncertainty induced by the material budget before the aluminum target is expected to cancel out by computing the ratio between ^{27}Al and ^{184}W .

26.4 Summary of the Final Uncertainties

The summary of the systematic uncertainty is shown in Tab. 26.3. Each line was detailed throughout this Ph.D. work. It shows the overall systematic uncertainty that can be combined with the statistical one using a quadratic sum. Finally, a specific systematic uncertainty for the A -dependence study will be quoted about 10% because of the cancellation of the beam attenuation uncertainty.

Table 26.3: Summary of the systematic uncertainties of the cross-section in the mass range between 4.3 GeV/c² and 8.5 GeV/c². The luminosity uncertainty includes also deadtime uncertainties. The relative target density uncertainty refers to the discrepancy between PT cell 1 and PT cell 2.

Additionally, these systematics might varies with the kinematics.

	Uncertainty target by target			
Systematic uncertainties	PT Cell 1	PT Cell 2	²⁷ Al	¹⁸⁴ W (10 cm)
Luminosity	7%	7%	7%	8%
Acceptance (Generator Model)	5%	5%	5%	5%
Background Contamination	3%	3%	1%	7%
Relative Target Density	–	+15%	–	–
Total uncertainty	±9%	+18% (-9%)	±9%	±12%

27 | Results: Extraction of the Drell-Yan 2015 Cross-Sections

27.1 Study of the Double Differential Drell-Yan Cross-Sections

The study of the double differential Drell-Yan cross-section in bins of x_F and $\sqrt{\tau}$ is a more accurate representation of the Drell-Yan cross-section. The differential cross-section using COMPASS data will be first compared with E615 data in few specific bins in τ . In a second time, the result will be extended on the complete kinematic range of COMPASS data.

27.1.1 Comparison with E615 data and DYNNLO simulation

The differential cross-section of the COMPASS 2015 data has a large overlap in kinematic variables with the results from E615 [45]. E615 data are Drell-Yan events originating from the interaction between a 252-GeV π^- beam and a ¹⁸⁴W target. The difference in the beam energy compared to COMPASS is large, the cross-section per nucleon will be rescaled as shown in Eq. 27.1, using the squared center-of-mass energy, denoted s . For COMPASS, $s_{\text{NA58}} = 356 \text{ GeV}^2$ and for E615, $s_{\text{E615}} = 473 \text{ GeV}^2$.

$$s \frac{d\sigma}{d\sqrt{\tau} dx_F} = \frac{1}{\sqrt{\tau}} \times \frac{2x_1 x_2}{x_1 + x_2} F(x_1, x_2) \quad (27.1)$$

The Drell-Yan cross-section is presented in a restricted range matching with E615 binning. The acceptance is computed in bins of $(Z_{vtx}, \sqrt{\tau}, x_F, q_T)$ with $4 \times 5 \times 11 \times 7$ bins as shown in Tab. 27.10.

Table 27.1: Summary of binning chosen for the computation of the double differential Drell-Yan cross-section extraction in bins of E615. The binning in mass just highlights a correspondence with $\sqrt{\tau}$ at $\sqrt{s} = 18.9 \text{ GeV}$ for COMPASS and 21.74 GeV for E615

Variable	Binning							
$Z_{vtx} [\text{cm}]$	[-294.5; -239.3]		[-219.5; -164.3]		[-63.5; -56.5]		[-30; -20]	
x_F	-0.20	-0.10	0.00	...	0.60	0.70	0.80	0.90
$q_T [\text{GeV}/c]$	0.00	0.40	0.68	0.95	1.25	1.70	3.00	5.00
$\sqrt{\tau}$	0.231	0.254	0.277	0.300	0.323	0.369	–	–
$M_{\mu\mu} [\text{GeV}/c^2] (\sqrt{s} = 18.90 \text{ GeV})$	4.36	4.80	5.23	5.67	6.10	6.97	–	–
$M_{\mu\mu} [\text{GeV}/c^2] (\sqrt{s} = 21.70 \text{ GeV})$	5.02	5.52	6.02	6.52	7.02	8.02	–	–

Discussion about the results on ^{184}W . Fig. 27.1 introduces the rescaled double differential cross-section in bins of $\sqrt{\tau}$ and x_F extracted from the COMPASS $\pi^- \text{W}$ data (in red) and for E615 data (in blue). Additionally, the error band shown in the figure takes into account the error on the PDF of the proton only. In the two first bins, namely $0.231 < \sqrt{\tau} < 0.254$ and $0.254 < \sqrt{\tau} < 0.277$, especially the small- x region ($-0.2 < x_F < 0.1$) the COMPASS data overshoots the prediction, while E615 data presents a quite good agreement. This discrepancy reduces as the mass increases, as showed by the ratio plot of the COMPASS data with the E615 data. Therefore, a reasonable agreement between E615 data and the COMPASS 2015 data is visible after the second bin in $\sqrt{\tau}$.

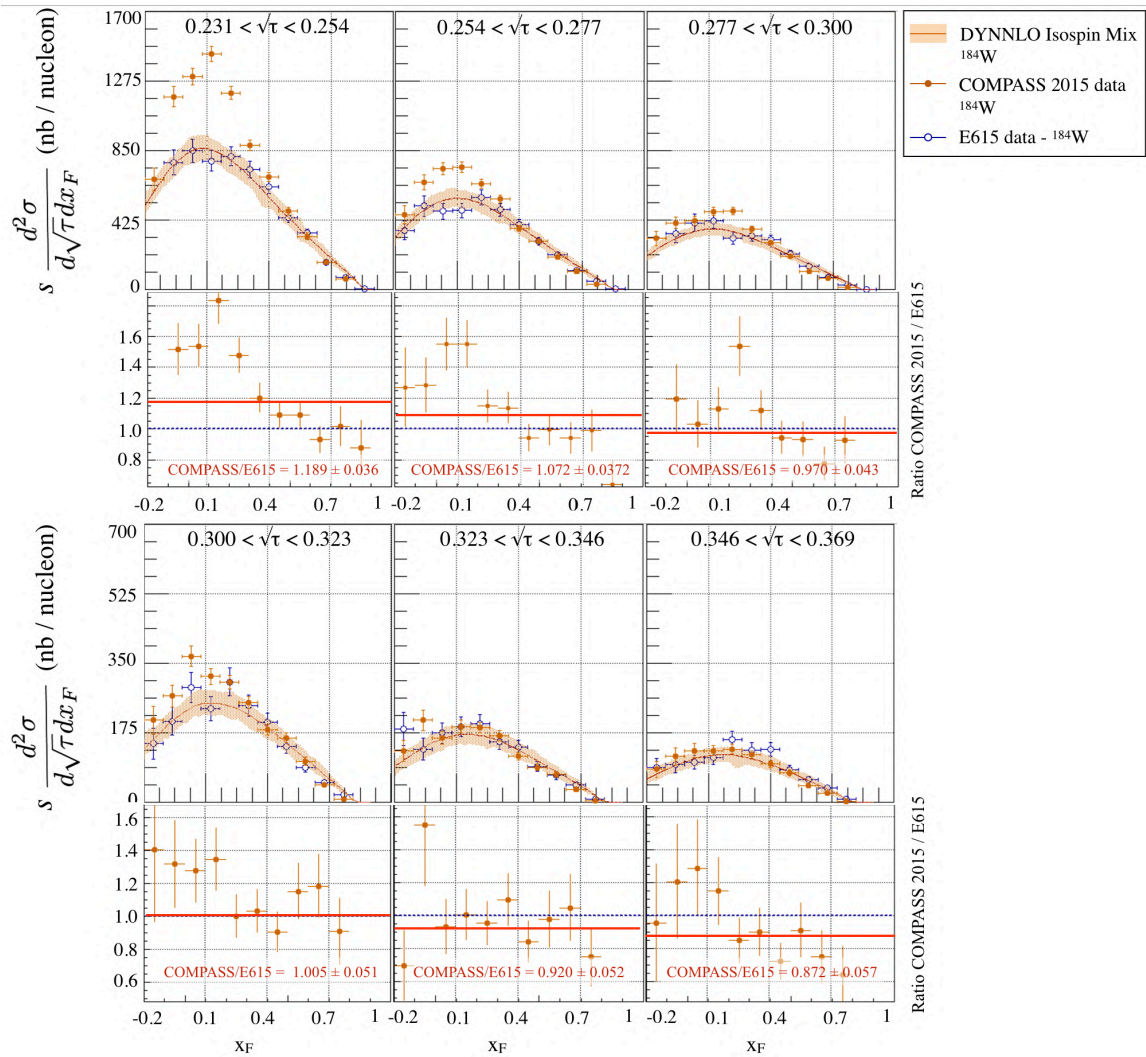


Figure 27.1: Comparison of the Drell-Yan cross-section per nucleon for the ^{184}W target, compared with E615 cross-section [45] and the DYNLO predictions, as a function of x_F in bin of $\sqrt{\tau}$

The two data sets, COMPASS and E615 data, show similar behavior regardless of the absolute normalization, especially at high- x_F , where both cross-sections present a similar fall-off compared to DYNLO predictions a slightly faster decrease with x_F is observed in all bins of $\sqrt{\tau}$. From COMPASS 2015 data, the dimuon background is expected to be slightly larger in this kinematic region. Therefore, this excess might be an indication of the background contamination already taken into account in the list of systematic uncertainties.

Discussion about the results on PT Cells Figure. 27.2 presents the comparison of the hybrid PT targets compared with the prediction at COMPASS energy. As a first observation, the large difference between cells is also confirmed as a function of the double differential cross-section and visible in the ratio plot which shows a constant ratio between the two cells.

Similarly to the ^{184}W , both cell 1 and cell 2 are expected to suffer from an increase of the background in the two first bins due to mainly J/Ψ contamination. However, the last bins show a reasonable agreement in comparison to the DYNNLO predictions.

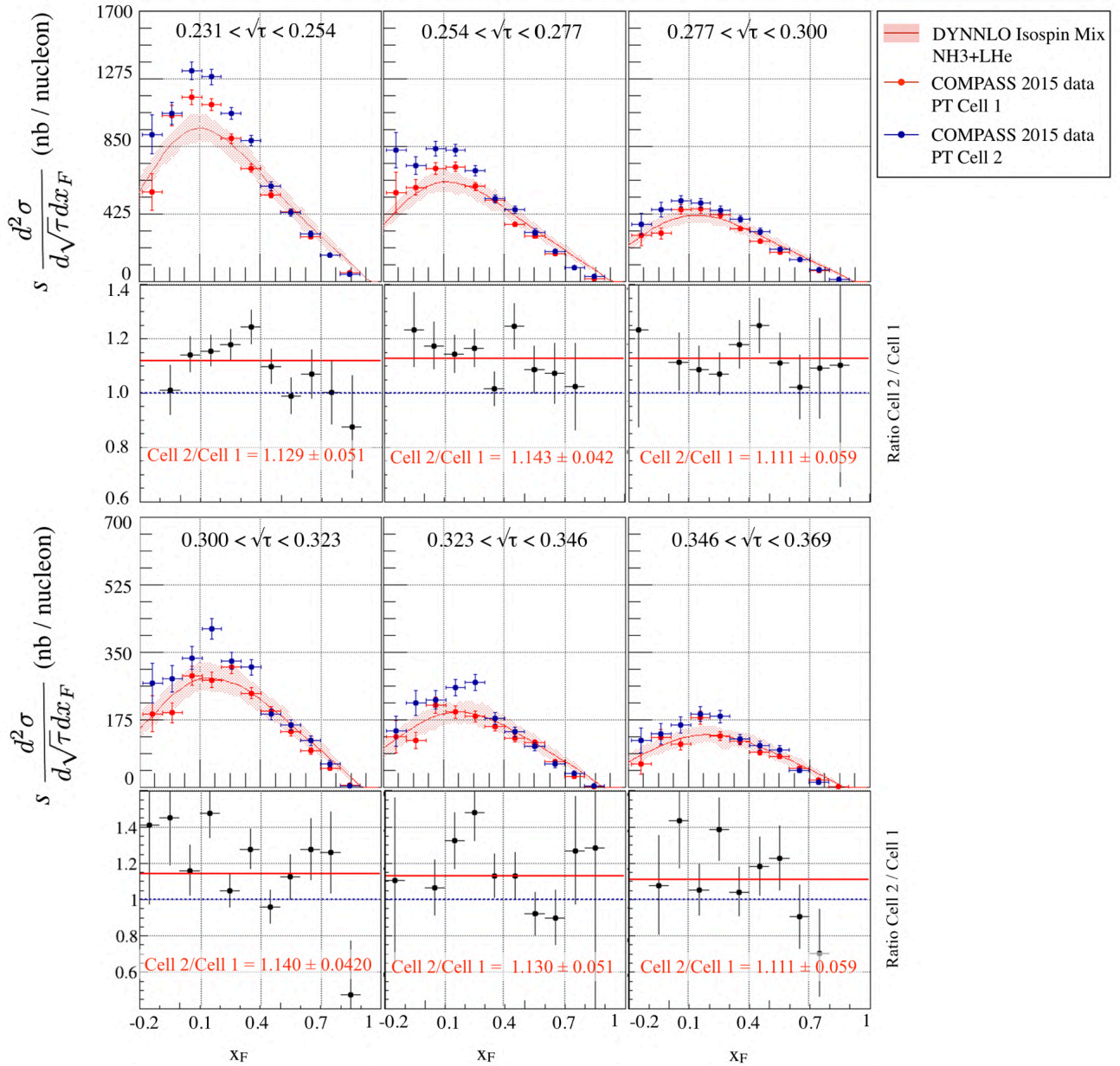


Figure 27.2: Comparison of the Drell-Yan cross-section per nucleon for the two PT cells, compared with the DYNNLO predictions as a function of x_F in bin of $\sqrt{\tau}$

Discussion about the results on ^{27}Al . Similarly to other targets, the first bin suffers from background contamination at lower mass. This target is simply compared with its DYNNLO prediction. Other bins appear to be in reasonably good agreement.

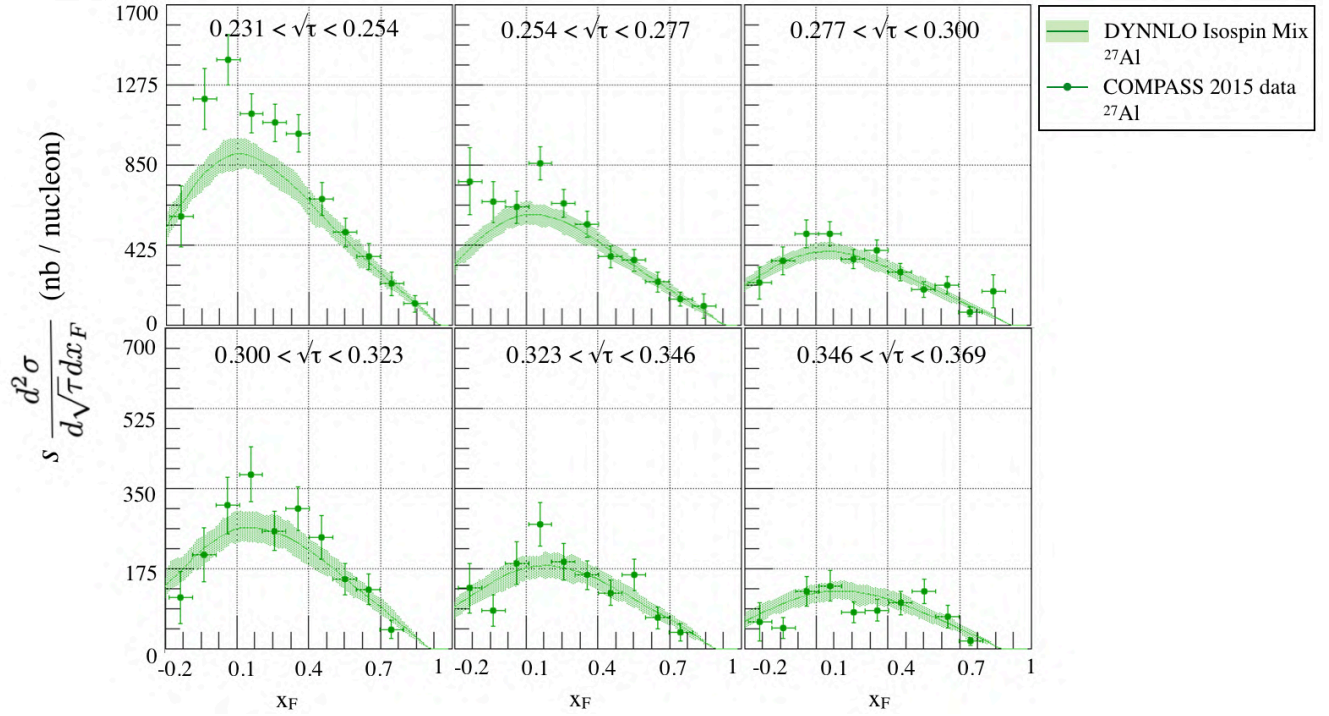


Figure 27.3: Comparison of the COMPASS ^{27}Al target results with the DYNNLO predictions as a function of x_F in bin of $\sqrt{\tau}$

27.1.2 Cross-Section $d^2\sigma/d\sqrt{\tau}dx_F$ in the COMPASS Kinematic Range

The result shown in the previous section (Fig. 27.1) were restricted to 6 bins of $\sqrt{\tau}$ in common with E615; however this result can be enlarged to cover a wider range in $\sqrt{\tau}$. In this section, the extraction of the Drell-Yan cross-section using COMPASS 2015 data is performed using an acceptance correction computed as a function of $(Z_{vtx}, \sqrt{\tau}, x_F, q_T)$ with $4 \times 10 \times 10 \times 7$ bins.

Table 27.2: Summary of the binning for the double differential Drell-Yan cross-section. The binning in mass just highlights a correspondence with $\sqrt{\tau}$ at $\sqrt{s} = 18.9$ GeV for COMPASS

Variable	Binning							
Z_{vtx} [cm]	[-294.5; -239.3]		[-219.5; -164.3]		[-63.5; -56.5]		[-30; -20]	
x_F	-0.20	-0.10	0.00	...	0.60	0.70	0.80	0.90
q_T [GeV/c]	0.00	0.40	0.68	0.95	1.25	1.70	3.00	5.00
$\sqrt{\tau}$	0.228	0.270	0.312	0.354	0.396	0.450	–	–
$M_{\mu\mu}$ [GeV/c ²] ($\sqrt{s} = 18.90$ GeV)	4.30	5.10	5.90	6.70	7.50	8.50	–	–

The result of the target by target comparison as a function of x_F in bins of $\sqrt{\tau}$ is presented in Fig. 27.4. These plots are staggered for visibility to highlight the similar trend target by target of the differential cross-sections per nucleon of each bin, and the conservation of the scale from one bin to the other in the limit of the statistics available. Values are presented in Tab. 27.3 and Tab. 27.4 as a function of the $\sqrt{\tau}$ and x_F .

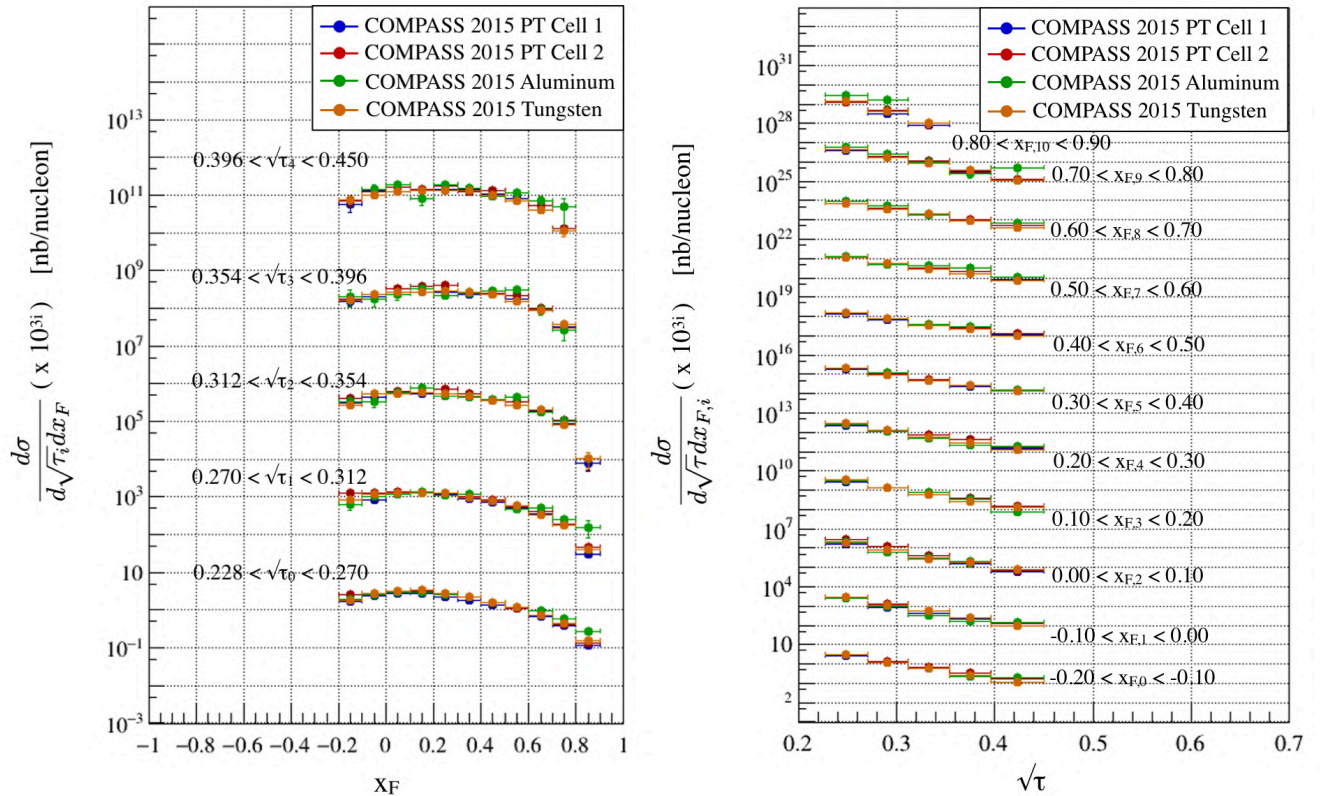


Figure 27.4: (a) Left: Comparison target by target as a function of x_F in bins of $\sqrt{\tau}_i$; (b) Right: Comparison target by target as a function of $\sqrt{\tau}$ in bins of $x_{F,i}$

27.1.3 Summary Table

Table 27.3: Double differential cross-section $d^2\sigma/dx_F d\sqrt{\tau}$ using COMPASS 2015 data. The errors shown are statistical only; there is an additional 9%, 18%, 9%, and 12% overall systematic uncertainty on the PT Cell 1 ($P_{F,1} = 0.5657$), PT Cell 2 ($P_{F,2} = 0.4797$), ^{27}Al , ^{184}W cross-sections, respectively.

COMPASS 2015 data				$\pi^- A \rightarrow \mu^+ \mu^- X$		$P_{\text{beam}} = 190 \text{ GeV/c}$	
Table 1/2							
				$d^2\sigma/dx_F d\sqrt{\tau}$ (in nb/nucleon)			
$\sqrt{\tau}$		x_F		PT Cell 1	PT Cell 2	^{27}Al	^{184}W (10 cm)
0.227 0.270	—	−0.20 −0.10		1.6522 ± 0.2360	2.6645 ± 0.2456	2.0111 ± 0.3519	1.8149 ± 0.1380
		−0.10 −0.00		2.4845 ± 0.1230	2.7207 ± 0.1330	2.6432 ± 0.2836	2.8272 ± 0.1175
		−0.00 0.10		2.8259 ± 0.0905	3.2291 ± 0.1062	3.0588 ± 0.2384	3.1510 ± 0.0934
		0.10 0.20		2.7577 ± 0.0732	3.2286 ± 0.0907	3.0656 ± 0.2087	3.4092 ± 0.0862
		0.20 0.30		2.2813 ± 0.0572	2.6029 ± 0.0732	2.6465 ± 0.1867	2.8668 ± 0.0732
		0.30 0.40		1.8354 ± 0.0478	2.1793 ± 0.0639	2.2438 ± 0.1759	2.2226 ± 0.0620
		0.40 0.50		1.3590 ± 0.0400	1.5897 ± 0.0533	1.5245 ± 0.1527	1.6013 ± 0.0531
		0.50 0.60		1.0758 ± 0.0360	1.1277 ± 0.0454	1.2252 ± 0.1431	1.1797 ± 0.0464
		0.60 0.70		0.6926 ± 0.0294	0.7379 ± 0.0373	0.9327 ± 0.1354	0.7512 ± 0.0379
		0.70 0.80		0.3807 ± 0.0227	0.4231 ± 0.0296	0.5850 ± 0.1159	0.4297 ± 0.0323
—	0.80 0.90		0.1201 ± 0.0124	0.1328 ± 0.0163	0.2800 ± 0.0864	0.1526 ± 0.0211	
0.270 0.312	—	−0.20 −0.10		0.8213 ± 0.1358	1.3072 ± 0.1651	0.6307 ± 0.1772	0.8379 ± 0.0879
		−0.10 −0.00		0.8414 ± 0.0699	1.2937 ± 0.0938	1.0414 ± 0.1605	1.1517 ± 0.0710
		−0.00 0.10		1.2907 ± 0.0622	1.3912 ± 0.0726	1.1818 ± 0.1395	1.2510 ± 0.0585
		0.10 0.20		1.2746 ± 0.0507	1.3972 ± 0.0608	1.3354 ± 0.1314	1.2741 ± 0.0507
		0.20 0.30		1.1726 ± 0.0423	1.2676 ± 0.0515	1.0929 ± 0.1129	1.2673 ± 0.0468
		0.30 0.40		0.9170 ± 0.0340	1.0296 ± 0.0441	1.1655 ± 0.1174	0.9959 ± 0.0390
		0.40 0.50		0.7213 ± 0.0290	0.8119 ± 0.0379	0.7553 ± 0.0923	0.7599 ± 0.0337
		0.50 0.60		0.5217 ± 0.0244	0.5469 ± 0.0311	0.4864 ± 0.0806	0.6014 ± 0.0306
		0.60 0.70		0.3560 ± 0.0204	0.4098 ± 0.0272	0.5135 ± 0.0826	0.3427 ± 0.0231
		0.70 0.80		0.1819 ± 0.0145	0.1942 ± 0.0192	0.2480 ± 0.0605	0.1766 ± 0.0167
—	0.80 0.90		0.0311 ± 0.0062	0.0458 ± 0.0099	0.1546 ± 0.0738	0.0415 ± 0.0086	
0.312 0.354	—	−0.20 −0.10		0.3055 ± 0.0658	0.4245 ± 0.0757	0.3227 ± 0.1084	0.2728 ± 0.0444
		−0.10 −0.00		0.4348 ± 0.0474	0.5576 ± 0.0573	0.3246 ± 0.0844	0.5359 ± 0.0500
		−0.00 0.10		0.5554 ± 0.0410	0.6445 ± 0.0498	0.5901 ± 0.0977	0.5612 ± 0.0377
		0.10 0.20		0.5622 ± 0.0343	0.7835 ± 0.0463	0.7532 ± 0.1004	0.5670 ± 0.0331
		0.20 0.30		0.5650 ± 0.0301	0.7087 ± 0.0404	0.4782 ± 0.0704	0.5453 ± 0.0292
		0.30 0.40		0.4844 ± 0.0248	0.5597 ± 0.0322	0.4514 ± 0.0646	0.4840 ± 0.0261
		0.40 0.50		0.3750 ± 0.0205	0.3810 ± 0.0252	0.3911 ± 0.0592	0.3572 ± 0.0221
		0.50 0.60		0.3294 ± 0.0191	0.3251 ± 0.0234	0.4373 ± 0.0679	0.2765 ± 0.0197
		0.60 0.70		0.1935 ± 0.0142	0.1830 ± 0.0177	0.1803 ± 0.0442	0.1973 ± 0.0163
		0.70 0.80		0.0907 ± 0.0097	0.1063 ± 0.0136	0.1014 ± 0.0361	0.0815 ± 0.0104
—	0.80 0.90		0.0079 ± 0.0030	0.0103 ± 0.0050	—	0.0105 ± 0.0046	

Table 27.4: Double differential cross-section $d^2\sigma/dx_F d\sqrt{\tau}$ using COMPASS 2015 data. The errors shown are statistical only; there is an additional 9%, 18%, 9%, and 12% overall systematic uncertainty on the PT Cell 1 ($P_{F,1} = 0.5657$), PT Cell 2 ($P_{F,2} = 0.4797$), ^{27}Al , ^{184}W cross-sections, respectively.

COMPASS 2015 data				$\pi^- A \rightarrow \mu^+ \mu^- X$		$P_{\text{beam}} = 190 \text{ GeV}/c$	
Table 2/2							
				$d^2\sigma/dx_F d\sqrt{\tau}$ (in nb/nucleon)			
$\sqrt{\tau}$		x_F		PT Cell 1	PT Cell 2	^{27}Al	^{184}W (10 cm)
0.3540	0.3960	−0.20	−0.10	0.1584 ± 0.0445	0.1818 ± 0.0463	0.2053 ± 0.0997	0.1692 ± 0.0363
—	—	−0.10	−0.00	0.2082 ± 0.0328	0.2397 ± 0.0386	0.1707 ± 0.0618	0.2368 ± 0.0321
—	—	−0.00	0.10	0.2750 ± 0.0290	0.3276 ± 0.0361	0.2265 ± 0.0578	0.2696 ± 0.0269
—	—	0.10	0.20	0.3300 ± 0.0273	0.3961 ± 0.0340	0.3412 ± 0.0602	0.2675 ± 0.0224
—	—	0.20	0.30	0.2717 ± 0.0211	0.4120 ± 0.0307	0.2161 ± 0.0440	0.2821 ± 0.0211
—	—	0.30	0.40	0.2399 ± 0.0178	0.2702 ± 0.0220	0.2576 ± 0.0484	0.2724 ± 0.0193
—	—	0.40	0.50	0.2367 ± 0.0165	0.2595 ± 0.0217	0.2915 ± 0.0549	0.2325 ± 0.0172
—	—	0.50	0.60	0.1721 ± 0.0136	0.2163 ± 0.0191	0.3062 ± 0.0535	0.1575 ± 0.0139
—	—	0.60	0.70	0.0998 ± 0.0101	0.1021 ± 0.0128	0.0948 ± 0.0306	0.0904 ± 0.0109
—	—	0.70	0.80	0.0315 ± 0.0055	0.0302 ± 0.0069	0.0263 ± 0.0123	0.0382 ± 0.0066
0.396	0.450	−0.20	−0.10	0.0564 ± 0.0214	0.0720 ± 0.0226	—	0.0777 ± 0.0196
—	—	−0.10	−0.00	0.1371 ± 0.0237	0.1224 ± 0.0230	0.1431 ± 0.0484	0.0993 ± 0.0175
—	—	−0.00	0.10	0.1201 ± 0.0170	0.1631 ± 0.0216	0.1925 ± 0.0483	0.1217 ± 0.0154
—	—	0.10	0.20	0.1435 ± 0.0156	0.1420 ± 0.0175	0.0796 ± 0.0268	0.1363 ± 0.0144
—	—	0.20	0.30	0.1437 ± 0.0138	0.1719 ± 0.0175	0.1839 ± 0.0366	0.1324 ± 0.0129
—	—	0.30	0.40	0.1431 ± 0.0120	0.1275 ± 0.0136	0.1560 ± 0.0330	0.1307 ± 0.0117
—	—	0.40	0.50	0.1083 ± 0.0097	0.1309 ± 0.0134	0.0956 ± 0.0235	0.0991 ± 0.0097
—	—	0.50	0.60	0.0797 ± 0.0078	0.0712 ± 0.0090	0.1151 ± 0.0291	0.0693 ± 0.0076
—	—	0.60	0.70	0.0389 ± 0.0054	0.0515 ± 0.0074	0.0691 ± 0.0231	0.0392 ± 0.0057
—	—	0.70	0.80	0.0117 ± 0.0028	0.0134 ± 0.0040	0.0488 ± 0.0345	0.0112 ± 0.0034

27.2 A-Dependence in Pion-Nucleus Interactions

In this section, the A-dependence of the Drell-Yan cross-section, introduced in the Sec. 4.3 Ch. I, will be discussed using aluminum and tungsten targets. This test is performed to evaluate the reliability of the cross-section measurement and verify some expected results.

27.2.1 Evaluation of the α parameter

The evaluation of the α parameter will be presented as a function of x_F , q_T , and $M_{\mu\mu}$. First, the Drell-Yan cross-sections for the two nuclear targets are measured based on the event selection previously introduced in Sec. 24.2, in the mass range, $4.3 < M_{\mu\mu}/(\text{GeV}/c^2) < 8.5$. The acceptance is computed based on the following parameters (Z_{vtx} , $\sqrt{\tau}$, x_F , q_T) with reasonable binning. Due to the limited statistics of the aluminum events, a more appropriate choice of binning is used in this section. This binning is computed to favor the explicit variable of the corresponding differential cross-section, as shown in Tab. 27.5.

Table 27.5: Summary of the binning for evaluation of the α parameter.

Variable	Binning							
Z_{vtx} [cm]	[-294.5; -239.3]	[-219.5; -164.3]	[-63.5; -56.5]	[-30; -20]				
$M_{\mu\mu}$ (if $d\sigma/dM_{\mu\mu}$)	4.30	4.70	5.10	5.50	...	7.50	7.90	8.50
$M_{\mu\mu}$ (else)	4.30	5.10	5.90	6.70	7.50	8.50	–	–
x_F (if $d\sigma/dx_F$)	-0.20	-0.10	0.00	0.10	...	0.70	0.80	0.90
x_F (else)	-0.20	0.00	0.20	0.40	0.60	0.80	0.90	–
q_T [GeV/c] (if $d\sigma/dq_T$)	0.00	0.25	0.50	0.75	...	4.50	4.75	5.00
q_T [GeV/c] (else)	0.00	0.40	0.68	0.95	1.25	1.70	3.00	5.00

In this analysis, the α parameter is evaluated using only ^{27}Al and ^{184}W target events to reduce the systematic uncertainty. As previously discussed in Sec. 26.4, a systematic uncertainty in the determination of the α parameter is about 10%. In consequence of the background contamination discussed in Sec. 27.1, an attempt to reject the low mass region was performed and the extracted α -parameters showed similar profiles. Finally, the result of the $\alpha(^{184}\text{W}/^{27}\text{Al})$ parameter for various dependences is presented in Fig. 27.5 and a summary table is shown in Tab. 27.6.

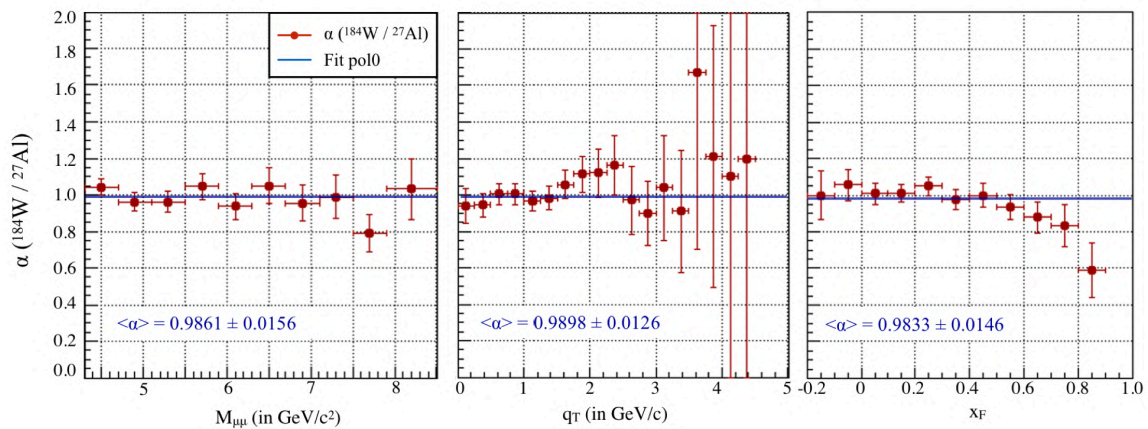


Figure 27.5: Evaluation of the α parameter as a function of $M_{\mu\mu}$ (left), q_T (middle) and x_F (right). The value of α is fitted by a straight line in red

As a first observation, the α -value as a function of the $M_{\mu\mu}$ appears to be constant. However, both q_T and x_F distributions show systematic trends that should be compared with prediction. As a reminder,

Fig. 27.6 shows the energy-loss effect and an illustration of the q_T dependence due to the Cronin effect. The q_T dependence presents some non-linear trend and an overall increasing going toward the high- q_T region. Moreover, the x_F dependence shows an interesting profile, which is expected according to the theory presented in the BDMPS model. Nonetheless, this first look requires to be much further studied in order to reach some precise conclusions, and it is beyond the scope of this Ph.D. work. Indeed, some refined corrections, such as the uncertainty on the pion PDF or the re-interaction of the beam might be additional uncertainties in the study of the α dependence, which should later be taken into account and further studied.

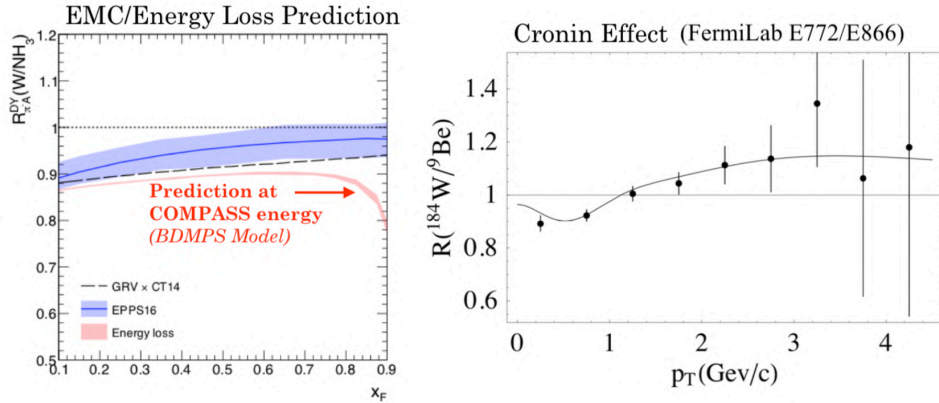


Figure 27.6: (a) Left: Energy loss prediction at COMPASS energy using the BDMPS formalism with the effects of LPM energy loss, which attempts to describe the energy loss of the quarks in the initial state [60]; (b) Right: Illustration of the Cronin effect as a function of the p_T distribution visible in the ratio plot between heavy and light targets [61].

Additionally, the mean value of α for each dependence is also presented in Fig. 27.5 and appears to be compatible with 1. In the past, the NA10 collaboration measured $\alpha_{\text{NA10}} = 0.998 \pm 0.006$ (stat.) ± 0.013 (sys.) and Ito *et al.* [31] measured $\alpha_{\text{Ito}} = 1.007 \pm 0.018$ (stat.) ± 0.028 (sys.). Consequently, the mean value for the extracted α value using COMPASS data is found compatible with past results.

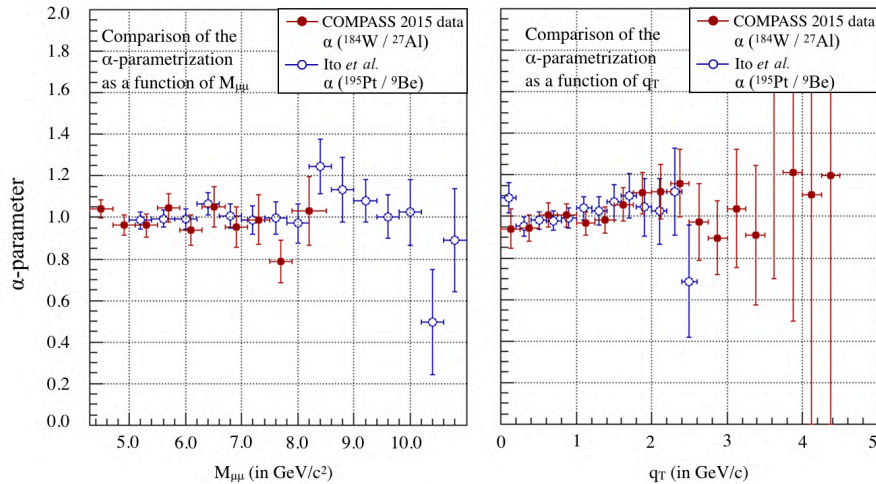


Figure 27.7: Extracted α parameter using $\sigma_W/\sigma_{\text{Al}}$ cross-sections as a function of x_F , q_T and $M_{\mu\mu}$. This extracted coefficients (in red) are compared with the coefficient from Ito *et al.* [31] (in blue)

The comparison of COMPASS data to Ito *et al.* for a kinematic dependence is also shown in Fig. 27.7. COMPASS reproduces very well the kinematic dependence observed by Ito *et al.* Only the $M_{\mu\mu}$ and q_T dependence were available. Finally, this comparison highlights similar trends in the A-dependence study in both COMPASS data and *et al.* results.

27.2.2 Summary Table

Table 27.6: Summary of the single differential Drell-Yan cross-sections for ^{27}Al and ^{184}W and the extracted α parameter. The errors shown are statistical only; there is an additional 9%, 12%, and 10% overall systematic uncertainty on the ^{27}Al cross-section, ^{184}W cross-section, and the α -parameter, respectively.

COMPASS 2015 data						$\pi^- A \rightarrow \mu^+ \mu^- X$		$P_{\text{beam}} = 190 \text{ GeV}/c$
						$d\sigma/dM$ (in nb/nuclei/GeV)		
$M_{\mu\mu}$		x_F		q_T		^{27}Al	^{184}W (10 cm)	α -parameter
4.30	4.70	-0.20	0.90	0.00	5.00	0.1322 ± 0.0055	0.1434 ± 0.0022	1.0423 ± 0.0437
4.70	5.10	—	—	—	—	0.0868 ± 0.0044	0.0807 ± 0.0016	0.9619 ± 0.0487
5.10	5.50	—	—	—	—	0.0575 ± 0.0034	0.0535 ± 0.0012	0.9618 ± 0.0563
5.50	5.90	—	—	—	—	0.0356 ± 0.0024	0.0388 ± 0.0011	1.0453 ± 0.0699
5.90	6.30	—	—	—	—	0.0275 ± 0.0021	0.0244 ± 0.0008	0.9372 ± 0.0722
6.30	6.70	—	—	—	—	0.0153 ± 0.0014	0.0168 ± 0.0007	1.0493 ± 0.0978
6.70	7.10	—	—	—	—	0.0138 ± 0.0014	0.0126 ± 0.0006	0.9543 ± 0.0969
7.10	7.50	—	—	—	—	0.0093 ± 0.0011	0.0091 ± 0.0005	0.9893 ± 0.1211
7.50	7.90	—	—	—	—	0.0090 ± 0.0012	0.0060 ± 0.0004	0.7878 ± 0.1010
7.90	8.50	—	—	—	—	0.0040 ± 0.0006	0.0043 ± 0.0003	1.0323 ± 0.1647
						$d\sigma/dx_F$ (in nb/nuclei/GeV)		
$M_{\mu\mu}$		x_F		q_T		^{27}Al	^{184}W (10 cm)	α -parameter
4.30	8.50	-0.20	-0.10	0.00	5.00	0.1382 ± 0.0184	0.1380 ± 0.0076	0.9991 ± 0.1332
—	—	-0.10	0.00	—	—	0.1890 ± 0.0151	0.2123 ± 0.0066	1.0564 ± 0.0843
—	—	0.00	0.10	—	—	0.2294 ± 0.0132	0.2339 ± 0.0053	1.0073 ± 0.0580
—	—	0.10	0.20	—	—	0.2417 ± 0.0119	0.2462 ± 0.0047	1.0092 ± 0.0497
—	—	0.20	0.30	—	—	0.2018 ± 0.0103	0.2211 ± 0.0041	1.0484 ± 0.0535
—	—	0.30	0.40	—	—	0.1862 ± 0.0099	0.1785 ± 0.0035	0.9777 ± 0.0522
—	—	0.40	0.50	—	—	0.1327 ± 0.0085	0.1330 ± 0.0030	0.9996 ± 0.0643
—	—	0.50	0.60	—	—	0.1119 ± 0.0082	0.0994 ± 0.0027	0.9370 ± 0.0684
—	—	0.60	0.70	—	—	0.0778 ± 0.0073	0.0619 ± 0.0021	0.8788 ± 0.0829
—	—	0.70	0.80	—	—	0.0440 ± 0.0062	0.0319 ± 0.0017	0.8320 ± 0.1166
—	—	0.80	0.90	—	—	0.0196 ± 0.0050	0.0091 ± 0.0010	0.5914 ± 0.1508
						$d\sigma/dq_T$ (in nb/nuclei/GeV)		
$M_{\mu\mu}$		x_F		q_T		^{27}Al	^{184}W (10 cm)	α -parameter
4.30	8.50	-0.20	0.90	0.00	0.25	0.0318 ± 0.0032	0.0283 ± 0.0012	0.9400 ± 0.0942
—	—	—	—	0.25	0.50	0.0841 ± 0.0057	0.0756 ± 0.0021	0.9443 ± 0.0637
—	—	—	—	0.50	0.75	0.1015 ± 0.0058	0.1028 ± 0.0023	1.0066 ± 0.0578
—	—	—	—	0.75	1.00	0.1058 ± 0.0059	0.1067 ± 0.0024	1.0045 ± 0.0562
—	—	—	—	1.00	1.25	0.0981 ± 0.0055	0.0920 ± 0.0021	0.9665 ± 0.0545
—	—	—	—	1.25	1.50	0.0762 ± 0.0050	0.0737 ± 0.0018	0.9829 ± 0.0649
—	—	—	—	1.50	1.75	0.0478 ± 0.0036	0.0533 ± 0.0015	1.0575 ± 0.0804
—	—	—	—	1.75	2.00	0.0280 ± 0.0025	0.0347 ± 0.0012	1.1120 ± 0.0990
—	—	—	—	2.00	2.25	0.0180 ± 0.0021	0.0226 ± 0.0010	1.1192 ± 0.1325
—	—	—	—	2.25	2.50	0.0107 ± 0.0015	0.0145 ± 0.0007	1.1602 ± 0.1625
—	—	—	—	2.50	2.75	0.0093 ± 0.0018	0.0088 ± 0.0006	0.9722 ± 0.1865
—	—	—	—	2.75	3.00	0.0057 ± 0.0011	0.0046 ± 0.0004	0.8971 ± 0.1762
—	—	—	—	3.00	3.25	0.0030 ± 0.0008	0.0033 ± 0.0003	1.0378 ± 0.2860
—	—	—	—	3.25	3.50	0.0021 ± 0.0008	0.0018 ± 0.0003	0.9107 ± 0.3359
—	—	—	—	3.50	3.75	0.0004 ± 0.0002	0.0014 ± 0.0003	1.6740 ± 0.9721
—	—	—	—	3.75	4.00	0.0004 ± 0.0003	0.0006 ± 0.0002	1.2134 ± 0.7187
—	—	—	—	4.00	4.25	0.0004 ± 0.0004	0.0005 ± 0.0001	1.1044 ± 1.1044
—	—	—	—	4.25	4.50	0.0001 ± 0.0001	0.0002 ± 0.0001	1.1953 ± 1.1953

27.3 Drell-Yan Cross-Sections at High- q_T

As the last verification, the study of the transverse momentum distribution is of great interest to understand the underlying mechanism induced by gluonic contributions. Moreover, the comparison with published results gives a further check for the extracted Drell-Yan cross-section.

27.3.1 Transverse Momentum Distributions

Various past experiments, such as E615, NA10, NA3 measured a mean transverse momenta of the muon pairs $\langle q_T \rangle$ larger than 1 GeV/c at different center-of-mass energy \sqrt{s} , as shown in Fig. 27.8 (right). Its dependence as a function of the $M_{\mu\mu}$, x_F variables might provide valuable input in the understanding of perturbative QCD effects. In Fig. 27.8, three distributions of the $\langle q_T^2 \rangle$ are presented. From this figure, a fall-off of the $\langle q_T^2 \rangle$ is observed as a function of x_F , while the dimuon mass dependence remains rather constant, with a slight increase toward larger masses.

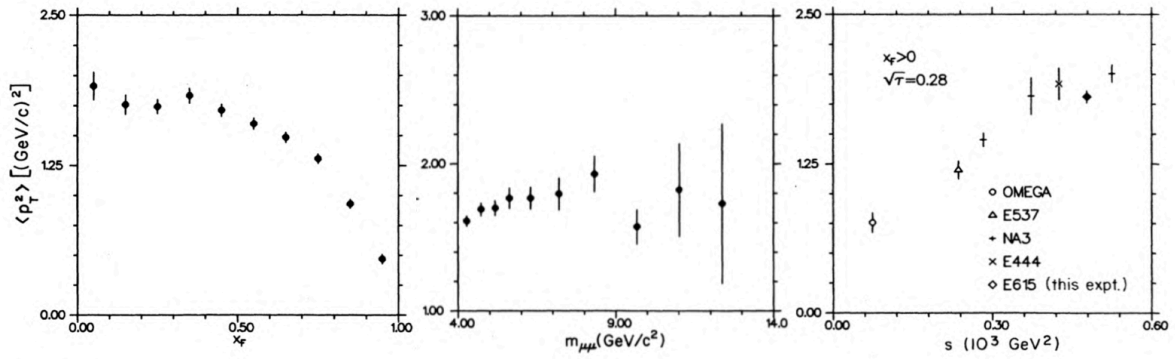


Figure 27.8: Mean squared transverse momentum, $\langle q_T^2 \rangle$ as a function of x_F (left), $M_{\mu\mu}$ (middle) and \sqrt{s} (right) from [45]

27.3.2 The *Kaplan Form*: *Ad-Hoc* Fitting Function

Similarly to the E615 analysis [45], an analysis of the COMPASS data and the available E615 data will be performed using an *ad-hoc* parametrization of the transverse momentum distribution for comparison purpose. As an introduction to the methodology to extract the $\langle q_T^2 \rangle$, an example of fit of the transverse momentum distribution, is given in Fig. 27.9 for ^{184}W .

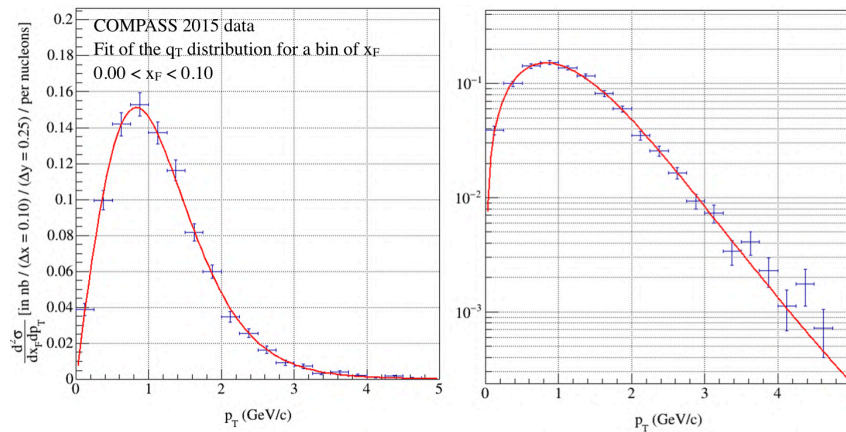


Figure 27.9: Example of Transverse momentum distribution q_T for ^{184}W as a function of q_T for a bin in x_F , with a linear Y-axis (left) and logarithmic Y-axis (right).

This distribution is fitted using a *Kaplan Form* defined by two parameters (a, b). In the previous example, the result of the fit provides a value of $\langle q_T^2 \rangle$ about 1.9 (GeV/c)^2 .

$$\frac{1}{2q_T} \times \frac{d\sigma}{dq_T} = a \left(1 + \frac{q_T^2}{b^2} \right)^{-6} \quad (27.2)$$

This form fits the full range of the q_T distribution simultaneously. Therefore, using the *Kaplan form*, we obtain an expression of $\langle q_T^2 \rangle$ independent of the absolute normalization:

$$\langle q_T^2 \rangle = \frac{1}{\int \frac{d\sigma}{dq_T} dq_T} \times \int q_T^2 \frac{d\sigma}{dq_T} dq_T = \frac{b^2}{4} \pm \frac{b}{2} \sigma_b \quad (27.3)$$

In this analysis, the differential cross-sections are computed as a function of the targets available at COMPASS. The extraction of $\langle q_T^2 \rangle$ does not depend on the global normalization. Therefore, despite the normalization issue between the two PT cells, the data are combined together in this section. Additionally, the data of the E615 experiment, being available in the range $4.05 < M_{\mu\mu}/(\text{GeV}/c^2) < 8.55$, were also re-fitted using the *Kaplan Form* to avoid inconsistency in the comparison between E615 and COMPASS data.

27.3.3 Studies as a function of x_F , $M_{\mu\mu}$, \sqrt{s}

An example of fit in bins of x_F and $M_{\mu\mu}$ is presented in Fig. 27.10 and Fig. 27.11 respectively. This fit matches as expected the experimental data both in the low- and high- q_T regions.

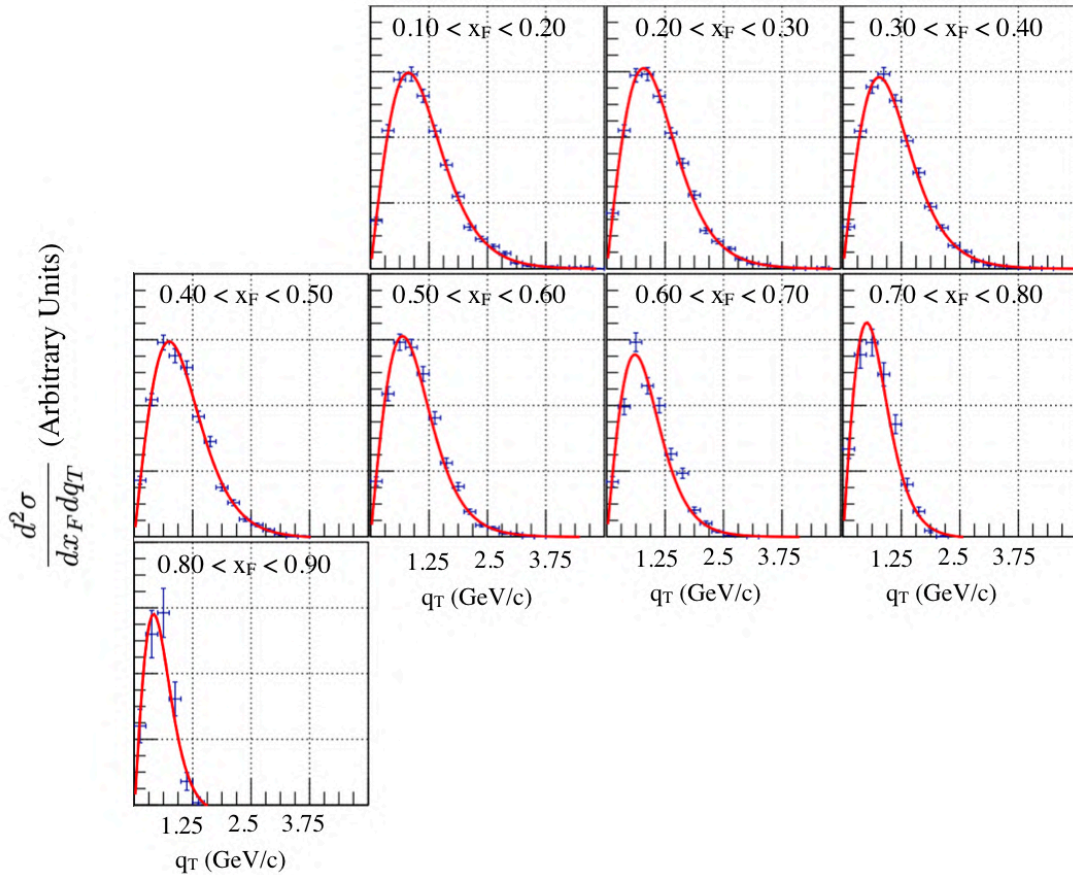


Figure 27.10: Fitting result of the transverse momentum distribution q_T in bins of x_F for PT cells

In Fig. 27.12, the comparison between COMPASS targets highlights a similar behavior either in bins

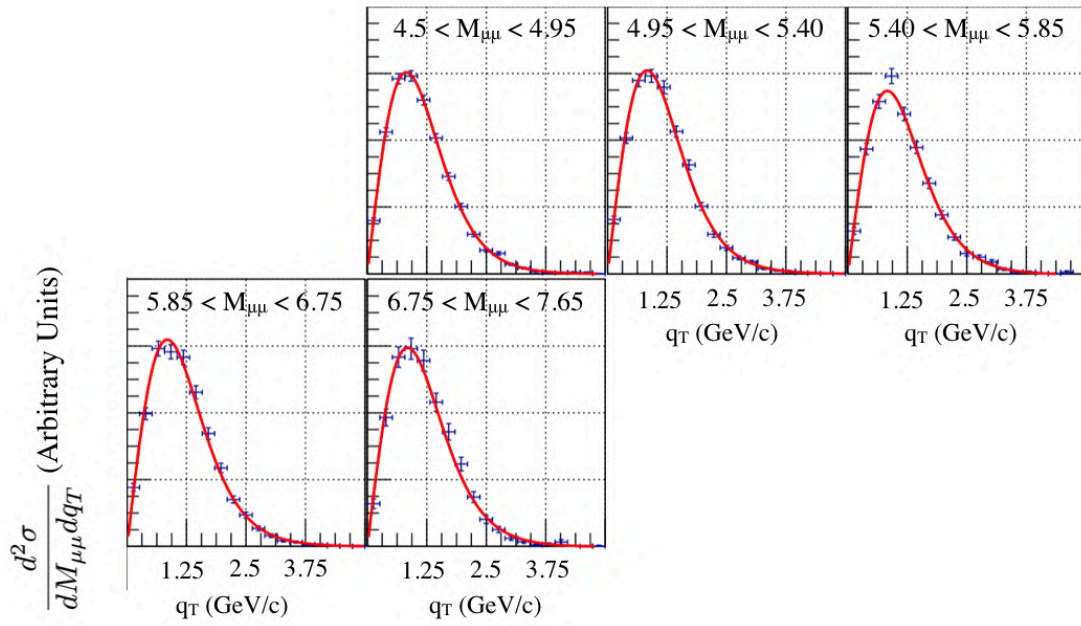


Figure 27.11: Fitting result of the transverse momentum distribution q_T in bins of $M_{\mu\mu}$ for PT cells

of x_F or $M_{\mu\mu}$. The $\langle q_T^2 \rangle$ as a function of x_F shows a large decreasing trend, while the M dependence is slightly increasing. In this extraction, the fit values of the aluminum show higher error bars, due to the limited statistics. This figure does not show clear evidence of an A-dependence between aluminum and tungsten, due to the way results are introduced and the large variation of the extracted $\langle q_T^2 \rangle$ for the ^{27}Al . Moreover, results obtained from COMPASS data compared with E615 data show similar trends.

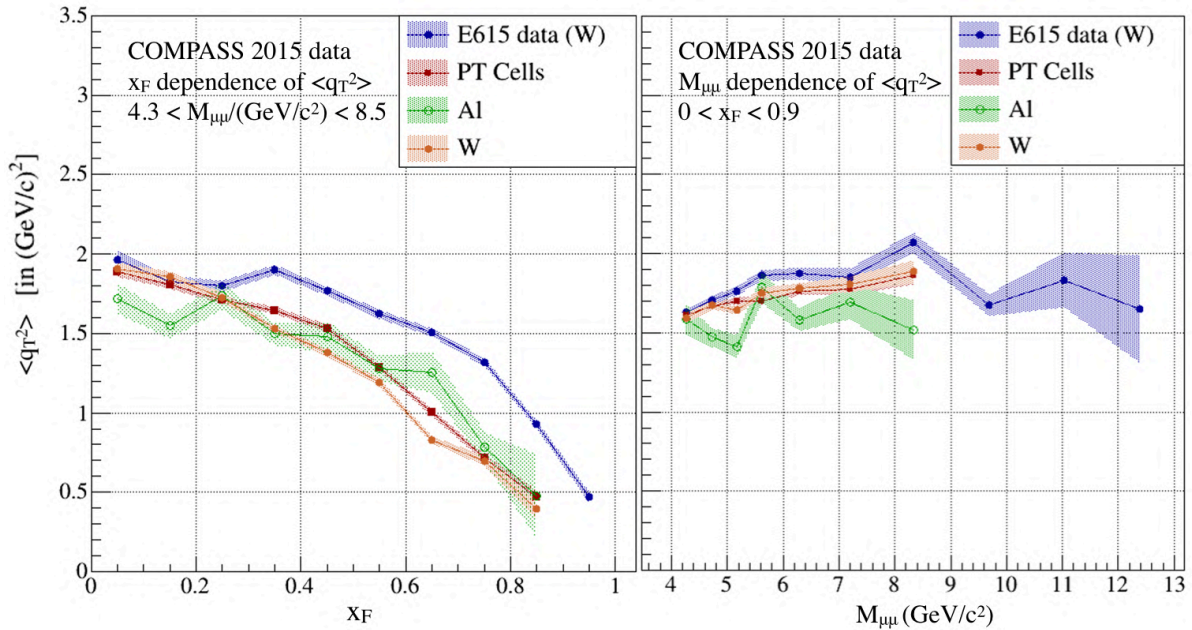


Figure 27.12: (a) Left: Mean q_T^2 distribution for $4.3 < M_{\mu\mu}/(\text{GeV}/c^2) < 8.5$ as a function of x_F ; (b) Right: Mean q_T^2 distribution for $0 < x_F < 0.9$ as a function of $M_{\mu\mu}$; E615 data are all shown in the range 4.05 and 8.55 GeV/c^2 and $0 < x_F < 1$

The extracted $\langle q_T^2 \rangle$ values based on COMPASS data are slightly smaller compared to E615 data

(Fig. 27.12). This observation is explained by the lower beam energy of 190-GeV at COMPASS compared to E615 data, as shown in Fig. 27.13. In this figure, the extracted $\langle q_T^2 \rangle$ value is compared as a function of \sqrt{s} with many other experiments for a bin of $\sqrt{\tau} \simeq 0.280$ and $0 < x_F < 0.9$. This figure shows a clear trend and is compatible with the COMPASS extracted results in red. Additionally, the extraction of the $\langle q_T^2 \rangle$ value in blue is based on the data published in [45] and uses the *Kaplan Form* fit. This data point has been refitted because of the new ad-hoc parametrization compared to the original paper. Consequently, this clear behavior confirms again that the COMPASS 2015 data might bring a valuable contribution to advanced phenomenological studies.

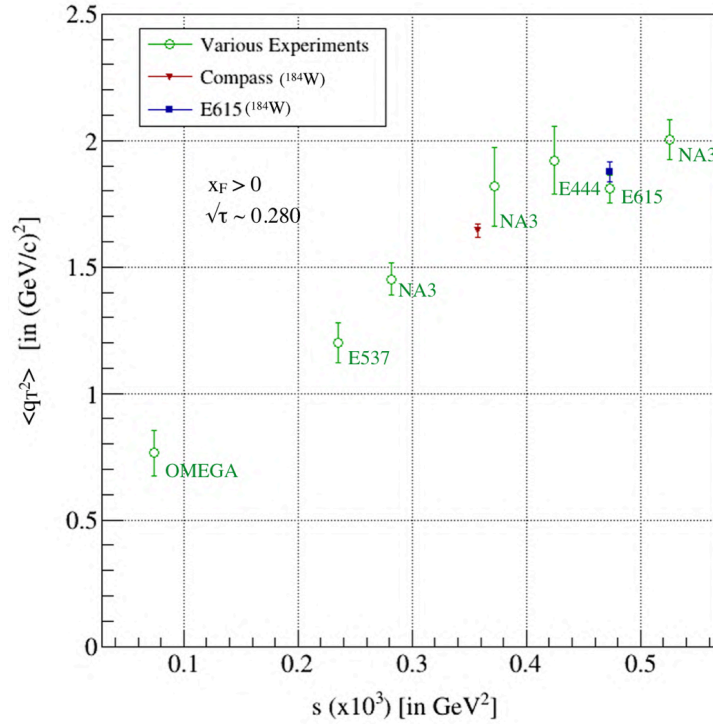


Figure 27.13: Evolution of $\langle q_T^2 \rangle$ as a function of the center-of-mass energy \sqrt{s} in comparison of the fit of various past experiments. The green data points are taken from [132]

27.3.4 Invariant Cross-Sections at High- q_T , $E d^3\sigma/dq^3$

In the continuity of the study of the transverse momentum distribution, the triple differential Drell-Yan cross-section is spanned in bins of x_F and q_T (Eq. 27.4). Moreover, this distribution is integrated over the azimuthal angle by symmetry.

$$E \frac{d^3\sigma}{dq^3} = \frac{2E}{\pi\sqrt{s}} \times \frac{d^2\sigma}{dx_F dq_T^2} \quad (27.4)$$

In this section, the extraction of the Drell-Yan cross-section using COMPASS 2015 data is performed using an acceptance correction computed as a function of $(Z_{vtx}, \sqrt{\tau}, x_F, q_T)$ with $4 \times 5 \times 11 \times 7$ bins.

Table 27.7: Summary of binning for the computation of the triple differential Drell-Yan cross-section. The binning in just mass highlights a correspondence with $\sqrt{\tau}$ at $\sqrt{s} = 18.9$ GeV for COMPASS

Variable	Binning							
Z_{vtx} [cm]	[-294.5; -239.3]		[-219.5; -164.3]		[-63.5; -56.5]		[-30; -20]	
x_F	-0.20	-0.10	0.00	...	0.60	0.70	0.80	0.90
q_T [GeV/c]	0.00	0.40	0.68	0.95	1.25	1.70	3.00	5.00
$\sqrt{\tau}$	0.228	0.270	0.312	0.354	0.396	0.450	–	–
$M_{\mu\mu}$ [GeV/c ²] ($\sqrt{s} = 18.90$ GeV)	4.30	5.10	5.90	6.70	7.50	8.50	–	–

The results of the target by target comparison as a function of x_F and q_T is presented in Fig. 27.14. These plots are staggered for visibility to highlight the similar trend target by target of the differential cross-sections per nucleon of each bin, and the conservation of the scale from one bin to the other. In this figure, the edges show decreasing trends due to the limited statistics, namely the q_T bin between 3.00 and 5.00 GeV/c and the x_F between 0.80 and 0.90. The values are summarized in Tab. 27.8 and Tab. 27.9 as a function of the x_F and q_T .

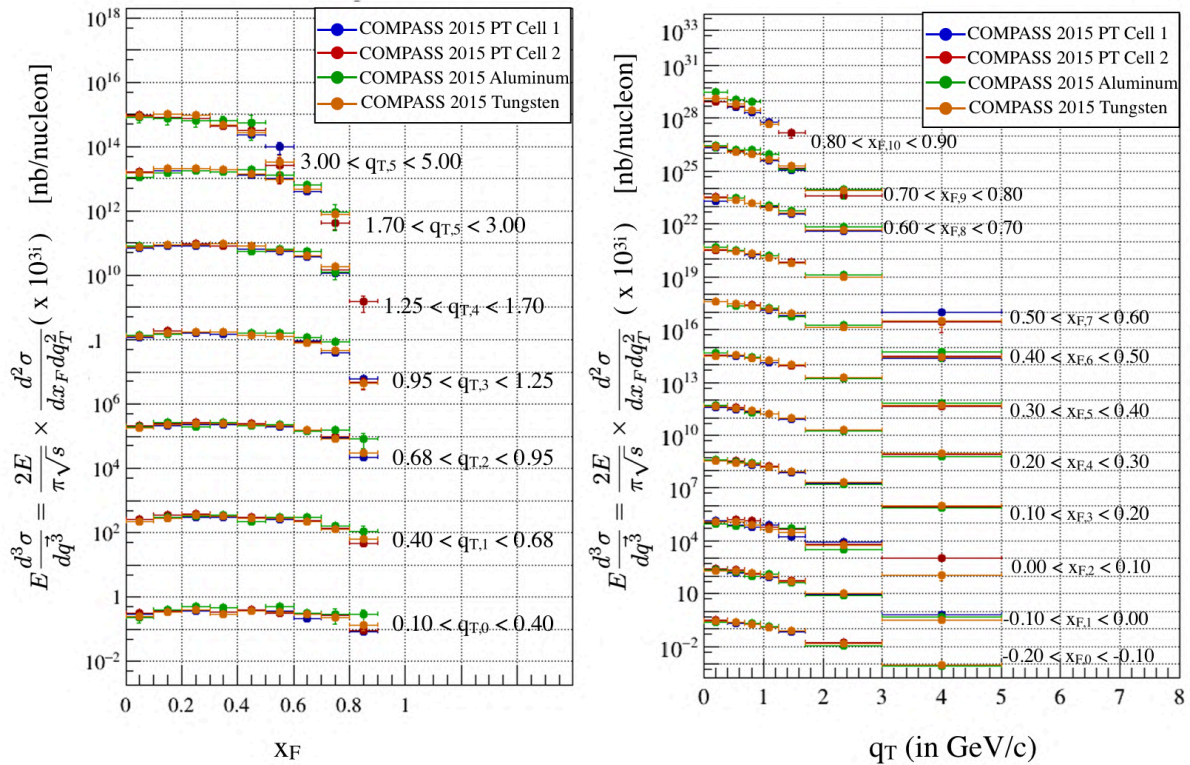


Figure 27.14: (a) Left : Triple cross-section as a function of x_F in bins of q_T integrated over the azimuthal angle (symmetry); (b) Right: Triple cross-section as a function of q_T in bins of x_F integrated over the azimuthal angle

27.3.5 Summary Table

Table 27.8: Triple differential cross-section $E^3 d\sigma/dq^3$ using COMPASS 2015 data. The errors shown are statistical only; there is an additional 9%, 18%, 9%, and 12% overall systematic uncertainty on the PT Cell 1 ($P_{F,1} = 0.5657$), PT Cell 2 ($P_{F,2} = 0.4797$), ^{27}Al , ^{184}W cross-sections, respectively.

COMPASS 2015 data				$\pi^- A \rightarrow \mu^+ \mu^- X$				$P_{\text{beam}} = 190 \text{ GeV}/c$	
Table 1/2				$E^3 d\sigma/dq^3 \text{ (nb/nucleon)}$					
q_T		x_F		PT Cell 1	PT Cell 2	^{27}Al	^{184}W (10 cm)		
0.00	0.40	-0.20	-0.10	$1.34 \times 10^{-1} \pm 4.93 \times 10^{-2}$	$1.24 \times 10^{-1} \pm 2.82 \times 10^{-2}$	$9.80 \times 10^{-2} \pm 3.63 \times 10^{-2}$	$1.21 \times 10^{-1} \pm 2.80 \times 10^{-2}$		
	—	-0.10	-0.00	$1.86 \times 10^{-1} \pm 2.48 \times 10^{-2}$	$2.58 \times 10^{-1} \pm 3.42 \times 10^{-2}$	$2.15 \times 10^{-1} \pm 5.88 \times 10^{-2}$	$2.10 \times 10^{-1} \pm 2.89 \times 10^{-2}$		
	—	-0.00	0.10	$2.94 \times 10^{-1} \pm 4.23 \times 10^{-2}$	$3.13 \times 10^{-1} \pm 3.16 \times 10^{-2}$	$2.30 \times 10^{-1} \pm 7.75 \times 10^{-2}$	$2.60 \times 10^{-1} \pm 2.39 \times 10^{-2}$		
	—	0.10	0.20	$3.34 \times 10^{-1} \pm 3.08 \times 10^{-2}$	$3.71 \times 10^{-1} \pm 3.11 \times 10^{-2}$	$4.07 \times 10^{-1} \pm 7.77 \times 10^{-2}$	$3.45 \times 10^{-1} \pm 2.92 \times 10^{-2}$		
	—	0.20	0.30	$3.80 \times 10^{-1} \pm 3.00 \times 10^{-2}$	$4.11 \times 10^{-1} \pm 3.12 \times 10^{-2}$	$5.03 \times 10^{-1} \pm 1.57 \times 10^{-1}$	$4.11 \times 10^{-1} \pm 3.72 \times 10^{-2}$		
	—	0.30	0.40	$3.35 \times 10^{-1} \pm 2.62 \times 10^{-2}$	$3.38 \times 10^{-1} \pm 2.69 \times 10^{-2}$	$4.69 \times 10^{-1} \pm 1.03 \times 10^{-1}$	$2.92 \times 10^{-1} \pm 2.50 \times 10^{-2}$		
	—	0.40	0.50	$3.83 \times 10^{-1} \pm 3.95 \times 10^{-2}$	$3.99 \times 10^{-1} \pm 3.76 \times 10^{-2}$	$3.72 \times 10^{-1} \pm 7.52 \times 10^{-2}$	$3.70 \times 10^{-1} \pm 3.51 \times 10^{-2}$		
	—	0.50	0.60	$3.66 \times 10^{-1} \pm 4.64 \times 10^{-2}$	$3.13 \times 10^{-1} \pm 3.20 \times 10^{-2}$	$4.89 \times 10^{-1} \pm 1.31 \times 10^{-1}$	$3.54 \times 10^{-1} \pm 3.75 \times 10^{-2}$		
	—	0.60	0.70	$2.10 \times 10^{-1} \pm 1.93 \times 10^{-2}$	$3.26 \times 10^{-1} \pm 3.80 \times 10^{-2}$	$3.18 \times 10^{-1} \pm 8.60 \times 10^{-2}$	$2.92 \times 10^{-1} \pm 3.36 \times 10^{-2}$		
	—	0.70	0.80	$2.25 \times 10^{-1} \pm 2.93 \times 10^{-2}$	$2.79 \times 10^{-1} \pm 3.39 \times 10^{-2}$	$2.83 \times 10^{-1} \pm 1.34 \times 10^{-1}$	$2.39 \times 10^{-1} \pm 3.72 \times 10^{-2}$		
	—	0.80	0.90	$8.65 \times 10^{-2} \pm 1.61 \times 10^{-2}$	$8.96 \times 10^{-2} \pm 1.92 \times 10^{-2}$	$2.89 \times 10^{-1} \pm 1.22 \times 10^{-1}$	$1.30 \times 10^{-1} \pm 3.81 \times 10^{-2}$		
0.40	0.68	-0.20	-0.10	$8.47 \times 10^{-2} \pm 1.94 \times 10^{-2}$	$1.57 \times 10^{-1} \pm 2.49 \times 10^{-2}$	$6.87 \times 10^{-2} \pm 2.64 \times 10^{-2}$	$1.16 \times 10^{-1} \pm 1.50 \times 10^{-2}$		
	—	-0.10	-0.00	$1.57 \times 10^{-1} \pm 1.51 \times 10^{-2}$	$2.33 \times 10^{-1} \pm 1.95 \times 10^{-2}$	$1.83 \times 10^{-1} \pm 3.65 \times 10^{-2}$	$1.87 \times 10^{-1} \pm 1.49 \times 10^{-2}$		
	—	-0.00	0.10	$2.14 \times 10^{-1} \pm 1.39 \times 10^{-2}$	$2.50 \times 10^{-1} \pm 1.68 \times 10^{-2}$	$2.28 \times 10^{-1} \pm 3.68 \times 10^{-2}$	$2.29 \times 10^{-1} \pm 1.45 \times 10^{-2}$		
	—	0.00	0.20	$2.86 \times 10^{-1} \pm 1.49 \times 10^{-2}$	$3.57 \times 10^{-1} \pm 1.83 \times 10^{-2}$	$3.14 \times 10^{-1} \pm 3.89 \times 10^{-2}$	$2.79 \times 10^{-1} \pm 1.48 \times 10^{-2}$		
	—	0.00	0.30	$2.98 \times 10^{-1} \pm 1.38 \times 10^{-2}$	$3.71 \times 10^{-1} \pm 1.86 \times 10^{-2}$	$3.30 \times 10^{-1} \pm 4.29 \times 10^{-2}$	$3.43 \times 10^{-1} \pm 1.69 \times 10^{-2}$		
	—	0.00	0.40	$2.94 \times 10^{-1} \pm 1.35 \times 10^{-2}$	$3.66 \times 10^{-1} \pm 1.84 \times 10^{-2}$	$3.60 \times 10^{-1} \pm 4.79 \times 10^{-2}$	$3.37 \times 10^{-1} \pm 1.74 \times 10^{-2}$		
	—	0.00	0.50	$2.82 \times 10^{-1} \pm 1.38 \times 10^{-2}$	$3.05 \times 10^{-1} \pm 1.78 \times 10^{-2}$	$2.25 \times 10^{-1} \pm 4.04 \times 10^{-2}$	$2.82 \times 10^{-1} \pm 1.72 \times 10^{-2}$		
	—	0.00	0.60	$2.62 \times 10^{-1} \pm 1.39 \times 10^{-2}$	$2.79 \times 10^{-1} \pm 1.77 \times 10^{-2}$	$3.04 \times 10^{-1} \pm 6.00 \times 10^{-2}$	$2.81 \times 10^{-1} \pm 1.87 \times 10^{-2}$		
	—	0.00	0.70	$2.26 \times 10^{-1} \pm 1.40 \times 10^{-2}$	$2.41 \times 10^{-1} \pm 1.82 \times 10^{-2}$	$3.01 \times 10^{-1} \pm 6.45 \times 10^{-2}$	$2.25 \times 10^{-1} \pm 1.78 \times 10^{-2}$		
	—	0.00	0.80	$1.57 \times 10^{-1} \pm 1.29 \times 10^{-2}$	$1.43 \times 10^{-1} \pm 1.57 \times 10^{-2}$	$1.67 \times 10^{-1} \pm 5.30 \times 10^{-2}$	$1.29 \times 10^{-1} \pm 1.51 \times 10^{-2}$		
	—	0.00	0.90	$4.59 \times 10^{-2} \pm 7.12 \times 10^{-3}$	$4.75 \times 10^{-2} \pm 9.29 \times 10^{-3}$	$1.12 \times 10^{-1} \pm 5.05 \times 10^{-2}$	$6.37 \times 10^{-2} \pm 1.25 \times 10^{-2}$		
0.68	0.95	-0.20	-0.10	$5.81 \times 10^{-2} \pm 1.27 \times 10^{-2}$	$1.44 \times 10^{-1} \pm 1.98 \times 10^{-2}$	$8.28 \times 10^{-2} \pm 2.32 \times 10^{-2}$	$8.10 \times 10^{-2} \pm 1.04 \times 10^{-2}$		
	—	-0.10	-0.00	$1.28 \times 10^{-1} \pm 1.15 \times 10^{-2}$	$1.35 \times 10^{-1} \pm 1.24 \times 10^{-2}$	$9.68 \times 10^{-2} \pm 2.08 \times 10^{-2}$	$1.51 \times 10^{-1} \pm 1.15 \times 10^{-2}$		
	—	-0.00	0.10	$1.74 \times 10^{-1} \pm 1.05 \times 10^{-2}$	$2.17 \times 10^{-1} \pm 1.28 \times 10^{-2}$	$1.98 \times 10^{-1} \pm 2.74 \times 10^{-2}$	$1.86 \times 10^{-1} \pm 1.01 \times 10^{-2}$		
	—	0.10	0.20	$2.08 \times 10^{-1} \pm 1.04 \times 10^{-2}$	$2.41 \times 10^{-1} \pm 1.24 \times 10^{-2}$	$2.60 \times 10^{-1} \pm 3.05 \times 10^{-2}$	$2.34 \times 10^{-1} \pm 1.12 \times 10^{-2}$		
	—	0.20	0.30	$2.27 \times 10^{-1} \pm 9.89 \times 10^{-3}$	$2.60 \times 10^{-1} \pm 1.26 \times 10^{-2}$	$1.96 \times 10^{-1} \pm 2.63 \times 10^{-2}$	$2.56 \times 10^{-1} \pm 1.18 \times 10^{-2}$		
	—	0.30	0.40	$2.24 \times 10^{-1} \pm 9.72 \times 10^{-3}$	$2.68 \times 10^{-1} \pm 1.29 \times 10^{-2}$	$2.62 \times 10^{-1} \pm 3.38 \times 10^{-2}$	$2.39 \times 10^{-1} \pm 1.17 \times 10^{-2}$		
	—	0.40	0.50	$2.12 \times 10^{-1} \pm 9.87 \times 10^{-3}$	$2.38 \times 10^{-1} \pm 1.29 \times 10^{-2}$	$2.14 \times 10^{-1} \pm 3.31 \times 10^{-2}$	$2.26 \times 10^{-1} \pm 1.22 \times 10^{-2}$		
	—	0.50	0.60	$1.90 \times 10^{-1} \pm 9.96 \times 10^{-3}$	$2.11 \times 10^{-1} \pm 1.30 \times 10^{-2}$	$2.21 \times 10^{-1} \pm 3.71 \times 10^{-2}$	$2.10 \times 10^{-1} \pm 1.26 \times 10^{-2}$		
	—	0.60	0.70	$1.46 \times 10^{-1} \pm 9.17 \times 10^{-3}$	$1.54 \times 10^{-1} \pm 1.18 \times 10^{-2}$	$1.47 \times 10^{-1} \pm 3.37 \times 10^{-2}$	$1.49 \times 10^{-1} \pm 1.10 \times 10^{-2}$		
	—	0.70	0.80	$8.97 \times 10^{-2} \pm 7.76 \times 10^{-3}$	$9.59 \times 10^{-2} \pm 9.83 \times 10^{-3}$	$1.59 \times 10^{-1} \pm 4.25 \times 10^{-2}$	$8.56 \times 10^{-2} \pm 9.06 \times 10^{-3}$		
	—	0.80	0.90	$2.14 \times 10^{-2} \pm 3.76 \times 10^{-3}$	$3.01 \times 10^{-2} \pm 5.57 \times 10^{-3}$	$8.20 \times 10^{-2} \pm 4.01 \times 10^{-2}$	$2.94 \times 10^{-2} \pm 5.86 \times 10^{-3}$		
0.95	1.25	-0.20	-0.10	$7.52 \times 10^{-2} \pm 1.39 \times 10^{-2}$	$6.48 \times 10^{-2} \pm 1.04 \times 10^{-2}$	$4.36 \times 10^{-2} \pm 1.40 \times 10^{-2}$	$4.79 \times 10^{-2} \pm 6.59 \times 10^{-3}$		
	—	-0.10	-0.00	$7.99 \times 10^{-2} \pm 7.72 \times 10^{-3}$	$1.00 \times 10^{-1} \pm 8.53 \times 10^{-3}$	$1.22 \times 10^{-1} \pm 1.92 \times 10^{-2}$	$1.01 \times 10^{-1} \pm 7.33 \times 10^{-3}$		
	—	-0.00	0.10	$1.18 \times 10^{-1} \pm 6.95 \times 10^{-3}$	$1.38 \times 10^{-1} \pm 8.43 \times 10^{-3}$	$1.40 \times 10^{-1} \pm 1.80 \times 10^{-2}$	$1.24 \times 10^{-1} \pm 6.73 \times 10^{-3}$		
	—	0.10	0.20	$1.46 \times 10^{-1} \pm 6.94 \times 10^{-3}$	$1.81 \times 10^{-1} \pm 9.01 \times 10^{-3}$	$1.52 \times 10^{-1} \pm 1.86 \times 10^{-2}$	$1.59 \times 10^{-1} \pm 7.35 \times 10^{-3}$		
	—	0.20	0.30	$1.54 \times 10^{-1} \pm 6.63 \times 10^{-3}$	$1.70 \times 10^{-1} \pm 8.48 \times 10^{-3}$	$1.69 \times 10^{-1} \pm 1.97 \times 10^{-2}$	$1.75 \times 10^{-1} \pm 7.62 \times 10^{-3}$		
	—	0.30	0.40	$1.43 \times 10^{-1} \pm 6.32 \times 10^{-3}$	$1.69 \times 10^{-1} \pm 8.41 \times 10^{-3}$	$1.77 \times 10^{-1} \pm 2.10 \times 10^{-2}$	$1.67 \times 10^{-1} \pm 7.55 \times 10^{-3}$		
	—	0.40	0.50	$1.35 \times 10^{-1} \pm 6.31 \times 10^{-3}$	$1.53 \times 10^{-1} \pm 8.34 \times 10^{-3}$	$1.65 \times 10^{-1} \pm 2.23 \times 10^{-2}$	$1.40 \times 10^{-1} \pm 7.32 \times 10^{-3}$		
	—	0.50	0.60	$1.25 \times 10^{-1} \pm 6.60 \times 10^{-3}$	$1.25 \times 10^{-1} \pm 7.92 \times 10^{-3}$	$1.63 \times 10^{-1} \pm 2.52 \times 10^{-2}$	$1.25 \times 10^{-1} \pm 7.33 \times 10^{-3}$		
	—	0.60	0.70	$9.08 \times 10^{-2} \pm 5.86 \times 10^{-3}$	$8.44 \times 10^{-2} \pm 7.05 \times 10^{-3}$	$1.13 \times 10^{-1} \pm 2.45 \times 10^{-2}$	$8.02 \times 10^{-2} \pm 6.39 \times 10^{-3}$		
	—	0.70	0.80	$4.01 \times 10^{-2} \pm 4.06 \times 10^{-3}$	$4.69 \times 10^{-2} \pm 5.39 \times 10^{-3}$	$8.85 \times 10^{-2} \pm 2.32 \times 10^{-2}$	$4.41 \times 10^{-2} \pm 4.83 \times 10^{-3}$		
	—	0.80	0.90	$6.10 \times 10^{-3} \pm 1.78 \times 10^{-3}$	$4.75 \times 10^{-3} \pm 1.92 \times 10^{-3}$	—	$4.40 \times 10^{-3} \pm 1.51 \times 10^{-3}$		

Table 27.9: Triple differential cross-section $E^3 d\sigma/dq^3$ using COMPASS 2015 data; there is an additional 9%, 18%, 9%, and 12% overall systematic uncertainty on the PT Cell 1 ($P_{F,1} = 0.5657$), PT Cell 2 ($P_{F,2} = 0.4797$), ^{27}Al , ^{184}W cross-sections, respectively.

COMPASS 2015 data				$\pi^- A \rightarrow \mu^+ \mu^- X$				$P_{\text{beam}} = 190 \text{ GeV}/c$	
Table 2/2									
				$E^3 d\sigma/dq^3$ (nb/nucleon)					
q_T		x_F		PT Cell 1	PT Cell 2	^{27}Al	^{184}W (10 cm)		
1.2500	1.7000	−0.20	−0.10	$1.71 \times 10^{-2} \pm 4.59 \times 10^{-3}$	$4.50 \times 10^{-2} \pm 6.63 \times 10^{-3}$	$4.99 \times 10^{-2} \pm 1.34 \times 10^{-2}$	$2.88 \times 10^{-2} \pm 3.67 \times 10^{-3}$		
—	—	−0.10	−0.00	$4.26 \times 10^{-2} \pm 3.70 \times 10^{-3}$	$5.35 \times 10^{-2} \pm 4.49 \times 10^{-3}$	$4.26 \times 10^{-2} \pm 7.97 \times 10^{-3}$	$5.16 \times 10^{-2} \pm 3.56 \times 10^{-3}$		
—	—	−0.00	0.10	$7.02 \times 10^{-2} \pm 3.89 \times 10^{-3}$	$7.70 \times 10^{-2} \pm 4.52 \times 10^{-3}$	$8.42 \times 10^{-2} \pm 9.73 \times 10^{-3}$	$7.36 \times 10^{-2} \pm 3.60 \times 10^{-3}$		
—	—	0.10	0.20	$8.07 \times 10^{-2} \pm 3.60 \times 10^{-3}$	$8.99 \times 10^{-2} \pm 4.41 \times 10^{-3}$	$8.51 \times 10^{-2} \pm 9.27 \times 10^{-3}$	$9.11 \times 10^{-2} \pm 3.81 \times 10^{-3}$		
—	—	0.20	0.30	$8.08 \times 10^{-2} \pm 3.45 \times 10^{-3}$	$9.65 \times 10^{-2} \pm 4.47 \times 10^{-3}$	$9.00 \times 10^{-2} \pm 9.87 \times 10^{-3}$	$9.12 \times 10^{-2} \pm 3.78 \times 10^{-3}$		
—	—	0.30	0.40	$8.23 \times 10^{-2} \pm 3.48 \times 10^{-3}$	$8.43 \times 10^{-2} \pm 4.21 \times 10^{-3}$	$9.65 \times 10^{-2} \pm 1.12 \times 10^{-2}$	$9.49 \times 10^{-2} \pm 3.99 \times 10^{-3}$		
—	—	0.40	0.50	$6.65 \times 10^{-2} \pm 3.15 \times 10^{-3}$	$8.23 \times 10^{-2} \pm 4.36 \times 10^{-3}$	$5.41 \times 10^{-2} \pm 8.59 \times 10^{-3}$	$8.18 \times 10^{-2} \pm 3.87 \times 10^{-3}$		
—	—	0.50	0.60	$5.54 \times 10^{-2} \pm 3.06 \times 10^{-3}$	$6.51 \times 10^{-2} \pm 4.16 \times 10^{-3}$	$6.27 \times 10^{-2} \pm 1.04 \times 10^{-2}$	$5.86 \times 10^{-2} \pm 3.38 \times 10^{-3}$		
—	—	0.60	0.70	$3.82 \times 10^{-2} \pm 2.68 \times 10^{-3}$	$4.18 \times 10^{-2} \pm 3.35 \times 10^{-3}$	$5.34 \times 10^{-2} \pm 1.05 \times 10^{-2}$	$3.98 \times 10^{-2} \pm 2.93 \times 10^{-3}$		
—	—	0.70	0.80	$1.17 \times 10^{-2} \pm 1.51 \times 10^{-3}$	$1.52 \times 10^{-2} \pm 2.15 \times 10^{-3}$	$1.22 \times 10^{-2} \pm 5.23 \times 10^{-3}$	$1.89 \times 10^{-2} \pm 2.13 \times 10^{-3}$		
1.7000	3.0000	−0.20	−0.10	$8.00 \times 10^{-3} \pm 1.67 \times 10^{-3}$	$6.72 \times 10^{-3} \pm 1.20 \times 10^{-3}$	$3.28 \times 10^{-3} \pm 1.35 \times 10^{-3}$	$5.97 \times 10^{-3} \pm 7.52 \times 10^{-4}$		
—	—	−0.10	−0.00	$9.50 \times 10^{-3} \pm 8.54 \times 10^{-4}$	$9.80 \times 10^{-3} \pm 9.15 \times 10^{-4}$	$7.38 \times 10^{-3} \pm 1.57 \times 10^{-3}$	$1.07 \times 10^{-2} \pm 7.90 \times 10^{-4}$		
—	—	−0.00	0.10	$1.58 \times 10^{-2} \pm 8.60 \times 10^{-4}$	$1.64 \times 10^{-2} \pm 9.72 \times 10^{-4}$	$1.12 \times 10^{-2} \pm 1.66 \times 10^{-3}$	$1.54 \times 10^{-2} \pm 7.68 \times 10^{-4}$		
—	—	0.10	0.20	$1.80 \times 10^{-2} \pm 8.35 \times 10^{-4}$	$2.02 \times 10^{-2} \pm 1.03 \times 10^{-3}$	$1.52 \times 10^{-2} \pm 1.85 \times 10^{-3}$	$2.03 \times 10^{-2} \pm 8.39 \times 10^{-4}$		
—	—	0.20	0.30	$1.82 \times 10^{-2} \pm 8.16 \times 10^{-4}$	$2.05 \times 10^{-2} \pm 1.03 \times 10^{-3}$	$1.72 \times 10^{-2} \pm 1.99 \times 10^{-3}$	$2.00 \times 10^{-2} \pm 8.16 \times 10^{-4}$		
—	—	0.30	0.40	$1.64 \times 10^{-2} \pm 7.64 \times 10^{-4}$	$1.89 \times 10^{-2} \pm 9.98 \times 10^{-4}$	$1.67 \times 10^{-2} \pm 2.12 \times 10^{-3}$	$1.98 \times 10^{-2} \pm 8.36 \times 10^{-4}$		
—	—	0.40	0.50	$1.29 \times 10^{-2} \pm 7.00 \times 10^{-4}$	$1.39 \times 10^{-2} \pm 8.92 \times 10^{-4}$	$1.88 \times 10^{-2} \pm 2.65 \times 10^{-3}$	$1.42 \times 10^{-2} \pm 7.36 \times 10^{-4}$		
—	—	0.50	0.60	$1.01 \times 10^{-2} \pm 6.44 \times 10^{-4}$	$9.50 \times 10^{-3} \pm 7.81 \times 10^{-4}$	$1.30 \times 10^{-2} \pm 2.19 \times 10^{-3}$	$9.61 \times 10^{-3} \pm 6.22 \times 10^{-4}$		
—	—	0.60	0.70	$3.94 \times 10^{-3} \pm 4.20 \times 10^{-4}$	$4.72 \times 10^{-3} \pm 5.54 \times 10^{-4}$	$6.59 \times 10^{-3} \pm 1.87 \times 10^{-3}$	$4.62 \times 10^{-3} \pm 4.65 \times 10^{-4}$		
—	—	0.70	0.80	$7.52 \times 10^{-4} \pm 2.04 \times 10^{-4}$	$4.08 \times 10^{-4} \pm 1.47 \times 10^{-4}$	$9.36 \times 10^{-4} \pm 6.90 \times 10^{-4}$	$7.55 \times 10^{-4} \pm 1.99 \times 10^{-4}$		
3.0000	5.0000	−0.20	−0.10	—	$1.08 \times 10^{-3} \pm 4.58 \times 10^{-4}$	—	$1.08 \times 10^{-4} \pm 5.53 \times 10^{-5}$		
—	—	−0.10	−0.00	$6.47 \times 10^{-4} \pm 1.16 \times 10^{-4}$	$4.78 \times 10^{-4} \pm 1.17 \times 10^{-4}$	$5.12 \times 10^{-4} \pm 2.41 \times 10^{-4}$	$3.35 \times 10^{-4} \pm 7.64 \times 10^{-5}$		
—	—	−0.00	0.10	$8.38 \times 10^{-4} \pm 1.11 \times 10^{-4}$	$9.11 \times 10^{-4} \pm 1.40 \times 10^{-4}$	$8.14 \times 10^{-4} \pm 2.73 \times 10^{-4}$	$8.49 \times 10^{-4} \pm 1.08 \times 10^{-4}$		
—	—	0.10	0.20	$8.27 \times 10^{-4} \pm 1.05 \times 10^{-4}$	$8.07 \times 10^{-4} \pm 1.25 \times 10^{-4}$	$7.26 \times 10^{-4} \pm 2.59 \times 10^{-4}$	$1.02 \times 10^{-3} \pm 1.17 \times 10^{-4}$		
—	—	0.20	0.30	$6.42 \times 10^{-4} \pm 9.45 \times 10^{-5}$	$7.67 \times 10^{-4} \pm 1.29 \times 10^{-4}$	$6.23 \times 10^{-4} \pm 2.26 \times 10^{-4}$	$9.26 \times 10^{-4} \pm 1.04 \times 10^{-4}$		
—	—	0.30	0.40	$4.78 \times 10^{-4} \pm 8.30 \times 10^{-5}$	$4.20 \times 10^{-4} \pm 9.35 \times 10^{-5}$	$6.19 \times 10^{-4} \pm 2.63 \times 10^{-4}$	$4.68 \times 10^{-4} \pm 7.03 \times 10^{-5}$		
—	—	0.40	0.50	$2.24 \times 10^{-4} \pm 5.70 \times 10^{-5}$	$3.16 \times 10^{-4} \pm 9.11 \times 10^{-5}$	$5.32 \times 10^{-4} \pm 3.78 \times 10^{-4}$	$2.72 \times 10^{-4} \pm 6.49 \times 10^{-5}$		
—	—	0.50	0.60	$9.71 \times 10^{-5} \pm 4.08 \times 10^{-5}$	$2.54 \times 10^{-5} \pm 1.83 \times 10^{-5}$	—	$3.34 \times 10^{-5} \pm 1.94 \times 10^{-5}$		

27.4 Invariant Double Drell-Yan Cross-Sections $M^2 d^2\sigma/dx_1 dx_2$

27.4.1 Motivations

The distribution $\frac{d^2\sigma}{dx_1 dx_2}$, previously introduced in Sec. 27.4, Ch. I have the great advantage to be Lorentz invariant and consequently comparable with other experiments measuring $\pi^- A$ Drell-Yan cross-sections. This feature is indeed expected, because of the definition of the structure function $F(x_1, x_2)$, as shown in Eq. 27.5. From its definition, the $F(x_1, x_2)$ directly gives an access to a convolution between pion and proton PDFs using the COMPASS data.

$$F(x_1, x_2) = M^2 \frac{d^2\sigma}{dx_1 dx_2} = \left(\frac{4\pi\alpha^2}{9} \right) \sum_q e_q^2 [q_1(x_1)\bar{q}_2(x_2) + \bar{q}_1(x_1)q_2(x_2)] \quad (27.5)$$

In this analysis, the acceptance correction is computed as a function of (Z_{vtx}, x_1, x_2, q_T) with $4 \times 9 \times 6 \times 7$ bins as shown in Tab. 27.10. The invariant cross-section is presented as a function of x_1 and x_2 and shown in Fig. 27.15. A summary of the extracted cross-sections is shown in Tab. 27.11

Table 27.10: Summary of the binning chosen for the invariant double differential Drell-Yan cross-section $d^2\sigma/dx_1 dx_2$ extraction.

Variable	Binning							
Z_{vtx} [cm]	[-294.5; -239.3]		[-219.5; -164.3]		[-63.5; -56.5]		[-30; -20]	
x_1	0.10	0.20	0.30	..	0.70	0.80	0.90	1.00
x_2	0.00	0.10	0.20	0.30	0.40	0.50	0.60	—
q_T [GeV/c]	0.00	0.40	0.68	0.95	1.25	1.70	3.00	5.00

Figure 27.15 shows the evolution of the cross-section in bins of x_2 . This distribution is spread over a wide range in x_1 , which gives the opportunity to contribute to the global fit of the pion PDF, in particular, the valence-quark contribution thanks to an advanced analysis of these preliminary results.

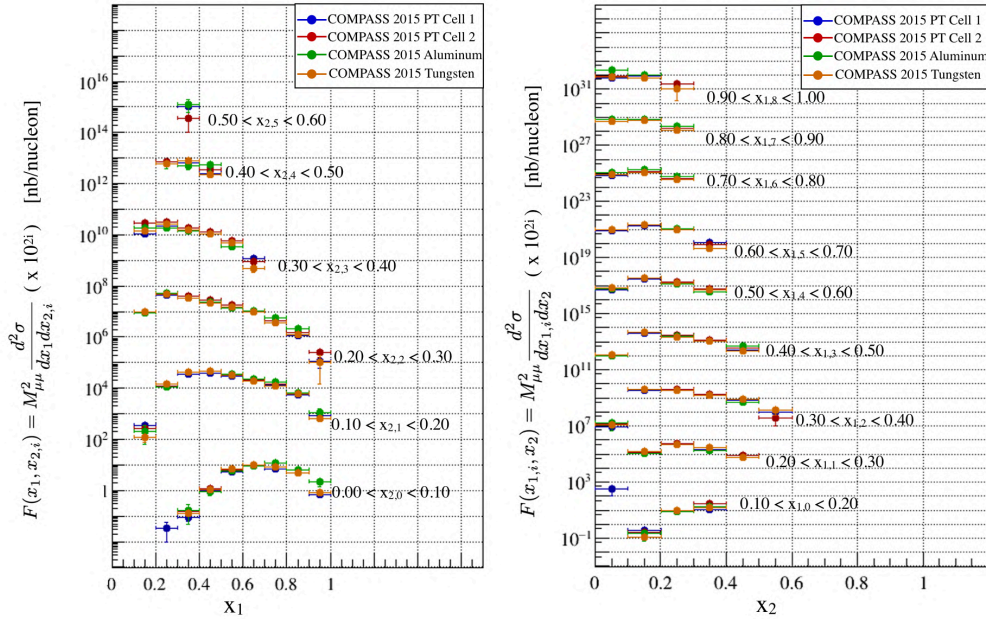


Figure 27.15: (a) Left: Comparison target by target as a function of bins in x_2 ; (b) Right: Comparison target by target as a function of bins in x_1

27.4.2 Summary Table

Table 27.11: Double differential cross-section $M^2 d^2\sigma/dx_1 dx_2$ using COMPASS 2015 data. The errors shown are statistical only; there is an additional 9%, 18%, 9%, and 12% overall systematic uncertainty on the PT Cell 1 ($P_{F,1} = 0.5657$), PT Cell 2 ($P_{F,2} = 0.4797$), ^{27}Al , ^{184}W cross-sections, respectively.

COMPASS 2015 data				$\pi^- A \rightarrow \mu^+ \mu^- X$				$P_{\text{beam}} = 190 \text{ GeV}/c$	
				$M^2 d^2\sigma/dx_1 dx_2 \text{ (GeV}^2 \text{ nb/nucleon)}$					
x_1		x_2		PT Cell 1	PT Cell 2	^{27}Al	^{184}W (10 cm)		
0.10	0.20	0.10	0.20	$3.41 \times 10^{-1} \pm 8.57 \times 10^{-2}$	$2.69 \times 10^{-1} \pm 9.13 \times 10^{-2}$	$2.12 \times 10^{-1} \pm 1.50 \times 10^{-1}$	$1.25 \times 10^{-1} \pm 5.01 \times 10^{-2}$		
—	—	0.20	0.30	$9.87 \times 10^0 \pm 9.69 \times 10^{-1}$	$8.81 \times 10^0 \pm 8.90 \times 10^{-1}$	$8.50 \times 10^0 \pm 1.80 \times 10^0$	$9.26 \times 10^0 \pm 7.23 \times 10^{-1}$		
—	—	0.30	0.40	$1.13 \times 10^1 \pm 2.53 \times 10^0$	$2.85 \times 10^1 \pm 3.07 \times 10^0$	$1.90 \times 10^1 \pm 3.71 \times 10^0$	$1.46 \times 10^1 \pm 1.33 \times 10^0$		
0.20	0.30	0.10	0.20	$1.15 \times 10^1 \pm 4.84 \times 10^{-1}$	$1.24 \times 10^1 \pm 5.70 \times 10^{-1}$	$1.12 \times 10^1 \pm 1.28 \times 10^0$	$1.46 \times 10^1 \pm 5.60 \times 10^{-1}$		
—	—	0.20	0.30	$4.52 \times 10^1 \pm 1.34 \times 10^0$	$5.24 \times 10^1 \pm 1.57 \times 10^0$	$5.04 \times 10^1 \pm 3.37 \times 10^0$	$4.81 \times 10^1 \pm 1.29 \times 10^0$		
—	—	0.30	0.40	$2.14 \times 10^1 \pm 1.64 \times 10^0$	$3.06 \times 10^1 \pm 2.00 \times 10^0$	$1.80 \times 10^1 \pm 2.82 \times 10^0$	$2.71 \times 10^1 \pm 1.48 \times 10^0$		
0.30	0.40	0.10	0.20	$3.63 \times 10^1 \pm 7.81 \times 10^{-1}$	$4.20 \times 10^1 \pm 9.78 \times 10^{-1}$	$4.16 \times 10^1 \pm 2.35 \times 10^0$	$4.31 \times 10^1 \pm 9.10 \times 10^{-1}$		
—	—	0.20	0.30	$3.25 \times 10^1 \pm 1.02 \times 10^0$	$3.87 \times 10^1 \pm 1.27 \times 10^0$	$3.33 \times 10^1 \pm 2.51 \times 10^0$	$3.48 \times 10^1 \pm 1.02 \times 10^0$		
—	—	0.30	0.40	$1.55 \times 10^1 \pm 1.06 \times 10^0$	$1.92 \times 10^1 \pm 1.31 \times 10^0$	$1.47 \times 10^1 \pm 2.20 \times 10^0$	$1.52 \times 10^1 \pm 9.51 \times 10^{-1}$		
—	—	0.40	0.50	$6.61 \times 10^0 \pm 1.06 \times 10^0$	$7.99 \times 10^0 \pm 1.22 \times 10^0$	$5.15 \times 10^0 \pm 1.68 \times 10^0$	$7.54 \times 10^0 \pm 9.80 \times 10^{-1}$		
—	—	0.50	0.60	$1.04 \times 10^0 \pm 6.12 \times 10^{-1}$	$3.64 \times 10^{-1} \pm 2.57 \times 10^{-1}$	—	$1.26 \times 10^0 \pm 6.41 \times 10^{-1}$		
0.40	0.50	0.00	0.10	$9.66 \times 10^{-1} \pm 1.05 \times 10^{-1}$	$1.13 \times 10^0 \pm 1.35 \times 10^{-1}$	$9.29 \times 10^{-1} \pm 2.94 \times 10^{-1}$	$1.12 \times 10^0 \pm 1.09 \times 10^{-1}$		
—	—	0.10	0.20	$4.00 \times 10^1 \pm 7.70 \times 10^{-1}$	$4.48 \times 10^1 \pm 9.87 \times 10^{-1}$	$4.63 \times 10^1 \pm 2.54 \times 10^0$	$4.58 \times 10^1 \pm 9.21 \times 10^{-1}$		
—	—	0.20	0.30	$2.24 \times 10^1 \pm 8.29 \times 10^{-1}$	$2.79 \times 10^1 \pm 1.07 \times 10^0$	$2.40 \times 10^1 \pm 2.13 \times 10^0$	$2.19 \times 10^1 \pm 7.97 \times 10^{-1}$		
—	—	0.30	0.40	$1.11 \times 10^1 \pm 8.15 \times 10^{-1}$	$1.27 \times 10^1 \pm 9.87 \times 10^{-1}$	$1.11 \times 10^1 \pm 1.90 \times 10^0$	$1.04 \times 10^1 \pm 7.36 \times 10^{-1}$		
—	—	0.40	0.50	$2.51 \times 10^0 \pm 5.08 \times 10^{-1}$	$3.56 \times 10^0 \pm 6.76 \times 10^{-1}$	$5.31 \times 10^0 \pm 1.96 \times 10^0$	$2.34 \times 10^0 \pm 4.53 \times 10^{-1}$		
0.50	0.60	0.00	0.10	$5.25 \times 10^0 \pm 2.35 \times 10^{-1}$	$6.18 \times 10^0 \pm 3.17 \times 10^{-1}$	$5.88 \times 10^0 \pm 9.05 \times 10^{-1}$	$6.79 \times 10^0 \pm 3.25 \times 10^{-1}$		
—	—	0.10	0.20	$2.96 \times 10^1 \pm 6.70 \times 10^{-1}$	$3.38 \times 10^1 \pm 8.71 \times 10^{-1}$	$3.49 \times 10^1 \pm 2.32 \times 10^0$	$3.24 \times 10^1 \pm 7.92 \times 10^{-1}$		
—	—	0.20	0.30	$1.46 \times 10^1 \pm 6.57 \times 10^{-1}$	$1.72 \times 10^1 \pm 8.46 \times 10^{-1}$	$1.36 \times 10^1 \pm 1.60 \times 10^0$	$1.52 \times 10^1 \pm 6.84 \times 10^{-1}$		
—	—	0.30	0.40	$5.01 \times 10^0 \pm 5.05 \times 10^{-1}$	$5.86 \times 10^0 \pm 6.37 \times 10^{-1}$	$3.36 \times 10^0 \pm 9.56 \times 10^{-1}$	$4.82 \times 10^0 \pm 4.88 \times 10^{-1}$		
0.60	0.70	0.00	0.10	$8.78 \times 10^0 \pm 3.18 \times 10^{-1}$	$9.04 \times 10^0 \pm 3.93 \times 10^{-1}$	$9.39 \times 10^0 \pm 1.22 \times 10^0$	$9.98 \times 10^0 \pm 4.10 \times 10^{-1}$		
—	—	0.10	0.20	$1.96 \times 10^1 \pm 5.69 \times 10^{-1}$	$2.18 \times 10^1 \pm 7.49 \times 10^{-1}$	$2.21 \times 10^1 \pm 1.97 \times 10^0$	$1.99 \times 10^1 \pm 6.55 \times 10^{-1}$		
—	—	0.20	0.30	$1.02 \times 10^1 \pm 5.51 \times 10^{-1}$	$1.06 \times 10^1 \pm 6.75 \times 10^{-1}$	$1.04 \times 10^1 \pm 1.49 \times 10^0$	$9.68 \times 10^0 \pm 5.50 \times 10^{-1}$		
—	—	0.30	0.40	$1.17 \times 10^0 \pm 2.47 \times 10^{-1}$	$8.91 \times 10^{-1} \pm 2.41 \times 10^{-1}$	—	$4.75 \times 10^{-1} \pm 1.50 \times 10^{-1}$		
0.7000	0.80	0.00	0.10	$7.24 \times 10^0 \pm 2.98 \times 10^{-1}$	$8.02 \times 10^0 \pm 3.91 \times 10^{-1}$	$1.15 \times 10^1 \pm 1.53 \times 10^0$	$8.34 \times 10^0 \pm 4.01 \times 10^{-1}$		
—	—	0.10	0.20	$1.34 \times 10^1 \pm 5.01 \times 10^{-1}$	$1.40 \times 10^1 \pm 6.35 \times 10^{-1}$	$1.74 \times 10^1 \pm 1.82 \times 10^0$	$1.22 \times 10^1 \pm 5.32 \times 10^{-1}$		
—	—	0.20	0.30	$4.26 \times 10^0 \pm 3.40 \times 10^{-1}$	$4.41 \times 10^0 \pm 4.40 \times 10^{-1}$	$5.73 \times 10^0 \pm 1.13 \times 10^0$	$3.78 \times 10^0 \pm 3.43 \times 10^{-1}$		
0.80	0.90	0.00	0.10	$4.76 \times 10^0 \pm 2.58 \times 10^{-1}$	$4.81 \times 10^0 \pm 3.17 \times 10^{-1}$	$6.54 \times 10^0 \pm 1.22 \times 10^0$	$4.93 \times 10^0 \pm 3.39 \times 10^{-1}$		
—	—	0.10	0.20	$5.62 \times 10^0 \pm 3.25 \times 10^{-1}$	$6.77 \times 10^0 \pm 4.59 \times 10^{-1}$	$6.64 \times 10^0 \pm 1.12 \times 10^0$	$6.04 \times 10^0 \pm 3.90 \times 10^{-1}$		
—	—	0.20	0.30	$1.16 \times 10^0 \pm 1.74 \times 10^{-1}$	$1.53 \times 10^0 \pm 2.44 \times 10^{-1}$	$2.19 \times 10^0 \pm 7.41 \times 10^{-1}$	$1.21 \times 10^0 \pm 1.96 \times 10^{-1}$		
0.90	1.00	0.00	0.10	$6.69 \times 10^{-1} \pm 9.24 \times 10^{-2}$	$8.01 \times 10^{-1} \pm 1.30 \times 10^{-1}$	$2.17 \times 10^0 \pm 8.08 \times 10^{-1}$	$7.89 \times 10^{-1} \pm 1.40 \times 10^{-1}$		
—	—	0.10	0.20	$8.50 \times 10^{-1} \pm 1.31 \times 10^{-1}$	$6.44 \times 10^{-1} \pm 1.44 \times 10^{-1}$	$1.08 \times 10^0 \pm 4.87 \times 10^{-1}$	$6.63 \times 10^{-1} \pm 1.23 \times 10^{-1}$		
—	—	0.20	0.30	$1.10 \times 10^{-1} \pm 4.98 \times 10^{-2}$	$2.55 \times 10^{-1} \pm 9.08 \times 10^{-2}$	—	$1.06 \times 10^{-1} \pm 9.15 \times 10^{-2}$		

Conclusions and Future Prospects

In 2015, the COMPASS collaboration performed its first Drell-Yan measurement by scattering a negative pion beam off two transversely polarized ammonia targets, an aluminum target, and a tungsten target. The primary purpose of this experiment was to check a fundamental QCD prediction by comparing the transverse spin-dependent azimuthal asymmetries measured in the Drell-Yan process, on a transversely polarized target, with those obtained previously using semi-inclusive DIS measurements. A large amount of data collected allowed extracting unpolarized Drell-Yan cross-sections with statistical accuracies comparable to the best fixed-target experiments available. The Ph.D. thesis presents the first, although still preliminary, pion-induced cross-sections for more than two decades. Pion-nucleus cross-sections were obtained using three different targets: two cells filled out with NH_3 in a LHe bath, ^{27}Al , and ^{184}W .

A detailed overview of the current status of the analysis was presented. The methodology of the evaluation of the Drell-Yan cross-section was introduced. The first step of the analysis was a calculation of the experimental luminosity. A detailed evaluation of beam flux was given, and the target density, particularly the ammonia cells, were discussed. The selection criteria of the dimuon events were then reviewed. A number of corrections, including spectrometer acceptance and dead-time corrections, were also estimated. However, a series of systematic verifications and stability studies were made.

The results were presented as differential Drell-Yan cross-sections as a function of several kinematic variables. Moreover, these latter are in an overall good agreement with the theoretical Drell-Yan cross-sections, calculated at NNLO. A comparison with the E615 data from Fermilab was also performed. Given the systematic uncertainties presented in this Ph.D. work, the agreement with the E615 data appears good. The mean values of the distribution $\langle q_T^2 \rangle$ are consistent with the values obtained by past experiments. A first estimation of the A-dependence $\sigma = \sigma_0 A^\alpha$ was also made. Finally, the value of the parameter α is in line with the values previously obtained. The experience gained in the analysis of the 2015 data should greatly facilitate the analysis of the second set of Drell-Yan data collected by COMPASS in 2018. The 2018 data will provide results with improved statistical accuracy and reduced systematic errors. The comparison between 2015 and 2018 data should allow us to understand the largest systematic uncertainties from 2015 better. The combined 2015 and 2018 data could, therefore, be used for additional phenomenological studies. A major goal of these studies will be the determination of the pion valence PDF. Another important objective is a quantitative evaluation of nuclear PDFs and energy loss effects.

Drell-Yan measurements at CERN are expected to continue in the near future. At present, CERN remains the only laboratory in the world, where high-energy pion beams are available. A new experiment, called COMPASS++/AMBER proposes to perform Drell-Yan measurements with both positive and negative pion beams, with two objectives. First, access the presently poorly known sea quark distribution in the pion and second, study the isovector component of the nuclear mean-field by separately evaluating its effect on u and d quark distributions.

Appendix

A	DAQ Scaler Table	174
B	Trigger Coverage in 2015	175
C	Calibration plots of the ST03 detector in 2015	176
	C.1 R(T) relations	176
	C.2 Simple residuals along wires	177
	C.3 Efficiency plots	178
D	ST03 - Technical drawing of the gas line	179
E	Beam Ghost Tracks Issue	180
F	Detailed Dimuon Event Selection	183
G	Resolution study in 2015	184
H	Combinatorial Background Formula	187
I	Sci-Fi Detector Efficiency in 2015	188
J	Comparison E615 data and DYNNLO predictions	189

This chapter contains extra background information, as well as additional personal works related to COMPASS software and hardware.

A | DAQ Scaler Table

This DAQ scaler table is not exhaustive. It only lists the useful scalers used in the beam flux analysis. The table can be split into four parts:

- First part gives access to the ion2 chamber current. This signal can be converted into flux information.
- Second, the attempted trigger scalers are used to know the exact number of trigger fired and therefore compute a DAQ deadtime. Besides, DAQ deadtime on trigger by trigger is expected to be the same.
- Third, the SciFi scaler gives the information of the beam flux as seen by the active area of each SciFi planes.
- Fourth, the V_{Tot} and \overline{V}_{Tot} are interesting information regarding the evaluation of the VETO deadtime. It can be converted into timing to know the precise time range when a veto signal has been triggered.

Scaler name	Technical Name	Channel
Ion ² Chamber Signal	HMSC1	2
True Random trigger attempted	HMSC1	3
MT+LAST trigger attempted	HMSC1	17
OT+LAST trigger attempted	HMSC1	19
LAST 2mu trigger attempted	HMSC1	21
Total trigger attempted	HMSC1	14
SciFi01 Scaler	SCFI01__	[0-32]
SciFi15 Scaler	SCFI15__	[0-32]
SciFi03 Scaler	SCFI03__	[0-32]
Begin of total veto signal, V_{Tot}	SCsum	0
End of total veto signal, \overline{V}_{Tot}	SCsum	8

Table A.1: Scaler/counter table in 2015

B | Trigger Coverage in 2015

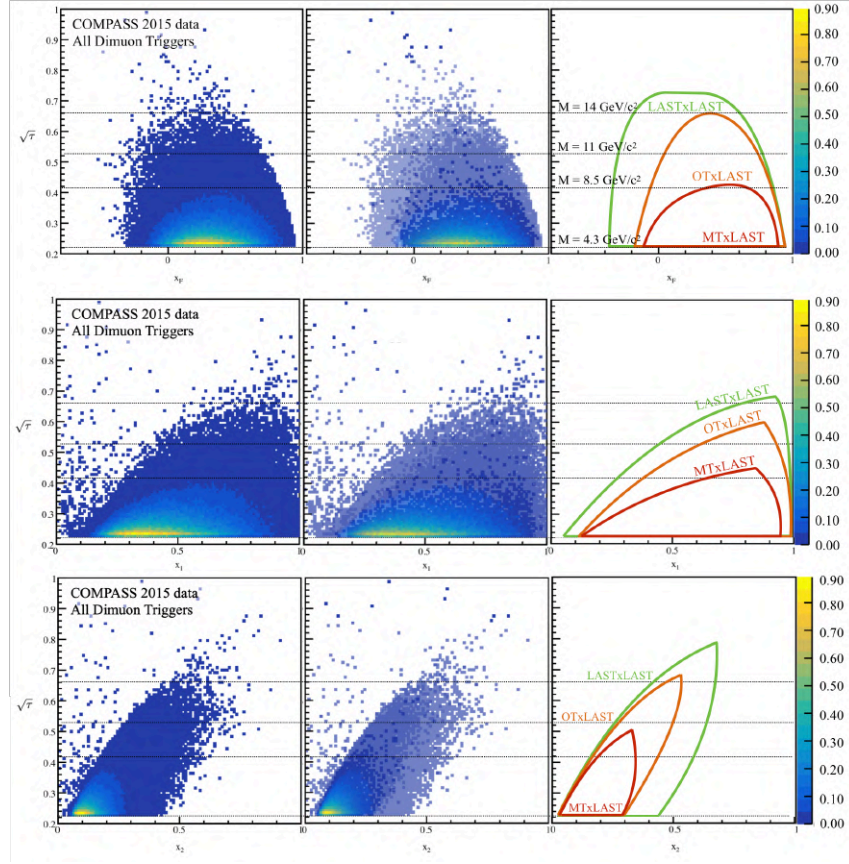


Figure B.1: Left: Trigger coverage in 2015 for all dimuon triggers as a function of x_1 , x_2 , x_F per bin of $\sqrt{\tau}$; Middle: Decomposition of the dimuon trigger coverage; Right: Contour of each dimuon trigger

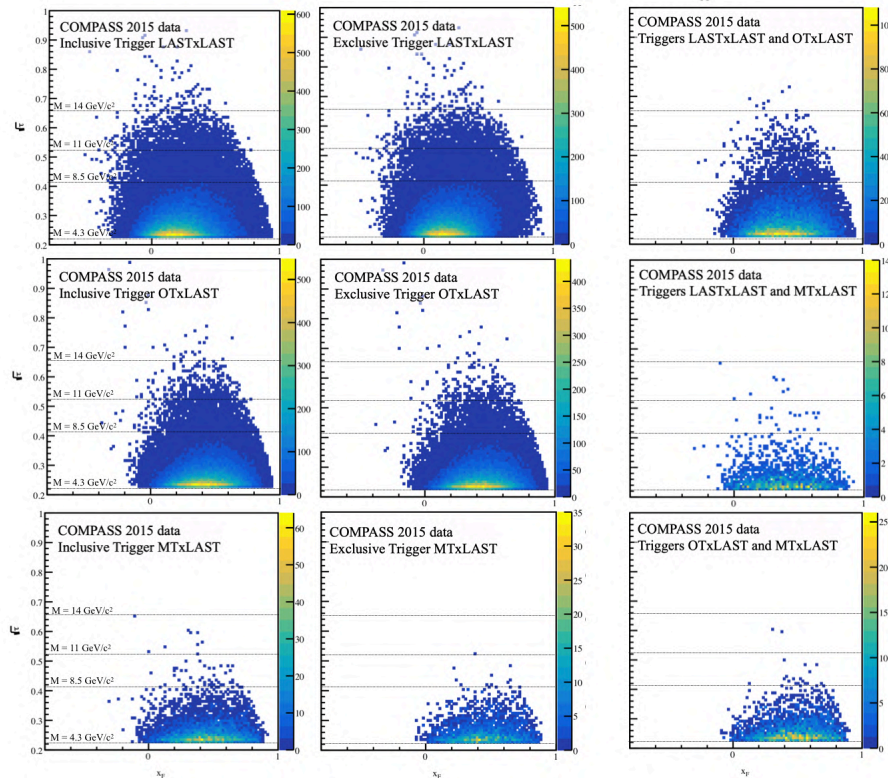


Figure B.2: Trigger Coverage in 2015 expressed in terms of $\sqrt{\tau}$ VS x_F for both inclusive and exclusive dimuon triggers and coincidences

C | Calibration plots of the ST03 detector in 2015

C.1 R(T) relations

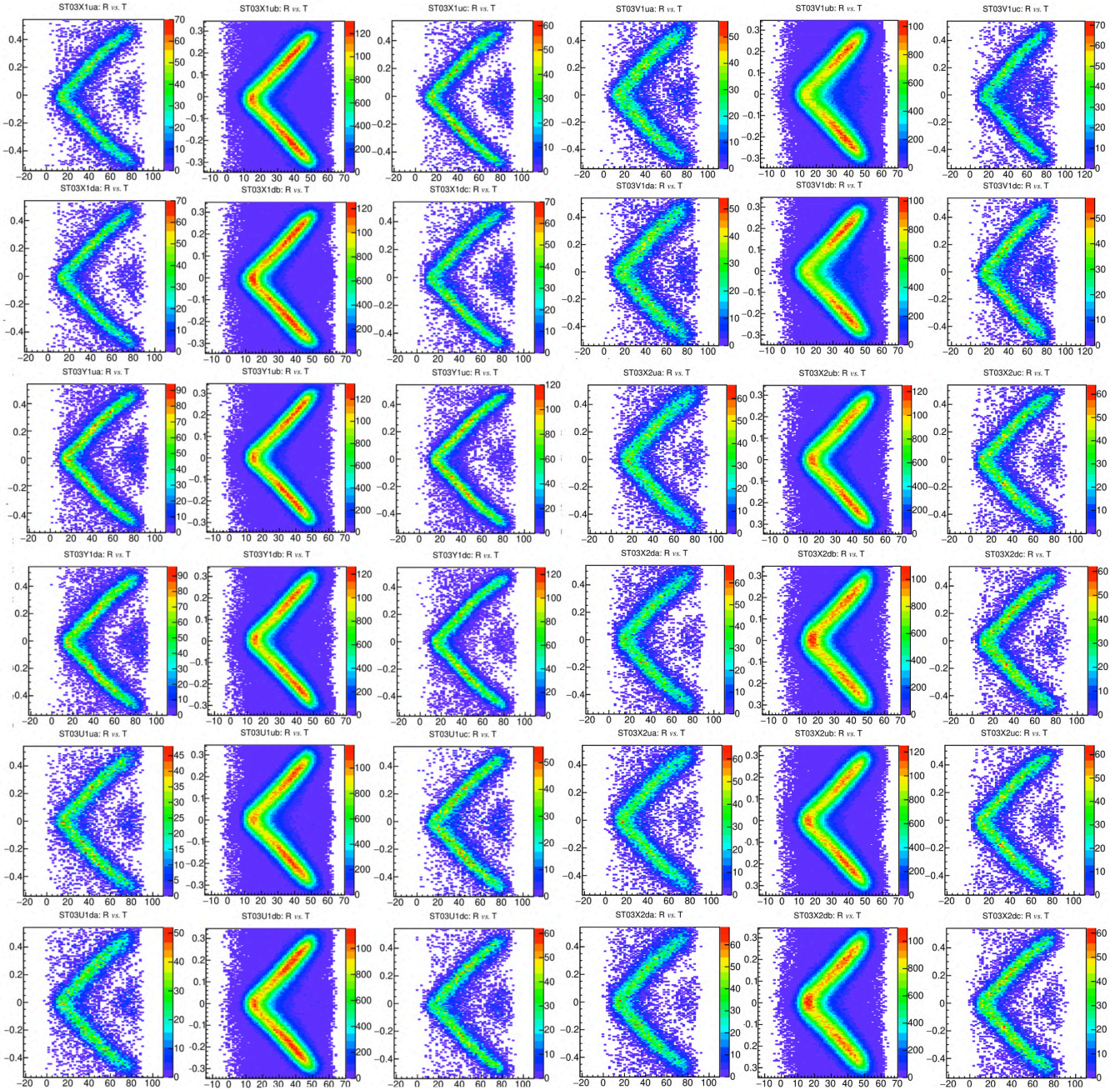


Figure C.1: R(T) relation : ST03X1ua/ub/uc/da/db/dc, ST03Y1/ub/uc/da/db/dc, ST03U1ua/ub/uc/da/db/dc, ST03V1/ub/uc/da/db/dc, ST03Y2ua/ub/uc/da/db/dc and ST03X2/ub/uc/da/db/dc.

C.2 Simple residuals along wires

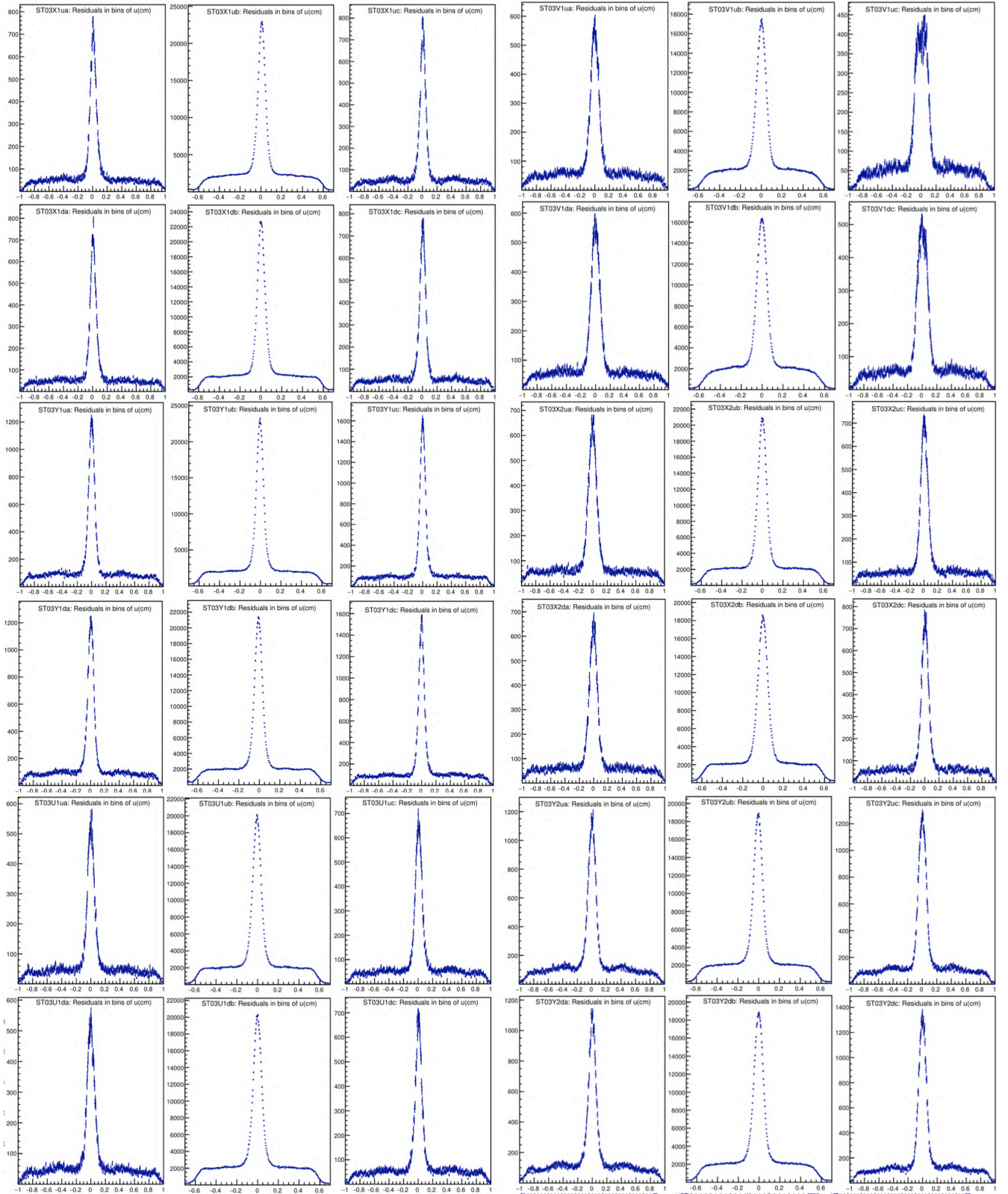


Figure C.2: Simple residual distributions : ST03X1ua/ub/uc/da/db/dc, ST03Y1/ub/uc/da/db/dc, ST03U1ua/ub/uc/da/db/dc, ST03V1/ub/uc/da/db/dc, ST03Y2ua/ub/uc/da/db/dc and ST03X2/ub/uc/da/db/dc.

C.3 Efficiency plots

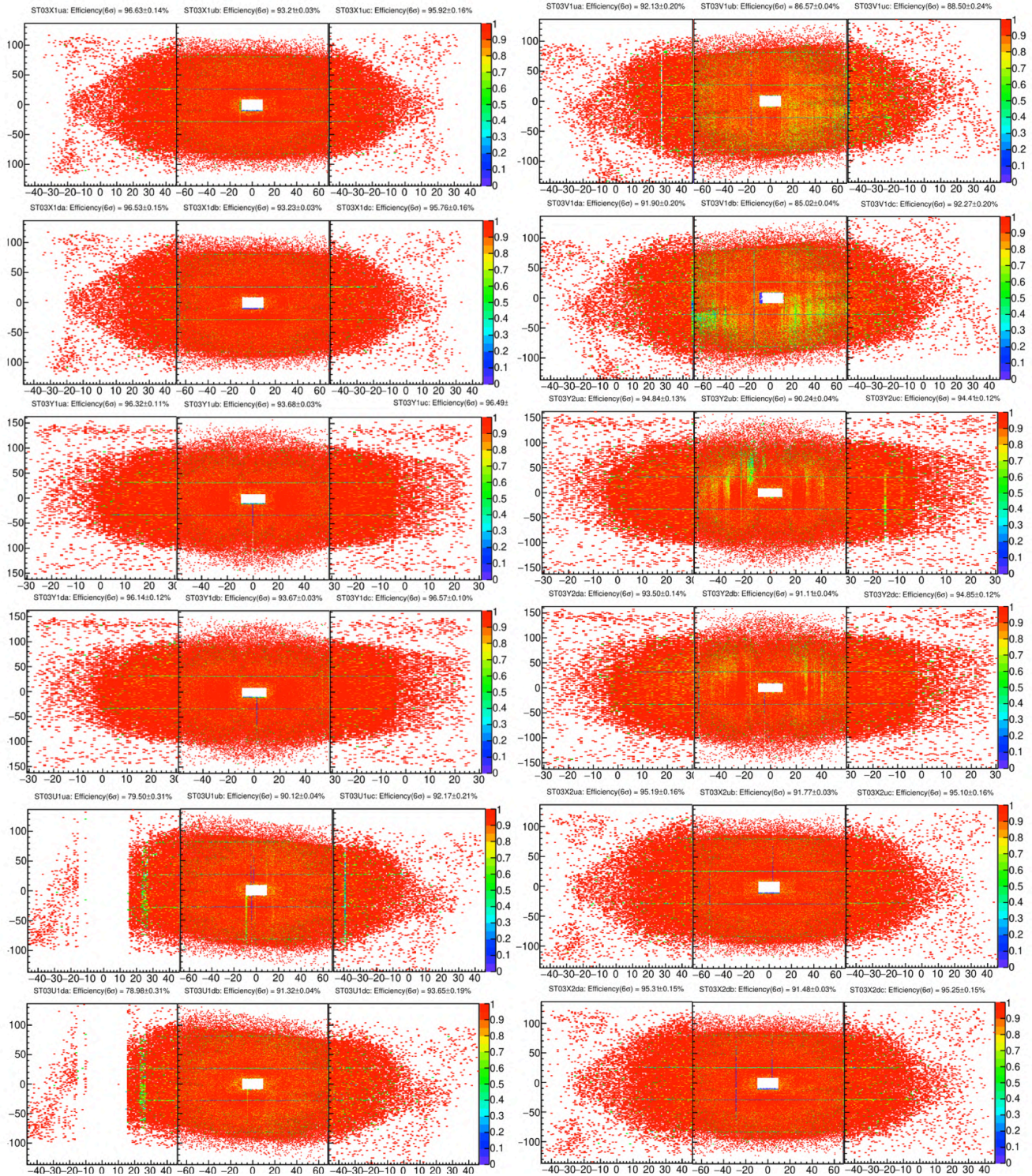


Figure C.3: Efficiency map for ST03X1ua/ub/uc/da/db/dc and ST03Y1/ub/uc/da/db/dc, ST03U1ua/ub/uc/da/db/dc, ST03Y2ua/ub/uc/da/db/dc, ST03X2/ub/uc/da/db/dc, and ST03V1/ub/uc/da/db/dc. ST03U1ua and ST03U1da are partially covered, because of missing electronic cards. The decrease of efficiency in the Y2 and V1 view is the consequences of a high threshold and high noise level. This effect can be explained by the missing x-ray correction.

D | ST03 - Technical drawing of the gas line

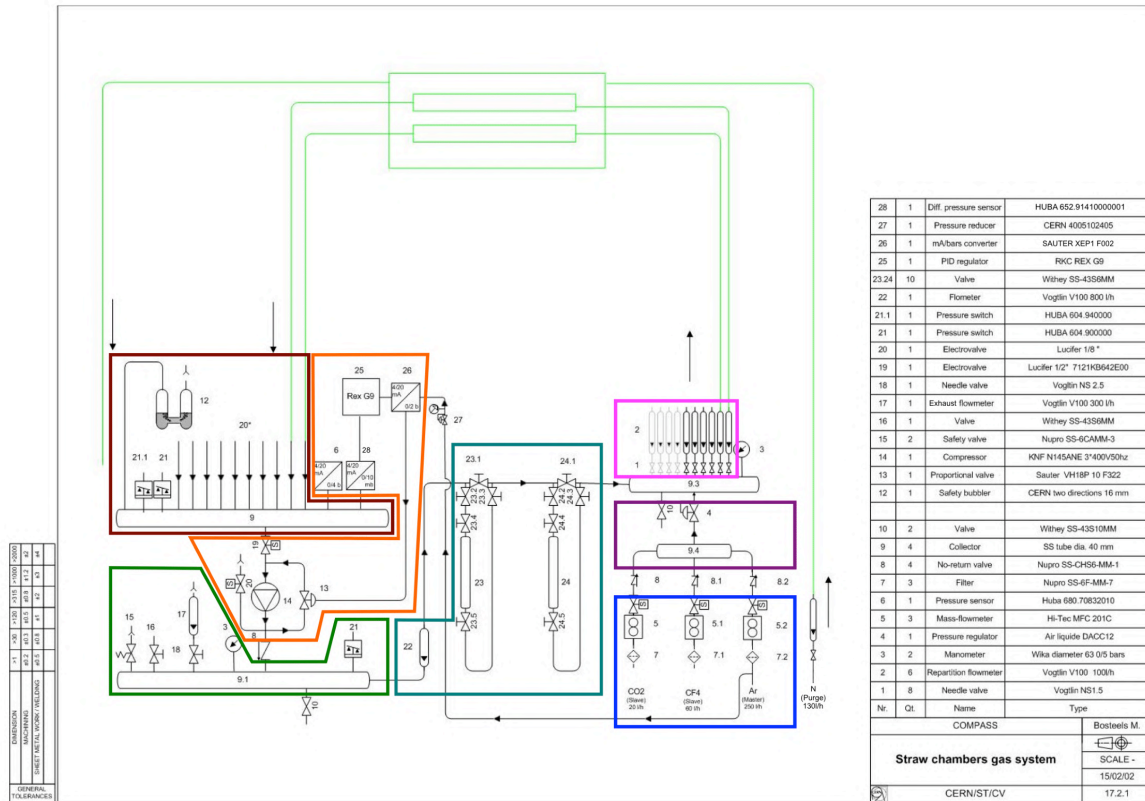


Figure D.1: Technical drawing of the straw gas circuit after the 2016 upgrade. The differential pressure sensor (6) has been replaced by a new HUBA differential pressure sensor. (28)

Each color corresponds to the highlighted area in the technical drawing :

- In blue, the mixing is made using three mass flow meters (5). The Argon mass flow meter is used as reference. Two other gas are mixed in good proportion based on the total rate injected into the chamber.
- In purple, a pressure regulator is in charge of the gas injection in the collector (9.4). In 2016, 4/5 of the gas going through the chamber is recycled.
- In purple, the needle valves (1) are used to inject gas into the chamber.
- In brown, the gas flow back from the chambers is mixed into a collector equipped with a safety bubbler in case of overpressure.
- In orange, the compressor (14) is re-injecting the gas into the recycling chamber (9.1)
- In light green, the recycling chamber (9.1) is equipped with a needle valve (18) in order to regulate the gas pressure and therefore to adjust the gas recycling rate.
- In dark green, two gas filters (23,24) are used in order to reduce humidity in the chamber before re-injection in the initial collector.

E | Beam Ghost Tracks Issue

The ghost beam track issue is a known issue related to the beam track reconstruction in the production dyt1, dyt2 and dyt3. This problem has been found during the flux analysis of the dyt3 production and fixed in the dyt4 and dyt5 productions. The term ghost track refers to the reconstruction of fake tracks, with hits only correlated in space but not in time, in the tracking of the Sci-Fi

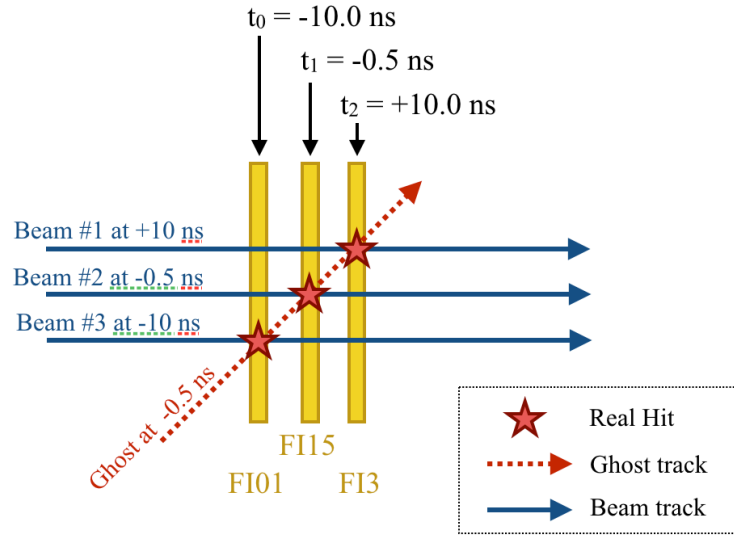


Figure E.1: Illustration of the ghost track reconstruction, assuming 3 real beam tracks not reconstructed and 3 hits in the Sci-Fi detectors. As the 3 hits are aligned, but out of time, a ghost track is reconstructed with a mean time of -0.5 ns.

Ghost tracks were clearly visible in Fig.E.2a at large angle, going up to 25 mrad, although the beam impinging is tuned to enter the PT cryostat with an angle of 1.63 mrad. The signature of a background signal was also visible in the beam mean time distribution, as shown in Fig.E.2b. The t5 production in red shows the expected beam mean time profile compared to other data taking years. Shoulders at -5 ns and 5 ns are an expected feature of the timing cut applied to the detector composing the beam telescope.

Finally, a strong argument, as a proof of the correction of this issue, is shown Fig.E.3. In Fig.E.3a, the number of beam track reconstruction around the origin of time depends on the choice of the time gate, which is an unexpected feature. In Fig.E.3b, the number of beam track reconstructed is flat as function of the time gate. Additional impact of the ghost track correction are shown in Fig.E.4 and Fig.E.6.

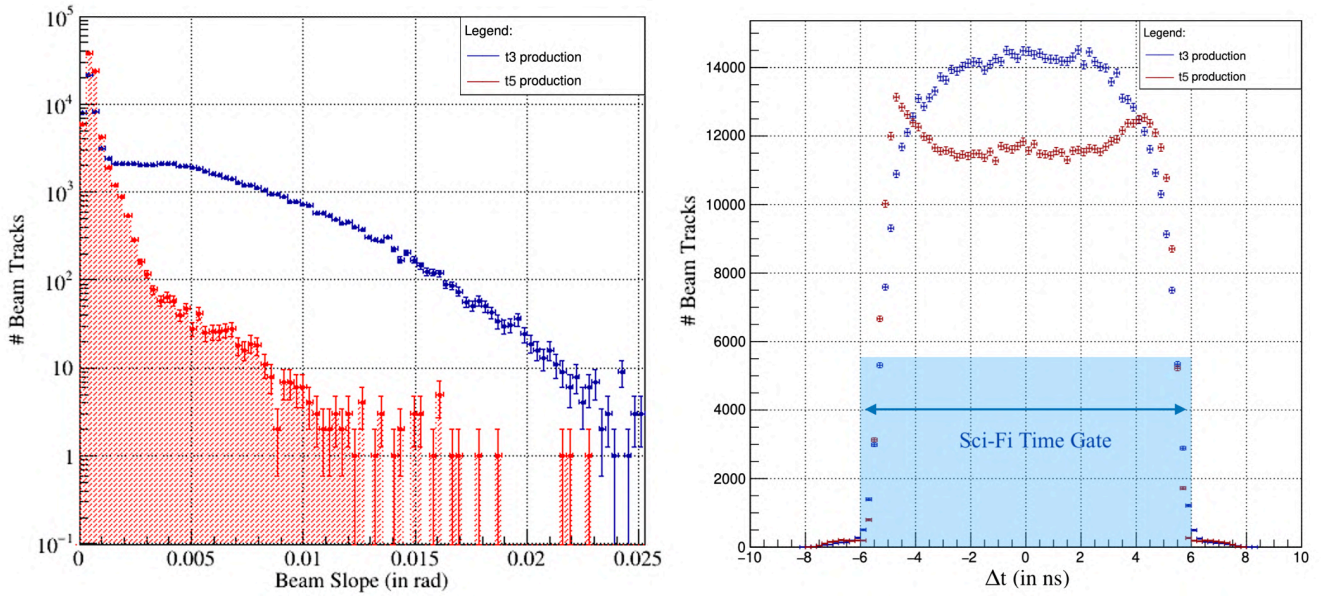


Figure E.2: (a) On the left: Comparison of the beam slopes between the t3 production (in blue), including ghost tracks, and after the fix of the issue in the t5 (slot-1) production (in red); (b) On the right: Beam Mean time profile before (in blue) and after (in red) correction of the beam track reconstruction

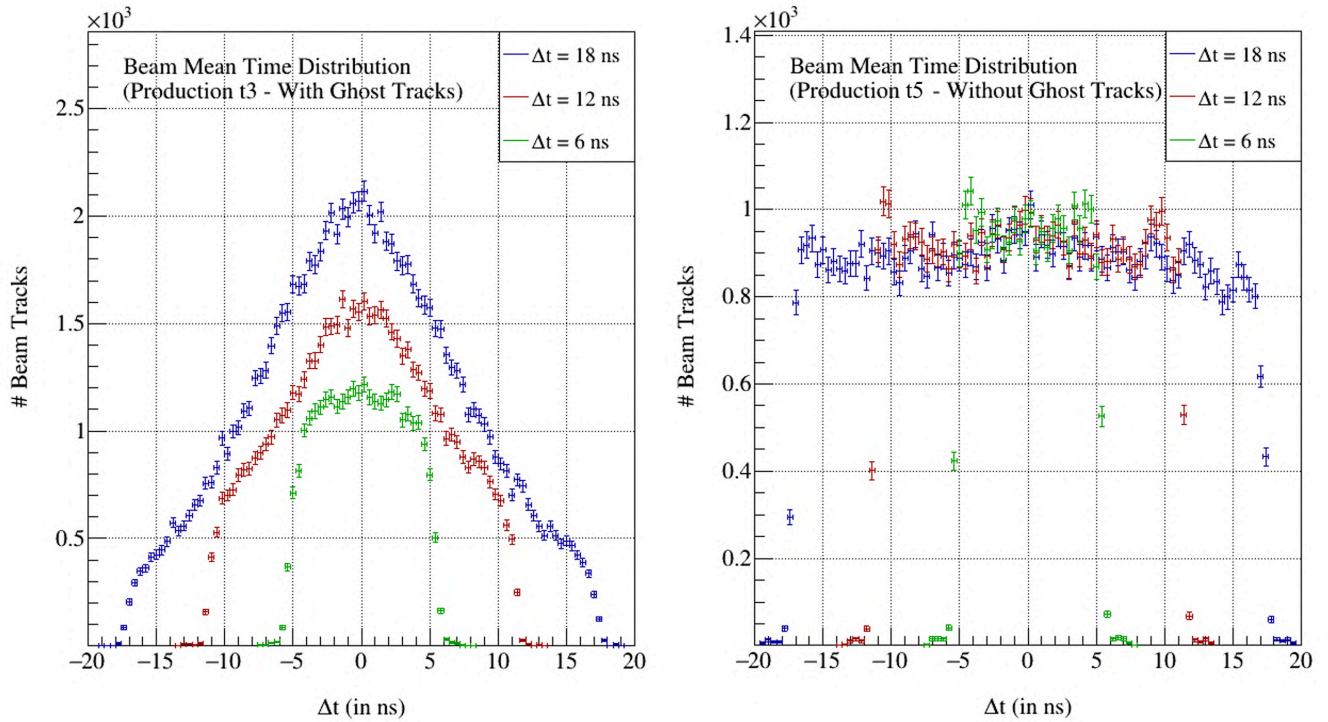


Figure E.3: (a) On the left: (b) Beam meantime distributions for various Sci-Fi time gate Δt before the ghost beam tracks issue was fixed. (b) On the right: Beam meantime distributions for various Sci-Fi time gates Δt after correction of the ghost beam tracks issue.

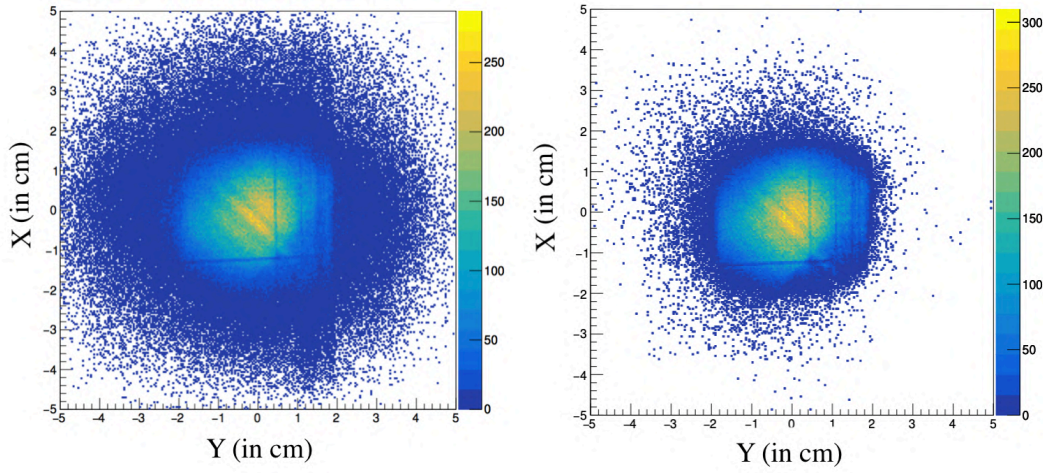


Figure E.4: Illustration of the impact of the ghost track on the left. The right plot shows the beam track profile after fixing the issue. The number of beam tracks is highly reduced at large angle.

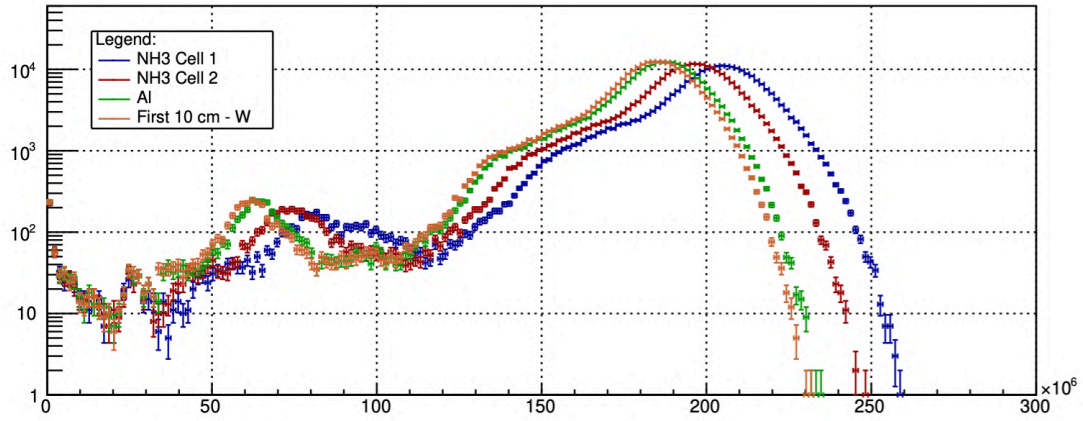


Figure E.5: The estimated flux distribution including ghost tracks highly depends on the choice of the target, which is an unexpected observation in the measurement of the flux as tracks are extrapolated from the beam telescope.

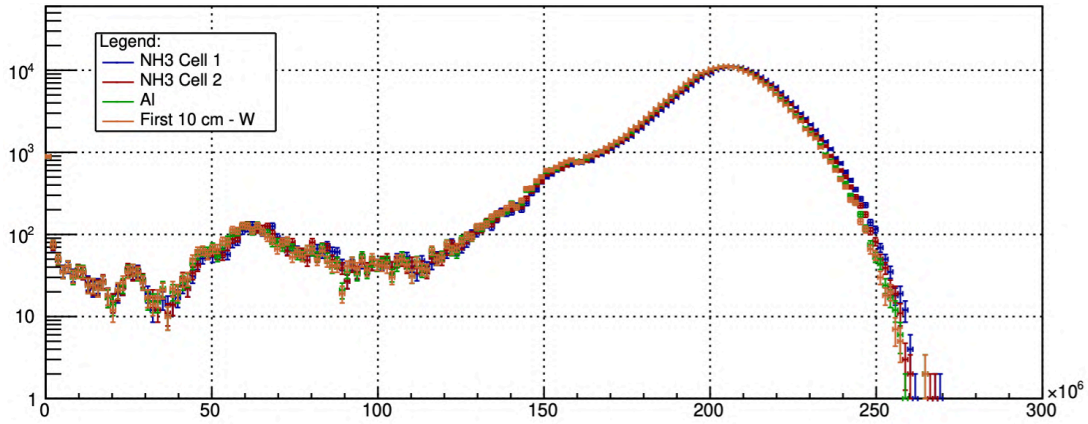


Figure E.6: After fixing the ghost track issue, the computation of the beam flux shows much stable distributions as function of the target.

F | Detailed Dimuon Event Selection

Table F.1: Detail of the number of dimuon pairs selected in the analysis of the dy2015 slot-1 production.

Pre-Selection of Events	W07	W08	W09	W10	W11	W12	W13	W14	W15	2015	% 2015
Initial events	–	–	–	–	–	–	–	–	–	3,150,672,496 evts	100.00%
Best Primary Vertex Selection	–	–	–	–	–	–	–	–	–	1,393,261,337 evts	44.22%
All Dimuon Triggers	–	–	–	–	–	–	–	–	–	1,379,312,812 evts	43.78%
Drell-Yan Pair Reduction	W07	W08	W09	W10	W11	W12	W13	W14	W15	2015	% 2015
Initial pairs	–	–	–	–	–	–	–	–	–	2,646,569,384 pairs	–
Oppositely Charged Muons	–	–	–	–	–	–	–	–	–	39,163,288 pairs	–
$4.3 < M_{\mu\mu}/(\text{GeV}/c^2) < 8.5$	147,547	152,985	140,957	143,572	210,145	169,394	148,454	102,403	55,839	1,271,296 pairs	100.00%
$Z_{\text{last}} > 1500 \text{ cm}$	139,673	144,747	133,322	135,800	198,741	159,650	139,950	96,366	52,677	1,200,926 pairs	94.46%
$Z_{\text{first}} < 300 \text{ cm}$	139,138	144,239	132,435	135,031	197,305	157,934	138,856	95,632	52,316	1,192,886 pairs	93.83%
$ t_{\mu-} - t_{\mu+} < 5 \text{ ns}$	74,923	76,125	75,179	78,088	114,700	90,806	81,494	54,675	30,468	676,458 pairs	53.21%
$\chi^2_{\text{track}}/n.d.f. \leq 10$	74,088	75,269	74,396	77,321	113,582	89,819	80,518	53,968	30,117	669,078 pairs	52.63%
Trigger validation	43,017	44,329	43,945	45,422	68,697	51,992	45,921	29,792	17,146	390,261 pairs	30.70%
$0 < x_N < 1, 0 < x_\pi < 1$	41,069	42,159	41,915	43,337	65,785	49,783	43,852	28,371	16,340	372,611 pairs	29.31%
$-1.0 < x_F < 1.0$	41,069	42,159	41,915	43,337	65,785	49,783	43,852	28,371	16,340	372,611 pairs	29.31%
$R_{\text{vtx}}/(\text{cm}) < 1.9$	33,908	34,926	34,633	35,956	54,433	41,214	36,270	23,360	13,526	308,226 pairs	24.25%
Refined Pair Selection	W07	W08	W09	W10	W11	W12	W13	W14	W15	2015	% 2015
Good spill selection	26,675	26,803	27,709	28,651	39,263	34,689	27,734	20,535	12,811	244,870 pairs	19.26%
LAST \otimes LAST or LAST \otimes OT	17,503	17,175	18,263	18,984	25,907	23,055	18,083	13,346	8,352	160,668 pairs	12.64%
$-0.2 < x_F < 0.9$	17,306	16,952	18,057	18,770	25,674	22,811	17,880	13,198	8,274	158,922 pairs	12.50%
Beam Quality Selection	W07	W08	W09	W10	W11	W12	W13	W14	W15	2015	% 2015
$1 \text{ s} < t_{\text{spill}} < 5.6 \text{ s}$	17,007	16,773	17,952	18,640	25,510	22,683	17,787	13,130	8,218	157,700 pairs	12.40%
$ t_{\text{beam}} < 3 \text{ ns}$	15,661	15,220	16,475	17,072	23,434	20,736	16,280	11,979	6,903	144,424 pairs	11.36%
$ t_{\text{beam}} - t_{\mu\pm} < 2 \text{ ns}$	14,096	13,552	14,947	15,386	21,077	18,742	14,796	10,845	6,903	130,344 pairs	10.25%
Beam decay muon rejection	11,677	11,065	12,347	12,821	17,454	15,618	12,272	8,878	5,752	107,884 pairs	8.49%
Target Selection	W07	W08	W09	W10	W11	W12	W13	W14	W15	2015	% 2015
Only for PT Cell 1:											
$-294.5 < Z_{\text{vtx}}/(\text{cm}) < -239.3$	1,943	1,900	2,119	2,220	3,089	2,782	2,190	1,507	1,053	18,803 pairs	1.48%
$R_{\text{vtx}}/(\text{cm}) < 1.7$	1,836	1,784	2,014	2,095	2,959	2,614	2,078	1,428	1,001	17,779 pairs	1.40%
Cross upstream targets	1,824	1,774	2,005	2,081	2,911	2,601	2,069	1,425	999	17,689 pairs	1.39%
Only for PT Cell 2:											
$-219.5 < Z_{\text{vtx}}/(\text{cm}) < -164.3$	1,639	1,486	1,614	1,748	2,348	2,121	1,674	1,239	769	15,306 pairs	1.20%
$R_{\text{vtx}}/(\text{cm}) < 1.7$	1,559	1,486	1,601	1,720	2,300	2,099	1,662	1,226	769	14,558 pairs	1.14%
Cross upstream targets	1,538	1,468	1,601	1,720	2,300	2,099	1,662	1,226	759	14,373 pairs	1.13%
Only for Aluminium :											
$-63.5 < Z_{\text{vtx}}/(\text{cm}) < -56.5$	257	263	303	295	443	382	290	211	136	2,580 pairs	0.20%
$R_{\text{vtx}}/(\text{cm}) < 1.7$	238	256	291	280	425	365	280	197	127	2,459 pairs	0.19%
Cross upstream targets	235	249	285	272	413	358	278	195	125	2,410 pairs	0.19%
Only for Tungsten :											
$-30.0 < Z_{\text{vtx}}/(\text{cm}) < -20.0$	2,085	1,985	2,182	2,269	3,057	2,741	2,135	1,587	1,019	19,060 pairs	1.49%
$R_{\text{vtx}}/(\text{cm}) < 1.7$	1,992	1,876	2,076	2,166	2,936	2,611	2,048	1,503	984	18,192 pairs	1.43%
Cross upstream targets	1,962	1,842	2,036	2,135	2,880	2,573	2,024	1,476	963	17,891 pairs	1.41%

G | Resolution study in 2015

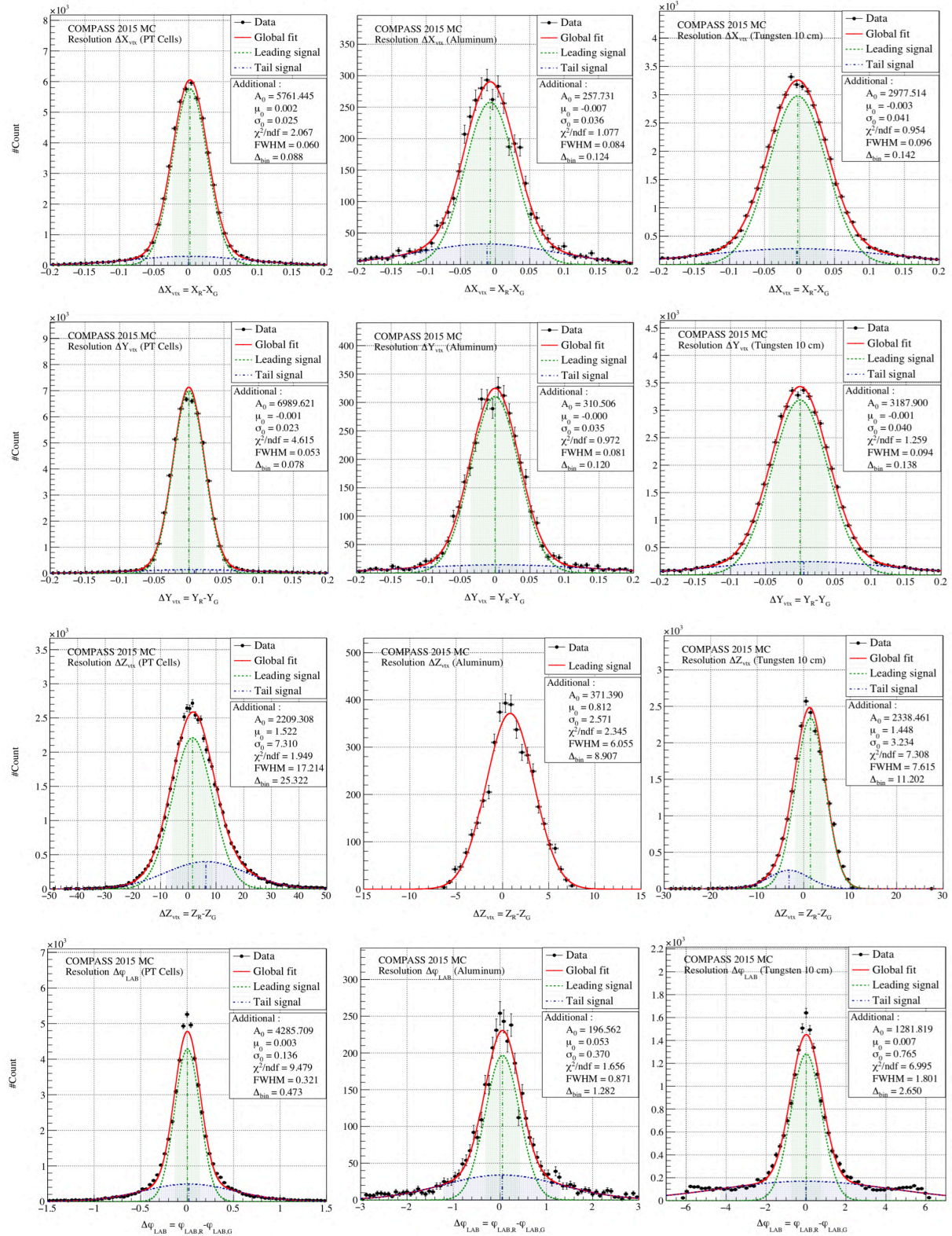


Figure G.1: Residual plot in 2015 to estimate the resolution of kinematic variables

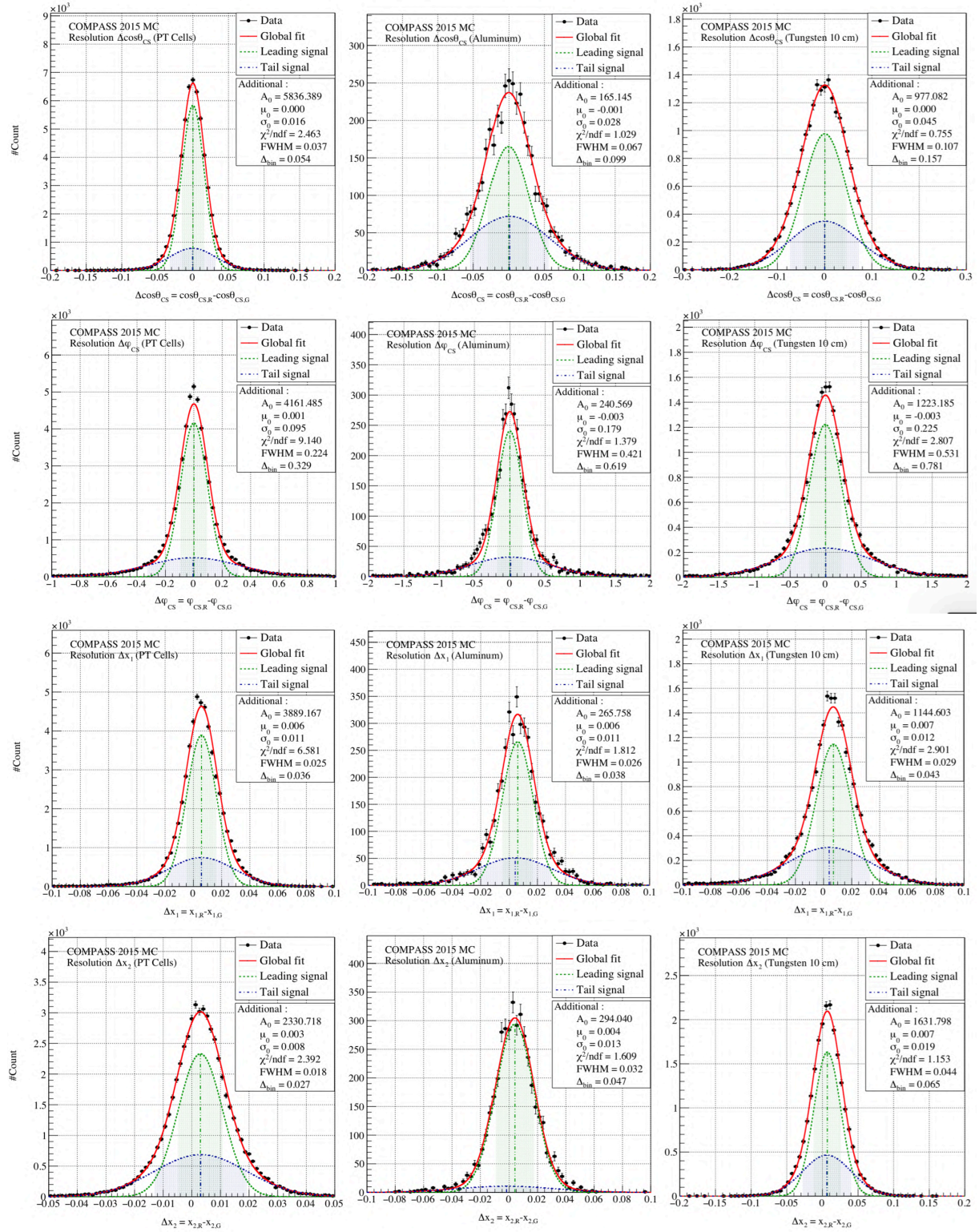


Figure G.2: Residual plot in 2015 to estimate the resolution of kinematic variables

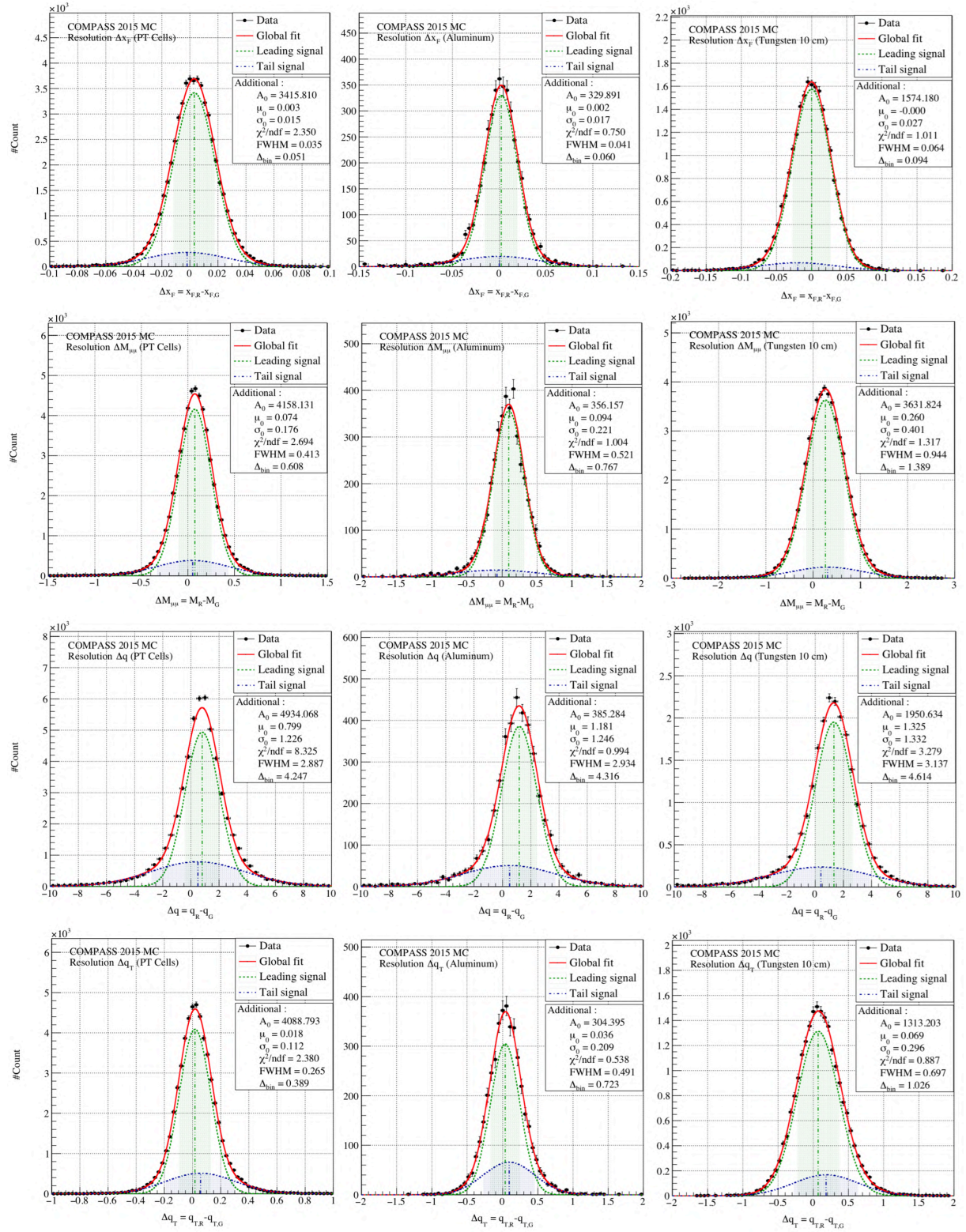


Figure G.3: Residual plot in 2015 to estimate the resolution of kinematic variables

H | Combinatorial Background Formula

The opposite sign combinatorial background N_{+-} can be determined, by assuming an equal acceptance in the detection of μ^+ and μ^- . The single muon distributions N_+ and N_- are assumed to follow poissonian laws and have an uncorrelated origin, which lead to the following relations :

$$\begin{cases} Var(N_+) = \mathbb{E}[N_+] \\ Var(N_-) = \mathbb{E}[N_-] \\ Cov(N_+, N_-) = 0 \end{cases} \quad (\text{H.1})$$

The number of permutations of N_+ and N_- to obtain N_{++} , N_{--} and N_{+-} are defined as follows:

$$N_{++} = \frac{N_+(N_+ - 1)}{2} \quad N_{--} = \frac{N_-(N_- - 1)}{2} \quad N_{+-} = N_+ N_- \quad (\text{H.2})$$

Moreover, the expected value associated to these variables can be summarized as following :

$$\begin{cases} \mathbb{E}[N_{++}] = \frac{1}{2} (\mathbb{E}[N_+^2] - \mathbb{E}[N_+]) = \frac{1}{2} \mathbb{E}[N_+]^2 \\ \mathbb{E}[N_{--}] = \frac{1}{2} (\mathbb{E}[N_-^2] - \mathbb{E}[N_-]) = \frac{1}{2} \mathbb{E}[N_-]^2 \\ \mathbb{E}[N_{+-}] = \mathbb{E}[N_+] \mathbb{E}[N_-] + Cov(N_+, N_-) \end{cases} \quad \Rightarrow \quad \mathbb{E}[N_{+-}] = 2\sqrt{\mathbb{E}[N_{++}] \mathbb{E}[N_{--}]}$$

I | Sci-Fi Detector Efficiency in 2015

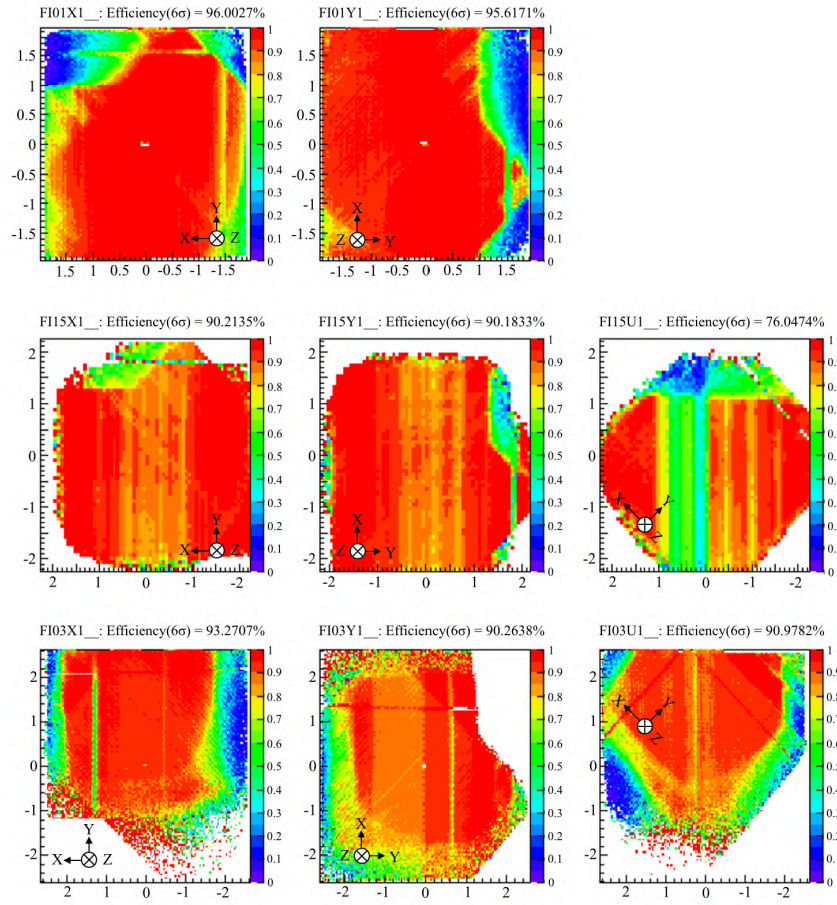


Figure I.1: Sci-Fi Efficiencies in 2015, produced during the 2D-Efficiency Campaign at Blue Waters

J | Comparison E615 data and DYNNLO predictions

The Fig.J.1 shown the double differential cross-section as a function of x_F per bin of $\sqrt{\tau}$ in the range $[0.185; 0.393]$. Higher $\sqrt{\tau}$ bins are shown in Fig.J.2. The mass bins corresponding to the upsilon are highlighted in green from $\sqrt{\tau} = 0.392$ to $\sqrt{\tau} = 0.484$ and might be the explanation of the cross-section increase.

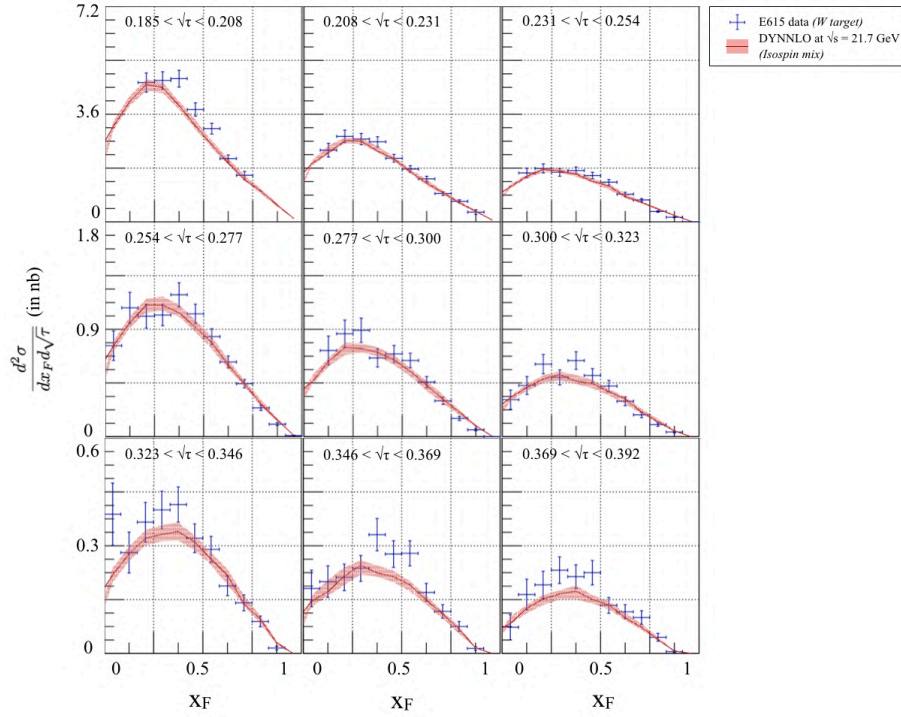


Figure J.1: Comparison between E615 cross-section and DYNNLO predictions per bin of $\sqrt{\tau}$ and x_F

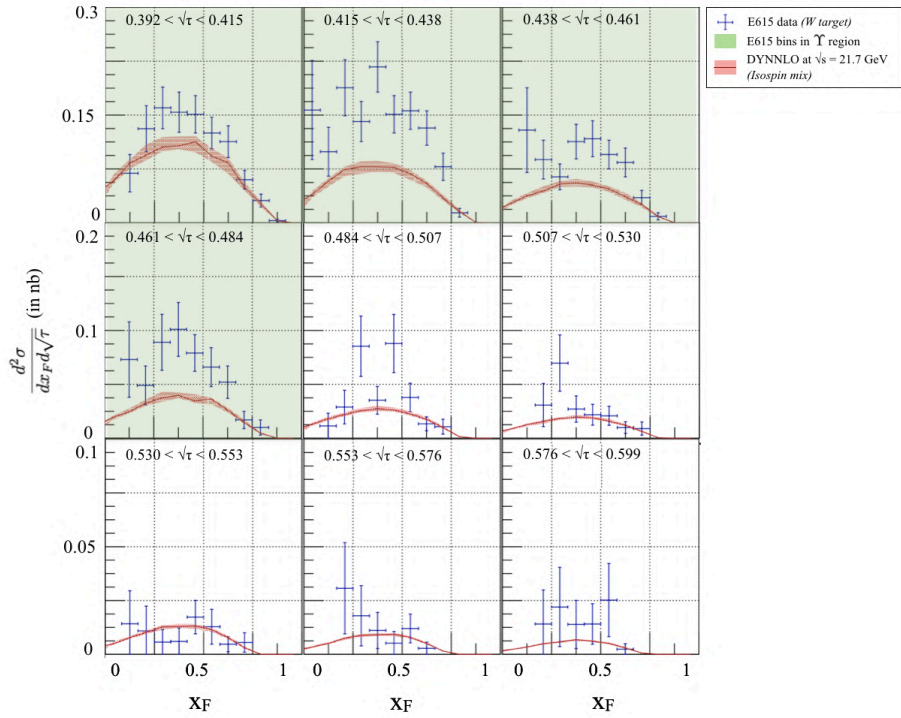


Figure J.2: Comparison between E615 cross-section and DYNNLO predictions per bin of $\sqrt{\tau}$ and x_F ; The green bins correspond to the known upsilon resonance mass region

Résumé en Français

Dans la perspective d'améliorer notre compréhension de la structure interne des hadrons, le processus Drell-Yan a été mesuré grâce à l'expérience COMPASS en 2015 avec un faisceau de π^- de 190-GeV produit dans la ligne faisceau M2, auprès de l'accélérateur SPS du CERN. Le processus est schématisé sur la Fig. 1 et les principales relations sont données par l'Eq. J.1. Enfin, la couverture cinématique Drell-Yan sondée par l'expérience COMPASS est présentée Fig. 2. Une interprétation plus poussée de ce canal de dimuon, sur cible fixe, donnera accès aux distributions des partons dans le pion et à l'étude des effets de la matière froide dans les noyaux.

$$H_1(P_1) + H_2(P_2, \vec{S}) \longrightarrow \ell^-(p_{\ell^-}) + \ell^+(p_{\ell^+}) + X_1 + X_2$$

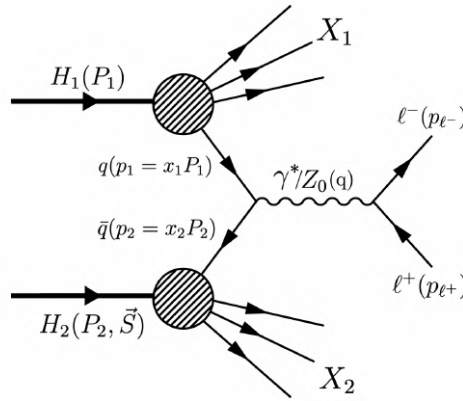


Figure 1: Diagramme de Feynman du processus Drell-Yan, générant une paire de lepton $\ell\bar{\ell}$ issue de l'annihilation d'une paire de quark-antiquark $q\bar{q}$. X_1 et X_2 sont des éléments résultant de l'interaction inélastique des hadrons H_1 and H_2 et ne sont pas mesurés.

$$\begin{cases} Q^2 &= q^2 = M^2 \\ s &= (P_1 + P_2)^2 \end{cases} \quad \text{et} \quad \begin{cases} x_F &= x_1 - x_2 \\ \tau &= M^2/s \end{cases} \quad \text{avec } x_{1,2} \text{ définis par } x_{1,2} = \frac{Q^2}{2P_{1,2} \cdot q} \quad (\text{J.1})$$

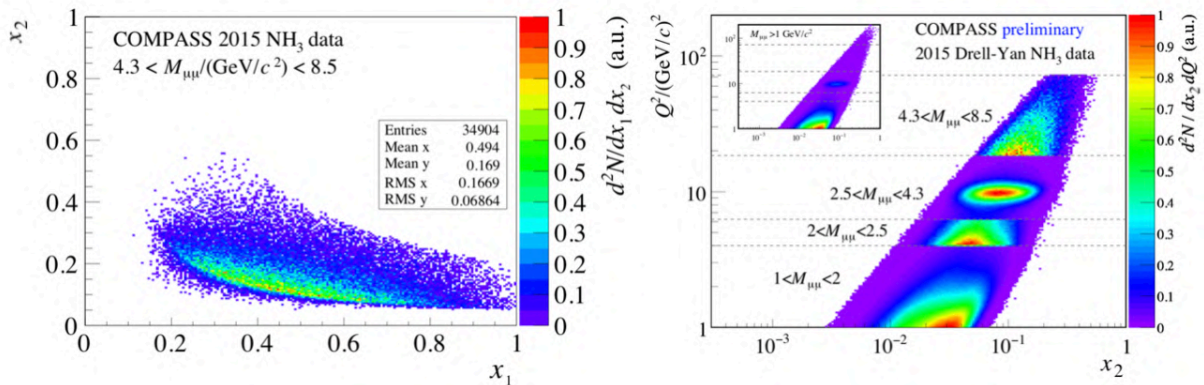


Figure 2: Aperçu de la couverture cinématique Drell-Yan des données COMPASS 2015 en fonction de x_1 et x_2 (gauche), et en fonction x_2 et Q^2 (droite)

La collaboration COMPASS dispose d'un appareillage de détection permettant la mesure de la trajectoire, de l'impulsion et l'identification des particules qui le traverse. En 2015, le spectromètre COMPASS (Fig. 3) a permis l'acquisition de nouvelles données Drell-Yan sur cibles d'ammoniac (NH_3), d'aluminium (^{27}Al) ou de tungstène (^{184}W). L'ensemble des cibles ainsi que le telescope faisceau sont présentés en Fig. 4.

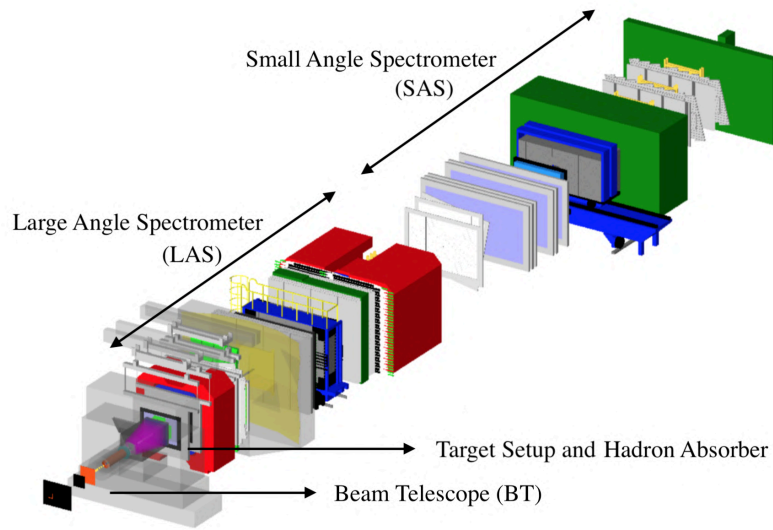


Figure 3: Appareillage COMPASS (2015) employé pour détecter les paires de muon Drell-Yan

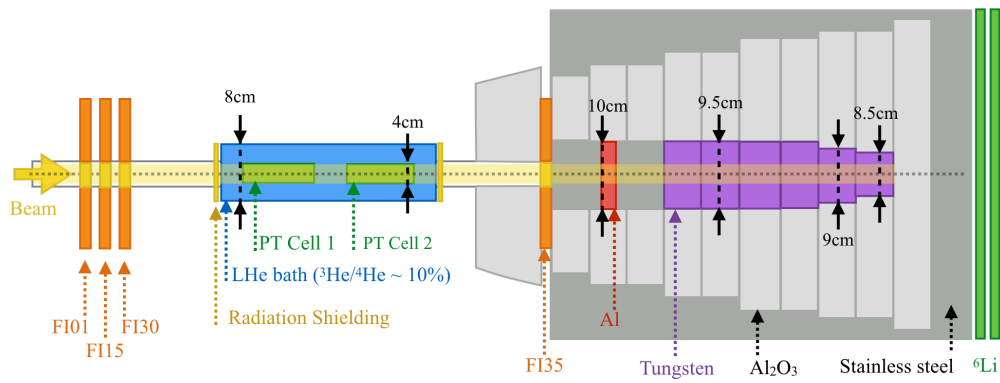


Figure 4: Ensemble cible utilisé en 2015 et composé de trois différentes cibles (NH_3 , ^{27}Al , ^{184}W). Le télescope faisceau composé de Sci-Fi (FI01 FI15, FI03), utilisé pour la détection des traces faisceau, est aussi représenté sur ce schéma.

Le premier point développé dans cette thèse est lié à mes contributions techniques réalisées auprès du détecteur gazeux Straw tube durant la période 2016-2018. La maintenance et la calibration du dernier détecteur ST03 sont assurées par l'Université d'Illinois (USA) depuis 2014. Ce détecteur est composé de six plans de détection individuel orientés comme indiqué sur la Fig. 5.

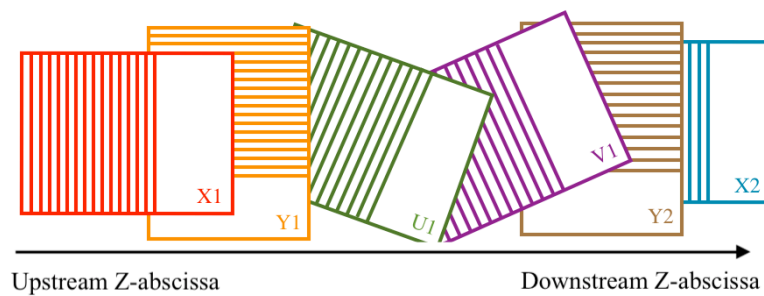


Figure 5: Illustration de l'orientation des six plans du détecteur Straw ST03.

La calibration dite $R(T)$, présentée en Fig. 6 assure la bonne conversion du temps de détection en une distance au fil pour optimiser la résolution de détection. Enfin, une efficacité de détection est produite à l'aide des données de calibration 2015 (un exemple ST03X1ub est donné sur la Fig. 7). Les traces de référence sont reconstruites avec le spectromètre sans le détecteur ST03.

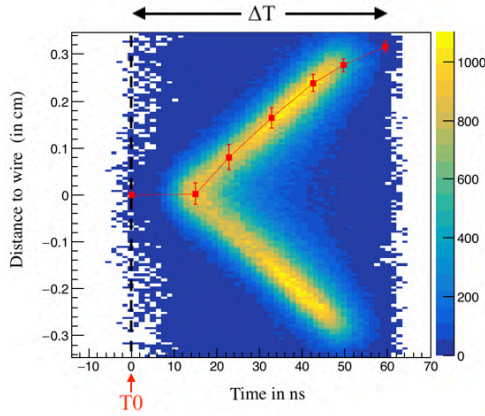


Figure 6: Exemple de relation RT pour le plan ST03Y2ub, incluant le fit de la courbe RT en rouge

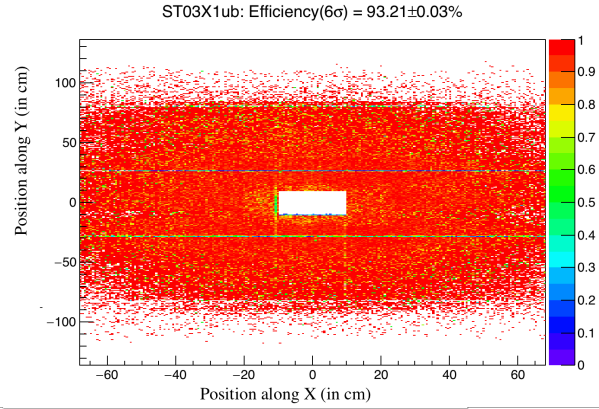


Figure 7: Efficiency of the ST03X1ub, $\varepsilon = 93.21 \pm 0.03\%$

La reconstruction des traces est produite par un logiciel nommé CORAL et développé par la collaboration COMPASS. Aussi, la contribution de ce travail de thèse a permis la production officielle sur le super-calculateur Blue Waters (Illinois, USA) des données 2015, ainsi que les simulations Monte-Carlo pour l'ensemble des collaborateurs COMPASS. Ceci a été possible grâce à l'utilisation du logiciel de production appelé ESCALADE et développé dans le but d'assurer une production à grande échelle (≥ 1 PB) sans erreur.

Le second point développé est mon travail pour l'évaluation des sections efficaces grâce à la détermination précise des différents termes présentés par l'Eq. J.2. Une première estimation des erreurs systématiques est présentée dans la Tab. J.1.

$$\sigma_{\text{nucleon}} = \frac{1}{\varepsilon} \times \frac{N_{\mu\mu}}{\mathcal{L}} \quad \sigma_{\text{nucleus}} = A \times \sigma_{\text{nucleon}} \quad (\text{J.2})$$

- où
- σ_{nucleon} définit la section-efficace par nucleon.
 - σ_{nucleus} est la section-efficace par noyau.
 - $N_{\mu\mu}$ est le nombre de paires de muon reconstruit.
 - ε est le terme d'acceptance incluant l'acceptance géométrique ε_{acc} ainsi que l'efficacité du spectromètre ε_{eff}
 - $\mathcal{L} = \mathcal{F}_{\text{eff}} \times \varrho_T$ est la luminosité totale effective pion-nucléon intégrée sur le temps utile de l'analyse (e.g. run, période ou année complète).
 - $(\mathcal{F}_{\text{eff}}, \varrho_T)$ sont les termes de flux effectif et de densité de cible, respectivement.)
 - A fait référence au numéro de masse atomique.

Les résultats de sections efficaces absolues sont obtenus cible par cible, tabulés, et présentés en fonction de x_F en bins de $\sqrt{\tau}$ et comparées aux prédictions théoriques. Le résultat obtenu pour la cible de W est présenté sur la Fig. 8 et comparé avec les sections efficaces extraites par l'expérience E615. Cette figure

Table J.1: Résumé des erreurs systématiques dans l'intervalle de masse $[4.3 \text{ GeV}/c^2, 8.5 \text{ GeV}/c^2]$. Le terme de luminosité inclut aussi l'incertitude sur le temps mort de la DAQ et du VETO.

Incertitudes Systematiques	Incertitude cible par cible			
	PT Cell 1	PT Cell 2	Al	W (10 cm)
Incertitude sur la luminosité	7%	7%	7%	8%
Incertitude sur la densité de cible	–	15%	–	–
Incertitude du modèle de génération	5%	5%	5%	5%
Estimation de la contamination dimuon	3%	3%	1%	7%
Incertitude Totale	9%	18%	9%	12%

montre un bon accord des résultats COMPASS avec les prédictions théoriques et les sections efficaces E615, à l'exception des deux premiers bins en $\sqrt{\tau}$, dû à la contamination d'autres processus dimuon à basse masse ($\sim 4.3 \text{ GeV}/c^2$).

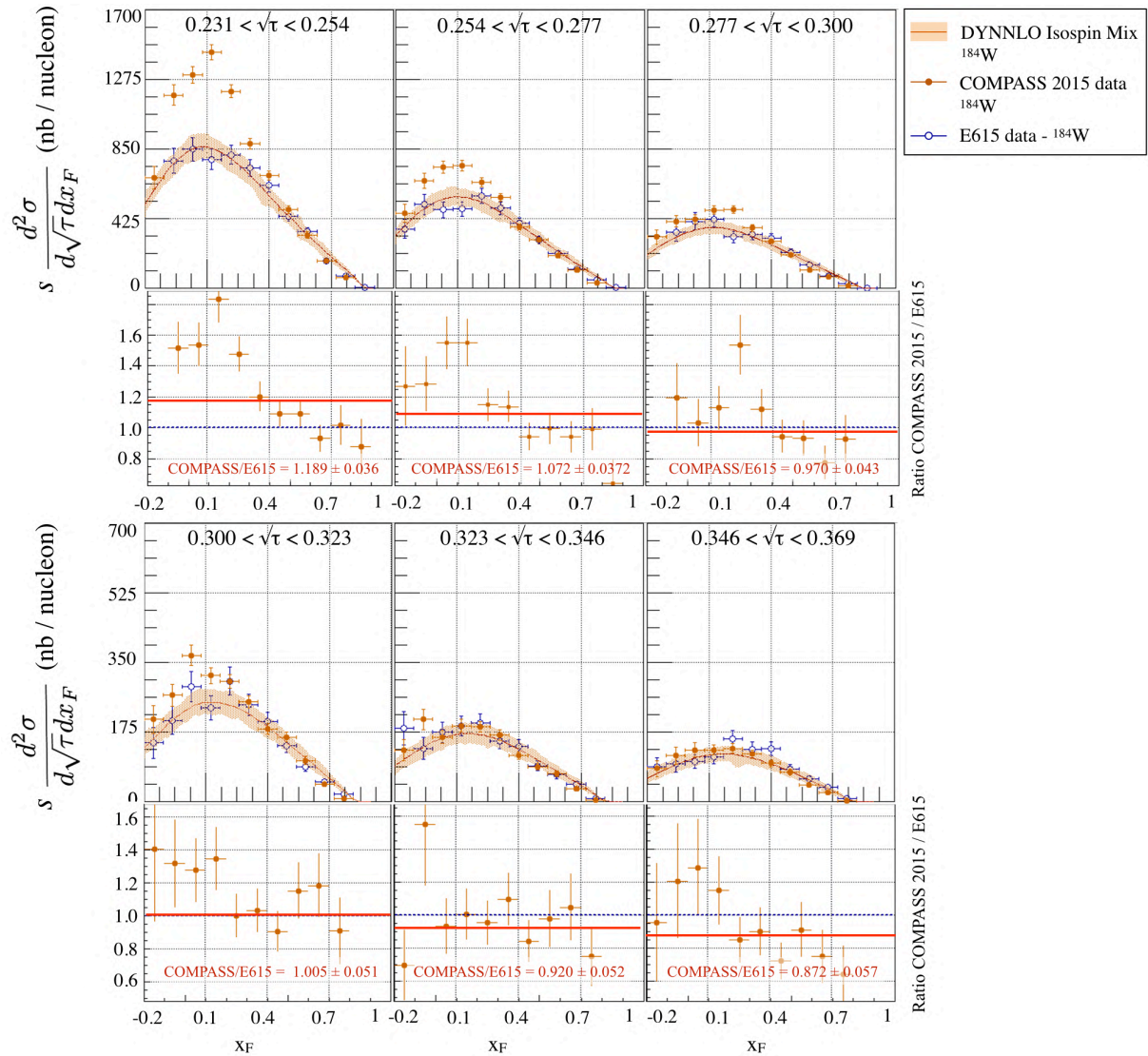


Figure 8: Sections efficaces absolues par nucléon obtenues pour la cible de W en fonction de x_F en bins de $\sqrt{\tau}$ et comparées avec les prédictions théoriques DYNLO [128]

Des comparaisons supplémentaires ont été effectuées pour vérifier la robustesse de la section efficace extraite. Entre autre, la dépendance de ces sections efficaces en fonction du numéro de masse atomique a été brièvement évaluée au travers du paramètre α . Ce paramètre exprimé en fonction de la masse $M_{\mu\mu}$ et de l'impulsion transverse q_T du photon virtuel a été comparé avec les résultats obtenus par Ito *et al.* [31] et est proche de 1 en moyenne. De plus, la dépendance en fonction de x_F est présentée et met en évidence une chute à grand x_F attendue par la théorie. Une étude plus approfondie permettra de mieux comprendre les effets nucléaires associés aux différents noyaux, et les processus de pertes d'énergie.

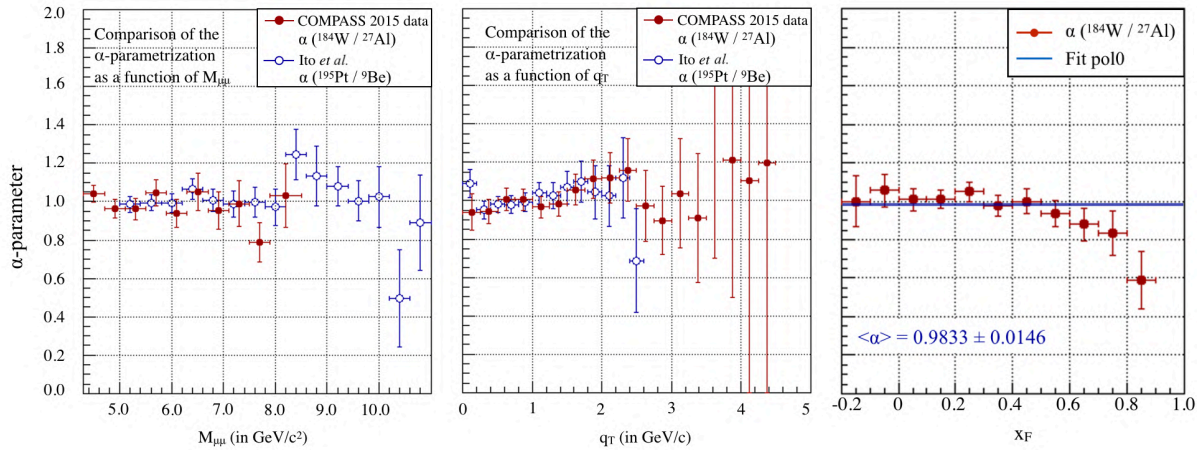


Figure 9: Présentation du paramètre $\alpha(\sigma_W/\sigma_{Al})$ en fonction de x_F , q_T et $M_{\mu\mu}$. Ces coefficients fonction de q_T et $M_{\mu\mu}$ (en rouge) sont également comparés avec les résultats de Ito *et al.* [31] (en bleu)

Enfin la dépendance de $\langle q_T \rangle$ en fonction de x_F et $M_{\mu\mu}$ est étudiée en fonction des différentes cibles du dispositif COMPASS 2015 (Fig. 10). Les résultats obtenus sont plus précisément comparés aux données extraites par l'expérience E615. Enfin la dépendance de $\langle q_T \rangle$ pour la cible de ^{184}W est comparée en fonction de \sqrt{s} avec de nombreuses autres expériences et semble suivre une tendance commune ce qui confirme la qualité des données collectées par la collaboration COMPASS.

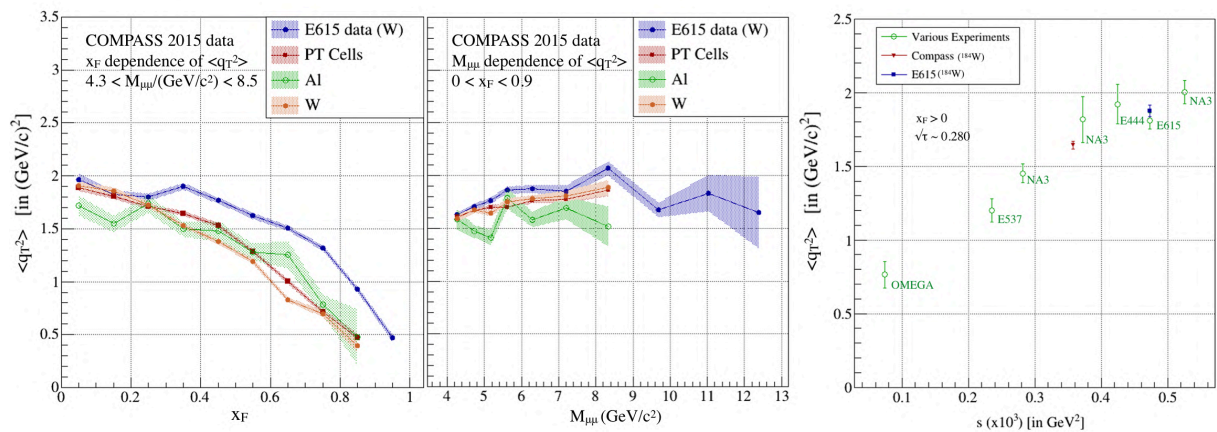


Figure 10: (a) Gauche: Distribution moyenne q_T^2 pour $4.3 < M_{\mu\mu}/(\text{GeV}/c^2) < 8.5$ en fonction de x_F ; (b) Milieu: Distribution moyenne q_T^2 pour $0 < x_F < 0.9$ en fonction de $M_{\mu\mu}$; Les données de E615 sont toutes exprimées entre 4.05 et 8.55 GeV/c^2 et pour $0 < x_F < 0.9$; (c) Droite: Evolution de $\langle q_T^2 \rangle$ en fonction \sqrt{s} pour différentes expériences. Les données en vert ont été extraites de [132]

Bibliography

- [1] M. Gell-Mann. *The Eightfold Way: A Theory of Strong Interaction Symmetry*. Tech. rep. CTSI-20, TID-12608. 1961. DOI: 10.2172/4008239.
- [2] M. Gell-Mann. “A schematic model of baryons and mesons”. In: *Physics Letters* 8.3 (1964), pp. 214–215. DOI: 10.1016/S0031-9163(64)92001-3.
- [3] G. Zweig. “An SU(3) model for strong interaction symmetry and its breaking. Version 2”. In: *DEVELOPMENTS IN THE QUARK THEORY OF HADRONS. VOL. 1. 1964 - 1978*. Ed. by D.B. Lichtenberg and Simon Peter Rosen. 1964, pp. 22–101.
- [4] J I Friedman and H W Kendall. “Deep Inelastic Electron Scattering”. In: *Annual Review of Nuclear Science* 22.1 (1972), pp. 203–254. DOI: 10.1146/annurev.ns.22.120172.001223.
- [5] Samuel C.C. Ting. “The discovery of the J particle”. In: *Nobel Lecture* (1976).
- [6] B.J. Björken and S.L. Glashow. “Elementary particles and SU(4)”. In: *Physics Letters* 11.3 (1964), pp. 255–257. DOI: 10.1016/0031-9163(64)90433-0.
- [7] S. L. Glashow, J. Iliopoulos, and L. Maiani. “Weak Interactions with Lepton-Hadron Symmetry”. In: *Phys. Rev. D* 2 (7 Oct. 1970), pp. 1285–1292. DOI: 10.1103/PhysRevD.2.1285.
- [8] J. -E. Augustin et al. “Discovery of a Narrow Resonance in e^+e^- Annihilation”. In: *Phys. Rev. Lett.* 33 (23 Dec. 1974), pp. 1406–1408. DOI: 10.1103/PhysRevLett.33.1406.
- [9] J. Ashman et al. “A measurement of the spin asymmetry and determination of the structure function g_1 in deep inelastic muon-proton scattering”. In: *Physics Letters B* 206.2 (1988), pp. 364–370. DOI: 10.1016/0370-2693(88)91523-7.
- [10] Florent Robinet. *New measurement of $\Delta G/G$ at COMPASS from open charm events. Direct Measurement of the Gluon Polarization from Open Charm Events at COMPASS*. Tech. rep. 2008.
- [11] A. Airapetian et al. “Single-Spin Asymmetries in Semi-Inclusive Deep-Inelastic Scattering on a Transversely Polarized Hydrogen Target”. In: *Phys. Rev. Lett.* 94 (1 Jan. 2005), p. 012002. DOI: 10.1103/PhysRevLett.94.012002.
- [12] Paolo [COMPASS Collaboration] Pagano. “Measurements of Collins and Sivers asymmetries at COMPASS”. In: hep-ex/0501035 (Jan. 2005). 4 pages, 1 figure, presented at SPIN2004 International Symposium, October 10-16 2004, Trieste, Italy, 369–372. 4 p. DOI: 10.1142/9789812701909_0067.
- [13] J.C. Collins, Davison E. Soper, and George Sterman. “Transverse momentum distribution in Drell-Yan pair and W and Z boson production”. In: *Nuclear Physics B* 250.1 (1985), pp. 199–224. DOI: 10.1016/0550-3213(85)90479-1.
- [14] M. Breidenbach et al. “Observed Behavior of Highly Inelastic Electron-Proton Scattering”. In: *Phys. Rev. Lett.* 23 (16 Oct. 1969), pp. 935–939. DOI: 10.1103/PhysRevLett.23.935.
- [15] John C. Collins, Davison E. Soper, and George Sterman. “Factorization for short distance hadron-hadron scattering”. In: *Nuclear Physics B* 261 (1985), pp. 104–142. DOI: 10.1016/0550-3213(85)90565-6.
- [16] John C. Collins, Davison E. Soper, and George F. Sterman. “Factorization of Hard Processes in QCD”. In: *Adv. Ser. Direct. High Energy Phys.* 5 (1989), pp. 1–91. DOI: 10.1142/9789814503266_0001. arXiv: hep-ph/0409313 [hep-ph].
- [17] H. David Politzer. “Reliable Perturbative Results for Strong Interactions?” In: *Phys. Rev. Lett.* 30 (26 June 1973), pp. 1346–1349. DOI: 10.1103/PhysRevLett.30.1346.
- [18] David J. Gross and Frank Wilczek. “Ultraviolet Behavior of Non-Abelian Gauge Theories”. In: *Phys. Rev. Lett.* 30 (26 June 1973), pp. 1343–1346. DOI: 10.1103/PhysRevLett.30.1343.
- [19] J. Beringer et al. “Review of Particle Physics”. In: *Phys. Rev. D* 86 (1 July 2012), p. 010001. DOI: 10.1103/PhysRevD.86.010001.

- [20] G. Altarelli and G. Parisi. “Asymptotic freedom in parton language”. In: *Nuclear Physics B* 126.2 (1977), pp. 298–318. DOI: 10.1016/0550-3213(77)90384-4.
- [21] W. Bartel *et al.* “Electroproduction of pions near the $\Delta(1236)$ isobar and the form-factor $G_M^*(q^2)$ of the $(\gamma N \Delta)$ vertex”. In: *Phys.Lett.* 28B (1968), pp. 148–151. DOI: 10.1016/0370-2693(68)90155-X.
- [22] Claude Amsler. “Deep inelastic electron–proton scattering”. In: *Nuclear and Particle Physics*. 2053-2563. IOP Publishing, 2015, 18-1 to 18-12. DOI: 10.1088/978-0-7503-1140-3ch18.
- [23] K.A. Olive. “Review of Particle Physics”. In: *Chinese Physics C* 38.9 (Aug. 2014), p. 090001. DOI: 10.1088/1674-1137/38/9/090001.
- [24] J. H. Christenson *et al.* “Observation of Massive Muon Pairs in Hadron Collisions”. In: *Phys. Rev. Lett.* 25 (21 Nov. 1970), pp. 1523–1526. DOI: 10.1103/PhysRevLett.25.1523.
- [25] Sidney D. Drell and Tung-Mow Yan. “Massive Lepton-Pair Production in Hadron-Hadron Collisions at High Energies”. In: *Phys. Rev. Lett.* 25 (13 Sept. 1970), pp. 902–902. DOI: 10.1103/PhysRevLett.25.902.2.
- [26] F Gautheron *et al.* *COMPASS-II Proposal*. Tech. rep. CERN-SPSC-2010-014. SPSC-P-340. Geneva: CERN, May 2010.
- [27] W J Stirling and M R Whalley. “A compilation of Drell-Yan cross sections”. In: *Journal of Physics G: Nuclear and Particle Physics* 19.D (Dec. 1993), pp. D1–D102. DOI: 10.1088/0954-3899/19/d/001.
- [28] Angelis *et al.* In: *Phys.Lett.* 87B (1979), p. 398.
- [29] Kourkoumelis *et al.* In: *Phys. Lett.* 91B (1979), p. 475.
- [30] Antreasyan *et al.* In: *Phys.Rev.Lett.* 48 (1981), p. 302.
- [31] A. S. Ito *et al.* “Measurement of the continuum of dimuons produced in high-energy proton-nucleus collisions”. In: *Phys. Rev. D* 23 (3 Feb. 1981), pp. 604–633. DOI: 10.1103/PhysRevD.23.604.
- [32] Antreasyan *et al.* In: *Phys.Rev.Lett.* (39 1979), p. 906.
- [33] K. J. Anderson *et al.* “Production of Muon Pairs by 225-GeV/c π^\pm , K^+ , p^\pm Beams on Nuclear Targets”. In: *Phys. Rev. Lett.* 42 (15 Apr. 1979), pp. 944–947. DOI: 10.1103/PhysRevLett.42.944. URL: <https://link.aps.org/doi/10.1103/PhysRevLett.42.944>.
- [34] S. R. Smith *et al.* “Experimental Test of the Drell-Yan Model in $p + W \rightarrow \mu^+ + \mu^- + X$ ”. In: *Phys. Rev. Lett.* 46 (25 June 1981), pp. 1607–1610. DOI: 10.1103/PhysRevLett.46.1607.
- [35] J. *et al.* Badier. “Drell-Yan events from 400 GeV/c protons: Determination of the K-factor in a large kinematical domain”. In: 26.4 (1985), pp. 489–494. DOI: 10.1007/BF01551789.
- [36] D. M. Alde *et al.* “Nuclear dependence of dimuon production at 800 GeV”. In: *Phys. Rev. Lett.* 64 (21 1990), pp. 2479–2482. DOI: 10.1103/PhysRevLett.64.2479.
- [37] G. Moreno *et al.* “Dimuon production in proton-copper collisions at $\sqrt{s} = 38.8$ GeV”. In: *Phys. Rev. D* 43 (9 May 1991), pp. 2815–2835. DOI: 10.1103/PhysRevD.43.2815.
- [38] Alitti *et al.* In: *Phys. Lett.* 275B (1992), p. 202.
- [39] Anassontzis *et al.* In: *Phys. Rev.* D38 (1988), p. 1377.
- [40] Greenlee *et al.* In: *Phys. Rev. Lett.* 55 (1985), p. 1555.
- [41] Barate *et al.* In: *Phys.Rev.Lett.* 43 (1979), p. 1541.
- [42] Corden *et al.* In: *Phys. Lett.* 96B (1980), p. 417.
- [43] J. *et al.* Badier. “Experimental Determination of the pi Meson Structure Functions by the Drell-Yan Mechanism”. In: *Z. Phys.* C18 (1983), p. 281.
- [44] NA10 Collaboration *et al.* “Differential cross-section of high-mass muon pairs produced by a 194 GeV/c π^- beam on a tungsten target”. In: *Zeitschrift für Physik C Particles and Fields* 28.1 (Mar. 1985), pp. 9–14. DOI: 10.1007/BF01550243.

- [45] J. S. Conway et al. “Experimental study of muon pairs produced by 252-GeV pions on tungsten”. In: *Phys. Rev. D* 39 (1 Jan. 1989), pp. 92–122. DOI: 10.1103/PhysRevD.39.92.
- [46] E. Braaten, S. Fleming, and T.C. Yuan. “Production of heavy quarkonium in high-energy colliders”. In: *Annual Review of Nuclear and Particle Science* 46.1 (1996), pp. 197–235. DOI: 10.1146/annurev.nucl.46.1.197.
- [47] P. L. McGaughey et al. “Cross sections for the production of high-mass muon pairs from 800 GeV proton bombardment of ^2H ”. In: *Phys. Rev. D* 50 (5 Sept. 1994), pp. 3038–3045. DOI: 10.1103/PhysRevD.50.3038.
- [48] H. L. Lai et al. “Improved parton distributions from global analysis of recent deep inelastic scattering and inclusive jet data”. In: *Phys. Rev. D* 55 (3 Feb. 1997), pp. 1280–1296. DOI: 10.1103/PhysRevD.55.1280.
- [49] P. L. McGaughey, J. M. Moss, and J. C. Peng. “High-Energy Hadron-Induced Dilepton Production from Nucleons and Nuclei”. In: *Annual Review of Nuclear and Particle Science* 49.1 (1999), pp. 217–253. DOI: 10.1146/annurev.nucl.49.1.217.
- [50] C. S. Lam and Wu-Ki Tung. “Systematic approach to inclusive lepton pair production in hadronic collisions”. In: *Phys. Rev. D* 18 (7 Oct. 1978), pp. 2447–2461. DOI: 10.1103/PhysRevD.18.2447.
- [51] NA10 Collaboration et al. “Angular distributions of muon pairs produced by 194 GeV/c negative pions”. In: *Zeitschrift für Physik C Particles and Fields* 31.4 (Dec. 1986), pp. 513–526. DOI: 10.1007/BF01551072.
- [52] L. Y. Zhu et al. “Measurement of Angular Distributions of Drell-Yan Dimuons in $p+d$ Interactions at 800 GeV/c”. In: *Phys. Rev. Lett.* 99 (8 Aug. 2007), p. 082301. DOI: 10.1103/PhysRevLett.99.082301.
- [53] L. Y. Zhu et al. “Measurement of Angular Distributions of Drell-Yan Dimuons in $p+p$ Interactions at 800 GeV/c”. In: *Phys. Rev. Lett.* 102 (18 May 2009), p. 182001. DOI: 10.1103/PhysRevLett.102.182001.
- [54] D. Boer and P. J. Mulders. “Time-reversal odd distribution functions in lepton production”. In: *Phys. Rev. D* 57 (9 May 1998), pp. 5780–5786. DOI: 10.1103/PhysRevD.57.5780.
- [55] Jen-Chieh Peng et al. “Interpretation of angular distributions of Z-boson production at colliders”. In: *Physics Letters B* 758 (2016), pp. 384–388. DOI: 10.1016/j.physletb.2016.05.035.
- [56] T. Aaltonen et al. “First Measurement of the Angular Coefficients of Drell-Yan e^+e^- Pairs in the Z Mass Region from $p\bar{p}$ Collisions at $\sqrt{s} = 1.96$ TeV”. In: *Phys. Rev. Lett.* 106 (24 June 2011), p. 241801. DOI: 10.1103/PhysRevLett.106.241801.
- [57] V. Khachatryan et al. “Angular coefficients of Z bosons produced in pp collisions at $\sqrt{s}=8$ TeV and decaying to $+ -$ as a function of transverse momentum and rapidity”. In: *Physics Letters B* 750 (2015), pp. 154–175. DOI: 10.1016/j.physletb.2015.08.061.
- [58] J.J. Aubert et al. “The ratio of the nucleon structure functions F2N for iron and deuterium”. In: *Physics Letters B* 123.3 (1983), pp. 275–278. DOI: 10.1016/0370-2693(83)90437-9.
- [59] R. Baier et al. “Radiative energy loss of high energy partons traversing an expanding QCD plasma”. In: *Phys. Rev. C* 58 (3 Sept. 1998), pp. 1706–1713. DOI: 10.1103/PhysRevC.58.1706.
- [60] François Arleo, Charles-Joseph Naim, and Stephane Platchkov. “Initial-state energy loss in cold QCD matter and the Drell-Yan process”. In: *Journal of High Energy Physics* 2019.1 (Jan. 2019), p. 129. DOI: 10.1007/JHEP01(2019)129.
- [61] M. B. Johnson, B. Z. Kopeliovich, and Ivan Schmidt. “Cronin effect in the Drell-Yan reaction”. In: *Phys. Rev. C* 75 (6 June 2007), p. 064905. DOI: 10.1103/PhysRevC.75.064905.
- [62] K Ackerstaff et al. “Nuclear effects on $R = L/T$ in deep-inelastic scattering”. In: *Physics Letters B* 475.3 (2000), pp. 386–394. DOI: 10.1016/S0370-2693(99)01493-8.

- [63] S. Dasu et al. “Measurement of the Difference in $R = \frac{\sigma_L}{\sigma_T}$ and of $\frac{\sigma_A}{\sigma_D}$ in Deep-Inelastic $e - D$, $e - Fe$, and $e - Au$ Scattering”. In: *Phys. Rev. Lett.* 60 (25 June 1988), pp. 2591–2594. DOI: 10.1103/PhysRevLett.60.2591.
- [64] J. Seely et al. “New Measurements of the European Muon Collaboration Effect in Very Light Nuclei”. In: *Phys. Rev. Lett.* 103 (20 Nov. 2009), p. 202301. DOI: 10.1103/PhysRevLett.103.202301.
- [65] Klaus Rith. “Present Status of the EMC effect”. In: *Subnucl. Ser.* 51 (2015), pp. 431–449. arXiv: 1402.5000 [hep-ex].
- [66] Ivan Schmidt. *Physics of Nuclear Antishadowing*. 2005. arXiv: hep-ph/0511173 [hep-ph].
- [67] V. Guzey. *Leading twist nuclear shadowing in tagged unpolarized and polarized DIS on deuterium*. 2014.
- [68] C. Vallee. “Study Of Nuclear Effects On The Structure Function Of The Nucleon By Comparing Anti-neutrinos Interactions On Neon And Deuterium”. PhD thesis. Orsay, LAL, 1984.
- [69] K. J. Anderson et al. “Production of Muon Pairs by 225-GeV/c π^\pm , K^+ , p^\pm Beams on Nuclear Targets”. In: *Phys. Rev. Lett.* 42 (15 Apr. 1979), pp. 944–947. DOI: 10.1103/PhysRevLett.42.944.
- [70] D. M. Kaplan et al. “Study of the High-Mass Dimuon Continuum in 400-GeV Proton-Nucleus Collisions”. In: *Phys. Rev. Lett.* 40 (7 Feb. 1978), pp. 435–438. DOI: 10.1103/PhysRevLett.40.435.
- [71] Matthias Aicher, Andreas Schäfer, and Werner Vogelsang. “Threshold-resummed cross section for the Drell-Yan process in pion-nucleon collisions at COMPASS”. In: *Phys. Rev. D* 83 (11 June 2011), p. 114023. DOI: 10.1103/PhysRevD.83.114023.
- [72] Matthias Aicher, Andreas Schäfer, and Werner Vogelsang. “Soft-Gluon Resummation and the Valence Parton Distribution Function of the Pion”. In: *Phys. Rev. Lett.* 105 (25 Dec. 2010), p. 252003. DOI: 10.1103/PhysRevLett.105.252003.
- [73] K. Wijesooriya, P. E. Reimer, and R. J. Holt. “Pion parton distribution function in the valence region”. In: *Phys. Rev. C* 72 (6 Dec. 2005), p. 065203. DOI: 10.1103/PhysRevC.72.065203.
- [74] B Adams et al. “COMPASS++/AMBER: Proposal for Measurements at the M2 beam line of the CERN SPS Phase-1: 2022-2024”. In: CERN-SPSC-2019-022. SPSC-P-360 (May 2019). The collaboration has not yet constituted itself, thus instead of a Spokesperson currently the nominated Contact Person is acting in place.
- [75] M. Przybycień, A. Szczurek, and G. Ingelman. “Properties of HERA events from DIS on pions in the proton”. In: *Zeitschrift für Physik C Particles and Fields* 74.3 (Sept. 1997), pp. 509–515. DOI: 10.1007/s002880050413.
- [76] WA70-Collaboration et al. “High transverse momentum prompt photon production by π^- and π^+ on protons at 280 GeV/c”. In: *Zeitschrift für Physik C Particles and Fields* 37.4 (Dec. 1988), pp. 535–544. DOI: 10.1007/BF01549712.
- [77] A. Bordner et al. “Experimental information on the pion gluon distribution function”. In: *Zeitschrift für Physik C: Particles and Fields* 72.2 (June 1996), p. 249. DOI: 10.1007/s002880050242.
- [78] P. C. Barry et al. “First Monte Carlo Global QCD Analysis of Pion Parton Distributions”. In: *Phys. Rev. Lett.* 121 (15 Oct. 2018), p. 152001. DOI: 10.1103/PhysRevLett.121.152001.
- [79] J. F. Owens. “ Q^2 -dependent parametrizations of pion parton distribution functions”. In: *Phys. Rev. D* 30 (5 Sept. 1984), pp. 943–946. DOI: 10.1103/PhysRevD.30.943.
- [80] P. Aurenche et al. “The gluon content of the pion from high-pt photon production”. In: *Physics Letters B* 233.3 (1989), pp. 517–521. DOI: 10.1016/0370-2693(89)91351-8.
- [81] M. Glück, E. Reya, and A. Vogt. “Pionic parton distributions”. In: *Zeitschrift für Physik C Particles and Fields* 53.4 (Dec. 1992), pp. 651–655. DOI: 10.1007/BF01559743.
- [82] P. J. Sutton et al. “Parton distributions for the pion extracted from Drell-Yan and prompt photon experiments”. In: *Phys. Rev. D* 45 (7 Apr. 1992), pp. 2349–2359. DOI: 10.1103/PhysRevD.45.2349.

- [83] M. Glück, E. Reya, and I. Schienbein. “Pionic parton distributions revisited”. In: *The European Physical Journal C - Particles and Fields* 10.2 (Sept. 1999), pp. 313–317. DOI: 10.1007/s100529900124.
- [84] Raza Sabbir Sufian et al. “Pion valence quark distribution from matrix element calculated in lattice QCD”. In: *Phys. Rev. D* 99 (7 Apr. 2019), p. 074507. DOI: 10.1103/PhysRevD.99.074507.
- [85] G Baum, J Kynäräinen, and A Tripet. *COMPASS: a proposal for a common muon and proton apparatus for structure and spectroscopy*. Tech. rep. CERN-SPSLC-96-14. SPSLC-P-297. Geneva: CERN, 1996.
- [86] P. Abbon et al. “The COMPASS experiment at CERN”. In: *Nuclear Instruments and Methods in Physics Research Section A: Accelerators, Spectrometers, Detectors and Associated Equipment* 577.3 (2007), pp. 455–518. DOI: 10.1016/j.nima.2007.03.026.
- [87] P. Abbon et al. “The COMPASS setup for physics with hadron beams”. In: *Nuclear Instruments and Methods in Physics Research Section A: Accelerators, Spectrometers, Detectors and Associated Equipment* 779 (2015), pp. 69–115. DOI: 10.1016/j.nima.2015.01.035.
- [88] V. Agoritsas. “A Sealed Metal Argon Ionization Chamber (Argonion)”. In: *IEEE* 28.3 (1981).
- [89] H. W. Atherton et al. “Precise Measurements of Particle Production by 400-GeV/c Protons on Beryllium Targets”. In: (1980).
- [90] A. Abragam. “The Principles of Nuclear Magnetism”. In: *The Clarendon Press Oxford* (1961).
- [91] B.M.Veit [COMPASS Analysis Meeting]. *Drell-Yan trigger studies (2015/2018 data)*. Tech. rep. Mar. 2019.
- [92] Fabio Sauli. “The gas electron multiplier (GEM): Operating principles and applications”. In: *Nuclear Instruments and Methods in Physics Research Section A: Accelerators, Spectrometers, Detectors and Associated Equipment* 805 (2016). Special Issue in memory of Glenn F. Knoll, pp. 2–24. DOI: 10.1016/j.nima.2015.07.060.
- [93] F. Thibaud. “Développement de détecteurs Micromegas pixellisés pour les hauts flux de particules et évaluation de la contribution diffractive à la leptoproduction de hadrons à COMPASS.” PhD thesis. Instrumentation and Detectors: Université Paris Sud - Paris XI, French. <NNT : 2014PA112239>. <tel-01084556>, 2014.
- [94] M Bodlak et al. “New data acquisition system for the COMPASS experiment”. In: *Journal of Instrumentation* 8.02 (Feb. 2013), pp. C02009–C02009. DOI: 10.1088/1748-0221/8/02/c02009.
- [95] R. Heitz. “A Drift Chamber to Measure Charged Particles at COMPASS-II”. In: *APS Division Nuclear Physics Newport News Meeting, abstract id. KJ.004* (2013).
- [96] Nikhef Harry van der Graaf. *Gaseous Detectors History and New Developments*. Mar. 2008.
- [97] Charles T. R. Wilson. “On an expansion apparatus for making visible the tracks of ionising particles in gases and some results obtained by its use”. In: *Proc.Roy.Soc.Lond.* A87.595 (1912), pp. 277–292. DOI: 10.1098/rspa.1912.0081.
- [98] A. Roberts. “Development of the Spark Chamber: A Review”. In: *Review of Scientific Instruments* 32, 482 (1961).
- [99] Nuclear Power. 2019. URL: <https://www.nuclear-power.net/nuclear-engineering/radiation-detection/gaseous-ionization-detector/>.
- [100] 674, ed. Vol. 246. AIP Conference Proceedings, 2003.
- [101] V.N. Bychkov et al. “The large size straw drift chambers of the COMPASS experiment”. In: *Nuclear Instruments and Methods in Physics Research Section A: Accelerators, Spectrometers, Detectors and Associated Equipment* 556.1 (2006), pp. 66–79. DOI: <https://doi.org/10.1016/j.nima.2005.10.026>.
- [102] K. Platzer et al. “Mapping the large area straw detectors of the COMPASS experiment with X-rays”. In: *IEEE Transactions on Nuclear Science* 52.3 (June 2005), pp. 793–798. DOI: 10.1109/TNS.2005.850971.

- [103] H. Pereira. “Développement de chambres à derive pour les hauts flux dans l’expérience COMPASS”. PhD thesis. 2001.
- [104] J.A. Merlin. “Study of long-term sustained operation of gaseous detectors in CMS”. PhD thesis. 2016.
- [105] T. Ferguson et al. “Swelling phenomena in anode wires aging under a high accumulated dose”. In: *Nuclear Instruments and Methods in Physics Research Section A: Accelerators, Spectrometers, Detectors and Associated Equipment* 515.1 (2003). Proceedings of the International Workshop on Aging Phenomena in Gaseous Detectors, pp. 266–277. DOI: 10.1016/j.nima.2003.09.009.
- [106] T. Szameitat. “New Geant4-based Monte Carlo Software for the COMPASS- II Experiment at CERN”. PhD thesis. 2017.
- [107] R. Frühwirth. “Application of Kalman filtering to track and vertex fitting”. In: *Nuclear Instruments and Methods in Physics Research Section A: Accelerators, Spectrometers, Detectors and Associated Equipment* 262.2 (1987), pp. 444–450. DOI: [https://doi.org/10.1016/0168-9002\(87\)90887-4](https://doi.org/10.1016/0168-9002(87)90887-4).
- [108] E.J Wolin and L.L Ho. “Covariance matrices for track fitting with the Kalman filter”. In: *Nuclear Instruments and Methods in Physics Research Section A: Accelerators, Spectrometers, Detectors and Associated Equipment* 329.3 (1993), pp. 493–500. DOI: 10.1016/0168-9002(93)91285-U.
- [109] Torbjörn Sjöstrand, Stephen Mrenna, and Peter Skands. “PYTHIA 6.4 physics and manual”. In: *Journal of High Energy Physics* 2006.05 (May 2006), pp. 026–026. DOI: 10.1088/1126-6708/2006/05/026.
- [110] Torbjörn Sjöstrand, Stephen Mrenna, and Peter Skands. “A brief introduction to PYTHIA 8.1”. In: *Computer Physics Communications* 178.11 (2008), pp. 852–867. DOI: 10.1016/j.cpc.2008.01.036.
- [111] R.Longo. “Target spin (in)dependent asymmetries in Drell-Yan at COMPASS experiment”. PhD thesis. 2018.
- [112] R.Longo. *HPC at COMPASS: The Blue-Waters project*. 2018.
- [113] C. et al. Riedl. “Exploratory phase report, Mapping Proton Quark Structure using Petabytes of COMPASS data”. In: (2017).
- [114] M. Meyer. “Blue Waters, A Petascale Computer Facility, for the reconstruction of CERN COMPASS-II data”. <https://indico.cern.ch/event/570680/contributions/2311100/>. In: *Conference SPIN16* (2016).
- [115] *Frontera Facility at the Texas Advanced Computing Center*. URL: <https://www.tacc.utexas.edu/systems/frontera>.
- [116] B. Adeva. In: *NIMA* 419 60 (1998).
- [117] W. Meyer. “Ammonia as a polarized solid target material”. In: *NIMA* 526 12 (2004).
- [118] A. Berlin. “Polarized Solid Ammonia Targets for the COMPASS Experiment at CERN”. PhD thesis. Ruhr-Universität Bochum, 2015.
- [119] J. Koivuniemi et al. “COMPASS: Target material data of run 2015”. In: https://compassum03.cern.ch/elog/target_polar/215 (2015).
- [120] F.A.L. Dullien. *Porous Media Fluid Transport and Pore Structure (2nd ed.)*. 1991. DOI: 10.1016/C2009-0-26184-8.
- [121] F. Pobell. *Matter and Methods at Low Temperatures*. Springer, 2007.
- [122] *Helium Phase Diagram*. URL: <http://universe-review.ca/F13-atom06.htm>.
- [123] L Skrbek. “Quantum turbulence”. In: *Journal of Physics: Conference Series* 318.1 (Dec. 2011), p. 012004. DOI: 10.1088/1742-6596/318/1/012004.
- [124] S. Striganov (FNAL). “Atomic and nuclear properties of materials”. In: *PDG* (2018).
- [125] Geant4 Collaboration. *Physics Reference Manual 10.4*. Tech. rep. 2017.

- [126] V.Andrieux *et al.* “Transverse-spin-dependent azimuthal Drell-Yan asymmetries from COMPASS 2015 data”. In: (2017).
- [127] M. Aghasyan et al. “First Measurement of Transverse-Spin-Dependent Azimuthal Asymmetries in the Drell-Yan Process”. In: *Phys. Rev. Lett.* 119 (11 Sept. 2017), p. 112002. DOI: 10.1103/PhysRevLett.119.112002.
- [128] Stefano Catani and Massimiliano Grazzini. “Next-to-Next-to-Leading-Order Subtraction Formalism in Hadron Collisions and its Application to Higgs-Boson Production at the Large Hadron Collider”. In: *Phys. Rev. Lett.* 98 (22 May 2007), p. 222002. DOI: 10.1103/PhysRevLett.98.222002.
- [129] Sayipjamal Dulat et al. “New parton distribution functions from a global analysis of quantum chromodynamics”. In: *Phys. Rev. D* 93 (3 Feb. 2016), p. 033006. DOI: 10.1103/PhysRevD.93.033006.
- [130] Tie-Jiun Hou et al. “Reconstruction of Monte Carlo replicas from Hessian parton distributions”. In: *Journal of High Energy Physics* 2017.3 (Mar. 2017), p. 99. DOI: 10.1007/JHEP03(2017)099.
- [131] M.T.Simnad. “Nuclear Reactors: Shielding Materials”. In: *Encyclopedia of Materials: Science and Technology (Second Edition) Pages 6377-6384* (2001).
- [132] P. K. Malhotra. “A compilation of results from different experiments”. In: *Proceedings of the Drell-Yan Workshop (Fermilab)* (1982).

Titre: Mesure de Sections Efficaces Absolues Drell-Yan à l'aide d'un faisceau de π^- de 190-GeV à COMPASS

Mots clés: Drell-Yan, Section Efficace, Pion

Résumé: La prise de données réalisée en 2015 par la collaboration COMPASS au CERN a permis de collecter un nombre significatif de paires de muons de grande masse. Ces dernières proviennent de l'interaction d'un faisceau de pions négatifs d'impulsion 190 GeV/c sur des cibles d'ammoniac (NH_3), d'aluminium (Al) ou de tungstène (W). Ce travail de thèse décrit les différentes étapes d'analyse des données de Drell-Yan dans la région de masse entre 4.3 et 8.5 GeV/ c^2 , depuis la reconstruction des traces du pion incident et des muons diffusés, jusqu'à l'extraction des sections efficaces finales. Ces étapes comprennent la détermination du flux incident et des den-

sités des trois cibles, l'évaluation des différentes efficacités expérimentales, le calcul de l'acceptance de l'appareillage par simulation Monte-Carlo et la réduction des données à des paires de muons. Présentées en fonction de la variable de Feynman x_F et de l'impulsion transverse p_T , les sections efficaces Drell-Yan sont comparées aux calculs théoriques aux ordres NLO et NNLO, ainsi qu'aux résultats des expériences antérieures. Une interprétation plus poussée des résultats donnera accès aux distributions des partons dans le pion et à l'étude des effets de la matière froide dans les noyaux.

Title: Measurement of Absolute Drell-Yan Cross-Sections using a 190-GeV π^- beam at the COMPASS-II Experiment

Keywords: Drell-Yan, Cross-Section, Pion

Abstract: The COMPASS collaboration at CERN collected a significant amount of Drell-Yan data in 2015. The measured lepton pairs originate from the interaction of a negatively charged pion beam at 190 GeV/c with ammonia targets (NH_3), aluminum (Al) or tungsten (W). The analysis step using the Drell-Yan data are discussed in the mass range between 4.3 and 8.5 GeV/ c^2 , starting from the reconstruction of the incoming pion beam and the scattered muons, until the extraction of the Drell-Yan cross-sections. These steps include the determination of the incoming beam flux and the

three target densities, the overall efficiency of the experimental apparatus, the acceptance of this spectrometer using Monte-Carlo simulations, and the reduction of the initial data to muon pairs. The Drell-Yan cross-sections, expressed in terms of the scaling variable x_F and the transverse momentum p_T , are compared with theoretical predictions at NLO and NNLO, as well as some previously published results. An advanced interpretation of these results would give access to the partonic distribution of the pion and lead to the study of cold nuclear matter effects.

